Strongly Correlated Multi-Orbital Systems

A Continuous-Time Quantum Monte Carlo Analysis

Dissertation zur Erlangung
des naturwissenschaftlichen Doktorgrades
der Julius-Maximilians-Universität Würzburg

Nicolaus Parragh

December 17, 2013

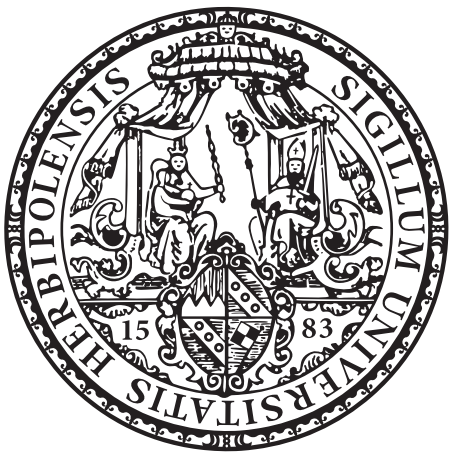

vorgelegt von *Dipl.-Ing. Nicolaus Parragh* aus Salzburg.

Eingereicht am *30. September 2013* bei der Fakultät für Physik und Astronomie

1. Gutachter: *Prof. Dr. Giorgio Sangiovanni* (Universität Würzburg)
2. Gutachter: *Prof. Dr. Fakher F. Assaad* (Universität Würzburg)
der Dissertation.

Vorsitzender: *Prof. Dr. Edwin Batke* (Universität Würzburg)

1. Prüfer: *Prof. Dr. Giorgio Sangiovanni* (Universität Würzburg)
2. Prüfer: *Prof. Dr. Fakher F. Assaad* (Universität Würzburg)
3. Prüfer: *Prof. Dr. Ralph Claessen* (Universität Würzburg)
im Promotionskolloquium.

Tag des Promotionskolloquiums: *9. Dezember 2013*
Doktorurkunde ausgehändigt am:

Abstract

In this thesis I present results concerning realistic calculations of correlated fermionic many-body systems. One of the main objectives of this work was the implementation of a hybridization expansion continuous-time quantum Monte Carlo (CT-HYB) algorithm and of a flexible self-consistency loop based on the dynamical mean-field theory (DMFT). DMFT enables us to treat strongly correlated electron systems numerically. After the implementation and extensive testing of the program we investigated different problems to answer open questions concerning correlated systems and their numerical treatment.
In Chapter 1 I will introduce the Anderson impurity model and different solvers for it, with more focus on the specific one which I implemented. The implementation of the solver is based on the Krylov algorithm which is highly efficient for solving the Anderson impurity model for many correlated orbitals at low temperatures. At the end of chapter 1 I will present some benchmark results.
In Chapter 2 I will introduce the density-functional theory and the dynamical mean-field theory. I will then come to the first methodological problem in the context of the treatment of strongly correlated systems. This concerns the downfolding of the Hamiltonian which is needed to obtain low-energy problems that can be treated numerically in the dynamical mean-field theory. I will first briefly introduce different methods and then present two studies on the effect of the basis set in DMFT. Another still open problem is the question how the splitting up between the correlated and uncorrelated electrons has to be calculated if the input of the electronic bands is coming from first principle calculations. In this work a scheme to treat such a splitting up by a self-consistently determined Hartree interaction is studied. In the end of the chapter I will show results for two extensions to the DMFT which allow the treatment of more complex structures.
The second class of problems I worked on, which I am going to present in Chapter 3, are the different types of local interactions. Since the only recently introduced CT-HYB is able to treat very general interactions the question arises which interaction to use for certain problems. This is an especially crucial point since certain (approximations of) interactions enable us to optimize the runtime of simulations. For one such approximation we found a new set of quantum numbers and studied a system of up to seven orbitals which undergoes the orbital selective Mott transition with it. This set of quantum numbers was also successfully used for a study on $SrCoO_3$ in which the spin ground state of the Co atom was investigated. For general interactions a numerical algorithm is described which enables us to find the minimal basis for the CT-HYB and thus the

maximal speedup for calculations without approximations. Finally I will present a study of the different types of local interactions which are currently used for studying strongly correlated electron systems using Tanabe-Sugano diagrams.
In Appendix A I will give a general overview of the implementation and an explanation of the parameters which serve as an input for the program.

Zusammenfassung

Die vorliegende Dissertation beschäftigt sich mit der numerischen Berechnung von realistischen stark korrelierten fermionischen Vielteilchensystemen. Die Hauptzielsetzung dieser Arbeit war die Implementierung und das Testen einer zeitkontinuum Quanten Monte Carlo Methode in der Hybridisierungsentwicklung und einer flexiblen selbstkonsistenten Schleife basierend auf der dynamischen Molekularfeldtheorie die es uns ermöglicht solch stark korrelierte Systeme zu berechnen. Nach der Implementierung wurde das Programm ausführlich getest und es wurden Studien an unterschiedlichen Problemen durchgeführt.
In Kapitel 1 werde ich das Anderson Störstellen-Problem und verschiedene Lösungsansätze für dieses Problem vorstellen. Besonderes Augenmerk werde ich auf den speziellen Lösungsansatz legen den ich implementiert habe. Am Ende des Kapitels werde ich Benchmark-Ergebnisse präsentieren.
In Kapitel 2 werde ich die Dichte-Funktional-Theorie und die dynamische Molekularfeld-Theorie vorstellen. Danach komme ich zu den ersten methodischen Problemen im Zusammenhang mit der Behandlung von stark korrelierten Systemen. Dies betrifft das so genannte downfolding des Hamilton Operators das benötigt wird um niedrig Energie Hamilton Operatoren zu erhalten welche numerisch im Rahmen der dynamischen Molekularfeldtheorie behandelt werden können. Ich werde zuerst die Methodik erläutern und danach zwei Studien präsentieren, die mit dem Programm gemacht wurden, über die Auswirkungen eines vergrößerten Basissatzes auf Modellrechnungen. Eine weitere noch offene Frage, die bei der realistischen Berechnung von Fesktörpern auftritt, ist wie die Aufspaltung zwischen korrelierten und unkorrelierten Bändern berechnet werden muss wenn die Bandstruktur ab-initio berechnet wurde. In dieser Arbeit wird ein Schema angewandt welches physikalisch durch die Hartree Wechselwirkung motiviert ist. Im Rahmen einer Studie werde ich Ergebnisse präsentieren die mit diesem Schema berechnet wurden.
In Kapitel 3 beschäfitge ich mich mit lokalen Wechselwirkungen. Da die erst vor kurzem vorgestellte zeitkontinuum Quanten Monte Carlo Methode in der hybridisierungs Entwicklung in der Lage ist allgemeine lokale Wechselwirkungen zu behandeln stellt sich die Frage welche lokale Wechselwirkung für welche Probleme verwendet werden muss. Dies ist besonders deswegen wichtig weil die Laufzeit des Programms stark von der gewählten Wechselwirkung abhängt. Für eine spezielle Wechselwirkung konnte im Laufe dieser Arbeit ein neuer Satz von Quantenzahlen gefunden werden die diese Wechselwirkung speziell für Rechnungen mit vielen Orbitalen erheblich billiger macht. Dies

wurde auch für die Studie von $SrCoO_3$ verwendet die im Anschlußpräsentiert wird. Für allgemeine Wechselwirkungen werde ich einen Algorithmus vorstellen der die Wechselwirkung auf eine minimale Form bringt und somit Rechnungen so billig wie möglich macht. Schließlich werde die verschiedenen Wechselwirkungen die zur Zeit zum Einsatz kommen mit Hilfe der Tanabe Sugano Diagramme diskutieren. Im Anhang A gebe ich allgemeine Erläuterungen über die Implementationsdetails und einen Überblick über die meist verwendeten Parameter des Programms.

Contents

Introduction

Since the dawn of mankind the fortune of civilizations is deeply connected with their ability to form and manipulate solids to their liking. This is reflected in the classification of cultural ages by stone age, bronze age or iron age. The current time period might well be labeled the silicon age [1, 2] or the plastic age [3]. This age is also responsible for a paradigm shift in the treatment of materials. The advances in experimental techniques and theoretical descriptions allowed us to understand the "inner workings" of solids and thus enabled us to describe and create novel materials. These novel materials do not only have properties like hard or flexible, but are responding to changes in their environment which makes a categorization of these materials as *smart* or *functional* reasonable. Also completely new states of matter were found in the last century with the most prominent being the superconducting state, which allows electrons to travel through a material without resistance. The high-temperature superconductivity is currently considered the *holy grail* of solid-state physics. For a description of these phenomena and properties of solids a treatment of the electrons is often sufficient. In recent years a new class of materials has been in the spot light of the solid state community due to their interesting properties. These materials show a large internal reaction to small external perturbations and are thus the ideal candidates for functional materials. From a theoretical point of view these materials pose a new challenge since they are not treatable by the standard single-particle approximation, which describes particles as products of each individual particle influenced by a mean cloud consisting of the rest of the system, but rather by a description of all particles. Mathematically this can be formulated as the inequality of a product of physical observables, O_1 for particle one and O_2 for particle two, and the observable of the product

$$\langle O_1 \rangle \langle O_2 \rangle \neq \langle O_1 O_2 \rangle \,.$$

The above formula is expressing that two quantities are correlated and hence these materials are called (strongly) correlated systems or, if we specify the particles to be electrons, (strongly) correlated electron systems.
In condensed matter physics we in principle know how the constituents in a solid affected by all other constituents behave exactly. Actually the equation which describes the

constituents in a solid, if relativistic effects can be neglected, is written down easily

$$\begin{aligned} H = &\sum_{il} \frac{-e^2}{4\pi\epsilon_0} \frac{Z_l}{|\vec{r}_i - \vec{R}_l|} + \\ &\sum_i -\frac{\hbar^2 \Delta_i}{2m_e} + \frac{1}{2} \sum_{i \neq j} \frac{e^2}{4\pi\epsilon_0} \frac{1}{|\vec{r}_i - \vec{r}_j|} + \\ &\sum_l -\frac{\hbar^2 \Delta_l}{2M_l} + \frac{1}{2} \sum_{l \neq m} \frac{e^2}{4\pi\epsilon_0} \frac{Z_l Z_m}{|\vec{R}_l - \vec{R}_m|} \end{aligned}$$

where $\vec{r}_i$ and $\vec{R}_l$ denote the position of electron i and ion l with charge $-e$ and $Z_l e$ respectively. Δ_i is the Laplace operator, m_e and M_l is the mass of electrons and nuclei respectively, ϵ_0 is the vacuum dielectric constant and $\hbar$ is the reduced Planck constant. It is however, due to the sheer number of particles involved in a macroscopic material, impossible to solve. To make the problem more tractable the description has to be approximated and this is the crucial step in theoretical solid state physics. We want to keep the features necessary to describe the physics we are interested in and dispose of the rest. One can even go one step further: We already know that that a full description of the system would yield the result of the experiment and thus a solution of the full Hamiltonian would not tell us anything about the underlying principles. A model, on the other hand, in which we can easily tune the parameters, and that describes the system sufficiently leads to the understanding of physics in the system.
The first approximation one typically performs is the Born-Oppenheimer approximation [4] which decouples the electrons from the dynamics of the lattice. What we are left with to solve is an equation depending on a large number of electrons and a solution can only be found for a very small number of them. If we assume that the electrons are not correlated, or that the correlation can be expressed as a mean-field, the equation factorizes into a product of equations and the effort grows linearly with the number electrons one wants to treat. The effort can be further reduced by using symmetries and one finally ends up with a description which is numerically tractable. For correlated systems the factorization is not possible anymore and the numerical effort grows exponentially with the number of electrons, for this the name exponential wall was coined [5]. This led to the development of new approximations and numerical techniques which allow us to treat correlated systems to understand some of the processes which are responsible for the physical properties.
This work is dedicated to implement, improve and investigate the applicability of such a method. As a first step to achieve this goal we implemented a numerical method to treat correlated systems and improved its usability for multi-orbital systems by code optimization. We then used this implementation for investigations on different open questions regarding the method. I am going to present these investigations in this work. The implementation was also used by us for studying a realistic system which I am also

going to present. During these studies we developed novel techniques which enlarge the space of tractable problems and I am also going to discuss them in this work.
The thesis is divided into three parts:
In Chapter 1 I will first introduce the Anderson impurity model (AIM) describing an impurity with an on-site interaction coupling to a bath of non-interacting electrons. This model, although it is quite simple, is not solvable analytically and there are many different methods available to solve it numerically. I will give an overview of these methods and then in detail discuss the one which was also implemented during the course of this work. The chosen method is especially useful for impurities with a lot of orbitals and can treat arbitrary local interactions. A great effort was put into speeding up the implementation for systems with many interacting orbitals. I will also give a description of the Monte Carlo method which is used by the solver. After the introduction of different algorithms which can be used for the implementation of the solver the measurement of quantities is discussed and finally some benchmark results of our newly implemented solver are presented.
In Chapter 2 I will focus more on infinite lattice problems and I will introduce the merger of two methods, the density functional theory in its local density approximation and the dynamical mean-field theory, called LDA+DMFT. In the following sections I will describe the two methods and also explain the techniques necessary to combine the two. One is the calculation of the double counting correction which is still an open problem and I will briefly introduce several proposed double counting corrections. The second technique which enables us to obtain a low-energy description of the electrons in the single particle approximation suitable as an input for further calculations also still poses some problems. It is e.g. not clear if the low-energy Hamiltonian should contain only the correlated electrons or also uncorrelated electrons. One would in principle expect that the description of the system becomes better when more orbitals are included. In a study conducted for two models, one with correlated d-electrons only and the other one with additional uncorrelated p-electrons, which I am going to present, we showed that the Fermi surface has a different shape for the two models and it also shows different behavior when the crystal-field between the two d-electrons is changed. After this I will present another study we conducted for a simple model with varying hybdridization strengths. In this study we were more concerned about the effects of the inclusion of uncorrelated orbitals on other quantities i.e. the spin susceptibility and the expansion order of the solver. After that I will review the maximum entropy method (MEM), for performing the numerical analytical continuation to the real axis. Then I will introduce an extension of the DMFT which consists of the inclusion of a Hartree-type interaction, in the p-manifold and between the d- and p-electrons, for which I will also present a study for which we use the analytical continuation discussed before. Finally I will present two further extensions to the DMFT which were implemented into the program. The first extension is the "layer"-DMFT which allows us to treat heterostructures and the second extension, the nano-DΓA, enables us to deal with complex structures in real space.

In Chapter 3 I will first introduce the Coulomb interaction for the free atom and its interaction matrix U. This interaction matrix is then transformed into cubic harmonics, the eigenbasis of the octahedral crystal-field operator, which I am going to use as a starting point for introducing other approximations. The first approximation is the until recently most often used density-density approximation which only takes density-density interactions of the correlated electrons into account. In the next section I will introduce an SU(2)-symmetric interaction, often called Kanamori interaction. For this interaction a special set of quantum numbers was found by us which is accelerating the numerical solution of the Anderson impurity model of up to a factor of $\mathcal{O}(100)$ depending on the number of orbitals compared to the typically used conserved quantities. Using this set of quantum numbers we studied the orbital selective Mott transition in a system with up to seven orbitals with the Kanamori interaction. After that I will discuss a study we conducted which examines the spin state of $SrCoO_3$. Then I will introduce an algorithm using the experience we have obtained from the study of the Kanamori interaction that is able to generate a minimal structure of any local Hamiltonian, thus resulting in the minimal numerical effort possible for general interactions without approximations. Finally I will discuss the atomic energy level of the different approximations of the local interaction introduced in this chapter using Tanabe-Sugano diagrams.
In Appendix A I will give an introduction to the program, which we called *w2dynamics*. I will motivate the two building blocks of the program, which consists of a block containing the self-consistency written in Python and another block for the solver of the AIM. Then I will give some explanatory notes on these blocks and finally I will present a list of all the parameters which can be used in the program and explain them.
During this thesis I will give useful information, which are highlighted by a blue background, for users and developers of *w2dynamics*. I am going to use natural units in this work and if somebody is not familiar with the Greens function formalism I recommend to read [6] or another good book on this subject.

1. The Anderson Impurity Model

In this chapter I will first introduce the Anderson Impurity Model (AIM), then, in Section 1.1, I will briefly discuss some methods standardly used to solve the AIM model numerically. After that, in Section 1.2, I will give a short theoretical introduction to Monte Carlo algorithms which we are going to need in the next Section 1.3. There I will introduce the Continuous Time Hybridization Expansion Quantum Monte Carlo algorithm (CT-HYB), whose implementation was a major part of this thesis. In the final Section 1.4 I will show how one can measure observables and other important quantities in CT-HYB simulations.

Introduction

In the 30s of the last century experimentalists started to study pure metallic systems with a few impurities added. In such doped systems, e.g. Cu with an addition of a magnetic impurity of the order of 10^{-5} per unit volume, the conductivity reaches a minimum at a certain temperature and then increases as $-\ln T$ when the temperature is further decreased. To find a theoretical description for such a behaviour in the 1940s and 1950s models with an exchange interaction were proposed which consist of a local spin around the impurity

$$\vec{s} = \sum_{kk'\sigma\sigma'} c^{\dagger}_{k\sigma} \vec{\sigma}_{\sigma\sigma'} c_{k'\sigma'}$$

where $\vec{\sigma}$ are the Pauli matrices and $c^{(\dagger)}$ the (creation) annihilation operators of the free electrons. The Hamiltonian describing the impurity in the host material, which is known as the Kondo Hamiltonian is then given by

$$H_{Kondo} = \sum_{k\sigma} \epsilon_k n_{k\sigma} + J\vec{S} \cdot \vec{s}$$

where ϵ_k is the dispersion relation of the free electrons, S is the local atomic spin, as Anderson noted, *given by God* [9] which is connected by the empirical exchange integral J. In 1964 Kondo [8] was able to show that the $-lnT$ behaviour of the conductance appears in second order perturbation theory of the Kondo model, thus solving this long-standing mystery. The increase of the resistivity is due to the scattering of conductance electrons on the local impurity. This scattering processes lead to the formation of a Kondo cloud consisting of the conductance electrons screening the magnetic moment of the impurity. The peak in the spectrum of the system due to this resonance is called

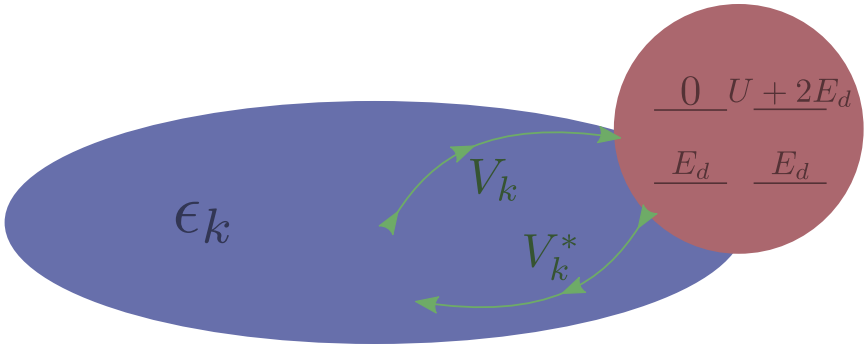

Figure 1.1.: The Anderson Impurity Model is depicted above. The green arrows denote the hopping with an amplitude of V_k to and from the impurity into the bath. The bath is visualized by the blue circle consisting of electrons with a dispersion relation of ϵ_k. The impurity, the red circle, has the discrete atomic energy levels 0 if it is empty, $U + 2E_d$ if 2 electrons are on the impurity and E_d when it is singly occupied with a spin degeneracy of 2, which is needed to form the singlet.

the Kondo peak. This explanation could, however, not answer the question of why such local moments form.
In 1961 the AIM was proposed by P. W. Anderson [7] which extends the Kondo model to identify the source of the local moment. In the model he replaced the local magnetic spin by an impurity with an on-site interaction and a bath coupled to it. In its simplest one band form the AIM Hamiltonian is given by

$$H_{AIM} = \sum_{k\sigma} \epsilon_k n_{k\sigma} + U n_{d\uparrow} n_{d\downarrow} + E_d(n_{d\uparrow} + n_{d\downarrow}) + \sum_{k\sigma} V_k(d_\sigma^\dagger c_{k\sigma} + cc). \tag{1.1}$$

In this Hamiltonian one can still identify the atomic Hamiltonian which is described by the on-site energy E_d of each electron and the Coulomb repulsion U if both orbitals of the atom are occupied. Then we have the term of the free electron with the dispersion relation ϵ_k in the lead. Finally, the term which makes this model interesting and impossible to solve analytically, is the hybridization term V_k which describes the hopping amplitude to and from the atom into or out of the lead. The $d^{(\dagger)}$ and $c^{(\dagger)}$ are the (creation)/annihilation operators on the atom and in the lead respectively. For an in-depth discussion of the AIM and its interesting physics I refer the interested reader to [11]. From a pictorial perspective one can think of the AIM as an atom in a bath of electrons as depicted in Figure 1.1. These electrons can hop onto the atom, the hopping process is however suppressed if the orbital of the opposing spin direction is already occupied since the electron is repelled by the other electron. Due to the Pauli-principle the motion is completely suppressed if the equal spin direction is occupied.

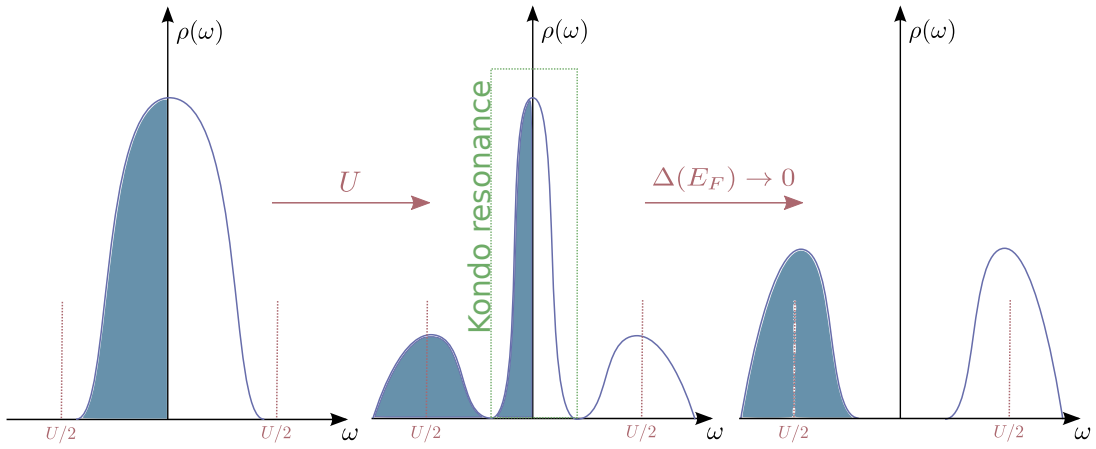

Figure 1.2.: The spectra of the AIM at half-filling in different states. On the left side of the figure the non-interacting density of states is sketched. When one turns on U one obtains the famous three peak structure of the AIM. In the middle the Kondo resonance of the conduction electrons with the local impurity forms. Left and right of it with a distance of $|U/2|$ the satellite peaks are building up. When the hybridization function Δ at the Fermi energy vanishes the resonance disappears and one recovers atomic physics.

The new physics included in the AIM is that one not only models the resonance peak typically seen in the Kondo model but one also understands the underlying physics of the formation of the central peak seen in Figure 1.2. As discussed in detail in [10] the central peak forms due to the resonance of the local atomic state with the conduction electrons. The central peak gets separated from the satellites if the local interaction U is greater than the critical value of $\pi\Delta$, where Δ is the width of the resonance which can be calculated by Fermi's Golden rule. This application of the AIM to describe dilute atoms in a host material or the application to adatoms on surfaces is still an ongoing research topic as e.g. the study in [12, 13].

Another very interesting application of the AIM are the studies of so called quantum dots, small electric pools realized in doped semi-conductors. The spatial expansion of the quantum dot is so small that quantum effects cannot be neglected and quantized energy levels form. The individual energy levels are only separated by a few m-electron volts, opposed to electron volts in atoms. The quantum dot is connected to two leads and if one measures the differential conductance of such a quantum dot a periodicity of the conductance is observed as a function of the gate voltage. This phenomenon is called Coulomb blockade and can be explained by the AIM. If the dot is at integer filling the U blocks the addition of another electron and thus the system is insulating. If, however,

the energy to add another electron is degenerate with the Fermi energy of the lead the system is conducting [202].
Yet another reason why solvers for the AIM are important is their application in the context of the dynamical mean-field theory (DMFT), for solving a model of interacting fermions on an infinite lattice, which I am going to discuss in 2.2. With the DMFT a self-consistency cycle can be formulated which makes the solution of lattice problems including local electronic correlations possible. In one step of the self-consistency cycle the lattice problem, which we want to solve, is mapped onto an auxiliary AIM. The solution of the AIM is numerically the most demanding part of this method and thus the performance and the accuracy of the solver is very important for the final result. In the next section I will give a brief overview of available solvers for the AIM.

1.1. Solving the Anderson Impurity Model

Although the Anderson Impurity Model (AIM) Equation (1.1), which was introduced in the beginning of this chapter, looks very simple no analytical solution for it is known. The interest in the AIM has led to a whole zoo of different semi-analytical and fully numerical approaches of which I am going to give an overview in this section. I am also going to mention the advantages and disadvantages of the different solvers, so that one can choose the solver which captures the physics one is interested in. In the following discussions we are going to drop all spin and band indices to not clutter up the formulas. Since most solvers are based on diagrammatic techniques they involve approximations or numerically exact solutions of the self-energy. The local interacting one-particle propagator is given by the Greens function of the AIM:

$$G_{AIM}(\omega) = \frac{1}{\omega^+ - \Sigma(\omega) - \sum_k \frac{V_k V_k^*}{\omega^+ - \epsilon_k}}, \tag{1.2}$$

where $\omega^+ = \omega + i0^+$ which is needed for obtaining the retarded Greens function.

Hubbard I

In the Hubbard I approximation, which dates back to the paper of Hubbard in 1963 [14], we approximate the self-energy by one expression in the atomic limit. The approximation can be derived from the equation-of-motions approach to Greens functions, which is lengthy, but can be quite easily understood from a physical point of view [134].
If we write the Greens function for the atomic limit we obtain

$$\begin{aligned} G^{\text{atom}}(\omega) &= \frac{n_{-\sigma}}{\omega^+ - (U-\mu)} + \frac{1-n_{-\sigma}}{\omega^+ + \mu} + \\ &\equiv \frac{1}{\omega^+ + \mu - \Sigma^{\text{atom}_\sigma}(\omega^+)} \end{aligned} \tag{1.3}$$

from which we can calculate the self-energy which is given by

$$\Sigma^{atom}(\omega) = Un_{-\sigma} + U^2 \frac{n_{-\sigma}(1-n_{-\sigma})}{\omega^+ + \mu - U(1-n_{-\sigma})}.$$

In the equation above $n_{-\sigma}$ is the density of the electrons of one spin-direction on the impurity. Since the self-energy in this limit is a real quantity, this approximation cannot deal with finite life time effects. Hubbard I is exact in the atomic limit and in the non-interacting limit. This can be easily understood if we look at the Greens function Equation (1.2) and realize that the two limits are $\epsilon_{\boldsymbol{k}} \to 0$, the atomic limit, and $\Sigma^{atom} \to 0$, the non-interacting limit. Also arbitrary interactions can be used in Hubbard I without any further approximations. One problem is the spurious singularity in the self-energy at $\omega = -\mu + U(1-n_{-\sigma})$ without a physical origin. This can be cured by using two self-energies for the two Hubbard bands which also fixes the electron-hole asymmetry of the Hubbard I description, see [134].

Iterated Perturbation Theory

In Iterated Perturbation Theory (IPT), which was one of the first solvers used for calculating the self-consistent Dynamical Mean Field Theory (DMFT) equations, one approximates the self-energy by [18]:

$$\Sigma^{ipt}(\omega) \sim U\frac{n}{2} + U^2 \int_0^\beta dt e^{i\omega t} G_0(t)^3,$$

which is the self-energy in second order perturbation theory in the interaction U. In the above formula the first term yields the correct Hartree self-energy in the high frequency limit and the second term is given by the following Feynman diagram:

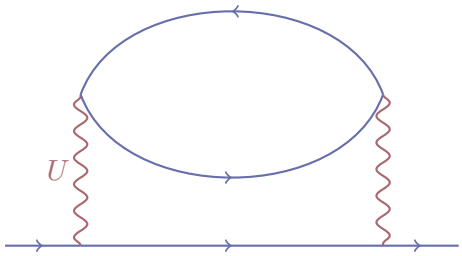

This approximation is correct in the non-interacting limit, but it also reproduces the atomic-limit expression for Σ^{ipt} in the large U limit. It qualitatively captures the right spectral properties of the satellite peaks and the Kondo resonance for single-band systems at half-filling, but the results are quantitatively wrong and the method could not be successfully extended to arbitrary number of bands and fillings. On can in principle also use the interacting Greens function in the IPT which, however, does not yield reasonable results [137].

Non-Crossing Approximation

The Non-Crossing Approximation (NCA) [19] is a diagrammatic technique which approximates the self-energy by a sum of all non-crossing self-energy diagrams. This is done by iteratively solving the following two coupled Feynman diagrams [11]:

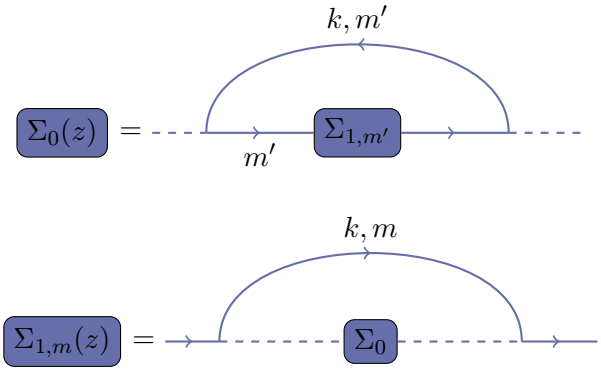

where k, m denotes a conduction electron and m denotes an electron on the impurity. The equations for the self-energy are then given by

$$\Sigma_0(z) = \frac{N\Delta}{\pi}\int_{-D}^{D} d\varepsilon \frac{f(\varepsilon)}{z - E_{1,m} + \varepsilon - \Sigma_{1,m}(z+\varepsilon)}$$
$$\Sigma_{1,m}(z) = \frac{\Delta}{\pi}\int_{-D}^{D} d\varepsilon \frac{(1-f(\varepsilon))}{z - E_0 - \varepsilon - \Sigma_0(z-\varepsilon)}$$

for a flat band of width $2D$, with Δ the width of the resonance, $f(\varepsilon)$ the Fermi distribution function and N the degeneracy of spin state on the impurity. The deficits of the NCA [22] are that for finite U the Kondo temperature is too small since the hopping processes to empty and doubly occupied states are not treated symmetrically. The NCA was compared to results for the Kondo problem and it was found that the results are reliable as long as the frequencies are $\omega/T_K > 0.1$ and $T/T_k > 0.1$, where T_k is the Kondo temperature [134].

Slave Boson

Slave boson is the name for a whole family of conceptually similar approaches to solving model Hamiltonians. The slave bosons are introduced by enlarging the Hilbert space of, e.g., the Hubbard model by bosonic operators e.g.:

$$\hat{d} : \text{double occupancy}$$
$$\hat{s}_\sigma : \text{single occupancy of spin}\,\sigma$$
$$\hat{e} : \text{empty site or hole.}$$

To recover the physical space of the original Hamiltonian we have to impose the following local constraints

$$\begin{aligned} \hat{n}^e + \hat{n}^s_\uparrow + \hat{n}^s_\downarrow + \hat{n}^d = 1, \\ \hat{n}^s_\sigma + \hat{n}^d = \hat{n}_\sigma \end{aligned} \tag{1.4}$$

where the first equation enforces that a correlated site is in one of the four physically possible states and the second equation states that the presence of an electron implies either a single or double occupancy. By introducing the bosonic operators we can rewrite the interaction part of the Hamiltonian as a bosonic occupation number operator while the part of the kinetic energy becomes more complicated.
The constraints are typically replaced by their time- (and space-) independent expectation values which leads to an uncontrolled approximation. Another disadvantage of the slave boson approach are the problems which arise due to the enlarged Hilbert space [134].

Exact Diagonalization

The Exact Diagonalization [15] (ED) method is probably the most straightforward approach to numerically solving the AIM. The idea is to simply write the AIM as a finite Hamiltonian which of course makes it necessary to discretize the bath levels. Since only a finite, and typically small number, of bath sites can be treated numerically a discretization error is introduced. In the simplest form, an impurity with one state hybridizing with one bath site, leads to a Hamiltonian of the form

$$\begin{pmatrix} E_d & -V_k \\ -V_k^* & \varepsilon_k \end{pmatrix} \tag{1.5}$$

The matrix size grows exponentially with the number of impurity sites and bath sites which limits this method to $\approx \mathcal{O}(20)$ impurity/bath-sites. The band discretization is most often done by a least square fit in Matsubara frequencies to avoid the discontinuities of the bath on the real axis. This method is otherwise exact and is for this reason ideal for benchmarking purposes. Another advantage of the method is the possibility to treat every local interaction and bath, e.g. complex bath wave functions for spin-orbit calculations, without problems.

Lanczos

The Lanczos method was first introduced in 1950 [17] and was "rediscovered" in the fields of numerics since it has advantageous properties for a numerical method. It is iterative, so every step brings us closer to the real solution compared to exact methods which need to be fully calculated to obtain meaningful results. It is optimal for finding

extremal eigenvalues, which are the eigenvalues one is typically interested in. Another advantage of the Lanczos method is that it can work with sparse matrices which allows us to treat system sizes which are prohibitively large when full matrices are used. Similar to the ED the bath needs to be approximated.
Since we are going to need the Lanczos method in 1.3.1 for the time evolution I am going to give a short introduction to it based on [40]. The starting point of the Lanczos method is to create a vector which has an overlap with the ground state, if one wishes to find the ground state energy. Typically a random, normalized vector is created $|v_0\rangle$. Then a vector is created which is orthogonal to this vector, which lies in the direction of the steepest descent $H|v_0\rangle$

$$b_1|v_1\rangle = |\tilde{v}_1\rangle = H|v_0\rangle - a_0|v_0\rangle \tag{1.6}$$

where $a_0 = \langle v_0|H|v_0\rangle$ and $b_1 = \sqrt{\langle\tilde{v_1}|\tilde{v_1}\rangle}$. In the following step again a vector, orthogonal to the previous vectors with the additional property of following the gradient is generated

$$b_2|v_2\rangle = |\tilde{v}_2\rangle = H|v_1\rangle - \sum_{i=0}^{1}|v_i\rangle\langle v_i|H|v_1\rangle \tag{1.7}$$

$$= H|v_1\rangle - a_1|v_1\rangle - b_1 v_0 \tag{1.8}$$

where b_2 and a_1 are calculated as above with the corresponding indices. The next step

$$b_3|v_3\rangle = |\tilde{v}_2\rangle = H|v_2\rangle - \sum_{i=0}^{2}|v_i\rangle\langle v_i|H|v_2\rangle \tag{1.9}$$

$$= H|v_2\rangle - a_2|v_2\rangle - b_2 v_1 \tag{1.10}$$

looks as the one before with incremented indices since $\langle v_2|H|v_0\rangle = 0$ by construction. We can therefore write down the formula for all basis vectors in the following way

$$b_{n+1}|v_{n+1}\rangle = |\tilde{v}_{n+1}\rangle = H|v_n\rangle - \sum_{i=0}^{n}|v_i\rangle\langle v_i|H|v_n\rangle \tag{1.11}$$

$$= H|v_n\rangle - a_n|v_n\rangle - b_n v_{n-1}. \tag{1.12}$$

If we rearrange the above equation we notice that we arrive at a tridiagonal matrix whose eigenvalues are the wanted eigenvalues of the hermitian matrix H.

$$H|v_n\rangle = b_n|v_{n-1}\rangle + a_n|v_n\rangle + b_{n+1}|v_{n+1}\rangle \tag{1.13}$$

With this recursion algorithm we build up the L-steps dimensional Krylov space of H over $|v_0\rangle$ denoted by $\mathcal{K}^L(|v_0\rangle)$. The Hamiltonian written in Krylov space is given by

$$H_{\mathcal{K}^L(|v_0\rangle)} = \begin{pmatrix} a_0 & b_1 & 0 & 0 & \cdots & 0 & 0 \\ b_1 & a_1 & b_2 & 0 & \cdots & 0 & 0 \\ 0 & b_2 & a_2 & b_3 & \cdots & 0 & 0 \\ 0 & 0 & b_3 & a_3 & \cdots & 0 & 0 \\ \vdots & \vdots & \vdots & \vdots & \ddots & \vdots & \vdots \\ 0 & 0 & 0 & 0 & \cdots & a_{L-1} & b_L \\ 0 & 0 & 0 & 0 & \cdots & b_L & a_L \end{pmatrix} \tag{1.14}$$

To obtain the eigenvalues we still have to diagonalize the tridiagonal matrix which is numerically very efficient. This method will later be used for a numerically cheap time-evolution in Section 1.3.1. The Lanczos method is also used for ED calculations at $T = 0$K since the most relevant contribution comes from the ground state and an approximate treatment of the excited states is sufficient.

Numerical Renormalization Group

This technique introduced by Wilson [23] makes use of the following steps. In the first step the bath is discretized into logarithmically growing intervals and then each interval is reduced to one state. The whole problem is then mapped onto a semi infinite chain with the impurity placed at the beginning, which can be physically interpreted as a sequence of shells centered around the impurity. The first interval would then be the shell with the wavefunction which has its maximum closest to the impurity [11]. One then starts by diagonalizing the impurity and iteratively adding more bath sites, which would let the matrices grow exponentially as more and more bath sites are added. In this step the renormalization group part of the name comes in. By only keeping the lowest energy many body states at each step the matrix size is kept fixed which is a plausible since the hopping falls off exponentially due to the logarithmic spacing. The down side of the NRG method is that it is only able to treat AIMs up to two orbitals and that it is more accurate at low frequencies than at high frequencies, which is due to the logarithmic discretization.

Density Matrix Renormalization Group

The density matrix renormalization group has its origin in 1992 when White and Noack [135] tried to apply the real-space renormalization group (RSRG) to quantum many body problems and failed to obtain reasonable results for low energy properties. They realized that the reason why the RSRG fails for the toy model of a particle in a box is that when one adds a box to the first box the lowest lying state of the two joint boxes is not composed of the wavefunctions of the two separate boxes. This can be

easily understood from the knowledge that each wavefunction for the box has a node at the border of the boxes but the wavefunction corresponding to the lowest energy of the joint boxes should have its maximum there. To overcome this the density matrix renormalization group (DMRG) works with a superblock which consists of a block for the system and a block mimicking the environment.
Similar as above one can also apply this method on the AIM as e.g. in [24] by representing the AIM as a linear chain

$$H_{AIM} = Un_{d\uparrow}n_{d\downarrow} + E_d(n_{d\uparrow} + n_{d\downarrow}) + V\sum_{\sigma}(d^{\dagger}_{\sigma}c_{0\sigma} + H.c.) + \sum_{n=0\sigma}^{\infty}\gamma_n(c^{\dagger}_{n\sigma}c_{n+1\sigma} + H.c.) \quad (1.15)$$

where again the correlation is only on the head of the chain with operators d. The main advantage of the DMRG is that, in contrast to the NRG, the DMRG yields reasonable results at all frequencies.

Hirsch-Fye Quantum Monte Carlo

The Hirsch-Fye Quantum Monte Carlo (QMC) was formulated by Hirsch and Fye in 1986 [26] and was one of the first QMCs available to treat the AIM. Similar to all the other QMC solvers for the AIM also the Hirsch-Fye QMC works in imaginary time τ and is therefore a finite temperature method. The algorithm consists of the following steps: (i) The imaginary time τ is discretized in λ slices of length $\Delta\tau$. (ii) The kinetic energy and the local interaction are separated via a Trotter [27, 28] decoupling which gives rise to a systematic error of $\mathcal{O}(\Delta\tau^2)$. (iii) The discrete Hubbard-Stratonovich [29] transformation is employed to decouple the electron-electron interaction and it is replaced by an interaction of the electrons to an auxiliary binary field. (iv) Monte-Carlo importance sampling is performed over the auxiliary fields to sample the Greens function.
One of the major shortcomings of the Hirsch-Fye method is its systematic error in $\Delta\tau$ which can be overcome by extrapolating the right values from calculations with different discretizations [136]. Another downside is the need of more time slices when going to lower temperatures which leads to a lower boundary of the reachable temperatures (typically room temperature can be reached with Hirsch-Fye). Also the restriction of the classical Hirsch-Fye to density-density type interactions is a major shortcoming. Different Hubbard-Stratonovich transformations, and therefore new auxiliary fields, allow for inclusion of other interaction terms, see e.g. [30], which we are going to discuss in 3, but this has to be done for each interaction separately.

Continuous-Time Quantum Monte Carlo

Since the Hirsch-Fye has some methodological shortcomings new numerical exact algorithms for solving the AIM where sought after. A way to circumvent the problems of the Hirsch-Fye is to drop the time discretization altogether and sample the terms in a

diagrammatic expansion. The idea of continuous-time methods stem from [31, 32] who employed the idea for bosonic systems. Since this method was very successful efforts were undertaken to adopt this technique for fermionic systems which however was at first unsuccessful due to the sign problem arising from the fermionic anti-commutation relation [33]. The breakthrough of the CT methods came with the insight that the sign problem is less severe for impurity models. This led to the development of the impurity solver in the weak-coupling formulation (CT-INT) [34], the hybridization expansion formulation (CT-HYB) [36, 35], the auxiliary field formulation (CT-AUX) [37] and the CT-J for Kondo-like models [39].
The common ground of all these methods is to separate the Hamiltonian H into two parts $H = H_a + H_b$ and rewrite the partition function in the interaction representation of H_a and then expand in powers of H_b. Doing this one arrives at

$$\begin{aligned} Z &= \mathrm{Tr}\, T_\tau e^{-\beta H_a} exp\left[-\int_0^\beta d\tau H_b(\tau)\right] \\ &= \sum_k (-1)^k \int_0^\beta d\tau_1 \ldots \int_{\tau_{k-1}}^\beta d\tau_k \times \mathrm{Tr}\left[e^{-\beta H_a} H_b(\tau_k) H_b(\tau_{k-1}) ... H_b(\tau_1)\right] \end{aligned} \tag{1.16}$$

where T_τ is the time ordering operator. This can now be sampled over all times, expansion orders and all topologies of diagrams [38]. In this sampling process it is helpful to sample whole groups of diagrams which differ only in the contractions of fermionic operators since otherwise a sign problem would arise.
Each of the impurity solvers has their own advantages and disadvantages. The CT-HYB is best suited for single-site calculations with arbitrary interactions since it does not suffer from a sign problem when treating complicated interactions. Its disadvantage is that the matrices treated grow exponentially with the system size. The CT-INT and CT-AUX are both expansions in the interaction term and best suited for cluster calculations with density-density type interactions, because the matrices do not grow exponentially as in the CT-HYB, but complicated interactions are difficult to treat. The CT-J is an expansion in the Kondo hybridization term and therefore useful for calculations of Kondo impurities.

1.2. Monte Carlo in a Nutshell

In the last section we discussed some possibilities to solve the AIM. In this thesis we will further on concentrate on the continuous-time quantum Monte Carlo in the hybridization expansion. To be able to implement the method we need some insight into the Monte Carlo procedure which we are going to discuss in this section.
In mechanics as well as quantum mechanics one is often faced with high dimensional sums or integrals over phase or configuration spaces which we are going to denote by $\mathcal{C}$

from now on. To solve a thermodynamical system the quantity we have to calculate is the partition function Z which is given by

$$Z = \int_{\mathcal{C}} dx\, p(x), \tag{1.17}$$

where $p(x)$ is the weight of one configuration/point in $\mathcal{C}$. In a classical system this is given by the Boltzmann weight $p(x) = exp(-\beta E(x))$ with $E(x)$ being the energy of the configuration x. For our approach the x is going to be a certain configuration in the space of all possible diagrammatic expansions of the partition function.
To solve the classical problem one could divide the phase space into discrete hypercubes and approximate the integral by a Riemann sum. The numerical effort to perform this sum grows as the number of times the function needs to be evaluated, which is exponential with the number of dimensions. If we, however, use a stochastic approach like Monte Carlo the central limit theorem tells us that the error decreases as $1/\sqrt{n}$, where n is the number of measurements, regardless of the dimensionality of the problem.

Markov Chain and Metropolis Algorithm

To actually generate configurations according to some probability distribution one can use a Markov process. In a Markov process the next move only depends on the current state the system is in with no memory of the past. It is fully characterized by a transition matrix W_{xy}, which has to fulfill the three properties. The first one given by

$$\sum_{\mathbf{y}} W_{xy} = 1,\ W_{xy} \geq 0 \tag{1.18}$$

which guarantees that the probability stays normalized in the Markov process.
The second property the transition matrix has to fulfill is ergodicity. This means that each configuration y has to be reachable from every configuration x with a finite number of Markov steps:

$$\forall x, y \in \mathcal{C}\, \exists\, n \mid (W^n)_{xy} > 0. \tag{1.19}$$

The final condition that the transition matrix has to obey is the stationary condition

$$\sum_{\mathbf{x}} p(x) W_{xy} = p(y). \tag{1.20}$$

This condition ensures that once we reach the desired distribution $p(x)$ we stay there. It is automatically satisfied if

$$W_{xy} p(x) = W_{yx} p(y). \tag{1.21}$$

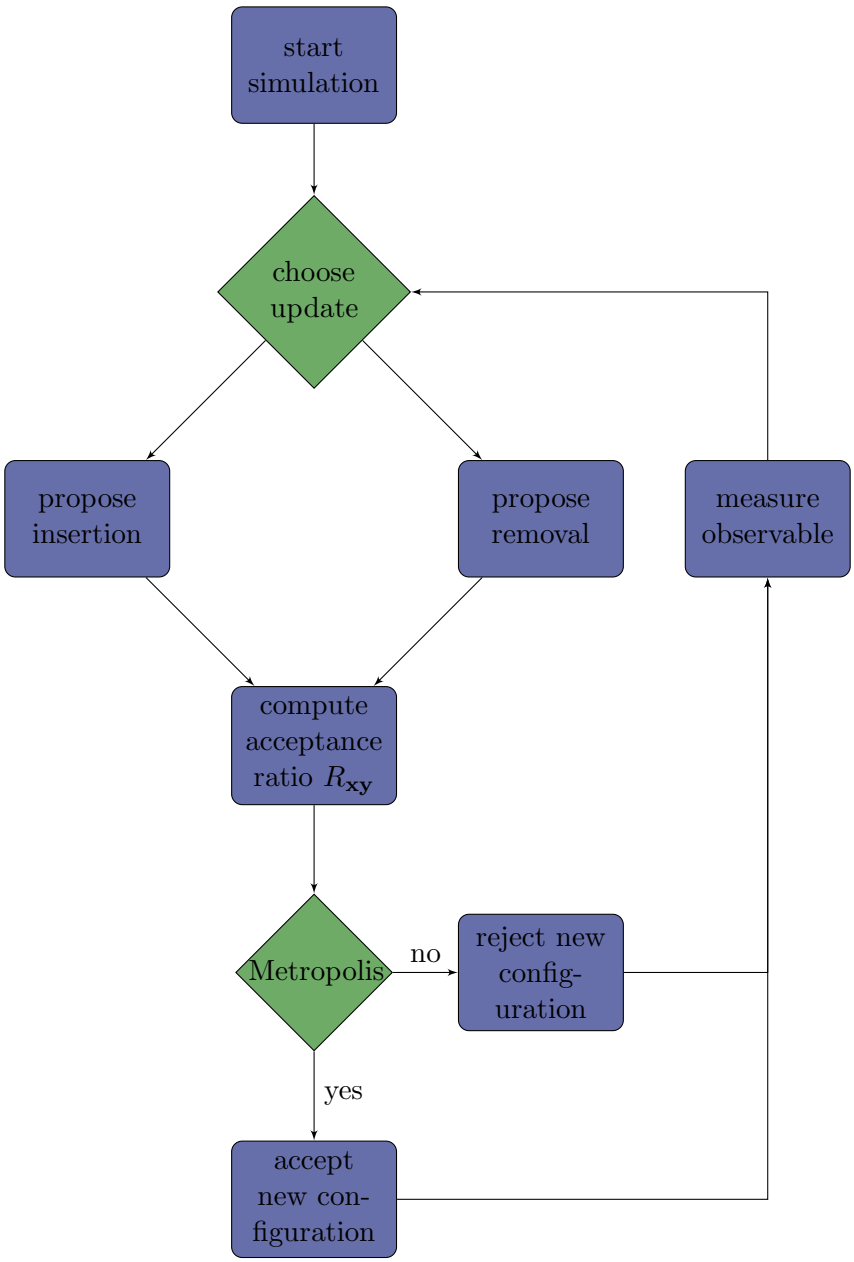

Figure 1.3.: A flow chart of the continuous-time quantum Monte Carlo algorithm. We choose an update randomly, in the case of the continuous-time an insertion or removal. Then we compute the acceptance ratio R_{xy}, see 1.24. Then the Metropolos algorithm is employed to decide if the new configuration is accepted. We then perform a measurement on the new configuration if accepted or on the old one if the new one was not accepted. Then the procedure starts from the beginning.

It can be proven by simply summing over x on both sides of the equation. This is known under the name detailed balance condition and is typically used for simulations.
The most widely used algorithm that fulfills the detailed balance condition is the Metropolis-Hastings algorithm [41, 42]. In this algorithm moves from the current configuration x to another configuration y are proposed with the probability W_{xy}^{prop} but only accepted with the probability W_{xy}^{acc}. If a move is rejected the old configuration is kept. The transition matrix is given by

$$W_{xy} = W_{xy}^{\text{prop}} W_{xy}^{\text{acc}} \tag{1.22}$$

To satisfy the detailed balance condition we use

$$W_{xy}^{\text{acc}} = \min[1, R_{xy}] \tag{1.23}$$

in the Metropolis algorithm, where R_{xy}, the acceptance ratio, is given by

$$R_{xy} = \frac{p(y) W_{yx}^{\text{prop}}}{p(x) W_{xy}^{\text{prop}}}. \tag{1.24}$$

The acceptance ratio for the inverse move is simply given by $R_{yx} = R_{xy}^{-1}$. In an actual calculation we would draw a random number $r \in [0, 1]$ and accept the move if $R_{xy} < r$, otherwise reject it. To ensure ergodicity the moves which are proposed during the simulation have to be generated in such a way that we can reach any configuration possible. In CTQMC simulations these are the addition and removal of vertices. In Fig. 1.3 a flow chart of the discussed Monte Carlo algorithm is shown.

Measurement and Derived Quantities

An observable O we want to measure is in general given by the average over the configuration space $\mathcal{C}$ with the weight p normalized by the partition function Z:

$$\langle O \rangle = \frac{1}{Z} \int_{\mathcal{C}} dx\, O(x) p(x). \tag{1.25}$$

In a Monte Carlo simulation we can approximate above measurement by sampling the configuration space using a Markov chain and measuring at configurations x_i

$$\langle O \rangle \approx \langle O \rangle_{MC} = \frac{1}{N} \sum_{i=1}^{N} O(x_i). \tag{1.26}$$

The measured quantity will be normally distributed around the real value if we sample a large number of statistically independent configurations, according to the central limit theorem, and the error can be estimated by

$$\sigma^2 \approx \frac{1}{N} \left(\frac{1}{N} \sum_{i=1}^{N} A(x_i)^2 - \left(\frac{1}{N} \sum_{i=1}^{N} A(x_i) \right)^2 \right). \tag{1.27}$$

w2d

Currently we are putting all measurements of each core into one bin. This provides us with a reasonable error if we are performing calculations on multiple cores.

If we want to estimate the error of a function $f(\langle O_1\rangle, ..., \langle O_n\rangle)$ depending on n observables sampled from N configurations x_i we can employ the bootstrap method. The idea behind the method is to construct N^N different sets of configurations which are defined by there indices $\mathbf{i} = (i_1, ..., i_N)$ and calculate a bootstrap sample given by

$$f_{\mathbf{i}}^B = f\left(\frac{1}{N}\sum_{k=1}^{N} A_1(x_{i_k}), ..., \frac{1}{N}\sum_{k=1}^{N} A_n(x_{i_k})\right) \tag{1.28}$$

for each of them. We can then approximate the error by

$$\left(\sigma_f^B\right)^2 \approx \frac{1}{N^N}\sum_{i_1,...,i_N=1}^{N}\left(f_{\mathbf{i}}^B\right)^2 - \left(\frac{1}{N^N}\sum_{i_1,...,i_N=1}^{N} f_{\mathbf{i}}^B\right)^2. \tag{1.29}$$

Since we cannot calculate all N^N different bootstrap samples in a realistic scenario one typically generates $\mathcal{O}(100)$ randomly generated bootstrap samples and approximates the error by 1.29.

Sign Problem

Until now we have assumed that we are sampling systems in which the probability in the partition function is positive definite. Of course this is only true as long as we are dealing with bosonic systems. We are, however, trying to solve fermionic problems in which the operators anticommute. For these systems we have to find a strategy how deal with the problem of changing signs in the probability.
The most often used approach is to sample the fermionic system with respect to the bosonic one by taking the absolute value of the weight $|p(x)|$ and to assign the sign $s(x) \equiv \operatorname{sgn} p(x)$ to the observable which we are measuring

$$\langle O\rangle = \frac{\sum_x O(x)s(x)|p(x)|/\sum_x |p(x)|}{\sum_x s(x)|p(x)|/\sum_x |p(x)|}. \tag{1.30}$$

The problem with the solution above is that if a sign problem occurs the error increases exponentially with the number of particles and the inverse temperature [43]. It is noteworthy to mention that the sign problem is dependent on the representation and algorithm chosen for solving the system. For certain systems and algorithms the absence of the sign problem can be proven, e.g. one orbital AIM with Hirsch-Fye [44].

For general problems we can only try a calculation and see if a sign problem occurs.
In [43] it could be shown that the sign problem is NP hard, which is the same complexity class as e.g. the traveling salesman problem. For such problems no solution could be found yet, after many decades of research, which if found would solve all NP hard problems since they could be mapped to the solved problem. This led people to the assumption that a general solution to the sign-problem is impossible and thus no general solution for the sign-problem is possible.

1.3. The Hybridization Expansion

As I mentioned in the introduction the main goal of this thesis was to enable us to treat multi orbital systems with general interactions. Already in the discussion about solvers of the AIM I mentioned that the CT-HYB is the best candidate for such models since it is able to treat general interactions without introducing a sign-problem.
The CT-HYB was developed by Werner *et al.* in 2006 [36] and was first applied to multi-orbital models with complex interactions in [35]. Haule then introduced an idea of the ED method to the CT-HYB community [45], which consists of separating the local Hamiltonian into a block diagonal form by using a set of quantum numbers QN which commute with the local Hamiltonian H_{loc}, to which we will get back later, and implemented the method for off-diagonal hybridization functions. Two years later Läuchli and Werner introduced the Krylov implementation [46] which is capable of treating systems of up to seven orbitals with general interactions, which was implemented and used during the course of this work. The discussion about the CT-HYB is following the lines of [47].
In line with the idea of CTQMC methods we divide the Anderson impurity model Hamiltonian Equation (1.1) into two parts $H_{\text{AIM}} = H_a + H_b$. In the CT-HYB we choose $H_a = H_{\text{bath}} + H_{\text{loc}}$ and H_b is set to be the hybridization which is given by

$$H_{\text{hyb}} = \sum_{pq} (V_{pq} c_q^\dagger d_p + V_{pq}^* d_p^\dagger c_q), \tag{1.31}$$

where p is a combined orbital and spin index and q is a combined momentum and spin index. The hybridization term of the Hamiltonian contains a creation and annihilation operator for the impurity and bath respectively and the inverted constellation, a creation for the bath and an annihilation for the impurity, for the conjugated term. This leads to traces equal to zero if there are more hybridizations of the one kind than of the other, which makes an expansion in both terms reasonable. If we now put our choice of H_a

and H_b into the partition function Equation (1.16) we obtain

$$\begin{aligned} Z =& \sum_{k=0}^{\infty} \int_0^\beta d\tau_1 \dots \int_{\tau_{k-1}}^\beta d\tau_k \int_0^\beta d\tau_1' \dots \int_{\tau_{k'-1}}^\beta d\tau_k' \\ & \times \mathrm{Tr}\left[T_\tau e^{-\beta H_a} \tilde{H}_{\mathrm{hyb}}(\tau_k) \tilde{H}^\dagger_{\mathrm{hyb}}(\tau_k') \dots \tilde{H}_{\mathrm{hyb}}(\tau_1) \tilde{H}^\dagger_{\mathrm{hyb}}(\tau_1') \right]. \end{aligned} \tag{1.32}$$

The factor $(-1)^k$ only appears with an even exponent due to the even expansion numbers considered and does not contribute to the expression above. Inserting the expressions for H_a and H_b explicitly we get

$$\begin{aligned} Z =& \sum_{k=0}^{\infty} \int_0^\beta d\tau_1 \dots \int_{\tau_{k-1}}^\beta d\tau_{k-1} \int_0^\beta d\tau_1' \dots \int_{\tau_{k'-1}}^\beta d\tau_k' \\ & \times \sum_{p_1 \dots p_k} \sum_{p_1' \dots p_k'} \sum_{q_1 \dots q_k} \sum_{q_1' \dots q_k'} V_{q_1 p_1} V^*_{q_1' p_1'} \dots V_{q_k p_k} V^*_{q_k' p_k'} \\ & \times \mathrm{Tr}\left[T_\tau e^{-\beta H_a} d_{p_k}(\tau_k) c^\dagger_{q_k}(\tau_k) d^\dagger_{p_k'}(\tau_k') c_{q_k'}(\tau_k') \right. \\ & \qquad \left. \dots d_{p_1}(\tau_1) c^\dagger_{q_1}(\tau_1) d^\dagger_{p_1'}(\tau_1') c_{q_1'}(\tau_1') \right]. \end{aligned} \tag{1.33}$$

Since the bath and impurity Hamiltonians do not mix we can separate the time-evolution of the bath and impurity operators

$$\begin{aligned} Z =& \sum_{k=0}^{\infty} \int_0^\beta d\tau_1 \dots \int_{\tau_{k-1}}^\beta d\tau_k \int_0^\beta d\tau_1' \dots \int_{\tau_{k'-1}}^\beta d\tau_k' \\ & \times \sum_{p_1 \dots p_k} \sum_{p_1' \dots p_k'} \sum_{q_1 \dots q_k} \sum_{q_1' \dots q_k'} V_{q_1 p_1} V^*_{q_1' p_1'} \dots V_{q_k p_k} V^*_{q_k' p_k'} \\ & \times \mathrm{Tr}_d \left[T_\tau e^{-\beta H_{\mathrm{loc}}} d_{p_k}(\tau_k) d^\dagger_{p_k'}(\tau_k') \dots d_{p_1}(\tau_1) d^\dagger_{p_1'}(\tau_1') \right] \\ & \times \mathrm{Tr}_c \left[T_\tau e^{-\beta H_{\mathrm{bath}}} c^\dagger_{q_k}(\tau_k) c_{q_k'}(\tau_k') \dots c^\dagger_{q_1}(\tau_1) c_{q_1'}(\tau_1') \right]. \end{aligned} \tag{1.34}$$

Looking at the above equation we realize that we can integrate out the bath degrees of freedom since the bath is non-interacting. To this end we first define the bath partition function Z_{bath}

$$Z_{\mathrm{bath}} = \mathrm{Tr}\, e^{-\beta H_{\mathrm{bath}}} = \prod_q (1 + e^{-\beta \varepsilon_q}) \tag{1.35}$$

and the anti-periodic hybridization function Δ

$$\Delta_{p_l p_m}(\tau) = \sum_q \frac{V^*_{q p_l} V_{q p_m}}{e^{\varepsilon_q \beta} + 1} \times \begin{cases} -e^{-\varepsilon_q(\tau - \beta)}, & 0 < \tau < \beta \\ e^{-\varepsilon_q \tau}, & -\beta < \tau < 0 \end{cases} \tag{1.36}$$

The hybridization function is connected to the non-interacting Greens function of the AIM via $\Delta_{lm}(-i\omega_n) = (i\omega_n + \mu_{\text{imp}})\delta_{lm} - G^0_{lm}(i\omega_n)^{-1}$, since we need to calculate the Fourier transformed propagator of the hole $\mathcal{F}\langle T_\tau c^\dagger(\tau)c(\tau)\rangle$. Using this we see that

$$\frac{1}{Z_{\text{bath}}}\,\text{Tr}_c\left[T_\tau e^{-\beta H_{\text{bath}}}\sum_{q_1\dots q_k}\sum_{q'_1\dots q'_k} V_{q_1p_1}V^*_{q'_1p'_1}\dots V_{q_kp_k}V^*_{q'_kp'_k}\right. \tag{1.37}$$

$$\left.\times c^\dagger_{p_k}(\tau_k)c_{p_{k'}}(\tau'_k)\cdots c^\dagger_{p_1}(\tau_1)c_{p'_1}(\tau'_1)\right] = |\mathbf{\Delta}|, \tag{1.38}$$

is just the determinant of the matrix $\mathbf{\Delta}$. This is a matrix with the dimensions of the expansion order $k \times k$. The element l, m of the matrix is the hybridization function evaluated for the orbitals/spins p_l, p_m at the time difference $\tau_l - \tau_m$:

$$\Delta_{lm} = \Delta_{p_lp_m}(\tau_l - \tau_m) \tag{1.39}$$

In the implementation we will always treat the quantity $\mathbf{M} = \mathbf{\Delta}^{-1}$ since we can easily calculate the ratio of determinants, which we are going to need to calculate the transition probability between two configurations, using inversion by partitioning. We are going to see later that the algorithm mostly consists of moves from one configuration to another and we thus need exactly this ratio to calculate the probabilities needed in the Monte Carlo.
The idea of inversion by partitioning is to find explicit formulas to calculate the inverse of matrices with rank $k+1$ without performing the explicit inversion. We assume that we add the row and column as the $k+1$th row and column of the matrix, which can easily be generalized by considering the sign we get for basic row and column exchanges. The new matrix and its inverse then have the following form:

$$\mathbf{\Delta}^{k+1} = \begin{pmatrix}(\mathbf{M}^k)^{-1} & Q\\ R & S\end{pmatrix} \tag{1.40}$$

$$\left[\mathbf{\Delta}^{k+1}\right]^{-1} = \mathbf{M}^{k+1} = \begin{pmatrix}\tilde{P} & \tilde{Q}\\ \tilde{R} & \tilde{S}\end{pmatrix}. \tag{1.41}$$

The matrix P is a $k \times k$ matrix, Q and $\tilde{Q}$ are $k \times 1$ vector, R and $\tilde{R}$ are $1 \times k$ vectors and S and $\tilde{S}$ are numbers. A simple calculation leads to the following expressions

$$\tilde{S} = (S - [R][\mathbf{M}^k - Q])^{-1} \tag{1.42}$$

$$\tilde{Q} = -[\mathbf{M}^k Q]\tilde{S} \tag{1.43}$$

$$\tilde{R} = -\tilde{S}[R\mathbf{M}^k] \tag{1.44}$$

$$\tilde{P} = \mathbf{M}^k + [\mathbf{M}^k Q]\tilde{S}[R\mathbf{M}^k], \tag{1.45}$$

which show that we can update the matrix in $\mathcal{O}(k^2)$ time if we only increase the rank of the matrix by one. The nice thing about this approach is that we can calculate the

ratio between two matrices with a rank difference of one by

$$\frac{|\mathbf{M}^{k+1}|^{-1}}{|\mathbf{M}^{k}|^{-1}} = \frac{1}{|\tilde{S}|} = |S - R\mathbf{M}^{k}Q|. \tag{1.46}$$

w2d

The formulas for inversion by partitioning and wrapper routines around Lapack calls for complete matrix updates, which are needed for global moves discussed later, are implemented in *MatrixUpdate.F90*.

The ratio of $k+1$-matrix if we already know the k-matrix can thus be computed in $\mathcal{O}(k^2)$ time and the inverse ratio in $\mathcal{O}(1)$ time.
After this small excursion on efficient computation of ratios of matrices we finally plug equation Section 1.3 into equation Equation (1.34) and obtain

$$\begin{aligned} Z =& Z_{\text{bath}} \sum_{k=0}^{\infty} \int_0^\beta d\tau_1 \dots \int_{\tau_{k-1}}^\beta d\tau_k \int_0^\beta d\tau'_1 \dots \int_{\tau_{k'-1}}^\beta d\tau'_k \sum_{p_1 \dots p_k} \sum_{p'_1 \dots p'_k} \\ & \times \mathrm{Tr}_d \left[T_\tau e^{-\beta H_{\text{loc}}} \, d_{p_k}(\tau_k) d^\dagger_{p'_k}(\tau'_k) \dots d_{p_1}(\tau_1) d^\dagger_{p'_1}(\tau'_1) \right] |\mathbf{\Delta}| \end{aligned} \tag{1.47}$$

In the current implementation of *w2dynamics* we assumed that the hybridization is diagonal in the flavors, i.e. orbital and spin, which adds a $\delta_{p_l p_m}$ to the above formula. This is in general a good assumption if the system we look at has symmetries, e.g. cubic systems without distortions, but one should look at each system at hand to see if this assumption is reasonable. The partition function with a diagonal bath is given by the factorized equation

$$\begin{aligned} Z =& Z_{\text{bath}} \sum_{k=0}^{\infty} \int_0^\beta d\tau_1 \dots \int_{\tau_{k-1}}^\beta d\tau_k \int_0^\beta d\tau'_1 \dots \int_{\tau_{k'-1}}^\beta d\tau'_k \sum_{p_1 \dots p_k} && (1.48) \\ & \times \mathrm{Tr}_d \left[T_\tau e^{-\beta H_{\text{loc}}} \, d_{p_k}(\tau_k) d^\dagger_{p_k}(\tau'_k) \dots d_{p_1}(\tau_1) d^\dagger_{p_1}(\tau'_1) \right] \prod_p |\mathbf{\Delta}_p| && (1.49) \end{aligned}$$

Here $\mathbf{\Delta}$ is block diagonal in the flavors and therefore the determinant of it becomes

$$|\mathbf{\Delta}| = \begin{vmatrix} \mathbf{\Delta}_1 & & \\ & \ddots & \\ & & \mathbf{\Delta}_{\text{max}} \end{vmatrix} = \prod_p |\mathbf{\Delta}_p| \tag{1.50}$$

With this we have discussed the bath part of the partition function and we now turn to the part which treats the local trace.

A Simple Example

Let us first look at a simple example to see how to calculate the local trace. We start with an impurity with one orbital and two spin directions. The local Fock space has the dimension of four and the four states are $|\,\square\,\rangle$, $|\,\uparrow\,\rangle$, $|\,\downarrow\,\rangle$, $|\,\uparrow\downarrow\,\rangle$. The interaction on the impurity is defined by the local Coulomb repulsion U and the chemical potential μ. In its one orbital form the density-density interaction is given by

$$H_{\text{d-d}} = -\sum_{\sigma} n_\sigma \mu + U n_\uparrow n_\downarrow, \tag{1.51}$$

where σ runs over the two spin directions. If we write the density-density interaction in Fock space as a matrix we obtain

$$H_{\text{loc}} = \begin{pmatrix} 0 & 0 & 0 & 0 \\ 0 & -\mu & 0 & 0 \\ 0 & 0 & -\mu & 0 \\ 0 & 0 & 0 & U - 2\mu \end{pmatrix} \tag{1.52}$$

which tells us that each state is an eigenstate of the local Hamiltonian and thus the exponential of the time evolution is easy to calculate. Let us now consider the case when the expansion order k is equal to zero, i.e. there are no hybridization events. We can depict this configuration by an empty line in imaginary time

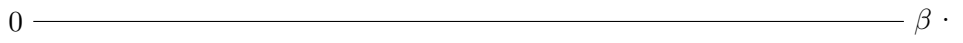

We can now calculate the weight of the local trace w_{loc} for this configuration which is given by:

$$\begin{aligned} w_{\text{loc}} =& \operatorname{Tr}_d \left[T_\tau e^{-\beta H_{\text{loc}}} \right] \\ =& \langle\,\square\,|\, e^{-\beta 0} \,|\,\square\,\rangle + \langle\,\uparrow\,|\, e^{\beta\mu} \,|\,\uparrow\,\rangle + \langle\,\downarrow\,|\, e^{\beta\mu} \,|\,\downarrow\,\rangle + \langle\,\uparrow\downarrow\,|\, e^{-\beta(U-2\mu)} \,|\,\uparrow\downarrow\,\rangle \\ =& 1 + 2e^{\beta\mu} + e^{-\beta(U-2\mu)} \end{aligned} \tag{1.53}$$

Let us make the whole thing more interesting and move on to the case of a first order expansion. In first order we obtain a line with two hybridization events. One hopping from the bath onto the impurity depicted by a filled symbol ● and a hopping from the impurity into the bath depicted by an empty symbol ○ at certain times on the imaginary time axis

Currently the blue round symbols depict operators for the spin up flavor. We now again calculate the local weight of this configuration and realize that certain states do not contribute to the trace any more since the local Hilbert space is left using creation or annihilation operators e.g. $c_\uparrow^\dagger |\boxed{\uparrow\downarrow}\rangle$ which leaves us with the following summands

$$\begin{aligned} w_{\text{loc}} = &\langle \boxed{} | \, e^{-(\beta-\tau_1)0} c_\uparrow^\dagger(\tau_1) e^{(\tau_1-\tau_1')\mu} c_\uparrow(\tau_1') e^{-\tau_1' 0} \, | \boxed{} \rangle \\ + &\langle \boxed{\downarrow} | \, e^{((\beta-\tau_1)\mu)} c_\uparrow^\dagger(\tau_1) e^{-(\tau_1-\tau_1')(U-2\mu)} c_\uparrow(\tau_1') e^{\tau_1'\mu} \, | \boxed{\downarrow} \rangle \end{aligned} \tag{1.54}$$

We now also obtain a weight for the determinant of $\mathbf{\Delta}$. With just two operators in the trace this is simply the number $\Delta_{up}(\tau_1 - \tau_1')$. For a more complex configuration with expansion order two as e.g.

we would obtain the matrix

$$\mathbf{\Delta} = \begin{pmatrix} \Delta_\uparrow(\tau_1 - \tau_1') & \Delta_\uparrow(\tau_1 - \tau_2') \\ \Delta_\uparrow(\tau_2 - \tau_1') & \Delta_\uparrow(\tau_2 - \tau_2') \end{pmatrix} \tag{1.55}$$

of which the determinant yields all possible contractions of the hybridization events. This is similar to Wicks theorem for non-interacting Greens functions here applied to the non-interacting bath. The treatment of all possible contractions at once avoids the sign problem which would otherwise arise if we would treat the terms with varying signs individually. The two possible contractions of the configuration above are depicted by the blue lines below:

Update

With this we know how to calculate the ingredients of the partition function and thus the weights for a random walk in the space of configurations, let us take a look at the updates we need to perform. To be ergodic in this random walk we have to implement two moves: the insertion and the removal of two hybridization events which change the configurations in the following way

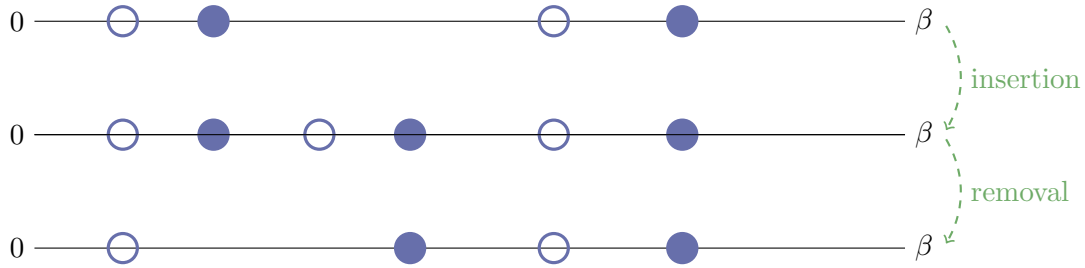

In the above example we first generated two new hybridization events and then removed two. Note that the hybridization events added or removed have to be chosen independently. So we do not remove pairs which were added previously.
We take a look again at the equation for the acceptance ratio Equation (1.24) for which we still need to identify the proposal probabilities for an insertion and a removal. The probability for choosing a random time out of the interval $(0, \beta)$ once for the annihilator and the creator is

$$W^{\text{prop}}_{k\to k+1} = \frac{d\tau^2}{\beta^2}$$

and the probability for picking one of the creation and annihilation operators randomly out of the $k+1$ operators, $(k+1)_p$ operators of one flavor p if the bath is diagonal in orbital and spin space, is given by

$$W^{\text{prop}}_{k+1\to k} = \frac{1}{(k+1)^2}.$$

Putting everything together we obtain the acceptance ratio for accepting the insertion move of

$$R_{k\to k+1} = \frac{\beta^2}{(k+1)^2}\frac{w_{\text{loc}}(k+1)|\mathbf{\Delta}(k+1)|}{w_{\text{loc}}(k)|\mathbf{\Delta}(k)|}. \tag{1.56}$$

The $d\tau^2$ of the insertion proposal probability cancels with the additional $d\tau^2$ of the weight of the configuration. The acceptance ratio of the inverse move, the removal of an annihilation/creation pair, is just the inverse of the acceptance ratio above $R_{k+1\to k} = R^{-1}_{k\to k+1}$.
To obtain shorter auto-correlation times and to reduce the risk of getting stuck in a local minimum one can also propose global moves which e.g. flip the spin of all operators or exchange orbitals. These moves can also be symmetry moves of the system which are then always accepted, e.g. flipping the spins in a paramagnetic system.

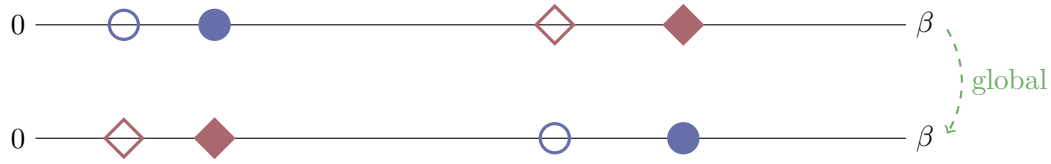

The acceptance ratio then consists only of the ratios of the two configurations, 1 if it is a symmetry move, since they are "self-balancing"

$$R_{k\to k'} = \frac{w_{\text{loc}}(k')|\mathbf{\Delta}(k')|}{w_{\text{loc}}(k)|\mathbf{\Delta}(k)|}.$$

These moves are expansive, since we have to calculate the whole matrix $\mathbf{\Delta}(k')$ from scratch, so they should only be proposed seldomly during the simulation.

w2d

In the Parameter file the parameter *PercentageGlobalMove*, which defaults to 0.001, defines how many percent of all moves should be global moves. If the parameter *ParaMag* is set to 1 then a given percentage, by default 10%, of all global moves are global spin-flip proposals.
General global moves can be given in the parameter file by setting *NSymMove* to the number N of symmetry moves one wants to define and then define *SymMove##* where the hashes are the number of the symmetry move e.g. 01 for the first one. The format of the symmetry move is a space separated list of numbers where the position of the number is the original flavor and the number on the position defines the new flavor.
Examples are SymMove01 = 2 1 for a spin flip move in a one orbital system and SymMove01 = 3 4 1 2 for an orbital exchange move in a two orbital system. The first m numbers, where m is the number of orbitals, always represent the spin up operators and the last m numbers denote the spin down operators.

1.3.1. Hybridization Expansion Algorithms

The biggest bottleneck for the CT-HYB algorithm is the calculation of the local trace. This can be understood if we look at the dimensionality of the local Hilbert space for a system with N_{orb} orbitals on the impurity and spin 1/2 which is $2^{2N_{\mathrm{orb}}}$. We have to perform time evolutions on these states, which boils down to matrix exponents, and apply the creation and annihilation operators onto the evolved states. This is a numerically very heavy task which can be tackled with different strategies.

Segment Algorithm

For density-density type of interactions, i.e. interactions which are diagonal in the occupation number Fock space, there is a special algorithm called segment algorithm. Since the interaction does not mix electrons of different orbitals one can think of an imaginary time line for each orbital which can only have two states, occupied or empty. This leads to a computationally cheap algorithm [47] in which we only have to calculate the overlapping parts of segments for the contribution of U and the length of segments for the contribution of μ. We depict this in the picture below where colored lines denote

occupation of an orbital and black lines emptiness.

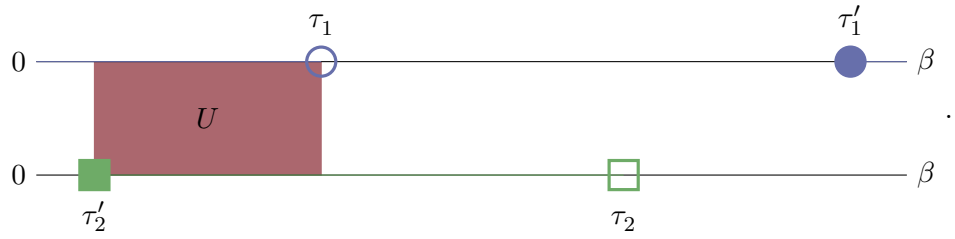

Matrix Algorithm

The formalism of the segment algorithm breaks down if we want to treat general interactions, i.e. interactions in which there is no $\delta_{i,k}\delta_{j,l}$ in the interaction term

$$U_{ijkl}c_i^\dagger c_j^\dagger c_k c_l.$$

Such interactions do not allow for a separation of time lines anymore which we can understand by looking at the following configuration

As is shown in the above time line it is possible to obtain two creation operators of the same green flavor after each other since the time evolution can mix states with empty orbitals and filled orbitals. For calculations with such general interaction terms the primary approach was to make a unitary transformation into the eigensystem of the local Hamiltonian in which the time evolution is cheap, since the local Hamiltonian is diagonal in this basis. The computationally heavy task is that we have to deal with dense creation and annihilation operators which leads to a complexity of $\mathcal{O}(N_{\text{orb}}^3)$ due to the matrix-matrix multiplications involved. The only way to speed up calculations is to reduce the size of these matrices. This is done by finding symmetries of the local Hamiltonian. Using these symmetries we can reduce the matrix to a block diagonal form and thus reduce the complexity to $\mathcal{O}(N_{\text{max}})$, where N_{max} is the size of the biggest block. Typically N_t, the total number of electrons on the impurity, is a quantity conserved by the Hamiltonian and therefore the Hamiltonian can be divided in blocks of equal number of electrons. I will further discuss this issue in section 3.1.1 and 3.3. This algorithm works well for systems with up to three orbitals, but reaches its limits for five orbital systems. To be able to calculate systems with even larger local Hilbert spaces a dynamical truncation of states considered in the evaluation of the local trace was proposed. In this dynamical truncation the partition function is sampled with all states included and a histogram of visited states is generated. Then states with only little contribution to the trace are truncated and only often visited states are retained for the rest of the

simulation. This method introduces an uncontrolled systematic error and criticism was raised on the validity of this approach.

Krylov Algorithm

In 2009 the Krylov implementation was put forward by Läuchli and Werner which approaches the problem of treating general interactions with a different strategy. In the Krylov approach the local trace is calculated in the occupation number basis in which the creation and annihilation operators are sparse matrices and the time evolution is performed in Krylov space [48]. The crucial point the in the Krylov algorithm is that we truncate the trace over the outer states to the ones corresponding to the lowest energy. This pins the trace at one point to certain states, which is reasonable if we are in a low temperature state of the system compared to the hybridization and interaction strength. It is important to note that the freedom of the system to evolve into any excited states is not restricted by this "outer"-truncation, which reduces the error of the algorithm compared to the dynamic truncation, in which certain excited states are completely excluded from the simulation. The Krylov algorithm allows to solve systems with up to seven orbitals. Below I will introduce the method and discuss the implementation of this approach.
The two main operations needed for the evaluation of the local trace are an application of a creation/annihilation operator $c/c^\dagger$ and the local Hamiltonian H_{loc} to a state vector ψ. The latter is used to build up the Krylov space which I introduced in section 1.1.

w2d

These operations can be efficiently implemented with a sparse matrix algorithm. In *w2dynamics* we chose the compressed sparse row (CSR) format as described in [49] for the representation of the sparse matrices. The creation of sparse matrices from dense matrices and the matrix vector operations of sparse matrices with dense vectors are implemented in *SparseMatrix.F90*.

As a first step we need to calculate the eigenvalues and eigenvectors of the local Hamiltonian H_{loc}. This is necessary to decide which states we want to keep in the "outer"-truncation of the trace. When we perform the truncation it is important that we do not destroy the multiplet structure of the retained states which needs to be handled with care!

w2d

We are generating H_{loc} in Fock space and diagonalize it with Lapack routines. The subroutines for generating the local Hamiltonian are implemented in *Operator.F90*, which also contains the routines for generating the creation and annihilation operators. The parameter *truncation* specifies how many of the lowest lying multiplets are retained for calculating the local trace.
For example if we calculate a less than half-filled one band system with truncation= 2 *the empty state and the singly occupied states would be retained. We have to use three states since the singly occupied state is degenerate.*
Since there are numerical inaccuracies in the calculated eigenvalues we have to introduce an epsilon which is the upper bound of the difference of two eigenvalues for them to be considered equal. This is epsilon is defined by the parameter *EPSDEG*.
Also the eigenvectors contain numerical errors which can lead to problems when we calculate the local trace and thus we are setting entries in the eigenvectors which are below the parameter *EPSEVEC* to zero. This parameter has to be handled with care and checks have to be performed that no necessary information is discarded.

After we have decided which states we keep for the calculation of the trace we propagate the eigenvectors of the retained eigenenergies of the Hamiltonian until the first operator in the trace. We then apply the first operator to the evolved state. The resulting state is then evolved again up to the next hybridization event. Since the state we have to evolve is in general not an eigenstate of the local Hamiltonian anymore we employ the Krylov method for the time evolution.
To this end we construct a Krylov space by iteratively applying H_{loc} to the current state. This yields the Hamiltonian in the Krylov space $H^L_{\mathcal{K}}(|v_0\rangle)$ and the vectors $|v_n\rangle$. These vectors are the transformation matrix $A_{N\times L} \equiv [|v_0\rangle, |v_1\rangle, \cdots |v_{L-1}\rangle]$, where N is the dimension of the local Hilbert space or if we divide the local Hamiltonian into block diagonal form the dimension of the block of the Hamiltonian the current state belongs to.
For the time evolution we define the vector $\mathbf{c}(t)$ which is a $L \times 1$ vector which contains the coefficients of the vectors $|v_n\rangle$. Now we can define the time evolution in the Krylov space by

$$\frac{\partial \mathbf{c}}{\partial t} = -iH^L_{\mathcal{K}}(|v_0\rangle)\mathbf{c}. \tag{1.57}$$

This equation is solved by

$$\mathbf{c}(t) = \exp(-iH^L_{\mathcal{K}}(|v_0\rangle))\mathbf{c}(0) \tag{1.58}$$

where $\mathbf{c}(0) = (1, 0, \cdots)$ since the initial vector $|v_0\rangle$ of the Krylov space is the vector which we want to evolve in time. The above equation is solved by diagonalizing the

tridiagonal Hamiltonian. We then transform into the eigenbasis of it and calculate the exponential using the eigenvalues. Then we back transform into the original basis and are done with this time evolution. The actual calculation of the eigensystem of the Hamiltonian $H_{\mathcal{K}}^{L}(|v_0\rangle)$ is cheap since the Hamiltonian is tridiagonal in Krylov space and the Krylov space is also typically smaller than the original space. It is important not to keep the dimension of the Krylov space fixed to a certain integer number L but to use a convergence criterion suitable for the time evolution in Krylov space. In our implementation we are using the one proposed in [48] which checks that the probability that the system is in the last reduced vector $|v_{L-1}\rangle$ is smaller than a certain threshold

$$|[\mathbf{c}(t)]_L| < \epsilon. \tag{1.59}$$

w2d

In the actual implementation, which is contained in the file *Lanczos.F90*, we use the convergence criterion described above, whose threshold is given by the parameter *EPSLANC*. A second convergence criterion we are using is that the last subdiagonal of the Hamiltonian in Krylov space is equal zero. This indicates that we found all eigenstates of the local Hamiltonian and thus that our time evolution is exact.

We use the steps described above until we iterated through the whole trace and add the contribution of this state to the trace. We then take the next retained state and iterate through the whole trace again. This is done for all the states kept for the specified truncation value.

w2d

The time evolution can lead to very small contributions of the trace which are checked against the parameter *EPSSANDWICH*, since otherwise numerical instabilities can occur. If the value of a part of the trace is lower than the value specified then this part of the trace is considered to be 0.
An additional problem arises when treating interactions with a lot of small mixing between states. This can lead to a non-reversibility of the trace which however is crucial if we want to store states at each operator to reuse them in the next calculations of the trace and for measuring observables. This is overcome by recalculating the trace, when we store the time evolved states, if we reach a state which is zero, where we already know which states led to a finite value of the trace.

The overall complexity of the Krylov approach is $\mathcal{O}(N_{\text{dim}} \times N_{\text{tr}} \times N_{\text{iter}})$ where N_{dim} is the dimension of the local Hilbert space, N_{tr} is the number of retained "outer"-states and N_{iter} is the dimension of the Krylov space L. It is not easy to estimate the dimension

of the Krylov space since this depends on a lot of factors like the time differences τ and the local interaction, but it is generally assumed to be much smaller than the dimension of the local Hilbert space [53].

1.4. Measurement in CT-HYB

In the last section we discussed how we can sample the partition function in the CT-HYB. To understand the physics of a system and to compare our results with experiments we typically also want to measure other quantities as e.g. the occupancies, the magnetization or the Greens function. Below I will explain how we can achieve this in a QMC simulation.

Local Time Independent Observables

In the Krylov approach it is very important to measure non-time dependent observables in the middle of the trace since there the "outer"-truncation of the trace is the least influential. The quantity which contains all information about the local state of the system, which we thus want to measure in the simulation, is the density matrix in Fock space which is given by

$$\rho^{\text{Fock}} = \sum_{i_{trunc}} \frac{|\psi_{i_{trunc}}(\beta/2)\rangle \langle\psi_{i_{trunc}}(\beta/2)|}{\sum_{i_{trunc}} \langle\psi_{i_{trunc}}(\beta/2)|\psi_{i_{trunc}}(\beta/2)\rangle} \tag{1.60}$$

where the sum runs over all the states retained in the "outer"-trace.

w2d

One can measure the full density matrix in Fock space by setting the parameter *MeasDensityMatrix*= 1 in the parameter file. This, however, is a very large object already for five orbital systems and we run into memory issues if we want to measure it for seven orbital systems. A quantity which is smaller and can therefore always be measured is the single particle quantity of the occupation and double occupation of each orbital and spin. The measurement is performed by

$$\langle\rho_{p,p'}\rangle = \sum_{i_{trunc}} \frac{\langle\psi_{i_{trunc}}(\beta/2)|\,\hat{n}_p\hat{n}_{p'}\,|\psi_{i_{trunc}}(\beta/2)\rangle}{\langle\psi_{i_{trunc}}(\beta/2)|\psi_{i_{trunc}}(\beta/2)\rangle}. \tag{1.61}$$

Since we can store the evolved states at each operator and we are performing an equal time insertion of two operators we do not need to recalculate the local trace to measure this quantity and it is thus also a cheap measurement. Measuring more involved quantities like time dependent correlation functions would force us to recalculate the local

trace since the creation and annihilation operators change the state of the trace.
An easy example to see this is the measurement of the density-density correlation function $\langle n(0)n(\tau)\rangle$. At the time τ we are in the state $1/\sqrt{2}|\boxed{\uparrow}\boxed{\downarrow}\rangle + 1/\sqrt{2}|\boxed{\downarrow}\boxed{\uparrow}\rangle$ at this point we insert the operator $\hat{n}_{1,\uparrow}$. Therefore the state after the insertion of the operator is going to be $1/\sqrt{2}|\boxed{\uparrow}\boxed{\downarrow}\rangle$ changing the rest of the trace until the second insertion of $\hat{n}$ which makes a recalculation of the trace necessary. This tells us that the only possible measurements with stored states of the trace are measurements of time independent observables for general interactions. For the density-density interactions which commutes with $\hat{n}$ we can calculate correlation functions which only depend on $\hat{n}$ from the stored quantities.
In the program we are actually not measuring the value at $\beta/2$ but the value at the operator closest to $\beta/2$. When we do this it is very important to measure on the right "side" of the operator, the side which faces to $\beta/2$ since we would otherwise introduce a systematic error.

Measurement of the Greens Function

To measure the Greens function we employ a different measurement strategy. As shown in [54] the Greens functions can be obtained as functional derivatives of the partition function Z with respect to the hybridization function Δ

$$G_{p,p'}(\tau,\tau') = -\frac{1}{Z}\frac{\partial Z}{\partial \Delta_{p,p'}(\tau,\tau')}. \tag{1.62}$$

This derivative is equal to the following measurement in the simulation

$$G_{p,p'}(\tau,\tau') \overset{MC}{\approx} -\left\langle \sum_{m,n} M^{\mathcal{C}}_{mn}\delta(\tau-\tau_m)\delta(\tau'-\tau_n)\delta_{p_m,p}\delta_{p_n,p'}\right\rangle, \tag{1.63}$$

where $M^{\mathcal{C}}_{mn}$ is an element of the inverse of the hybridization matrix corresponding to a certain configuration $\mathcal{C}$ which I defined in Section 1.3.

It corresponds to removing the hybridization lines of a creation and annihilation operator in a configuration and thereby generating a new configuration which is the same as the previous one, except for two additional local creation and annihilation operators added

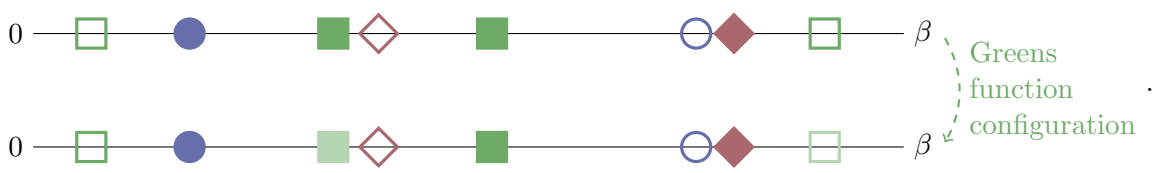

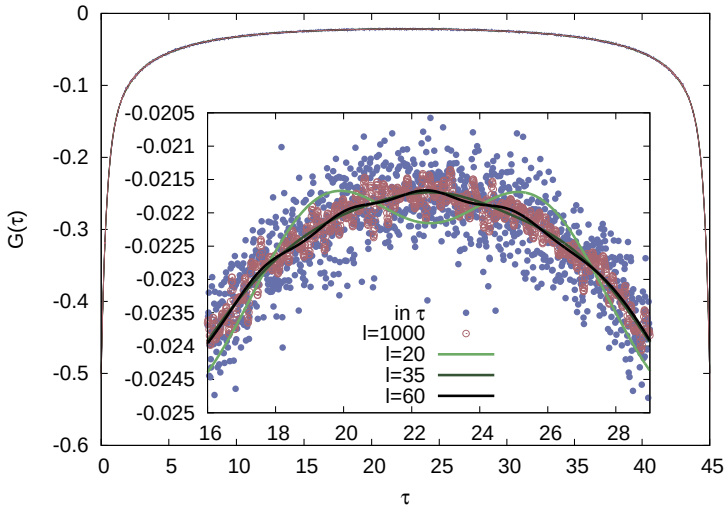

Figure 1.4.: The measurement of the Greens function. The blue dots are measurements directly performed in τ. The measurement in τ is noisy even at high statistics. The Greens function calculated from the measurement of 35 Legendre coefficients (dark green) is smooth, canceling out all the noise.

where the Greens function is denoted in lighter colors. One can think of another measurement method for the Greens function, which would consist of adding a creation and annihilation operator at random times with random spin/orbital indices into the local trace. This measurement, however, is not ergodic as we can see by the following example. Let us start from the configuration below and then remove hybridization lines to generate a Greens function configuration. To keep it simple we look at a single band single spin system with density-density interaction. A possible configuration and a Greens function configuration generated from it, where the operators corresponding to the Greens function are again denoted by lighter colors, would be

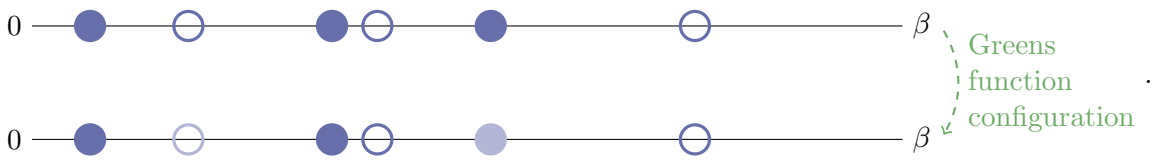

If one would start from a configuration without the Greens function one would have the

following scenario:

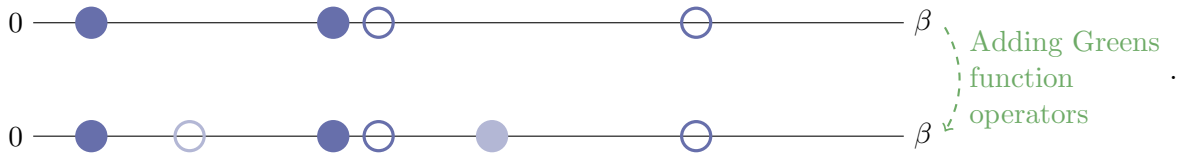

The first configuration in the picture above would never be created since it is forbidden by the Pauli principle, two annihilation operators after each other, thus also the Greens function configuration is impossible to reach. This tells us that not all possible Greens function configurations can be generated from partition function configurations if we generate the Greens function configuration by insertion of operators in the local trace. This method for accumulating the Greens function is therefore not ergodic and should not be used.

w2d

Since we are measuring a continuous quantity we need to bin the measurement into time slices. To set the number of bins the Greens function is measured into one can set the parameter *NTau* to the desired value. The default value is 1000. The Greens function in τ is always measured since its accumulation is cheap.

The down-side of measurements in the imaginary time is that τ which is continuous needs to be discretized. To remedy the need to discretize τ in our simulations one can measure the Greens function directly in Matsubara frequencies which are by definition discrete. This is possible by inserting the unitary Fourier transformation operators into the measurement

$$G_{p,p'}(i\omega_n) \overset{MC}{\approx} -\left\langle \int_0^\beta d\tau \int_0^\beta d\tau' \sum_{m,n} e^{i\omega_n \tau} M^{\mathcal{C}}_{mn} e^{i\omega_n \tau'} \delta(\tau - \tau_m)\delta(\tau' - \tau_n)\delta_{p_m,p}\delta_{p_n,p'} \right\rangle \tag{1.64}$$

The measurement directly in Matsubara frequencies is expansive, since one typically needs a lot of Matsubara frequencies $\mathcal{O}(100)$ and the calculation of the phase factors for the Fourier transformation is numerically demanding, and thus not often used.

Measurement in the Legendre Basis

Following the lines of measuring the Greens function directly in Matsubara frequencies one can think of other basis in which one can measure the continuous quantities in CTQMC. For the measurement of the Greens function a reasonable choice for such a

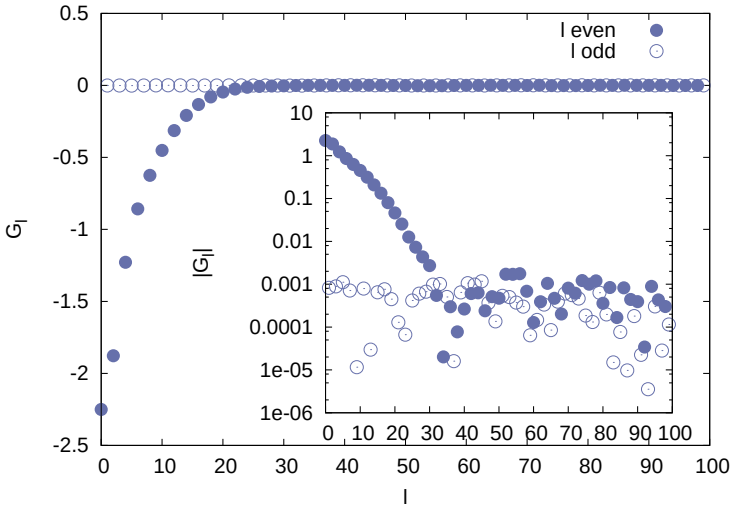

Figure 1.5.: A measurement in Legendre polynomials. One can see that in this case, starting from $l \approx 30$ the Legendre coefficients are small.

basis are the Legendre polynomials [54]. The advantage of the Legendre polynomials as opposed to other basis sets is twofold. First the transformation of the Legendre polynomials to the Matsubara frequencies can be written as a unitary transformation and second only few Legendre coefficients are needed to express the Greens function as we can see in Fig. Figure 1.5. In fact it could be shown in the above paper that the Legendre coefficients for a Greens function decay faster than any power of the Legendre expansion l.
To obtain the Greens function from Legendre Polynomials we use:

$$G(\tau) = \sum_{l \geq 0} \frac{\sqrt{2l+1}}{\beta} P_l[x(\tau)] G_l \tag{1.65}$$

where $x(\tau) = 2\tau/\beta - 1$ transforms the variable τ which lives on the interval $[0, \beta]$ to the interval $[-1, 1]$ on which the Legendre polynomials are defined. The inverse transformation from imaginary time τ to Legendre coefficients is given by

$$G_l = \sqrt{2l+1} \int_0^\beta d\tau P_l[x(\tau)] G(\tau). \tag{1.66}$$

We can also directly measure the Greens function projected onto Legendre polynomials during the Monte Carlo sampling. To this end we use

$$G_{p,p',l} \overset{MC}{\approx} -\frac{\sqrt{2l+1}}{\beta} \left\langle \sum_{m,n} M^{\mathcal{C}}_{mn} \tilde{P}_l(\tau_m - \tau_n) \delta_{p_m,p} \delta_{p_n,p'} \right\rangle \tag{1.67}$$

where $\tilde{P}_l(\Delta\tau)$ is defined as

$$\tilde{P}_l(\Delta\tau) = \begin{cases} P_l[x(\Delta\tau)], & \Delta\tau > 0, \\ -P_l[x(\Delta\tau+\beta)], & \Delta\tau < 0. \end{cases} \tag{1.68}$$

Above we have used the anti-periodicity of the Greens function.
Since we also need the Greens function on Matsubara frequencies, as we will see in 2.2 we also need the unitary transformation from Legendre polynomials to the Matsubara frequencies

$$G(i\omega_n) = \sum_{l\geq 0} G_l (-1)^n i^{l+1} \sqrt{2l+1} j_l \left(\frac{(2n+1)\pi}{2}\right) \tag{1.69}$$

where j_l is the spherical Bessel function.
A valuable side effect of using a smooth function to represent the Greens function is its use as a noise filter due to the cutoff at a certain expansion order. The effect of the cutoff on the Greens function can be seen in Fig. 1.4 where, when we use 35 Legendre coefficients, the Greens function is reproduced but the noise is filtered out. If we increase the expansion order further we obtain more and more noise. If we would use an infinite amount of Legendre polynomials we would get back the directly measured Greens function including all the noise.
For most application a reasonable choice for the cutoff of the Legendre polynomials is in our experience $30-100$. This of course has to be checked for each calculation since it depends on the temperature and interaction parameters. One can check if the cutoff is reasonable by plotting the Legendre coefficients, see Figure 1.5, and check if a plateau is reached.
As we can see in Fig. 1.6 also the moments of the Greens function converge to the right value at a low number of Legendre polynomials which are given by $c_1 = 1$, $c_2 = 0$ and $c_3 = 5$.

The equations for calculating the moments of the Greens function directly from the Legendre coefficients are:

$$c_1 = -\sum_{l\geq 0,\text{even}} \frac{2\sqrt{2l+1}}{\beta} G_l, \tag{1.70}$$

$$c_2 = \sum_{l>0,\text{odd}} \frac{2\sqrt{2l+1}}{\beta^2} G_l l(l+1), \tag{1.71}$$

$$c_3 = -\sum_{l\geq 0,\text{even}} \frac{\sqrt{2l+1}}{\beta^3} G_l (l+2)(l+1)(l-1). \tag{1.72}$$

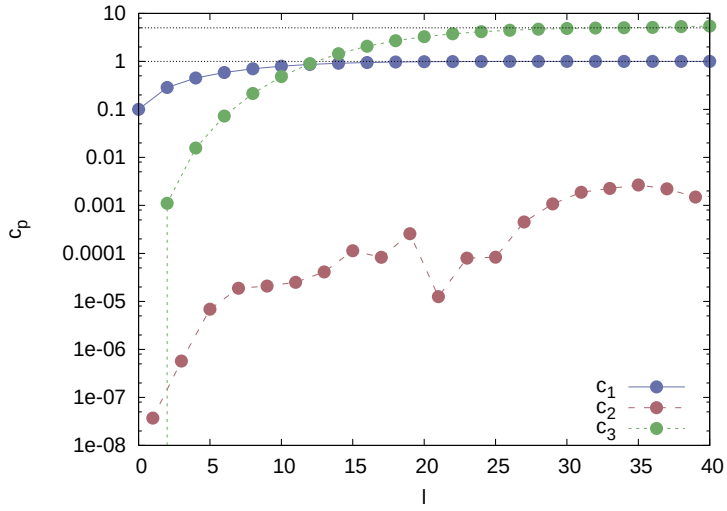

Figure 1.6.: The moments of the Greens function calculated from the Legendre coefficients. The analytical moments are denoted by the dashed lines. The analytical second moment c_2 is 0 since the calculation was performed at half-filling and therefore the odd coefficients vanish.

w2d

In *w2dynamics* the two parameters *NLegMax* and *NLegOrder* declare how many Legendre parameters are measured in the QMC and how many are used for calculating the Greens function in $i\omega_n$ respectively. The quantity in the output file *gtau* is always directly measured in τ-bins.

1.5. Testing the CT-HYB implementation

In the previous sections I introduced the QMC, the CT-HYB and the algorithm of the Krylov implementation. Finally I also showed how one can measure non-time dependent quantities and the Greens function in the CT-HYB. I, however, did not yet comment on the actual implementation which I am going to use throughout this work (I actually already presented one application of the implementation when I presented the plots for the Legendre measurement in Section 1.4).
To test the implementation a simple check with a, if possible, exact method would be most convenient. This can actually be achieved for the CT-HYB by testing against exact diagonalization (ED) results. In the ED, as I already mentioned in Section 1.1, one diagonalizes the whole system, impurity and bath, and thus obtains the exact solution.

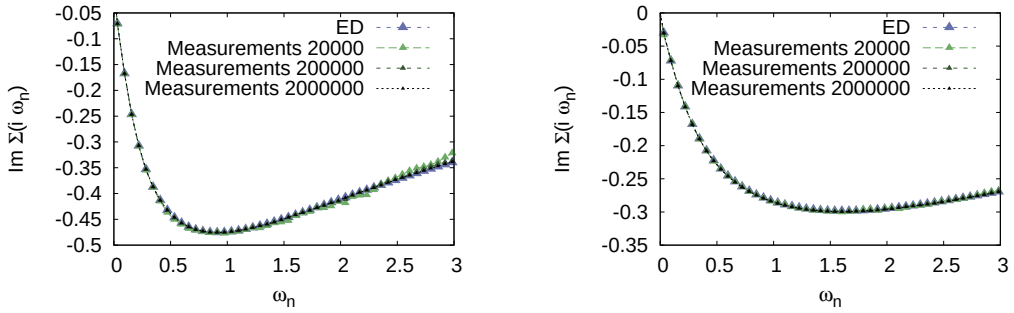

(a) Orbital 1

(b) Orbital 2

Figure 1.7.: Comparison of the CT-HYB self-energy with the self-energy of the ED calculation. One can nicely see that with an increasing number of measurements the agreement of the CT-HYB self-energy with the ED self-energy is getting better.

This is only true as long as the bath is discrete, which of course is not the case anymore for realistic systems with a continuous density of state.

If only a finite number of bath-sites exist one can write the hybridization function, which is the input for the CT-HYB, as

$$\Delta(\omega) = \sum_{p_i} \frac{V(p_i)V^*(p_i)}{\omega - \varepsilon(p_i)} \tag{1.73}$$

and the Fourier transformed hybridization function

$$\Delta(t) = \sum_{p_i} \frac{V(p_i)V^*(p_i)e^{\varepsilon(p_i)t}}{e^{\beta\varepsilon(p_i)} + 1}. \tag{1.74}$$

In the above equations $\varepsilon(p_i)$ is the energy the bath-site p_i is located at and $V(p_i)$ is the hybridization strength with the impurity. Using $\Delta(t)$ one can perform ED and CT-HYB calculations with identical parameter sets.

For testing our implementation we performed a CT-HYB calculation with the following $\varepsilon(p_i)$ and $V(p_i)$ for a paramagnetic system where the indices a and b denote the first and second band.

The chemical potential was set to $\mu = 1.0$ and the interaction parameters $U = 2$, $V = 1$ and $J = 0.5$. With these parameters the system is out of half-filling which is important for a test case since otherwise one does not check for errors which occur only if the system is not particle-hole symmetric. The truncation is set to 5 therefore we retain all states in the CT-HYB calculation and the result is numerically exact. The temperature is set

	$\varepsilon_a(p_i)$	$\varepsilon_b(p_i)$	$V_a(p_i)$	$V_b(p_i)$
p_1	5.0206E-002	6.4962E-002	0.1510	0.2747
p_2	-0.9585	-0.8959	0.3012	0.5992
p_3	0.9581	0.9114	0.3012	0.5980
p_4	-5.0263E-002	-6.1760E-002	0.1510	0.2693

to $\beta = 100$. In this calculation we used the Kanamori interaction which I am going to discuss in detail in Section 3.1. The results of the calculation are in very good agreement with the results of the ED calculation. The self-energy is shown for a different number of measurements in Figure 1.7. The results for the ED-calculation were provided by Massimo Capone.

w2d

To run a calculation with a set of hybridization parameters $\varepsilon(p_i)$ and $V(p_i)$ one needs to set the parameter *DOS* to *EDcheck*. Additionally one needs to provide the following two files: *Vk* and *epsk* which have as columns the bands and as rows the data for the different p_i.

2. Realistic Calculations of Complex Structures

After giving a brief introduction to the local density approximation plus dynamical mean field theory (LDA+DMFT) I will explain each step of such realistic calculations. First I will give a short introduction of the density functional theory (DFT) and its local density approximation (LDA) in Section 2.1. Then, Section 2.2, I will introduce the DMFT. Following this introduction, in Section 2.3, I will briefly discuss the double counting correction in Section 2.3. Following this discussion, in Section 2.4, I will write about methods which link the LDA and the DMFT method, the so called downfolding. Then, in Section 2.5, I will show how one can include additional bands in the DMFT calculation and discuss two studies of what happens in calculations with such enlarged basis sets. To compare results from calculations with experiments one still needs to perform the continuation on to the real axis which I will outline in Section 2.6. Following this, in Section 2.7, I will show how to add non-local interactions to the method and I will present a study of such a calculation. Finally, Section 2.8 I will present two extensions to the LDA+DMFT method.

Introduction

One of the most interesting and difficult problems in physics is the calculation of the electronic properties of solids. In the last chapter I explained what the Anderson Impurity Problem is and how one can solve it, focusing on the CT-HYB algorithm in the Krylov implementation. The AIM only describes a small subset of physical situations, e.g. impurity problems in solids as I already pointed out in Chapter 1. For treating the electronic properties of bulk materials consisting of alloys with transition metal compounds we need to use different models. Since the calculation of the electronic structure of such materials is of great interest to the solid state community, large efforts were undertaken in the last decades to develop methods to treat models which can describe such systems. One of the most successful is the merger of the local density approximation with the dynamical mean-field theory for which the abbreviation LDA+DMFT was coined.
One of these methods, the density functional theory (DFT) in its local density approximation (LDA) has for decades been the method of choice if one wants to calculate the band structure of real materials. It works very well for a large class of materials, in

which the interaction strength in relation to the bandwidth is small. As soon as this requirement is not fulfilled the concept of treating the wave function as a product of single particle wave functions breaks down and the LDA is not able to correctly predict the properties of the system anymore. I will shortly introduce this method in Section 2.1.
The DMFT, on the other hand, was developed by the model Hamiltonian community and is able to describe the Mott metal insulator transition [91], a long standing problem of the solid state community. The starting point of the DMFT is the Hubbard Hamiltonian

$$H = \sum_{iljm} t_{iljm} c_{il}^{\dagger} c_{jm} + \sum_{ilmno} U_{ilmno} c_{il}^{\dagger} c_{im}^{\dagger} c_{in} c_{io} \tag{2.1}$$

which describes the hopping of electrons, which are annihilated (created) $c^{(\dagger)}$ on sites i, j and orbitals l, m, on a lattice with a local interaction U_{ilmno} on each lattice site i between the orbitals l, m, n, o. The Hubbard Hamiltonian is, similarly to the Anderson Impurity Hamiltonian, impossible to solve analytically (for $d > 1$). The DMFT makes use of a new analytical limit, the limit of infinite dimensions, which makes the solution tractable numerically. I will describe this method in 2.2.
The merger of these two methods LDA+DMFT [137] is in principle able to treat all periodic materials in which local correlations play a major role if the dimensionality or the coordination number of the problem is not too small. The starting point to combine the two methods is the output of the LDA Hamiltonian H_{LDA} in k-space. One assumes that the output of LDA is a good description of the kinetics of the system and one thus uses it to describe the hopping in the Hubbard Hamiltonian. Which bands one wants to take into account depends on the problem at hand. If there are only correlated electrons close to the Fermi edge, as it is the case e.g. for $SrVO_3$, it becomes rather trivial. I will discuss some downfolding techniques, which are used to obtain the relevant hopping parameters, in Section 2.4 and some problems which come into play if one wants to consider additional bands.
One can then easily write the LDA+DMFT Hamiltonian as

$$H = H_{LDA} + \sum_{ilmno} U_{lmno} c_{il}^{\dagger} c_{im}^{\dagger} c_{in} c_{io} - \sum_{i\sigma} DC_{il} n_{il} \tag{2.2}$$

where the combined orbital and spin indices $lmno$ only run over a subset of the LDA orbitals which we want to treat. The n denotes the orbital occupation of orbital and spin l and U_{lmno} is a general interaction matrix. The subset of bands could for example be the d-orbitals of a transition metal. The last term of the Hamiltonian above is the double counting correction which is necessary since some part of the interaction is already included in LDA+DMFT calculations. How exactly this double counting correction term looks like is not known and therefore there are a lot of different ways to treat it. I will present some in Section 2.3.
The LDA+DMFT method was already successfully applied to a multitude of systems.

It could for example correctly describe the Mott transition in V_2O_3 [92], the δ phase of Pu [94], the correlation effects in Fe and Ni [93] and the spin state of $SrCoO_3$ [95] to name just a few. This success also led to extensions of the DMFT scheme which we are going to discuss in the last section of this chapter. Two extensions of the commonly found LDA+DMFT scheme, for which the names "layer"-DMFT and nano-DMFT were coined, which can be used in the *w2dynamics* package are going to be discussed there. Summing up the ingredients for a LDA+DMFT calculations are: (i) make a LDA calculation, (ii) identify the bands which need to be kept in the calculation, (iii) calculate the interaction, (iv) perform a DMFT calculation with (v) a reasonable double counting correction. This scheme can in principle be extended to a fully charge self-consistent scheme if one feeds the densities from the DMFT calculation back into the LDA. I will discuss each step in the following sections with the exception of the local interaction which I am going to treat in more detail in the last chapter.

2.1. Density Functional Theory

The Density Functional Theory (DFT) is based on the Hohenberg-Kohn theorem [55] which states that the ground-state property of a system is a unique functional of the density. This means that once we know the density of system we have complete knowledge its ground-state properties. Furthermore the ground-state can be found by minimizing the Energy $E[\rho]$ with respect to the density. This theorem can be proven easily see [56]. Using this theorem it is possible to work with the less complicated density ρ as opposed to the many particle wave functions. Since we can express everything as a functional of the density we can write the energy as a sum over the kinetic energy functional $E_{\text{kin}}[\rho]$, the ionic functional which can easily be expressed via the density

$$E_{\text{ion}} = \int d\vec{r}\, V_{\text{ion}}(\vec{r})\rho(\vec{r}),$$

the Hartree term which can also be expressed via the density

$$E_{\text{H}}[\rho] = \frac{1}{2}\int d\vec{r} \int d\vec{r}' V_{ee}(\vec{r}-\vec{r}')\rho(\vec{r})\rho(\vec{r}')$$

and finally a term in which we hide all the exchange and correlation part which we do not know E_{xc}. So the complete functional is given by

$$E[\rho] = E_{\text{kin}}[\rho] + E_{\text{ion}}[\rho] + E_{\text{H}}[\rho] + E_{\text{xc}}[\rho]$$

It is quite interesting that the only functional which actually depends on material specific parameters is E_{ion} (see e.g. [57]) so we would know the solution to any material by simply adding the analytically known expression for $E_{\text{ion}}[\rho]$.

Since the term for the kinetic energy can not be easily expressed in terms of the density Kohn and Sham [58] introduced auxiliary one-particle wave functions which yield the total density

$$\rho(\vec{r}) = \sum_{i=1}^{N} |\phi_i(\vec{r})|^2.$$

With the help of these auxiliary wave functions one minimizes the energy with respect to ϕ_i instead of ρ and introduces the Lagrange parameters ε_i which guarantee normalization. Thus we get $\delta\{E[\rho] - \varepsilon_i[\int d\vec{r}|\phi_i(\vec{r})|^2] - 1\}/\delta\phi_i(\vec{r}) = 0$. This minimization procedure leads to the Kohn-Sham equations which describe a single electron moving in the time averaged potential of the other electrons

$$\left[-\frac{\hbar^2}{2m_e}\nabla^2 + V_{\text{ion}}(\vec{r}) + \int d\vec{r}' V_{\text{ee}}(\vec{r} - \vec{r}')\rho(\vec{r}') + \frac{E_{\text{xc}}[\rho]}{\delta\rho(\vec{r})}\right]\phi_i(\vec{r}) = \varepsilon_i\phi_i(\vec{r}).$$

Since the exchange and the Hartree functional depend on the density which is in turn needed for the computation of the energy we need to employ a self-consistent scheme. We start with a guess for the density and calculate an effective single particle potential $V_{\text{eff}} = V_{\text{ion}}(\vec{r}) + \int d\vec{r}' V_{\text{ee}}(\vec{r} - \vec{r}')\rho(\vec{r}') + \frac{E_{\text{xc}}[\rho]}{\delta\rho(\vec{r})}$. Then we solve the Schrödinger equation [59], obtain the ϕ_i and with these we calculate a new density. We stop the iteration scheme if the new density and the old density are similar enough. If not, we perform another iteration with the new density.
In principle the constructed auxiliary wave functions and Lagrange parameters have no physical meaning whatsoever. Comparing the spectra and band structures of the auxiliary wave functions calculated by this procedure to experimental data, however, often gives very good agreement. This made the identification of the auxiliary wave functions and "energies" ε_i in the theoretical state theory community a de-facto standard.
We still have not made any approximations so far, but we also cannot solve the equation above since we do not know how $E_{\text{xc}}[\rho]$ looks like. One typical approximation is the Local Density Approximation (LDA) which defines

$$E_{\text{xc}}^{\text{LDA}}[\rho] = \int d\vec{r}\rho(\vec{r})\varepsilon_{\text{xc}}^{\text{LDA}}(\rho(\vec{r})).$$

In the equation above $\varepsilon_{\text{xc}}^{\text{LDA}}(\rho(\vec{r}))$ is the local exchange-correlation energy density of the homogeneous electron gas. For actual calculations $\varepsilon_{\text{xc}}^{\text{LDA}}(\rho(\vec{r}))$ is produced by numerical simulations of the jellium model for which $V_{\text{ion}}(\vec{r})$ is constant. This already tells us for what systems the LDA approximation will give reasonable results. When the density of the electrons only varies slowly as a function of $\vec{r}$ then the jellium model might be justified for the system. This is the case for s- and p-electron systems. For d- or f-electron systems, whose electrons are more localized and where the density variations are large, the approximation of the exchange and correlation energy is not justified

anymore and LDA calculations do not yield satisfactory results. To remedy this other approximations, e.g. the generalized gradient approximation [212, 213] and the hybrid functionals [214, 215], were developed. The DFT is, however, intrinsically unable to describe local moments and therefore the Mott transition [97] thus extensions to this method are needed.

2.2. Dynamical Mean Field Theory

A complimentary approach, to the one I discussed in the last section, for describing electrons in solids is their description by model Hamiltonians. One of the most well known, if one is interested in strongly correlated electrons, is the Hubbard Hamiltonian Equation (2.1). As I mentioned in Chapter 2 the Hubbard model, even in its simplest one band form, is impossible to solve analytically, thus one would typically think of a perturbative approach. The two most straightforward approaches would be to perform an expansion around the atomic limit in t or to perform an expansion around the non-interacting limit in U. If we follow one of these perturbative approaches we miss the most interesting regime where the two parameters are of similar order and where the physics of strongly correlated metallic systems and the Mott-Hubbard metal insulator transition happen.
In 1989 Metzner and Vollhardt [60] put a new limit for correlated electron systems forward, the limit of infinite dimensions. Since we do not treat any of the two parameters, t and U, perturbatively the interesting physics, the interplay between iterative and localized electrons, is captured in this approach. Soon after the publication Müller-Hartmann [61, 62, 63] showed that only the local interaction yields frequency dependent self-energies whereas the non-local density-density interactions are reduced to their Hartree term. The breakthrough which made the theory applicable to the Hubbard Hamiltonian was the work by Georges and Kotliar [18] who showed that a many-body model can be mapped onto the self-consistent solution of an auxiliary AIM in the limit of infinite dimensions $d \to \infty$. This allowed the usage of solvers for the AIM, which were already developed and in wide use at that time, to be applied to the self-consistent solution of lattice problems making the solution of many physical problems regarding strongly correlated electronic systems for the first time theoretically tractable.
In the following derivation of the DMFT we will suppress the spin index and we will be using the many-body Hamiltonian Equation (2.1). For the discussion the limit of infinite coordination number, i.e. neighbouring site, $\mathcal{Z}_{||i-j||}$, where the distance $||i-j||$ is the distance to next equivalent sites and not the limit of infinite dimensions will be used. Since the number of neighbouring sites scales with the number of dimensions, e.g. $\mathcal{Z} = 2d$ for the hypercubic lattice, the two limits are equivalent.
To obtain a non-trivial result we have to make sure that the scaling of the individual terms of the Hamiltonian, when we take the limit of infinite coordination number, is

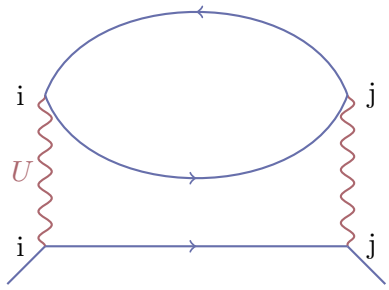

Figure 2.1.: Performing a power counting of the Greens function lines in the above second order diagram shows that its contribution vanishes in the limit of infinite dimensions and that only diagrams with $i = j$ give finite results.

non-trivial. It is easy to see that the interaction term in the Hamiltonian scales like

$$\left\langle \sum_{lmno} U_{lmno} c_{li}^{\dagger} c_{mi}^{\dagger} c_{ni} c_{oi} \right\rangle \xrightarrow{\mathcal{Z}_{||i-j||} \to \infty} const. \tag{2.3}$$

which tells us that we do not have to take care of the potential energy since it stays well defined.
Looking at the term of the kinetic energy, however, we see that when we increase the number of neighbouring sites the term grows as $\mathcal{Z}_{||i-j||}$ and it thus diverges when we take the limit. To keep the result non-trivial let us make the following ansatz for the hopping amplitude, which we will justify later,

$$t_{iljm} = \frac{t^*_{iljm}}{\sqrt{\mathcal{Z}_{||i-j||}}}. \tag{2.4}$$

In the equation above t^*_{iljm} is constant. The non-interacting Greens function, which is directly connected to t^*_{iljm}, scales the same way for $i \neq j$

$$G^0_{iljm}(\omega) = [(\omega \boldsymbol{\delta} - \mathbf{t})^{-1}]_{iljm} \propto \frac{1}{\sqrt{\mathcal{Z}_{||i-j||}}}. \tag{2.5}$$

The last quantity we have to take care of, is the Greens function. It is connected to the non-interacting Greens function via the Dyson equation

$$\mathbf{G}(\vec{k}, \omega) = \left(\left[\mathbf{G}^0(\vec{k}, \omega) \right]^{-1} - \mathbf{\Sigma}(\omega, \vec{k}) \right)^{-1}. \tag{2.6}$$

Since we already know that the non-interacting Greens function scales properly we only have to show that the self-energy also scales correctly. Let us first look at Figure 2.1

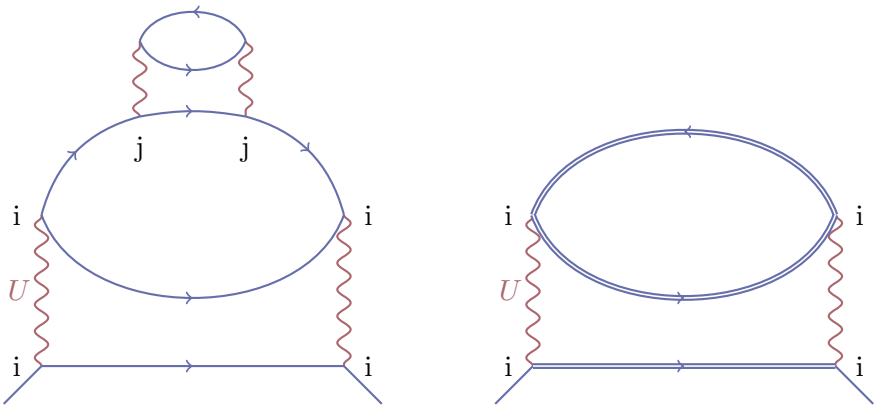

Figure 2.2.: On the left a diagram containing a hopping to another site and back again. Its contribution stays finite when we take the limit $\mathcal{Z}_{||i-j||} \to \infty$. It is contained in the skeleton diagram on the right.

where we see a Greens function (or self-energy if the legs are amputated) which connects two different sites. If we count the number of non-interacting Greens functions we notice that this diagram scales like $(\mathcal{Z}_{||i-j||})^{-3/2}$ and since we only obtain a factor of $\mathcal{Z}_{||i-j||}$ from the sum over sites j the total contribution of this diagram scales like $(\mathcal{Z}_{||i-j||})^{-1/2}$. In the limit $\mathcal{Z}_{||i-j||} \to \infty$ its contribution vanishes.

The other class of possible diagrams is the one depicted in Figure 2.2. In this example there is only two lines with different site indices. This class of diagrams contributes since a power counting yields a scaling of $(\mathcal{Z}_{||i-j||})^{-1}$ and thus the total scaling is 1. These contributions are, however, already included if we substitute the non-interacting Greens function by the interacting Greens function, depicted on the right of Figure 2.2. This means that the contributions to the Greens function in which an electron leaves the site and comes back at a later point are included and that the self-energy itself also is completely local in the limit of infinite dimensions

$$\mathbf{\Sigma}_{ij} \xrightarrow{\mathcal{Z}_{||i-j||}\to\infty} \delta_{ij}\mathbf{\Sigma}. \tag{2.7}$$

Thus also the interacting Greens function scales the same way as the non-interacting Greens function

$$\mathbf{G}_{ij}(\omega) \propto \frac{1}{\sqrt{\mathcal{Z}_{||i-j||}}} \tag{2.8}$$

Since we now know how all the contributions to the kinetic energy scale we can calculate the total scaling. We rescaled the hopping term as $(\mathcal{Z}_{||i-j||})^{-1/2}$, the Greens function also scales as $(\mathcal{Z}_{||i-j||})^{-1/2}$ and we obtain a scaling of $\mathcal{Z}_{||i-j||}$ from the sum over each

neighbouring site which yields the final result:

$$\left\langle \sum_{ljm} t_{iljm} c_{il}^{\dagger} c_{jm} \right\rangle \xrightarrow{\mathcal{Z}_{||i-j||\to\infty}} const. \tag{2.9}$$

The overall scaling of the kinetic energy is non-trivial and thus justifies our initial ansatz. A crucial part of the DMFT is still missing: How to obtain all the local topologically distinct self-energy diagrams in practice. This can be achieved by mapping the problem onto an auxiliary Anderson impurity model, since the solution of it are exactly all the local topologically distinct diagrams. For the solution to be the same the on-site interaction has to be the same as the one of the Hubbard Hamiltonian and the Greens function lines have to match. This can be achieved via a self-consistency scheme. To derive the self-consistency equation to make the mapping onto the AIM possible one can employ the cavity construction as shown in [138]. Similar to the cavity derivation of the self-consistency equation for the Ising model in infinite dimensions one can integrate out the lattice degrees of freedom except for a single site. The main difference to the classical system of Ising spins is that the Weiss field is now time dependent since the quantum fluctuations are kept in the description. The Weiss field has to be set in such a way that the local irreducible diagrams are the same and this is the case if the Greens function lines of the diagrams are the same. To achieve the equality of the Greens function lines the non-interacting Greens function has to fulfill

$$\left[\boldsymbol{\mathcal{G}}^0(i\omega_n)\right]^{-1} = \left[\mathbf{G}(i\omega_n)\right]^{-1} + \boldsymbol{\Sigma}(i\omega_n). \tag{2.10}$$

The non-interacting Greens function is the one which we already encountered in the discussion of the AIM

$$\left([\boldsymbol{\mathcal{G}}^0(i\omega_n)]^{-1}\right)_{mn} = (i\omega_n + \mu)\boldsymbol{\delta} - \sum_{il} \frac{V_{lm}^{\dagger}(p_i) V_{ln}(p_i)}{i\omega_n - \varepsilon_l(p_i)}. \tag{2.11}$$

With this equation which looks similar to a Dyson equation we have all ingredients needed to build up a self-consistency scheme to calculate the self-energy of a Hubbard model in infinite coordination number. This scheme is depicted in Figure 2.3. First we guess a self-energy to start the loop, in most cases since we do not know anything about the problem we simply set it to zero. Then we calculate the local Greens function of the lattice

$$\mathbf{G}^{\mathrm{loc}}(i\omega_n) = \frac{1}{V_{\mathrm{BZ}}} \int_{\mathrm{BZ}} d^3k \frac{1}{(i\omega_n + \mu)\boldsymbol{\delta} - \mathbf{DC} - \mathbf{H}(\vec{k}) - \boldsymbol{\Sigma}(i\omega_n)} \tag{2.12}$$

or its discrete version used for problems for which we know the hopping amplitudes from DFT calculations and therefore $\mathbf{H}(\vec{k})$ only numerically on a discrete grid

$$\mathbf{G}^{\mathrm{loc}}(i\omega_n) = \frac{1}{N_{\vec{k}}} \sum_{\vec{k}} \frac{1}{(i\omega_n + \mu)\boldsymbol{\delta} - \mathbf{DC} - \mathbf{H}_{\vec{k}} - \boldsymbol{\Sigma}(i\omega_n)} \tag{2.13}$$

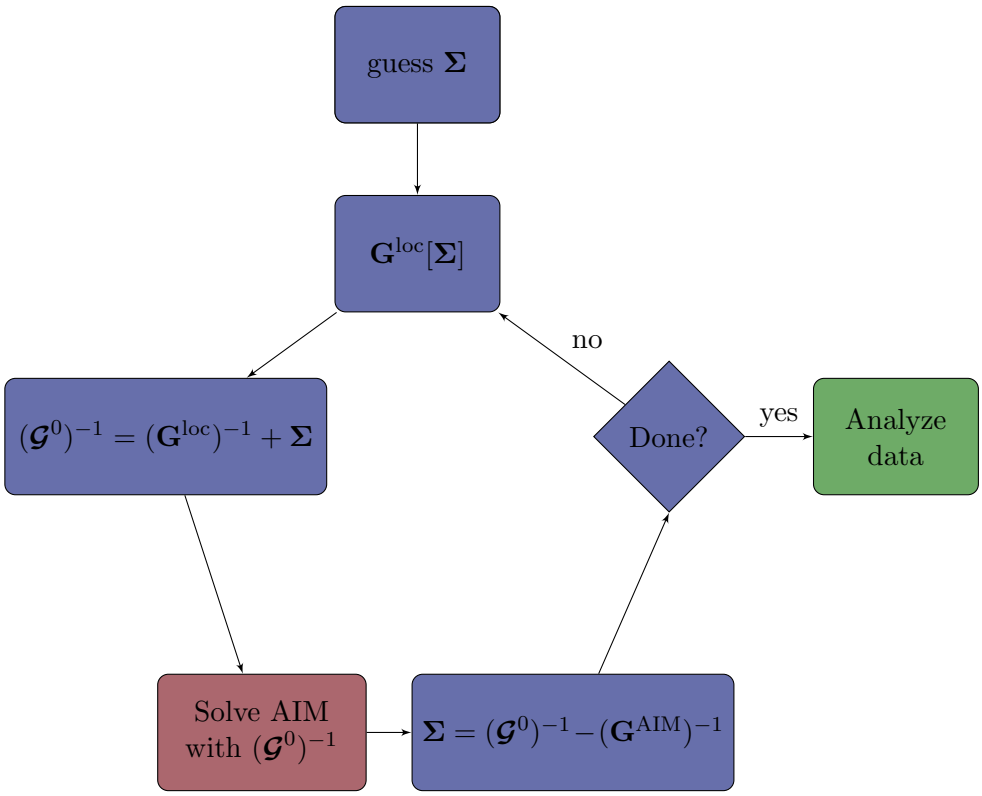

Figure 2.3.: A flow chart of the DMFT self-consistency loop. First we guess a self-energy $\mathbf{\Sigma}$. With this $\mathbf{\Sigma}$ we calculate a new local Greens function $\mathbf{G}^{loc}$ using Equation (2.13). Using the Dyson equation $\boldsymbol{\mathcal{G}}^0$ is calculated. The AIM defined by $\boldsymbol{\mathcal{G}}^0$ is then solved and a new self-energy with the Greens function of the AIM is calculated. New and old $\mathbf{\Sigma}$ are compared and we start a new iteration if the difference is too big. Otherwise we stop the cycle.

where $N_{\vec{k}}$ is the number of k-points, $\mathbf{H}_{\vec{k}}$ is the Hamiltonian of the localized downfolded bands and **DC** is the double counting correction, which I am going to discuss in the next section. In the above formula the size of each volume in $\vec{k}$-space is assumed to be the same. Using the Dyson equation of the AIM, Equation (2.10), we can calculate the non-interacting Greens function of the auxiliary AIM $\boldsymbol{\mathcal{G}}^0$. The AIM defined in such a way has to be solved with one of the solvers presented in Section 1.1. We can then calculate a new self-energy by using Equation (2.10) again using the Greens function of the AIM, which closes the loop. This is iterated until the change in the self-energy is beyond a certain threshold.

w2d

To control how many self-consistent steps are to be made in *w2dynamics* the parameter *DMFTsteps* is specified. For starting from an old self-energy one assigns *fileold* to the file which contains the self-energy and *readold* to the number which identifies the self-consistent iteration whose self-energy should be used.
The full self-consistency cycle is implemented in the file *DMFT.py*. Different classes for specific problems are implemented in *lattices.py* as described in Appendix A. One of them is the Bethe lattice in $d = \infty$, which corresponds to a semi-circular density of states. This lattice is especially suited for model calculations since its self-consistency equations are analytically known in τ and $i\omega_n$. To use this lattice the parameter *DOS* has to be set to *Bethe*. Another implemented class is *ReadIn* which reads a Hamiltonian specified by *HkFile*. This parameter specifies the file of the downfolded Hamiltonian which was obtained by a projection or downfolding method. I will discuss some of the methods in Section 2.4.

Since we are using the CT-HYB as the impurity solver the self-consistently determined bath enters by means of the hybridization function instead of $\boldsymbol{\mathcal{G}}^0$. The hybridization function is, as we discussed in the derivation of the CT-HYB in Section 1.3, connected to the non-interacting Greens function of the, in this context auxiliary, AIM by

$$\boldsymbol{\Delta}(-i\omega_n) = (i\omega_n + \mu_{imp})\boldsymbol{\delta} - [\boldsymbol{\mathcal{G}}^0(i\omega_n)]^{-1}. \tag{2.14}$$

The hybridization function which we are defining above is for the propagation of holes which we are generating by hybridization events with the impurity. The reason for this is that whenever we create an electron on the impurity we simultaneously create a hole in the bath by the hybridization $c^\dagger a$ which then propagates for a time until the inverse hybridization event occurs. Thus the hole propagator is needed.
In the equation above I now denote the chemical potential of the impurity by μ_{imp} since it has to be calculated to yield hybridization functions with the right high frequency behavior which should fall off as the one of a Greens function, namely as $\frac{1}{i\omega_n}$. To achieve this we define the impurity model as such that it fulfills this condition. As a starting

point we look at the inverse of the Greens function, defined in Equation (2.13), in its high-frequency limit

$$[\mathbf{G}^{loc}(i\omega_n)]^{-1} = (i\omega_n + \mu)\boldsymbol{\delta} - \langle \mathbf{H}_{\vec{k}} \rangle - \boldsymbol{\Sigma}(i\omega_n) - \mathbf{DC}, \tag{2.15}$$

where $\langle \mathbf{H}_{\vec{k}} \rangle = \frac{1}{N_{\vec{k}}} \sum_{\vec{k}} \mathbf{H}_{\vec{k}}$. Then we use the Dyson equation and obtain the following expression

$$(i\omega_n + \boldsymbol{\mu}_{imp})\boldsymbol{\delta} - \boldsymbol{\Delta}(-i\omega_n) = [\mathbf{G}^{loc}(i\omega_n)]^{-1} + \boldsymbol{\Sigma}(i\omega_n). \tag{2.16}$$

With the above two equations we get

$$\lim_{i\omega_n \to \infty} \boldsymbol{\Delta}(-i\omega_n) = \mu_{imp}\boldsymbol{\delta} - \boldsymbol{\Sigma}(i\omega_n) + \boldsymbol{\Sigma}(i\omega_n) - \mu\boldsymbol{\delta} + \langle \mathbf{H}_{\vec{k}} \rangle - \mathbf{DC}. \tag{2.17}$$

Taking the limit we arrive at the explicit expression of the impurity chemical potential

$$\boldsymbol{\mu}_{imp} = \mu\boldsymbol{\delta} - \langle \mathbf{H}_{\vec{k}} \rangle - \mathbf{DC}. \tag{2.18}$$

Using this chemical potential for the impurity we obtain a hybridization function with the right high frequency behavior.
The only thing we have not discussed yet is how we obtain the hybridization function in imaginary time τ. For the Fourier transformation of the impurity Greens function to $i\omega_n$ we use Equation (1.69). This Fourier transformation is necessary in every iteration since the CTQMC is working in τ while the self-consistency equations are formulated in $i\omega_n$.
The problem with naive Fourier transformations, discussions can be found in e.g. [139, 47, 110, 140], is that without a model the cut off at a finite number of $i\omega_n$ leads to inaccuracies of the Fourier transformed quantity. To cure this one can fix the high frequency behavior of the hybridization function before the Fourier transformation by subtracting a model with the correct high frequency behavior. The difference, i.e. the non-analytical information, is then Fourier transformed numerically, which is as we will see the part which behaves as $\frac{1}{(i\omega_n)^2}$ and thus falls off fast enough. After the Fourier transform the analytical part is then added back to the function.
To obtain the high-frequency behavior we start with the local Greens function and perform an expansion in $\frac{1}{i\omega_n}$, where $\boldsymbol{\mu}_{\vec{k}} = \mu\boldsymbol{\delta} - \mathbf{H}_{\vec{k}} - \mathbf{DC}$

$$\mathbf{G}^{loc}(i\omega_n) = \frac{\boldsymbol{\delta}}{i\omega_n} - \frac{1}{N_{\vec{k}}} \sum_{\vec{k}} \frac{\boldsymbol{\mu}_{\vec{k}} - \boldsymbol{\Sigma}_0}{(i\omega_n)^2} + \frac{1}{N_{\vec{k}}} \sum_{\vec{k}} \frac{\boldsymbol{\Sigma}_1 + (\boldsymbol{\mu}_{\vec{k}} - \boldsymbol{\Sigma}_0)(\boldsymbol{\mu}_{\vec{k}} - \boldsymbol{\Sigma}_0)}{(i\omega_n)^3} + \mathcal{O}\left(\frac{1}{(i\omega_n)^4}\right)\boldsymbol{\delta}, \tag{2.19}$$

where the $\boldsymbol{\Sigma}_n$ are the coefficients of the Taylor expansion of the self-energy $\boldsymbol{\Sigma}(i\omega_n) = \boldsymbol{\Sigma}_0 + \frac{\boldsymbol{\Sigma}_1}{i\omega_n} + \mathcal{O}\left(\frac{1}{(i\omega_n)^2}\right)\boldsymbol{\delta}$. By setting the self-energy to zero we get the non-interacting

Greens function of the impurity

$$\begin{aligned}\boldsymbol{\mathcal{G}}^0(i\omega_n) =& \frac{\boldsymbol{\delta}}{i\omega_n} - \frac{1}{N_{\vec{k}}}\sum_{\vec{k}}\frac{\boldsymbol{\mu}_{\vec{k}}}{(i\omega_n)^2} + \frac{1}{N_{\vec{k}}}\sum_{\vec{k}}\frac{\boldsymbol{\mu}_{\vec{k}}\boldsymbol{\mu}_{\vec{k}}}{(i\omega_n)^3} + \mathcal{O}\left(\frac{1}{(i\omega_n)^4}\right)\boldsymbol{\delta} \\ =& \frac{\boldsymbol{\delta}}{i\omega_n} + \frac{\mu\boldsymbol{\delta} - \langle\mathbf{H}_{\vec{k}}\rangle - \mathbf{DC}}{(i\omega_n)^2} + \frac{(\mu\boldsymbol{\delta} - \mathbf{DC})^2 - 2(\mu\boldsymbol{\delta} - \mathbf{DC})\langle\mathbf{H}_{\vec{k}}\rangle + \langle\mathbf{H}^2_{\vec{k}}\rangle}{(i\omega_n)^3} + \\ & \mathcal{O}\left(\frac{1}{(i\omega_n)^4}\right)\boldsymbol{\delta}.\end{aligned} \tag{2.20}$$

We then calculate the Taylor expansion of $\left[\boldsymbol{\mathcal{G}}^0(i\omega_n)\right]^{-1}$, obtain

$$\left[\boldsymbol{\mathcal{G}}^0(i\omega_n)\right]^{-1} = i\omega_n + \mu\boldsymbol{\delta} - \langle\mathbf{H}_{\vec{k}}\rangle - \mathbf{DC} + \frac{\langle\mathbf{H}_{\vec{k}}\rangle^2 - \langle\mathbf{H}^2_{\vec{k}}\rangle}{i\omega_n} + \mathcal{O}\left(\frac{1}{(i\omega_n)^2}\right)\boldsymbol{\delta} \tag{2.21}$$

and finally plugging the expression above into Equation (2.14) we get the high frequency behavior of the hybridization function which is given by

$$\boldsymbol{\Delta}(i\omega_n) = \frac{\langle\mathbf{H}_{\vec{k}}\rangle^2 - \langle\mathbf{H}^2_{\vec{k}}\rangle}{i\omega_n} + \mathcal{O}\left(\frac{1}{(i\omega_n)^2}\right)\boldsymbol{\delta} \tag{2.22}$$

as discussed in [47, 141].

w2d

To define how many points in imaginary time τ are calculated for the hybridization function $\boldsymbol{\Delta}(\tau)$ the parameter *Nftau* is used. The default is 10000 which is a safe guess even for involved calculations. For calculating points with an arbitrary τ in the simulation the hybridization function is linearized between the two points τ_1 and τ_2 where $\tau_1 < \tau < \tau_2$.

In general the chemical potential for a wanted filling in the LDA+DMFT calculations is not known. For calculating the chemical potential in a simulation one can use the identification of local lattice Greens function with the Greens function of the Anderson impurity model in the DMFT. At each iteration of the DMFT the current filling of the local lattice Greens function with the current chemical potential is checked against the wanted filling. If the filling is wrong the chemical potential is adjusted such that the filling of the lattice problem is correct. This can however change again due to the change of the self-energy and thus needs to be checked in each iteration. The filling of the system is calculated in Matsubara frequencies via the Matsubara sum of the Greens function

$$\frac{1}{\beta}\,\mathrm{Tr}\sum_n\left(\mathbf{G}^{loc}(i\omega_n) - \frac{\boldsymbol{\delta}}{i\omega_n}\right) + \frac{\boldsymbol{\delta}}{2} = \mathrm{Tr}\,\boldsymbol{\rho} \tag{2.23}$$

where we needed to include the conversion factor of $\frac{\delta}{2}$ because of the sum $\sum_n \frac{1}{i\omega_n}$.

w2d

For the search of the right chemical potential the parameters *EPSN* defines the maximal difference between the sought for filling, defined by *totdens*, and the filling calculated by the formula above. If the chemical potential should no be adjusted but stay fixed at the given chemical potential defined by *mu* then the parameter EPSN needs to be set to 0.
The half-filling condition for the mean density-density and Kanamori interaction which I am going to discuss in detail in Chapter 3 is given by:

$$\mu = (2N_{orb} - 1)\frac{U}{2} - (N_{orb} - 1)\frac{5J}{2}$$

where N_{orb} is the number of orbitals, U is the intra-orbital interaction and J is the Hund's coupling.

2.3. The Double Counting Correction

To combine first principle calculations like LDA with DMFT calculations we still have to include another important bit. If we downfold LDA bandstructures to low energy effective models which are well localized and can be treated in DMFT there is already a part of the interaction between electrons included, namely the Hartree interaction and some part of the exchange and correlation depending on the V_{xc} potential used in the LDA calculation. This part of the interaction has to be subtracted since we would otherwise double count it. This is not an issue if we are only treating one d-manifold in the DMFT since then the double counting correction can be absorbed into the chemical potential; it is, however, important if we are also treating p-bands, if we have more than one correlated atom in the unit cell or if we perform nano- or "layer"-DMFT calculations, where there are several inequivalent constituents or correlated sites.
The problem is that, since the two methods have a completely different background, there is no easy answer to the question what term exactly has to be subtracted. The double counting correction which is used, however, has a big effect on the results obtained, as is discussed in [64].
There are two well known attempts to find an analytical expression for the double counting correction. Both have their origins in the LDA+U development, a precursor of the LDA+DMFT method. The first one was introduced by Anisimov et al. [96], the around mean-field approximation (AMF). The starting point for the AMF is as Czyżyk

and Sawatzky [97] pointed out the identity

$$\begin{aligned} n_{m\uparrow}n_{m'\downarrow} =& n_{m\uparrow}\langle n_\downarrow\rangle + n_{m'\downarrow}\langle n_\uparrow\rangle - \langle n_\uparrow\rangle\langle n_\downarrow\rangle + \\ & (n_{m\uparrow} - \langle n_\uparrow\rangle)(n_{m'\downarrow} - \langle n_\downarrow\rangle). \end{aligned} \tag{2.24}$$

One can now identify the first three terms with the mean-field approximation and with this we can write the energy of the system with on-site Coulomb interaction and exchange interaction as

$$E^{\mathrm{LDA+AMF}} = E^{\mathrm{LDA}} + \frac{1}{2}\sum_{m,m',\sigma} U(n_{m\sigma} - n_L)(n_{m'-\sigma} - n_L) \tag{2.25}$$

$$+ \frac{1}{2}\sum_{m,m',m\neq m',\sigma} (U-J)(n_{m\sigma} - n_L)(n_{m'\sigma} - n_L), \tag{2.26}$$

where $n_{m\sigma}$ are the occupancies of the orbitals m with spin σ and $n_L = \frac{1}{N_{orb}}\sum_{m\sigma} n_{m\sigma}$ is the mean occupation per orbital with N_{orb} the number of orbitals. The above formula can also be adapted to general interaction matrices with a density-density part of $U_{mm'}$ and $J_{mm'}$ which I am going to discuss in Chapter 3. If we now take the derivative of $E^{\mathrm{LDA+AMF}}$ with respect to the particle number n_m we see that the first term in the brackets would yield the correct Hartree term in LDA+U calculations while the second term is subtracted to avoid double counting which thus leads to the following term

$$DC^{AMF} = \bar{U}(n_L - 1/2) \tag{2.27}$$

where $\bar{U}$ is the averaged interaction matrix for this angular momentum quantum number L which is given by

$$\bar{U} = \frac{U + (N_{orb}-1)(U-2J) + (N_{orb}-1)(U-3J)}{2N_{orb}-1}. \tag{2.28}$$

The occupancies used in the DC^{AMF} are the LDA occupancies.
The second widely used analytical expression is the so-called "fully localized limit" (FLL)[97]. The argument for the fully localized limit is that especially for insulators the description of an electronic interaction to the mean-field solution is wrong. A better description is a localized orbital embedded in a reservoir of delocalized electrons. Thus making the atomic limit for the DC the natural choice. The resulting double counting correction is then given by

$$DC^{FLL} = DC^{AMF} + (U-J)(n_L - 1/2) \tag{2.29}$$

In this correction the energy of the manifold is shifted downwards if it is more than half-filled and upwards if it is less than half-filled. This leads to a preference of integer

filled orbitals [98].
To overcome the arbitrariness of analytical models one can think of self-consistent double counting corrections which make use of observables of the impurity.
One possible approach is to set the rigid shift of the impurity self-energies to zero, thus

$$DC^{\Sigma} = \frac{1}{N_{orb}} Re(\mathrm{Tr}(\mathbf{\Sigma}(i\omega_n \to \infty))). \tag{2.30}$$

This double counting correction has been successfully applied to metallic systems in e.g. [99, 95].
Another possibility is to impose a constraint on the charge of the impurity. To this end the impurity Greens function and the non-interacting Greens function are required to have the same filling

$$\mathrm{Tr}\,\mathbf{G}^{AIM}(\beta) \stackrel{!}{=} \mathrm{Tr}\,\mathbf{G}^{0}(\beta). \tag{2.31}$$

This works nicely in metallic systems [100] but breaks down if we want to treat insulating systems since then the filling in the gap at the Fermi edge does not vary and thus the fixing of the occupancy does not work anymore.
In [64] another double counting correction was suggested. There the double counting correction was set such that the chemical potential was right in the middle of the gap at the Fermi edge. This, of course, only works for insulating systems.
The definite answer of what the best double counting correction is cannot be answered conclusively and might even vary from system to system. As we already mentioned in the beginning the main problem is that the LDA and the DMFT methods are different formal approaches. In recent years solutions to this problem are definitely going towards substituting the LDA part by the GW which is also a diagrammatic approximation. Thus the diagrams already treated in GW could in principle be subtracted exactly and the problem of double counting corrections would finally be solved. First successes in this direction were already made in [121, 122].

w2d

The double counting correction can be set in *w2dynamics* by setting *dc* to one of anisimov, fll, amf or number. If number is specified then one also has to set the parameter *dc_value* to the desired double counting values, a list which has to be as long as the number of correlated orbitals.
For a system with three *d*-bands e.g.: *dc_value*$= 1, 1, 1$

2.4. The Problem of Choosing the Basis

Once we have performed a LDA calculation there is still an open question: Which bands are the correlated bands which we want to treat in the DMFT. If there is only a well

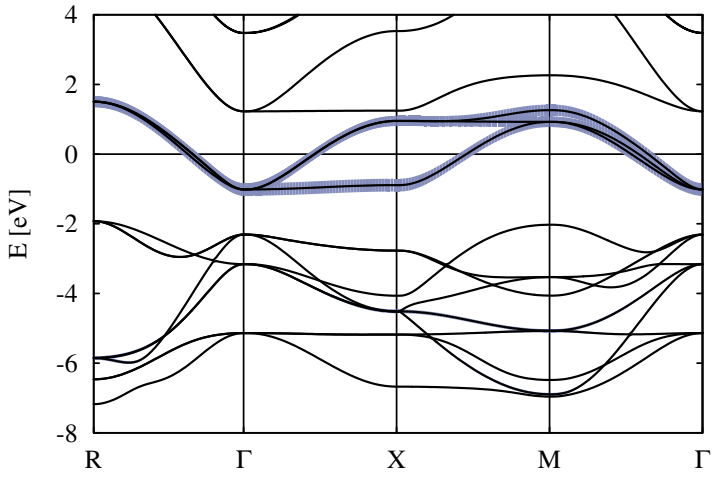

Figure 2.4.: The band structure of V_2O_3 along high symmetry points in the Brioullin zone. The weight of the t_{2g}-orbitals on the bands is denoted by the blue color. Since the t_{2g} are well separated from the rest of the band the downfolding onto a local Hamiltonian is straightforward.

separated band at the Fermi energy as it is, e.g., the case for $SrVO_3$, for which we show a band structure in 2.4, the answer is relatively simple. For such systems the downfolding onto a low-energy Hamiltonian is easy to accomplish with any of the methods presented below. If, however, many bands cross the Fermi energy, as is the case, e.g., of Iron shown in Figure 2.5, the downfolding procedure becomes more involved.
In this section I will discuss some downfolding methods, while in the next section I will discuss the procedure to include p-bands in the DMFT self-consistency cycle. This is necessary if the hybridization between d and s/p orbitals is strong. For a comparison of different downfolding techniques and results of calculations for physical systems see e.g. [65, 66, 67]. A good of different discussion of downfolding schemes can be found in [142].

Wannier functions In solid state physics calculations are often performed in the reciprocal $\vec{k}$-basis to make use of the periodic structure of the lattice. This is, e.g., the case in most DFT programs. For some applications, e.g., for performing LDA+DMFT calculations, but also for the visualization of chemical bonds and for a better understanding of the bonding mechanisms a representation in real space is necessary. In 1937 Wannier [143] introduced such a representation named after him. In contrast to the Bloch functions $|\Psi_{n\vec{k}}\rangle$ which are labeled by the crystal momentum $\vec{k}$ and a band index n, the Wannier functions $|\vec{R}n\rangle$ are labeled by a cell index $\vec{R}$ and a band-like index n.
As mentioned above typically calculations of electronic structures in the independent-

particle approximation are performed using periodic boundary conditions thus the Bloch wavefunctions are eigenfunctions of the lattice translation operator and the effective one-particle Hamiltonian. If for the moment we concentrate on one isolated band one can build up a localized wavefunction by superposition of Bloch functions of different $\vec{k}$. To build up wavefunctions in different cells $\vec{R}$ we can insert a phase factor

$$|\vec{R}n\rangle = \frac{V}{(2\pi)^3}\int_{BZ} d\vec{k} e^{-i\vec{k}\cdot\vec{R}} |\Psi_{n\vec{k}}\rangle \,. \tag{2.32}$$

The wavefunction of one cell transforms into the other under the translation by the lattice vector $\vec{R}$. The inverse transform back to Bloch functions is given by

$$|\Psi_{n\vec{k}}\rangle = \sum_{vecR} e^{i\vec{k}\cdot\vec{R}} |\vec{R}n\rangle \,. \tag{2.33}$$

Since the Fourier transformations given above are unitary the representation in the Wannier basis is equivalent to the one in the Bloch basis, although the Wannier basis is not an eigenbasis of the effective Hamiltonian anymore. One can think of it as an exchange of a localization in energy to a localization in space.
A peculiarity which has to be considered when treating Wannier functions is the fact that they are highly non-unique. This is due to the gauge freedom in the definition of wavefunctions in Bloch space:

$$|\bar{\Psi}_{n\vec{k}}\rangle = e^{i\phi_{n\vec{k}}} |\Psi_{n\vec{k}}\rangle \,, \tag{2.34}$$

where $\Phi_{n\vec{k}}$ is a real function which is periodic in reciprocal space. If the resulting wavefunctions are smooth, i.e. $\nabla_{\vec{k}} |u_{n\vec{k}}\rangle$ is well defined for all $\vec{k}$, then the resulting wavefunction in Wannier representation is well-localized. This is due to the nature of the Fourier-transform which gives more localized structures in real-space if the object in reciprocal-space is smooth. As noted in [142] the Wannier-functions are *more non-unique* than the Bloch-functions.
If one wants to treat not just one isolated band, but a manifold of M bands which are well separated from all other bands as in Figure 2.4 one can generalize the gauge transformation given above by

$$|\bar{\Psi}_{n\vec{k}}\rangle = \sum_{m=1}^{M} U_{mn}^{\vec{k}} |\Psi_{m\vec{k}}\rangle \,. \tag{2.35}$$

The unitary matrix $U_{mn}^{\vec{k}}$ is of the dimension $M \times M$ and it, of course, does not change the traces over this band manifold. The resulting wavefunctions $|\bar{\Psi}_{n\vec{k}}\rangle$ are, however, no longer eigenfunctions of the effective Hamiltonian and n is no longer a band index in the usual sense. We have to make use of this gauge freedom to obtain smooth wavefunctions

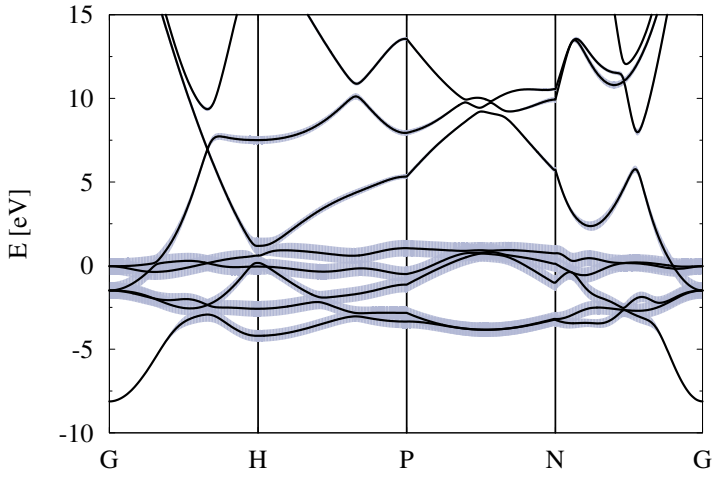

Figure 2.5.: The band structure of Fe along high symmetry points in the Brioullin zone. The weight of the d-orbitals on the bands is denoted by the blue color. The correlated d-bands which we want to treat in the DMFT are entangled with other bands, thus the downfolding procedure becomes more involved.

$|\bar{\Psi}_{n\vec{k}}\rangle$, and thereby well localized wavefunctions, if there are degeneracies as the ones in the Γ-point of Figure 2.4. There the wavefunction is not analytic anymore and a naive Fourier transform would lead to poorly localized objects. By a clever rotation using the gauge freedom one can restore the smoothness and thereby the localization in real space.

Disentanglement The problem of constructing well localized orbitals becomes more involved if the target bands we want to keep in the low-energy Hamiltonian are crossed by bands which we want to project out. An example of such a system is shown in Figure 2.5. For such systems it is difficult to choose which Bloch states are used to form the wavefunctions in Wannier representation.
One can break the problem down into two steps. The first step selects the Bloch functions and in the second step the unitary transformation matrix is constructed. The procedures to find the subset of Bloch wavefunctions to use is actually very similar to the techniques to find the localized wavefunctions. The simplest way to select a subspace of the Bloch bands is a projection onto local trial orbitals $|\chi^{\vec{R}}_{m\vec{k}}\rangle$ a technique which I am going to discuss in more detail later in this section. Another possibility is an iterative procedure which is based on the smoothness of the wavefunctions. For an in-depth discussion see [142].

Calculating the Greens function Whatever route we choose to obtain the wanted low-energy Hamiltonian in $\vec{k}$-space in the end we want to calculate the lattice Greens function as an input for DMFT calculations. The result of the construction of localized orbitals is going to be some projection matrix from m, possibly entangled bands, to n target bands. One has two possibilities to calculate the $\vec{k}$-dependent Greens function using these Projectors $\boldsymbol{\mathcal{P}}$.
If we suppress $\vec{k}$ indices, the lattice Greens function can be written as

$$\mathbf{G}^{lattice}(i\omega_n) = \boldsymbol{\mathcal{P}} \left[(i\omega_n + \mu)\boldsymbol{\delta} - \boldsymbol{\varepsilon} - \boldsymbol{\mathcal{P}}^\dagger \boldsymbol{\Sigma}(i\omega_n)\boldsymbol{\mathcal{P}} \right]^{-1} \boldsymbol{\mathcal{P}}^\dagger \tag{2.36}$$

where $\boldsymbol{\varepsilon}$ is a diagonal $m \times m$ matrix containing the eigenvalues from an LDA program. This expression is equal to the definition of the Greens function constructed with a Hamiltonian in $\mathcal{W}$ subspace, which we use in this work, as long as the projectors $\boldsymbol{\mathcal{P}}$ are quadratic. The Greens function calculated by using the Hamiltonian $\mathbf{H} = \boldsymbol{\mathcal{P}}\boldsymbol{\varepsilon}\boldsymbol{\mathcal{P}}^\dagger$ is given by

$$\mathbf{G}^{lattice}(i\omega_n) = \left[(i\omega_n + \mu)\boldsymbol{\delta} - \mathbf{H} - \boldsymbol{\Sigma}(i\omega_n) \right]^{-1} . \tag{2.37}$$

This equality can be easily proven:

$$\begin{aligned}
\mathbf{G}^{lattice} &= \left[(i\omega_n + \mu)\boldsymbol{\delta} - \mathbf{H} - \boldsymbol{\Sigma}(i\omega_n) \right]^{-1} \\
&= \left[(i\omega_n + \mu)\boldsymbol{\mathcal{P}}\boldsymbol{\delta}\boldsymbol{\mathcal{P}}^\dagger - \boldsymbol{\mathcal{P}}\boldsymbol{\varepsilon}\boldsymbol{\mathcal{P}}^\dagger - \boldsymbol{\mathcal{P}}\boldsymbol{\mathcal{P}}^\dagger\boldsymbol{\Sigma}\boldsymbol{\mathcal{P}}\boldsymbol{\mathcal{P}}^\dagger \right]^{-1} \\
&= \left[\boldsymbol{\mathcal{P}} \left((i\omega_n + \mu)\boldsymbol{\delta} - \boldsymbol{\varepsilon} - \boldsymbol{\mathcal{P}}^\dagger\boldsymbol{\Sigma}\boldsymbol{\mathcal{P}} \right) \boldsymbol{\mathcal{P}}^\dagger \right]^{-1} \\
&= \boldsymbol{\mathcal{P}} \left[\left((i\omega_n + \mu)\boldsymbol{\delta} - \boldsymbol{\varepsilon} - \boldsymbol{\mathcal{P}}^\dagger\boldsymbol{\Sigma}\boldsymbol{\mathcal{P}} \right) \right]^{-1} \boldsymbol{\mathcal{P}}^\dagger .
\end{aligned}$$

Since the inversion is not well defined anymore for rectangular matrices the equality of the two constructions is not guaranteed if the low-energy Hamiltonian is constructed with $m \neq n$.

Projection

A very simple approach for obtaining Wannier functions is taken by Amadon *et al.* [100], which is rooted in the analysis given in [144]. Amadon *et al.* use a projection onto local atomic like trial orbitals $|\chi^{\vec{R}}_{n\vec{k}}\rangle$, where $\vec{R}$ denotes the correlated atom, $\vec{k}$ is a wave vector and n is a local orbital. The projected quantities are all the Bloch states $\Psi_{m\vec{k}}$, which are, as previously mentioned, readily available from the output of most LDA programs. The projection is, however, restricted to the subset $\mathcal{W}$ of Bloch bands:

$$|\tilde{\chi}^{\vec{R}}_{n\vec{k}}\rangle \equiv \sum_{m \in \mathcal{W}} \langle \Psi_{m\vec{k}} | \, \chi^{\vec{R}}_{n\vec{k}} \rangle \, |\Psi_{m\vec{k}}\rangle . \tag{2.38}$$

The functions we obtain are not Wannier functions anymore since the projection is no longer a unitary operation. We can, however, make it unitary again by performing an orthonormalization,

$$|w_{\vec{k}n}^{\vec{R}}\rangle = \sum_{\vec{R}'n'} S_{nn'}^{\vec{R}\vec{R}'}(\vec{k})\,|\tilde{\chi}_{\vec{k}n'}^{\vec{R}'}\rangle\,, \tag{2.39}$$

where $\mathbf{S}_{\vec{k}}^{\vec{R}\vec{R}'}$ is the inverse square root of the overlap matrix

$$O_{nn'}^{\vec{R}\vec{R}'}(\vec{k}) \equiv \langle\tilde{\chi}_{\vec{k}n}^{\vec{R}}|\;\tilde{\chi}_{\vec{k}n'}^{\vec{R}'}\rangle$$
$$S_{nn'}^{\vec{R}\vec{R}'}(\vec{k}) \equiv \left\{\left[\mathbf{O}(\vec{k})\right]^{-1/2}\right\}_{nn'}^{\vec{R}\vec{R}'}.$$

Thus we finally obtain the projector onto a localized representation which is given by

$$P_{nm}^{\vec{R}}(\vec{k}) = \sum_{\vec{R}'n'} S_{nn'}^{\vec{R}\vec{R}'}(\vec{k})\,\langle\chi_{\vec{k}n}^{\vec{R}}|\;\Psi_{\vec{k}m}\rangle\,. \tag{2.40}$$

Restricting the sum in Equation (2.38) to $\mathcal{W}$ and then orthonormalizing the projector we create wave-functions which have a larger spread than χ, the atomic orbitals [100].

Maximally localized Wannier

The projection method described above can be refined by introducing a well-defined localization criterion. This localization criterion is non-unique, as discussed in [68], but a widely used criterion is the one introduced by Marzari and Vanderbilt [145]

$$\Omega = \sum_n [\langle\vec{0}n|r^2|\vec{0}n\rangle - \langle\vec{0}n|\vec{r}|\vec{0}n\rangle^2] \tag{2.41}$$

which measures the sum of the quadratic spreads of the M wavefunctions in the home cell around their centers. This spread is minimized by varying the unitary transformations U_{mn} iteratively. A description of this process can be found in [68].
For this procedure a package for the ab-initio program Wien2k is available [123]. Another ab-initio program VASP provides a direct interface to the Wannier90 [124] program which can used to generate such maximally localized Wannier functions.

NMTO

An alternative approach is the NMTO method which uses local orbitals as a basis set [69]. This scheme is based on the perturbative approach as introduced in [146]. For obtaining a description of the target bands one separates the original Hamiltonian into

two parts. The target bands, which are called "active" set, and the rest of the bands, the "passive" set. The effective Hamiltonian can be rewritten as

$$H = \begin{pmatrix} H_{00} & 0 \\ 0 & H_{11} \end{pmatrix} + \begin{pmatrix} 0 & V_{01} \\ V_{10} & 0 \end{pmatrix}. \tag{2.42}$$

We can express the wavefunctions as a sum of its projections by

$$\begin{aligned} (H_{00} - \varepsilon) |\Psi_0\rangle + V_{01} |\Psi_1\rangle = 0 \\ V_{10} |\Psi_0\rangle + (H_{11} - \varepsilon) |\Psi_1\rangle = 0 \end{aligned} \tag{2.43}$$

with ε the eigenvalues of $|\Psi\rangle$. If we accept an energy dependent Hamiltonian we can eliminate the dependence on the "passive" set and with Equation (2.43) we get

$$H_{00}(\varepsilon) = H_{00} - V_{01} \left[H_{11} - \varepsilon\right]^{-1} V_{10}. \tag{2.44}$$

One option is to set the energy to the center of mass of the bands. This can be used to generate tight-binding Hamiltonians from first-principle calculations as outlined in [147].
Another approach which is closely related to the Löwdin downfolding is the *N*MTO approach. For this approach the Löwdin partitioning is used in connection with muffin-tin orbitals (MTOs). Following the lines above we separate the muffin-tin orbitals into "active" and "passive" sets and using the separation of the Hamiltonian we obtain energy dependent orbitals for the active space [70]

$$\Phi_0(\varepsilon, \vec{r}) = \Phi_0(\vec{r}) - \Phi_1(\vec{r}) \left[H_{11} - \varepsilon\right]^{-1} V_{10}. \tag{2.45}$$

These orbitals are equivalent to the original orbitals and can be interpreted as the active space which is dressed by the energy-dependent linear combination of the passive orbitals. To get rid of the energy dependence an Nth order fit is made to the orbitals which sets the name of the method, e.g. 0MTO or LMTO (as in linear) if the energy dependence is simply set to an energy.

2.5. DMFT on a dp-basis

The DMFT loop I introduced in Section 2.2 is only reasonable if only the *d*-bands cross the Fermi energy. In many circumstances e.g. for iron as can be seen in Figure 2.5, however, the Fermi energy is crossed by *d*- and *p*-bands. This makes a downfolding, on *d*-orbitals only, unfeasible since the downfolded orbitals would have a lot of weight on the *p*-bands since this leads to a wider spread of the *d*-orbitals which breaks a description by the Hubbard model.
To remedy this one can downfold the LDA-Hamiltonian onto the *d*- and *p*-bands. In

this description the Hamiltonian which enters into the DMFT calculation will have the following form

$$\mathbf{H}_{\vec{k}} = \begin{pmatrix} \mathbf{H}^{d}_{\vec{k}} & \mathbf{H}^{dp}_{\vec{k}} \\ \left[\mathbf{H}^{dp}_{\vec{k}}\right]^{\dagger} & \mathbf{H}^{p}_{\vec{k}} \end{pmatrix} \tag{2.46}$$

where $\mathbf{H}^{d}/\mathbf{H}^{p}$ is the block containing the on-site energies and hopping of the d/p-orbitals and the hopping between the d and p orbitals is contained in $\mathbf{H}^{dp}$. In this scheme the p-orbitals can either be on-site or p-orbitals of ligands.
The DMFT self-consistency cycle then looks the following way:
(i) When we calculate the local Greens function for the DMFT self-consistency we use the large Hamiltonian

$$\mathbf{G}^{loc}_{full}(i\omega_n) = \frac{1}{N_{\vec{k}}} \sum_{\vec{k}} \left[(i\omega_n + \mu)\boldsymbol{\delta} - \mathbf{H}_{\vec{k}} - \boldsymbol{\Sigma}^{full}(i\omega_n) \right]^{-1}. \tag{2.47}$$

where $\boldsymbol{\Sigma}^{full}$ can also include additional energy shifts as I will discuss in Section 2.7.
(ii) We then project onto the correlated orbitals, which we are going to use to define the local AIM problem,

$$\mathbf{G}^{loc}_{d} = \boldsymbol{\mathcal{P}}_{d} \mathbf{G}^{loc}_{full} \left[\boldsymbol{\mathcal{P}}_{d}\right]^{-1}, \tag{2.48}$$

where $\boldsymbol{\mathcal{P}}_{d}$ projects from the full $(d+p)$-space to the correlated d-space.
(iii) And finally using the local Greens function in the correlated subspace we define the bath Greens function of the auxiliary AIM

$$\left[\boldsymbol{\mathcal{G}}^{0}_{d}\right]^{-1} = \left[\mathbf{G}^{loc}_{d}\right]^{-1} + \boldsymbol{\Sigma}_{d} \tag{2.49}$$

These steps are repeated in the self-consistency loop until convergence is reached.
One would naively expect that the addition of more bands always leads to a similar, more accurate description of the system at hand. This is, however not always the case as I am going to discuss in the following study, Section 2.5.1. To better understand the effect the inclusion of p-bands has on physical observables and the expansion order k in the CT-HYB algorithm the study I present in Section 2.5.2 was conducted.

2.5.1. DP-Model

This subsection is based on the following manuscript:
Effective crystal field and Fermi surface topology: a comparison of d- and dp-orbital models.
N. Parragh, G. Sangiovanni, P. Hansmann, S. Hummel, K. Held and A. Toschi
arXiv:1303.2099 [cond-mat.str-el].

There have been many big successes of the LDA+DMFT method to address open questions of strongly correlated electron systems. In these materials there are d-orbitals which are however often coupled to ligands such as O-p. Since the role of these ligands can be quite strong is partly surprising that most of the LDA+DMFT calculations have in the past been made with a basis-set which only includes the d-orbitals crossing or close to the Fermi level.
More recently some LDA+DMFT calculations have been made which also took into account less correlated orbitals, e.g. the ligand p-orbitals. One expects the LDA+DMFT calculations in larger basis sets to be more accurate than the ones in the smaller basis set. This expectation is based on two arguments. One: the downfolding of the LDA wave functions onto an enlarged basis set leads to better localized correlated manifolds, since the dp-hopping can now be explicitly included in the model. Two: the model includes the description of charge-transfer processes which is an important physical process in materials and thus should be included in the modelling of realistic systems.
In contrast to these general arguments actual calculations performed in enlarged basis-sets sometimes show very strong deviations from d-only calculations in cases where the d-only results were close to experiments. We are only going to mention a few examples for which the scheme with an enlarged basis set gave better results than without it. It improved the description of the insulating behavior of NiO [73] and of the MIT in NiS_2 [75] compared to the d-only calculation [76]. For the cobalt oxygen compounds the results of one- and two-particle properties are also quite accurate, e.g. $SrCoO_3$ [95], which I am going to discuss in more detail in section 3.2.1, and $LaCoO_3$ [133].
On the other hand there are also cases which, in contrast to the aforementioned examples, led to contradictory results compared with the d-only calculations and/or experiments. The MIT in V_2O_3, one of the prototypical materials for the treatment in LDA+DMFT, could not be reproduced even with very large values of the Coulomb interaction when the oxygen p-orbitals were included [81]. In recent years it was found that in La_2CuO_4 and in $LaNiO_3$ the Mott-Hubbard insulating phase was missing with calculations in the dp-basis set [82], whereas they are insulating in d-only calculations with realistic values of the dd-interaction. Especially the discrepancy of the results regarding the Mott-Hubbard metal insulator transition has led to a discussion in the recent literature. The dp-models

are, for reasons mentioned above, considered better and the absence of insulating behavior is ascribed to the neglected correlations. In [82] the proposed mechanism for the absence of the MIT is the disregard of non-local correlations. I will discuss this aspect in more detail in 2.7.1.
The non-local correlations can, however, not be the solution to the all the problems one encounters when including *p*-orbitals, which are present in a large parameter regime, also at high temperatures, where their contributions, not described within DMFT, should be negligible. In one very interesting LDA+DMFT *d*-only study which dealt with $LaNiO_3/LaAlO_3$ heterostructures [84, 85] it was observed that the electronic correlation always enhances a positive crystal-field splitting between the two e_g orbitals which cross the Fermi surface. By tuning this crystal-field one could eventually change the shape of the Fermi surface to a situation which resembles the one of the high-temperature superconducting cuprates. The striking difference between the calculations in the *d*- and *dp*-basis sets was reported in [83]. In this study it is shown that the correlation, in LDA+DMFT calculation with *dp*-basis sets, always reduces the crystal field splitting, thus prohibiting the realization of the cuprate like Fermi surface. This problem raises the general question of the proper use and interpretation of LDA+DMFT calculations in enlarged basis sets. Especially if one wants to use the LDA+DMFT as a method with predictive power to help with the creation of complex materials. A model similar to the one studied for the $LaNiO_3/LaAlO_3$ system will be used in this section to shed some light on the effect of enlarging the basis set.

The Models

Below I will describe the model which we used to study the discrepancies in the orbital polarization between the *d*-only and the *dp*-model. Since we already know from the study of the nickelates that two correlated e_g orbitals are enough to lead to a different result of the LDA+DMFT calculations we created two models with a cubic symmetry to study this behavior. The two models are similar to the models used for the nickelates, which corresponds to a quasi two-dimensional geometry. However since we are using DMFT the model only enters via the k-integrated local Greens function and thus the results depend mainly on the relation between the kinetic energy of the two correlated orbitals and the hybridization term. The results can therefore be seen in a more general context applicable to a wide range of mulitorbital systems at the DMFT level.

***d*-only two-band model** The e_g only model contains only two parameters, the hopping amplitude t_{dd} and the initial crystal-field parameter Δ_{CF}. To parametrize the hopping the table of Slater and Koster [86] was used while the crystal field potential Δ_{CF}, which accounts for the on-site difference between the two e_g states, is kept as a free parameter. The crystal-field corresponds to a tetragonal distortion, i.e. a compression or elongation of one of the cubic C^4 axis of the ligand octahedron.

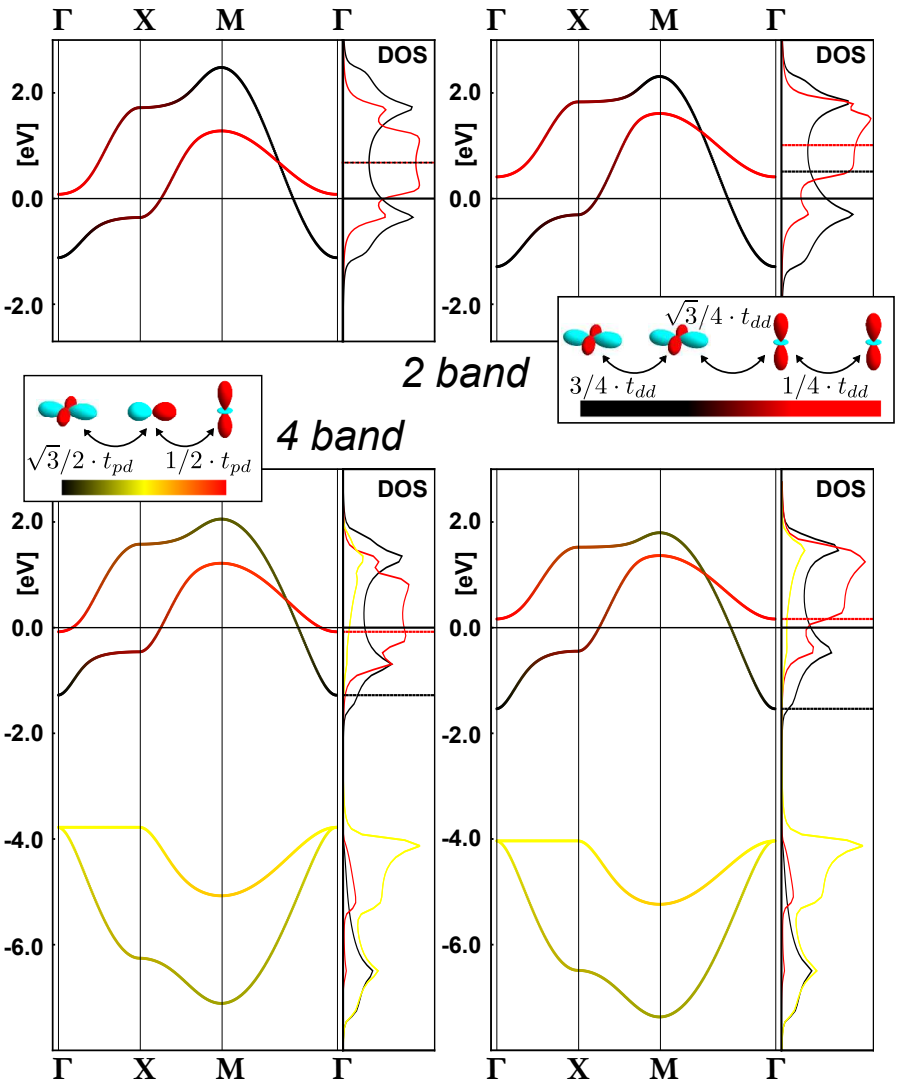

Figure 2.6.: Band-structure and DOS of the two-band d-model (upper panel) and the four-band dp-model (lower panel) for two different values of the crystal-field splitting Δ_{CF} between the two d-orbitals, i.e. $\Delta_{CF} = 0$ (left panels) and 0.5 (right panels). The orbital character is denoted by the following color-coding: black for the first d-orbital ($d_{x^2-y^2}$), red for the second ($d_{3z^2-r^2}$), and yellow for the p-orbitals. In the inset, the hopping processes for the two models are visualized. Taken from [74].

Additionally a restriction is imposed onto the filling. The total filling of the effec-

tive e_g manifold is kept at one electron. This manifold, however, is far from having pure d-character, actually, for the nickelates, the two bands would correspond to the anti-bonding hybrid between the on-site d- and the ligand p-orbitals. The effective e_g Hamiltonian in momentum space is given by

$$H^{2b}_{\mathbf{k}} = \begin{pmatrix} -\frac{3}{2}t_{dd}(\cos(k_x)+\cos(k_y)) & -\frac{\sqrt{3}}{2}t_{dd}(\cos(k_x)-\cos(k_y)) \\ -\frac{\sqrt{3}}{2}t_{dd}(\cos(k_x)-\cos(k_y)) & -\frac{1}{2}t_{dd}(\cos(k_x)+\cos(k_y))+\Delta_{CF} \end{pmatrix}, \quad (2.50)$$

where the diagonal entries represent the hopping from a $d_{x^2-y^2}$ ($d_{3z^2-r^2}$) to a $d_{x^2-y^2}$ ($d_{3z^2-r^2}$) in the next unit cell and the off diagonal elements represent the non-local e_g-e_g hybridization. A sketch of the hoppings is shown in Fig. 2.6 in the upper inset. For heterostructures there exists a quasi two-dimensional geometry, the hopping along the c-axis is highly suppressed, and thus the $d_{3z^2-r^2}$ has a smaller hopping amplitude and therefore a smaller bandwidth. A similar two-band model without hybridization between the orbitals, with reference to $BaVS_3$ and Na_xCoO_2, was studied in [87].
In Figure 2.6 the band-structure and the single particle density of states (DOS) corresponding to our model is plotted. The orbital character of the band structure and of the DOS are color coded; the black color denotes a $d_{x^2-y^2}$ character and the red color $d_{3z^2-r^2}$ character. Locally, as can be seen by the pure colors in the DOS, the two orbitals are eigenstates of the tetragonal point group and do not hybridize. If we look at, e.g., the X point of the band structure plot, however, one can see from the dark red color that there is a non-local mixing of the two orbitals.
In the model the hopping amplitude was fixed to a value of $t_{dd} = 0.6$eV to obtain a bandwidth of similar size as in the NMTO downfolded nickelates. In the following study the crystal field parameter was varied between $-0.5 < \Delta_{CF} < 0.5$eV. On the left side of Figure 2.6 the bandstructure and DOS for a crystal field of 0.0eV and on the right for 0.5eV is shown. One can see the values of the crystal-field in the center of mass of the DOS which is depicted as dashed red/black lines correspondingly.

dp four-band model In the second model the p-bands are added back to the model which makes it in a way the "upfolded" version of the d-only model. The two added orbitals can be thought of as oxygen ligand orbitals in the quasi two dimensional geometry of the model with one p-orbital at each ligand site. This model is the simplest realistic dp-model which can be constructed in a quasi two-dimensional cubic/tetragonal symmetry. The additional parameters which define the "upfolded" model have to be chosen in such a way that they correspond to the two band model, i.e. the parameters of the two band model must be derivable from parameters of the four band model. The crystal-field parameter of the d-only model stems, in fact, from a "ligand field" splitting which can, in principle, be decomposed into an electrostatic Mandelung potential and a dp-hybridization splitting. The effective dd-hopping processes are in the "upfolded" model mediated via the oxygen p-orbitals and there are no direct dd-hopping processes.

The parameters for the four-band model, i.e. dp-hopping amplitude and on-site d- and p-energies, can be chosen to mimic the two bands at the Fermi energy of the two-band model. The results obtained in this study are, however, robust with respect to the details of the model. The dp-Hamiltonian in momentum space is given by

$$H_{\mathbf{k}}^{4\mathrm{b}} = \begin{pmatrix} 0 & 0 & i\sqrt{3}t_{pd}\sin\left(\frac{k_x}{2}\right) & -i\sqrt{3}t_{pd}\sin\left(\frac{k_y}{2}\right) \\ 0 & \Delta_{CF} & it_{pd}\sin\left(\frac{k_x}{2}\right) & it_{pd}\sin\left(\frac{k_y}{2}\right) \\ -i\sqrt{3}t_{pd}\sin\left(\frac{k_x}{2}\right) & -it_{pd}\sin\left(\frac{k_x}{2}\right) & \epsilon_p & 0 \\ i\sqrt{3}t_{pd}\sin\left(\frac{k_y}{2}\right) & -it_{pd}\sin\left(\frac{k_y}{2}\right) & 0 & \epsilon_p \end{pmatrix}, \tag{2.51}$$

where Δ_{CF} can be identified with the parameter in the corresponding d-only model and the parameter t_{pd}, which defines the hopping between d- and p-orbitals, was set to the value $t_{pd} = 3t_{dd}$ with which the bandwidth of the anti bonding bands has the same bandwidth as in the d-only model. Finally the on-site energy of the p-states was set to $\varepsilon_p = -2.5\mathrm{eV}$, which is a realistic value, similar to the one in the nickelates.
The band structure and DOS is plotted in the lower panels of Figure 2.6 for the same crystal field splitting as in the d-only model. The additional p-bands are color coded in yellow. One can see the admixture of p-character in the DOS, due to the hybridization, at the Fermi energy.

Local Interaction and Double Counting Correction In this study we used the scheme described in Section 2.5 for the self-consistency and the Kanamori interaction which I am going to introduce in Section 3.1 as the local interaction. The interaction values are given by $U' = U - 2J = 4\mathrm{eV}$ and $J = 0.5\mathrm{eV}$ for the 2-band model. For the 4-band model the parameters were chosen as $U' = U - 2J = 8\mathrm{eV}$ and $J = 1\mathrm{eV}$ which is physically reasonable since dp-models are typically more localized than d-only models and thus the on-site interaction is stronger. We used the FLL double-counting correction which I introduced in Section 2.3 for all calculations in this study.

d- vs dp-Calculations at "quarter filling"

In this section we will compare the two model systems with a "quarter filled" correlated band, i.e. one d-electron. This corresponds to having $n = n_d = 1$ electron in the two-band model and $n = n_d + n_p = 5$ electrons in the four-band model. We will study the two models at different crystal-fields, ranging from $-0.5\mathrm{eV}$ to $0.5\mathrm{eV}$, to investigate the effect of the interaction on the Fermi surface.

Results for the d-only model Let us turn to the results of our calculations. First we discuss the occupations of the non-interacting model which are shown in Figure 2.7.

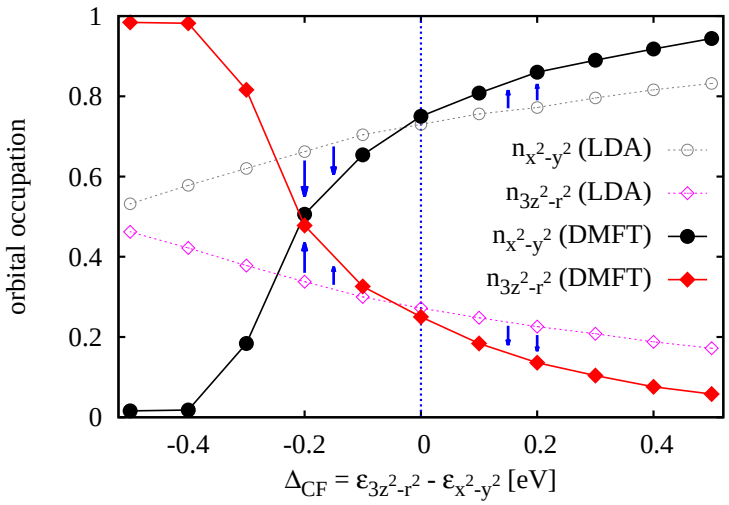

Figure 2.7.: The occupation of the $d_{x^2-y^2}$ and $d_{3z^2-r^2}$ orbitals in the d-only model for $n_d = 1$ and for different Δ_{CF}. The non-interacting values, denoted as LDA, (open symbols) are compared with the interacting values, denoted by DMFT, (filled symbols). The effect of the interaction on the occupancies is indicated by the arrows. Taken from [74].

The occupations show a monotonic behavior w.r.t. the crystal-field, but the dependence on the crystal-field is non-linear, which is in accordance to actual ab-initio calculations, since the band-width and dispersion relation is different for the two bands. Therefore the point at which both bands are equally occupied does not occur at $\Delta_{CF} = 0$eV but below the minimal value of Δ_{CF} shown here.
The occupancies of the model with interactions is also shown in Figure 2.7 and a quite interesting behavior can be observed. Not only for this model, but also for other models we studied, the interaction always seems to enhance the crystal-field, i.e. an increase (decrease) of the occupation of the $d_{3z^2-r^2}$ ($d_{x^2-y^2}$) orbital for $\Delta_{CF} < 0$ and vice versa for $\Delta_{CF} > 0$.
This can also be seen as a robust behavior for the changes in the orbital polarization P due to interaction, which we define analogously to [83, 196] as

$$P = \frac{n_{x^2-y^2} - n_{3z^2-r^2}}{n_{x^2-y^2} + n_{3z^2-r^2}}. \tag{2.52}$$

We found these results to be quite general, i.e. model independent, in line with what was previously found for calculations of the Fermi surface in LDA+DMFT calculations for the bulk nickelates [197, 198] and for the Ni-based heterostructures [84, 85].

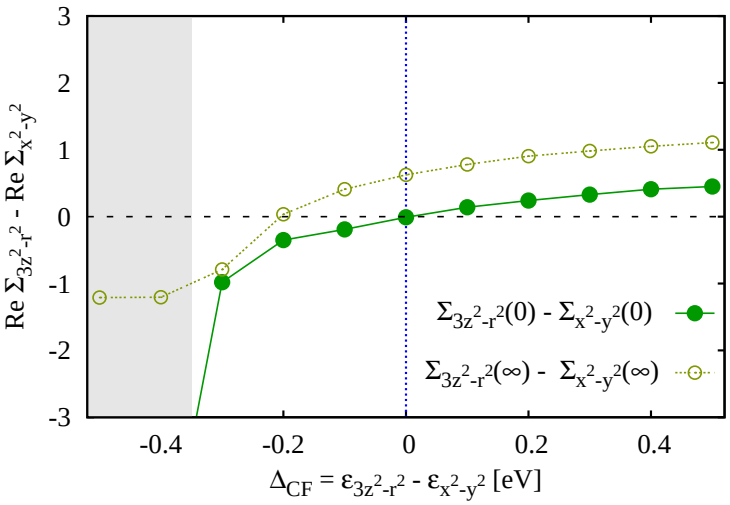

Figure 2.8.: The difference of the real part of the self-energies for the d-only model in the limit $\omega_n \to 0$ (filled symbols) and $\omega_n \to +\infty$ (open symbols), which is the Hartree contribution for various Δ_{CF}. The shaded area on the left denotes the onset of the metal-insulator transition for which the huge energy of one orbital is a precursor. Taken from [74].

To obtain a quantitative result of this enhancement we need to study the behavior of the self-energy. The results of the limit $\omega_n \to 0$ and $\omega_n \to \infty$ for the quantity $Re\Sigma_{3z^2-r^2}(i\omega_n) - Re\Sigma_{x^2-y^2}(i\omega_n)$ is shown in Figure 2.8. In the latter limit only the Hartree contribution to the self-energy remains and thus the difference of the self-energies can also be written in terms of densities as

$$\begin{aligned} Re\Sigma_{3z^2-r^2}(i\omega_n) - Re\Sigma_{x^2-y^2}(i\omega_n) &= U - 5J \\ n_{x^2-y^2} - n_{3z^2-r^2} &= (U-5J)P, \end{aligned} \tag{2.53}$$

where the second equality only holds for $n_d = 1$. This can be also seen if we compare the crystal-field value for which the sign change in the difference of the self-energies in $\omega_n \to \infty$ occurs in Figure 2.8 and where the two orbital occupancies are the same in Figure 2.7, which is at exactly the same Δ_{CF}.
The behavior of the increase or decrease of the orbital occupancies is however not connected to this quantity, but rather the difference of the self-energies at $\omega_n \to 0$ which controls the effective splitting of the two orbitals in the Fermi liquid regime. The splitting, which we will call effective crystal-field, is given by

$$\Delta_{eff} = \Delta_{CF} + Re\Sigma_{3z^2-r^2}(0) - Re\Sigma_{x^2-y^2}(0) \tag{2.54}$$

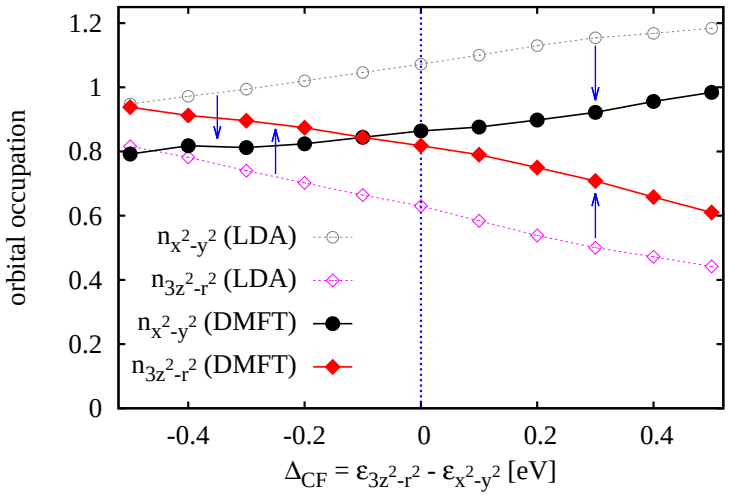

Figure 2.9.: The occupation of the $d_{x^2-y^2}$ and $d_{3z^2-r^2}$ orbitals in the dp-model for $n = 5$ w.r.t. Δ_{CF}. The non-interacting values, denoted as LDA, (open symbols) are compared with the interacting values, denoted by DMFT, (filled symbols). Taken from [74].

and it allows us to interpret the second set of data in Figure 2.8. Δ_{eff} follows the same trend as the Δ_{CF} and it confirms the observation that the interaction always increases the absolute value of the initial crystal-field. The abrupt change in Δ_{eff} when the metal-insulator transition is approached corresponds to an orbital which is empty while the other orbital is exactly half-filled. When the basis-set is extended, however, this simple picture changes which we are going to see in the following discussion.

Results for the dp-model In the model with d- and p-orbitals the filling of the system is set to $n = 5$ since the p-bands are lying below the Fermi energy and are therefore completely filled in the absence of hybridization. If we study the occupations w.r.t. Δ_{CF}, shown in Figure 2.9, we obtain different results than before.
Already for the non-interacting case there is a major difference between the results since, even though the p-bands are well separated from the d-bands, the occupation of the d-orbitals changes from $n_d = 1$ to $n_d \approx 1.7$, due to the hybridization. When the interaction is switched on the d-orbitals retain the same occupation as in the uncorrelated case. This leads to a completely different outcome when we calculate P which is in this model and parameter set independent of Δ_{CF} and always reduced compared to the non-interacting case.
This result can also be seen in the difference of the real part of the two d self-energies

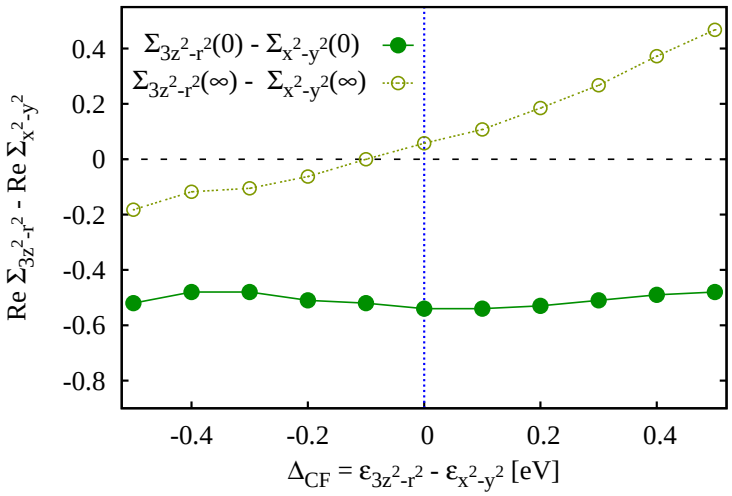

Figure 2.10.: The difference of the real part of the self-energies for the *dp* model in the limit $\omega_n \to 0$ (filled symbols) and $\omega_n \to +\infty$ (open symbols). Taken from [74].

which are shown in Figure 2.10. The effective crystal field Equation (2.54) is always reduced compared to Δ_{CF}, which is in agreement with the decrease of $n_{x^2-y^2}$ (reduction of P) which we observe in the whole parameter range of Δ_{CF}.
These results are in obvious qualitative disagreement with the ones for the *d*-only model for $\Delta_{CF} > 0$, which is what was also found in [83] for Ni-based heterostructures. In the study they argued that this difference between the results for *d*- and *dp*-models does not depend on the type of the local interaction which we could show in this study by using an SU(2) symmetric interaction.

Since the most obvious change between the two models is the filling we could try to tune the interaction to produce the same trend. The parameter which influences the relative occupancies off the *d*-orbitals the most is the Hund's coupling J. To this end we performed calculations for the *dp*-model for different values of J which we show in Figure 2.11. We note that already for a decrease of J from 1 to 0.5eV the results of our calculations change significantly since there is, for this parameter, again a similar trend as for the *d*-only model. For $J = 0$ the physical situation finally changes completely with a Δ_{eff} which is now almost always enhanced except for the lowest values of Δ_{CF}. A trend which can also be seen in the occupancies. This shows the sensitivity of the system to Hund's coupling which has attracted a lot of attention in recent literature [199, 130, 118].

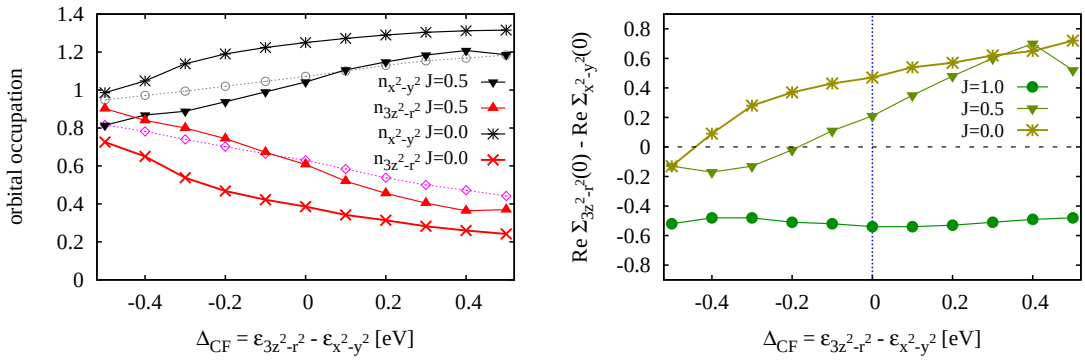

Figure 2.11.: Left panel: The occupation of the $d_{x^2-y^2}$ and $d_{3z^2-r^2}$ orbitals in the *dp* model for $n = 5$ w.r.t. Δ_{CF}. We used two different values for the Hund's coupling $J = 0.0$eV and $J = 0.5$eV while keeping $U' = 8$eV. The non-interacting values, denoted as LDA, (open symbols) are compared with the interacting values, denoted by DMFT, (filled symbols). Right panel: The difference of the real part of the self-energies for the *dp* model in the limit $\omega_n \to 0$ for the corresponding data and for $J = 1$ was already presented in Figure 2.10. Taken from [74].

The Role of the d-Orbital Occupation

The discussion before raises the question when one can expect the same results from *d*- and *dp*-model calculations. Typically for LDA+DMFT calculations one uses estimates for the interaction parameters and thus the variation of J was more an academical exercise. We already mentioned that the major difference between the *d*- and *dp*-model in the correlated subspace is the occupancy since the study of J suggests that the Hund mechanism is important. We thus studied of the behavior of the correlated subspace w.r.t. the filling. To this end we performed calculations for the *d*-only model setting the filling of the system to $n = 1.1$, 1.25 and 1.75, which is almost half-filing, i.e. the filling for which J plays the most important role. All the other parameters were set to the ones already previously used for the *d*-only model. The results of these calculations are shown in Figure 2.12.
When the filling of the system is changed we observe a slow change of the trend in the occupancies and effective crystal-fields to the ones we already observed for the *dp*-model. We focus on the interesting region of $\Delta_{CF} > 0$, i.e. the region for which the trend for the *d*-only model at $n = 1$ could not be reproduced by the *dp*-model at $n = 5$. We observe that for increasing values of n the region for which Δ_{CF} "drives" the final result is decreasing. For $n = 1.05$ the region is confined to $\Delta^* > 0.1$ which can also be seen for Δ_{eff} for a slightly larger value $\Delta^* > 0.15$. For the second value $n = 1.25$ this region

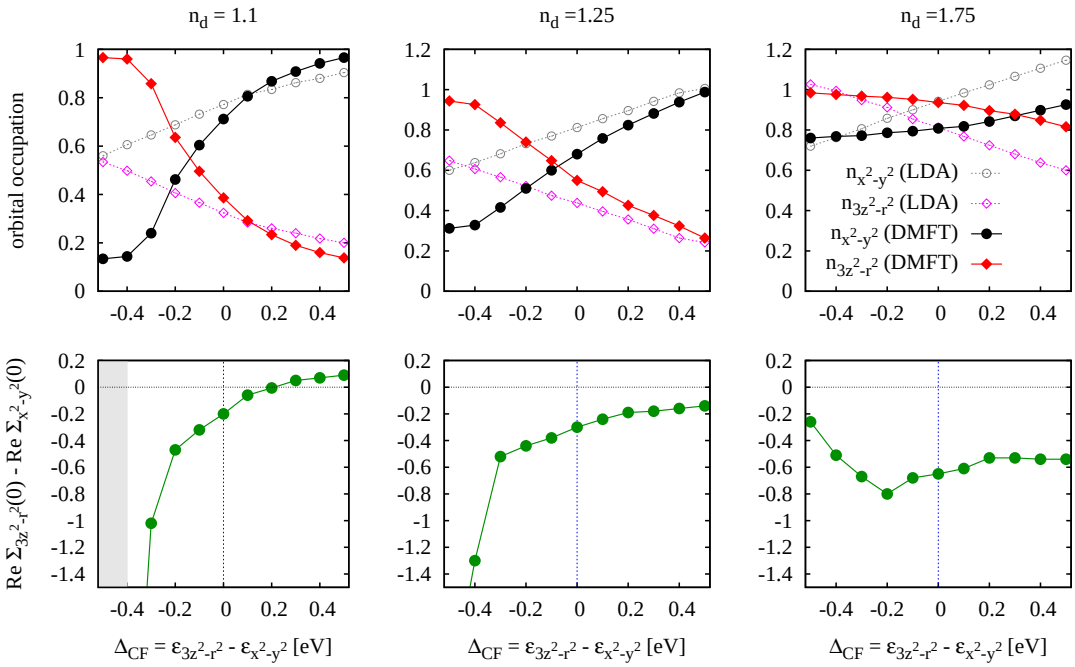

Figure 2.12.: Upper row: Orbital occupations of the two orbitals of the d-only model $n_d = 1.1, 1.25, 1.75$ w.r.t. Δ_{CF}. The interacting results (filled symbols) are compared with the corresponding non-interacting results (open symbols). Lower row: Difference of the real part of the DMFT self-energies for the two orbitals at $\omega_n \to 0$ (solid symbols) w.r.t. Δ_{CF} for the corresponding set of data. Taken from [74].

is already shifted to $\Delta^* > 0.5$ and at $n = 1.75$ we find a similar behavior as for the dp-model study.
Let us stress again that due to the asymmetry of the density of states no symmetric behavior of the occupancies or Δ_{eff} can be expected. In the region $\Delta_{CF} < 0$ the crystal-field enhancement is larger than in the region $\Delta_{CF} > 0$, which is also due to the closer proximity to the metal insulator transition. Thus the effect of an increased n are only visible as a weakening of the $n = 1$ trend and not by an inversion of the trend.

Conclusion

In our study we compared effective crystal-field Δ_{eff} of a d-only model with Δ_{eff} of a dp-model investigating the occupancies and Δ_{eff}. We could show that the trend of

Δ_{eff} strongly depends on the occupancies of the d-orbitals and that if one performs calculations with the d-only model with similar fillings for the d-manifold as the dp-model the general trend of the dp-model can be reproduced. This can be attributed to the Hund's coupling J which for the d-only model plays hardly any role since there is on average only one electron in the system while for the dp-model in which the correlated bands are filled by $n_d \approx 1.75$ electrons the Hund's coupling favors an equal distribution of the electrons. Since Δ_{eff} is the quantity which is relevant for the shape of the Fermi surface these results show that studies in LDA+DMFT with d-only and dp-models can lead to completely different physics. A result which was already previously known is that due to the non-integer filling of the d-orbitals in dp-models the metal insulator transition is more difficult to observe [81, 200]. In light of this study a general method to decide what model should be used in LDA+DMFT calculations is of big importance. As long as the problems with the double counting correction are not solved it is hard to make a direct comparison of d- and dp-models. But even if this problem is resolved the question remains if additional interactions are required to get the right physics of the problem. I will present an approach which at least includes the Hartree interaction of the uncorrelated bands in Section 2.7.

2.5.2. PAM

This subsection is based on the following manuscript:
Local moment dynamics and screening effects in the spin susceptibility of d- and f-electron systems
A.Amaricci, **N. Parragh**, M. Capone and G. Sangiovanni
In preparation

In the last study, in Section 2.5, we focused more on the effect of the interaction on the crystal-field and filling of the correlated orbitals. The conclusion of the study was that the most pronounced effect of the correlation was a change of the effective crystal-field and thereby the shape of the Fermi surface. Now we want to instead focus more on observables which show a fingerprint of the p-orbitals.
When we think about a system with an additional band hybridizing with the correlated band one thing which definitely changes is the number of screening channels of the system. The dynamical screening of a system with only d-orbitals can only be carried out by the d-electrons which results in a super-exchange mechanism captured by the Hubbard model. Another screening channel opens up as soon as the d-bands hybridize with p-bands and, if the hybridization between the d-orbitals is completely switched off, the Kondo like screening of the d-moment by the p-electrons is the only screening channel. As soon as we are in a situation with d- and p-orbitals with dispersion and hopping between the orbitals we are in a mixed case.
The physical quantity in which we would expect to see the different behavior of the two different screening channels is the frequency dependent local spin susceptibility which can be measured in experiment by inelastic neutron scattering (INS) or resonant inelastic X-ray scattering (RIXS). In the following study we will address the issue of what structures in the local spin susceptibility can be attributed to what screening channel. We chose a parametrization of the periodic Anderson model which is very suitable for this task since both screening channels are present and their relative importance can be easily tuned. We used the DMFT, which I introduced in Section 2.2, to study the evolution of the local dynamical spin response function, w.r.t. the hybridization and doping. We will see that two distinct features are present in the local spin susceptibility. These can be related to the two different processes. Additionally we will characterize these features in terms of different diagrams by using the CT-HYB, which I introduced in Section 1.3.

Model

As mentioned above we are trying to use a minimal model in which we can study the influence of an additional screening channel introduced by a p-band. The simplest model one can think of is the generalized periodic Anderson model (t_{dd}-PAM)[185] which describes a wide-band of conduction electrons hybridizing with a narrow-band of strongly interacting electrons. The Hamiltonian of the t_{dd}-PAM is given by

$$\begin{aligned} H = &\sum_{\vec{k}\sigma} \varepsilon_p(\vec{k}) p^\dagger_{\vec{k}\sigma} p_{\vec{k}\sigma} + \sum_{\vec{k}\sigma} \varepsilon_d(\vec{k}) d^\dagger_{\vec{k}\sigma} d_{\vec{k}\sigma} + \\ &t_{pd} \sum_{i\sigma} \left(d^\dagger_{i\sigma} p_{i\sigma} + p^\dagger_{i\sigma} d_{i\sigma} \right) - U \sum_i d^\dagger_{i\uparrow} d^\dagger_{i\downarrow} d_{i\uparrow} d_{i\downarrow}. \end{aligned} \tag{2.55}$$

In the equation above $p^{(\dagger)}_{i\sigma}$ annihilates (creates) an electron in the p-band with spin σ, the dispersion relation of the p-band is given by $\varepsilon_p(\vec{k}) = \epsilon_p - 2t_{pp}\left[\cos(k_x) + \cos(k_y)\right]$, the operators $d^{(\dagger)}_{i\sigma}$ annihilate (create) an electron in the d-band with spin σ and its dispersion relation is given by $\varepsilon_d(\vec{k}) = \epsilon_d - 2\alpha t_{pp}\left[\cos(k_x) + \cos(k_y)\right]$, where the parameter $\alpha \in [0, 1)$ denotes the bandwidth ratio. The hybridization between the two orbitals is given by t_{pd} and the last term describes the local interaction on the correlated d-orbital. In the following discussion we will set $W_{pp} = 4t_{pp} = 1$, $\alpha = 0.25$ and $\epsilon_d = 0$. The separation of the center of the mass of the two bands is given by the charge transfer energy $\Delta = \epsilon_p - \epsilon_d$. In the following discussion we will suppress the spin index since we focus on the paramagnetic properties of the system. One can think of the model Hamiltonian Equation (2.55) as an interpolation between the Hubbard model for d-electrons only ($t_{pd} = 0$, $\alpha \neq 0$) and the periodic Anderson model (PAM) ($\alpha = 0$, $t_{pd} \neq 0$), which describes localized electrons hybridizing with a wide-band [186, 187, 189].
The solution of the model Hamiltonian is obtained using the dynamical mean field theory (DMFT), as introduced in Section 2.2. As a solver for the auxiliary Anderson impurity model (AIM) two different methods were used, namely the exact-diagonalization method briefly described in Section 1.1 and the hybridization expansion continuous-time quantum Monte Carlo algorithm (CT-HYB) which I introduced in Section 1.3.

Spin Susceptibility

As mentioned in Section 1.1 the hybridization function in the ED needs to be discretized and it then takes the form $\Delta(\omega) = \sum_{k=1}^{N_s} V_k V_k^* / (\omega - \varepsilon_k)$ when we use N_s bath sites, where ε_k is the local energy and V_k the hybridization of the k^{th} bath site with the impurity All ED calculations were performed with $N_s = 8$. The spin susceptibility χ_{spin} is defined as the imaginary part of the dynamical response function

$$\chi(\omega) = i \int dt e^{i\omega(t-t')} \operatorname{Tr} \langle \left[\hat{S}_{zd}(t), \hat{S}_{zd}(t') \right] \rangle \, \theta(t - t'), \tag{2.56}$$

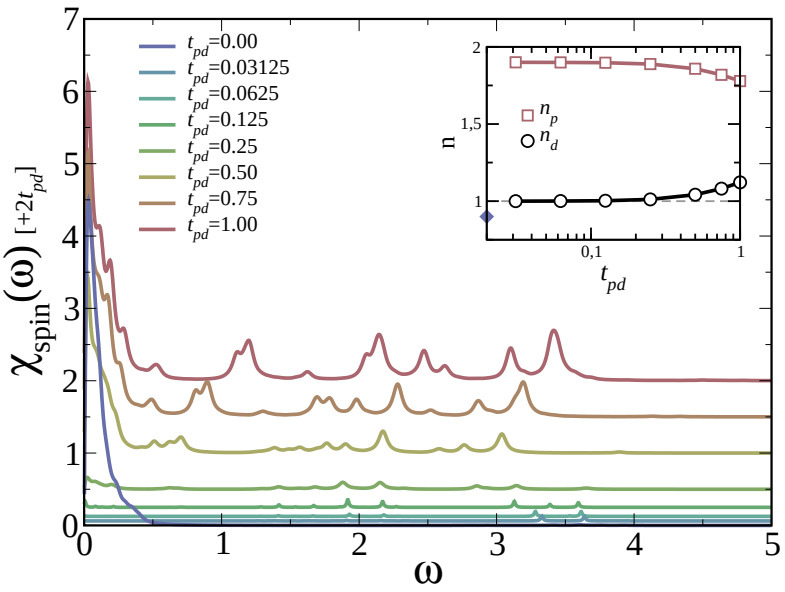

Figure 2.13.: The spin susceptibility $\chi_{\text{spin}}(\omega)$ of the t_{dd}-PAM for different values of t_{pd}. The curves are shifted by $2t_{pd}$ in y direction for better visibility. In the inset densities of the d- and p-orbitals w.r.t. t_{pd}. The arrow points to the value of the system with $t_{pd} = 0$.

where $\hat{S}_{zd}(t)$ is the spin in z direction at time t for the correlated orbital d. It can be easily obtained in the ED-calculation using the spectral decomposition

$$\chi_{spin}(\omega) = -Im \sum_{i,j} e^{-\beta E_i} \frac{|\langle i|S_{zd}|j\rangle|^2}{\mathcal{Z}} \frac{(1 - e^{-\beta(E_i - E_j)})}{\omega^+ - (E_i - E_j)}, \tag{2.57}$$

where $\omega^+ = \omega + i0^+$. We used the CT-HYB to study the diagrams which contribute to the screening process therefore a special analysis will be introduced to unveil information, concerning the local moment dynamics, hidden to other numerical methods.

For the following numerical study we set $\Delta = -0.5$, $U = 3.5$ and $\beta = 100$ and we recall that W_{pp} has been set to 1. The results shown in this section were obtained using ED-calculations and we therefore directly get the results on the real axis.
Let us first turn to the case of $t_{pd} = 0$, i.e. the Hubbard model. For this model we see in Figure 2.13 that most weight of the spin susceptibility is located close to $\omega = 0$ and only very small features can be found at $\omega \simeq U$ which we can relate to electronic excitations to the Hubbard bands. The only screening channel which is active is the $d - d$ channel and the leading coupling term constant is given by $J_{dd} = \alpha^2 t_{pp}^2/U$. In Figure 2.14 we can see that the instantaneous local moment is rather large and it is depending crucially

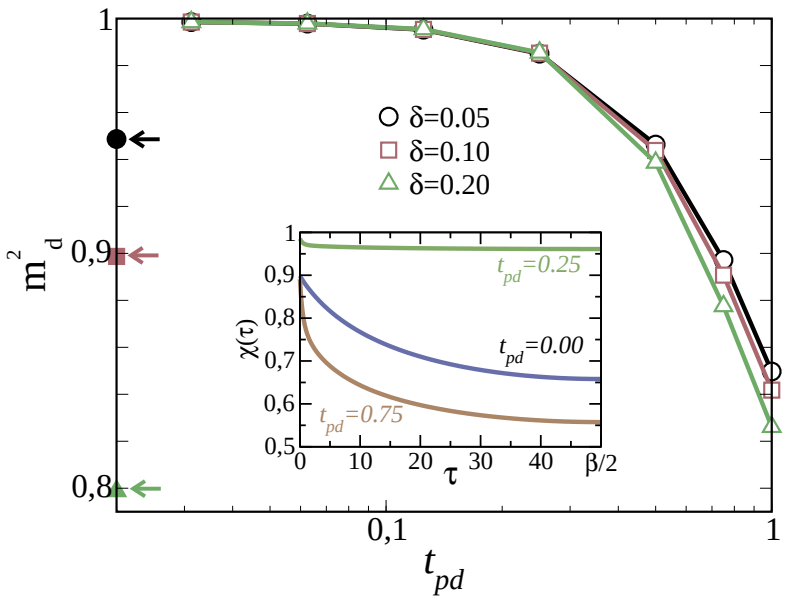

Figure 2.14.: The local moment $m_d^2 = \langle S_{zd}^2 \rangle$ of the correlated band w.r.t. t_{pd} and for different dopings δ. In the inset the spin susceptibility $\chi(\tau)$ for $\delta = 0.10$.

on the doping and from the small value of the self-energy, shown in Figure 2.15, we can conclude that the local interaction is effectively screened.

When we increase the hybridization between the d- and p-band from 0 to finite values $t_{pd} \leq 0.25$ the spin-susceptibility suddenly changes. The peak at $\omega = 0$ almost completely vanishes and a new structure at intermediate energies appears. This new feature is separated from the high energy feature at U and also separated from the low energy peak at 0. The sudden change of the spin susceptibility is accompanied by a loss of coherence which can be seen from Figure 2.15 by the large value of the imaginary part of the self-energy at the first Matsubara frequency. This can be understood by looking at the evolution of the d-density $\langle n_d \rangle$ (inset in Figure 2.13) and the local magnetic moment m^2 shown in Figure 2.14. When we switch on t_{pd} the d-density increases from 0.9 to 1. This is due to the fact that the p DOS (not shown) has weight below E_F and if d-p are hardly mixed, the doped holes go into the p-band. The small t_{pd} therefore brings the d-orbital effectively to half-filling and this suppresses the coherence scale. The saturation of the magnetic moment, shown in Figure 2.14, is also an indication of the absence of effective screening processes.
When the hybridization is increased further, to values > 0.25, the d-band filling increases above 1 as can be seen in the inset of Figure 2.13. With the deviation of integer filling also the imaginary part of the self-energy gets smaller, Figure 2.15, and the metallic

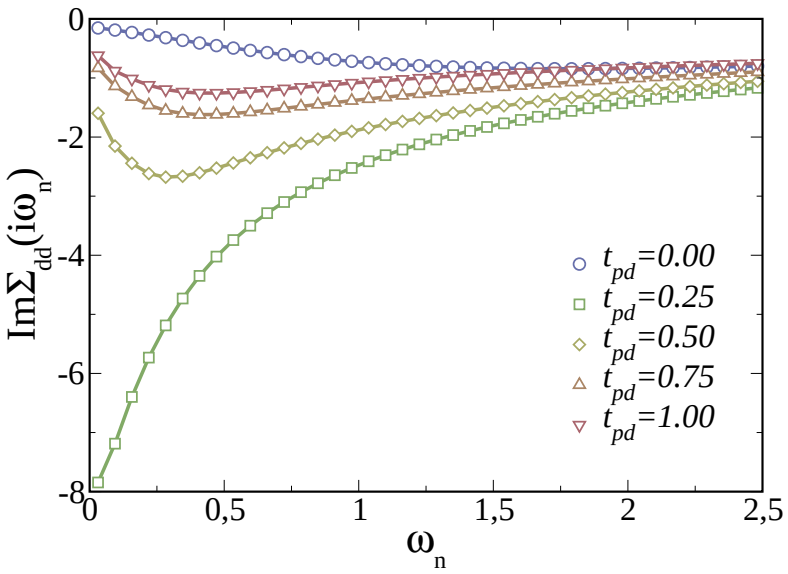

Figure 2.15.: The imaginary part of the d-electron self-energy $Im\Sigma_{dd}(i\omega_n)$ for different values of t_{pd}.

screening of the local moment becomes effective as signalled by the decrease of the value of the local moment, Figure 2.14. Another change in this parameter regime can be seen in the spin susceptibility, Figure 2.13, in which the low energy structure develops again. The features in the intermediate energy range are now more pronounced and span a wider energy window which has the width of the bandwidth of the p-bands. The position of these features are transposed by $\sqrt{\Delta^2 + 4t_{pd}^2}$ when t_{pd} is changed, which is the change in the charge-transfer energy coming from the band repulsion due to the hybridization. This is an indication that the structure at intermediate energies comes only from the p-electrons. The structure at low-energies, on the other hand, lies in such an energy range that we expect both screening processes, $d-d$ and $d-p$, to play a role in it.A comparison which is more in line to the study presented in Section 2.5.1 is the comparison of the spin susceptibility for the same d-density in the Hubbard and the t_{dd}-PAM model. As we can see in Figure 2.16 the behavior of the spin susceptibility of the t_{dd}-PAM is not in agreement with the Hubbard model with n_d fixed to the value of the t_{dd}-PAM. In contrast to the previous study the resemblance of the models with the same total system doping δ is better. In any case, the intermediate energy structures are a feature which only develop when the additional screening channel of the p-electrons is active.

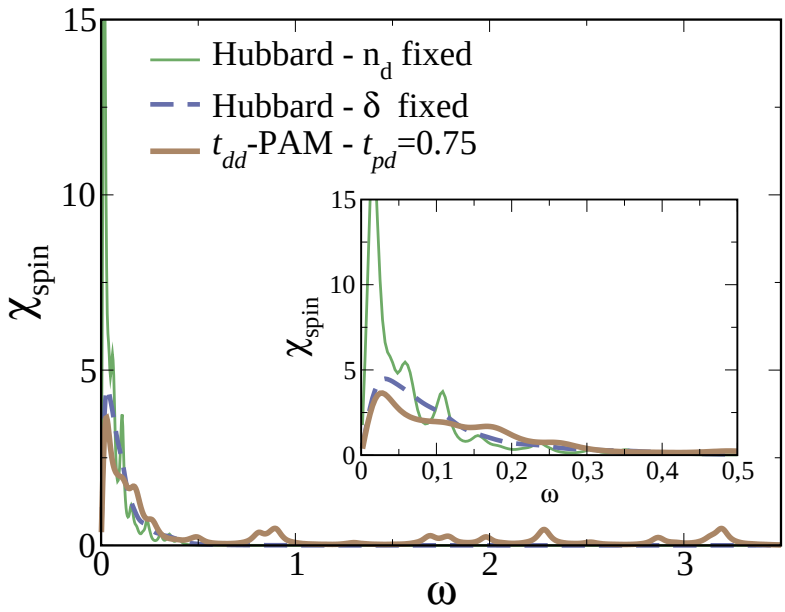

Figure 2.16.: The spin susceptibility $\chi_{\text{spin}}(\omega)$ for t_{dd}-PAM with $t_{pd} = 0.75$ and $\delta = 0.10$ (blue line) compare to a Hubbard model ($t_{pd} = 0$) with the same doping (red dashed line) and the same d-electron density (black line). In the inset a zoom on the low-frequency part.

Diagrammatic Characterization

To obtain a better understanding of the nature of the screening processes we use the converged hybridization function from the ED calculations as an input for *w2dynamics*. First we analyze the hybridization function and then we study the effect the hybridization with the p-bands has on the expansion order of the CT-HYB simulation.
The hybridization function for the different hybridization strengths t_{pd} is shown in Figure 2.17. For the Hubbard model, depicted in the inset, the hybridization has a rather large weight at the Fermi level and two features at higher energy which describes hybridization events with the Hubbard bands. When the hybridization with the p-bands is turned on the weight at the Fermi energy almost vanishes in agreement with the loss of coherence and structures below the Fermi energy appear as a result of the hybridization processes with the uncorrelated p-bands. When the hybridization is increased the features at and below the Fermi energy become more pronounced. This can be attributed to a gain in kinetic energy due to hybridization events.

Our interest now lies in the results of CT-HYB calculations starting from the various hybridization functions. The histogram of the diagrammatic expansion order of the CT-HYB can be easily accumulated in simulations by measuring the number of operators

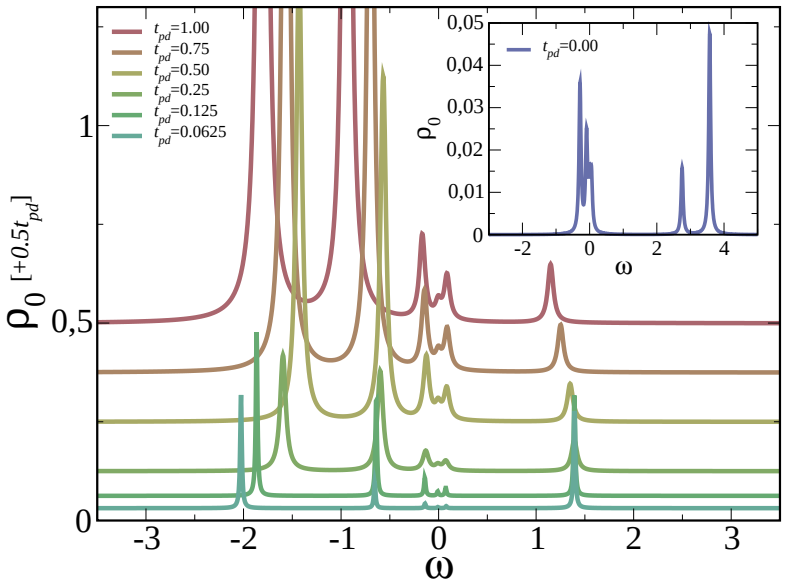

Figure 2.17.: Spectral density of the hybridization function $\rho_0(\omega) = -Im\Delta_{dd}(\omega)/\pi$ for different values of t_{pd}. In the inset the same quantity for $t_{pd} = 0$.

k in the local trace. For the Hubbard model there is only one peak in the histogram around $k = 0$, see Figure 2.18. When the hybridization is switched on, however, this quantity shows a very peculiar response. The peak around $k = 0$ develops a two peak structure. This second structure is shifted to higher expansion orders and the two peaks are broadened when the hybridization is increased as shown in Figure 2.18. The second structure seems to be a feature only present when the p-screening channel is active. The expansion order of the CT-HYB can be related to the kinetic energy with the mean value of the expansion order being proportional to the kinetic energy [45]. Thus the two peak structure points us to the presence of two different kinetic energy scales in the system when the p-channel is active.

We aim at putting labels onto the different histogram structures to connect the diagrammatic expansion with the local state of the system. For this purpose we implemented a new quantity: the expansion order-, spin- and orbital-resolved site-reduced density matrix. The site-reduced density matrix is simply the projector of the local many body state $\rho = |\psi\rangle \langle\psi|$, where ψ are the many body states of the impurity. I already described the measurement of this quantity in Section 1.4. Since we are dealing with only one correlated orbital the interaction is of a density-density type and we therefore only obtain diagonal elements in the site-reduced density matrix which are equivalent to the so called state-weights introduced in [35, 190]. It is the information how probable a certain state is in the local trace or, equivalently, how much time the system spends in a certain state.

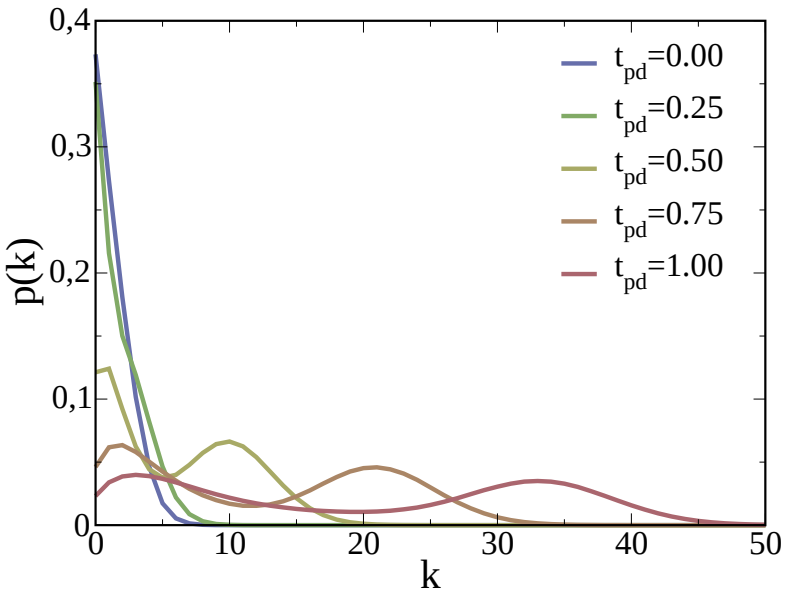

Figure 2.18.: Expansion order histograms of the CT-HYB calculations starting from the hybridization functions of the ED calculation with different t_{pd} and $\delta = 0.10$. One can see a peak developing with an increasing hybridization where the center of mass of the second peak scales quadratically with t_{pd}.

We are measuring this with the additional information of the spin- and orbital-resolved expansion order.
To clarify things I will give two examples. Let us first consider a trace of the following form

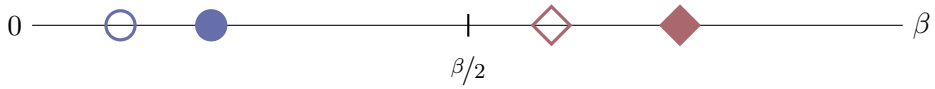

where the empty symbols are annihilation and the filled symbols are creation operators. The blues symbols are acting on $\uparrow$ and the red symbols on $\downarrow$ electrons. For this trace we would measure the normalized density matrix at $\beta/2$

$$\rho = \begin{pmatrix} 0 & 0 & 0 & 0 \\ 0 & 0 & 0 & 0 \\ 0 & 0 & 0 & 0 \\ 0 & 0 & 0 & 1 \end{pmatrix}$$

where the basis is given by $\{|\ \rangle, |\uparrow\rangle, |\downarrow\rangle, |\uparrow\downarrow\rangle\}$. There is only one outer state contributing to the trace, $|\uparrow\downarrow\rangle$, because we annihilate first and then create the electrons of

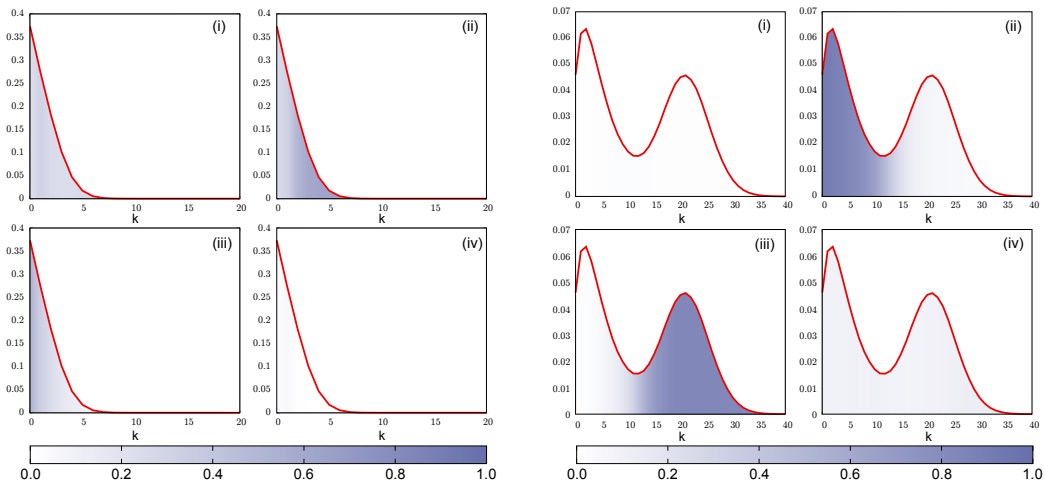

(a) Hubbard (b) t_{dd}-PAM

Figure 2.19.: The value of a certain state of the state resolved density matrix (see text) is color coded in the histogram for $t_{pd} = 0$ and $t_{pd} = 0.75$ with $\delta = 0.10$. The local state in the diagrams is given by $|0\rangle$ (i), $|\uparrow\rangle$ (ii), $|\downarrow\rangle$ (iii), $|\uparrow\downarrow\rangle$ (iv) and the hybridization events of the histogram have $\sigma = \uparrow$ character.

both spins. This density matrix is added to the matrix in the vector for expansion order 1, orbital 1 and spin $\uparrow$ in short $(1, 1, 1)$ and in the vector for expansion oder 1, orbital 1 and $\downarrow$ in short $(1, 1, 2)$.
Let us add two operators to the trace above

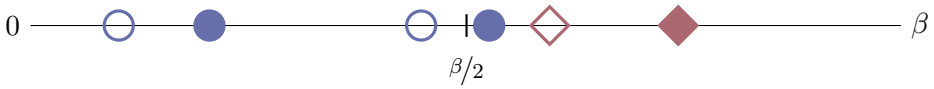

The normalized density matrix which we measure at $\beta/2$ is then given by

$$\rho = \begin{pmatrix} 0 & 0 & 0 & 0 \\ 0 & 0 & 0 & 0 \\ 0 & 0 & 1 & 0 \\ 0 & 0 & 0 & 0 \end{pmatrix}.$$

This matrix is added to the matrix in the array $(2, 1, 1)$, since there are two operator pairs of orbital 1 and spin $\uparrow$ in the trace, and to the matrix in the array $(1, 1, 2)$ again, since there was no change in the number of operators for this spin direction. The Monte Carlo average is performed by dividing the matrices by the number of times the number of operators was measured in the trace, i.e. the value of the unnormalized expansion

order.
We can thereby say in which state the system is when a certain number of hybridization events with a certain orbital- and spin-character occur. This is used in Figure 2.19 to make an intensity color coding of the expansion order histograms depending on how probable it is that the system is in a certain local state.
The outcome is very interesting. For the Hubbard model the most probable states are the empty or singly occupied ones. This can be understood if we remember that the d-density is 0.9. The probability for the impurity to be in the same spin state as the hybridization events is higher for higher expansion orders as can be seen from Figure 2.19(a) and the opposite for lower expansion order. This means that the hybridization "empties" the impurity, i.e. the same spin hops from the impurity into the bath.
For the t_{dd}-PAM, which we show in Figure 2.19(b) for $t_{pd} = 0.75$ the situation is completely different. The two structures present in the histogram correspond to two different sets of local states, which are clearly separated. Another result is that the state of the impurity is opposite to the one of the Hubbard model which can be explained by the different filling of the impurity model. When the expansion order is small the system is most likely in the state corresponding to hybridization events of this kind and the opposite is true for high expansion orders where the system is most likely in the opposite spin state. The empty state is almost never visited for all expansion orders, while the doubly occupied state is visited more often due to the electron doping of the d-orbitals coming from the hybridization. This means that we a have a lot of events which "fill" the impurity and since the electron donor in this system are the p-bands the second peak is coming from the hybridization with the p-electrons.

Conclusion

In this work we studied a minimal model of a correlated system hybridizing with an uncorrelated band. We focused on the evolution of the spin susceptibility w.r.t the hybridization of the correlated with the uncorrelated band and we could associate different features of the spin susceptibility with different screening processes. The feature which is already present in the model without hybridization is first suppressed by the hybridization. When the hybridization is increased the original feature develops again but also a completely novel structure, which can be associated with screening processes mediated via the uncorrelated band, develops. In the CT-HYB calculations of the system with uncorrelated electrons we could find a new structure in the expansion order histogram which we could relate to certain impurity states. While one screening channel is attributed to hole doping in the system which can hybridize with the same spin state on the impurity the other energy regime is connected to an electron doping of the system. Since we know the filling of the screening channels we can also conclude that the low energy scale corresponds to the screening already present in the Hubbard model and

thus also the low energy peak in the spin susceptibility. With the same argument we can attribute the high energy structures of the spin susceptibility to the p-screening channel.

2.6. Analytical Continuation to the Real Axis

In the last two studies we have compared quantities which are directly available from the QMC or we have used results from additional ED-calculations to obtain information about the physical system. Since the QMC is operating on the imaginary time axis quantities are not readily available on the real time/frequency-axis. The data on the real axis is, however, physically more intuitive to interpret and a connection to experiments can be made. Thus an analytical continuation of data to the real axis is often a desired post-processing step. In this section I will briefly discuss how this is performed.
The output of the QMC is typically the Greens function at a discrete number of imaginary time points τ_n or, if we Fourier transform it, the Greens function on a finite number of Matsubara frequencies $i\omega_n$. This measured function contains a statistical error σ and the data of two different points of the Greens function can be correlated. If we use a statistical method which uses the errors for the analytical continuation there must be no correlation between two data points. The input for a program which performs the analytical continuation to the real axis should therefore also contain the covariance matrix given by

$$C_{nm} = \overline{G_n G_m} - \overline{G_n}\,\overline{G_m}. \tag{2.58}$$

to perform a rotation into to the eigenbasis of the covariance matrix [188].
If we calculate the covariance matrix for our test case, which I am going to introduce later in this section, we can see in Figure 2.20 that there is no correlation between two data points and thus the covariance matrix was not used in the calculation of the analytical continuation. This was also the case for the data which we used in the upcoming study, which was always thoroughly checked.
The interesting quantity, the spectral function on the real axis, which we want to relate to experimental data,

$$A(\omega) = \frac{1}{\pi} ImG(\omega + i0^+) \tag{2.59}$$

can in principle be extracted by inverting the equation

$$G_n = \int_{-\infty}^{\infty} d\omega K_n(\omega) A(\omega), \tag{2.60}$$

where G_n is either $G(\tau_n)$ or $G(i\omega_n)$ depending on the kernel used. The kernel in the equation above is given by

$$K_n(\omega) = K(\tau_n, \omega) := -\frac{e^{-\omega\tau_n}}{1 + e^{-\omega\beta}} \tag{2.61}$$

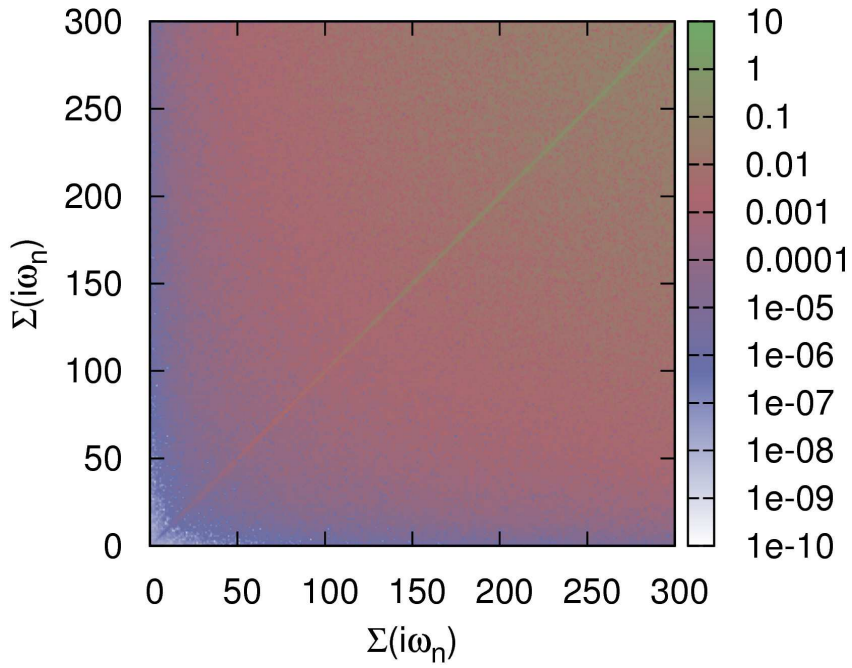

Figure 2.20.: The covariance of the self-energy in Matsubara frequencies. The only visible structure is on the diagonal, thus making a rotation into an uncorrelated basis unnecessary.

for data in imaginary time τ and

$$K_n(\omega) = K(i\omega_n, \omega) := -\frac{1}{i\omega_n - \omega} \tag{2.62}$$

if data is continued from Matsubara frequencies.
Since the problem of the direct inversion is ill-defined, due to the exponential behavior of the kernels, different approaches to perform the analytic continuation have been developed. One such approach is modeled after the following idea: If we would know the analytical form of the Greens function it would be easy since then we could simply perform the inverse rotation onto the real axis $i\omega_n \to \omega$. This can be used by generating an analytical expression for the quantity. One possibility of an analytical expression is a Pade approximation [205] which however has several limitations.
A different approach with a nature more akin to the QMC is the Maximum Entropy Method (MEM), often referred to as maxent. It can be formulated after the statement: If we know the spectral function, what is the a posteriori probability that this is the right Greens function. It is in principle similar to a least-squares fit with one additional

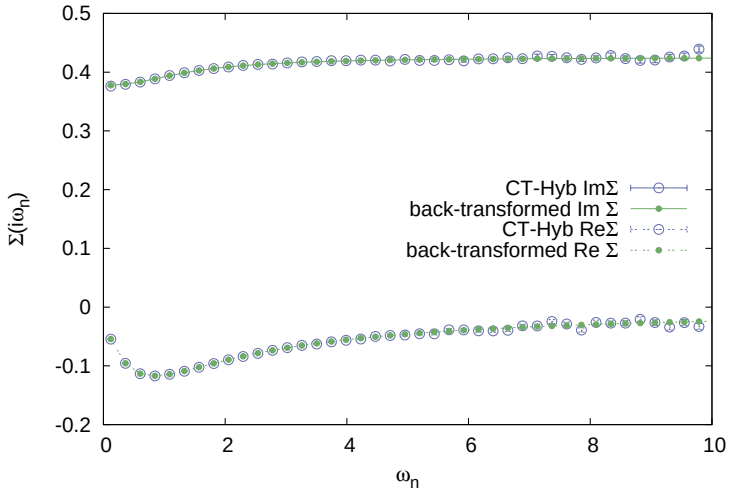

Figure 2.21.: Comparison of the analytically continued data back transformed onto the Matsubara axis with Σ'.

restriction. This restriction is the entropy defined by

$$S[A] = -\int_{-\infty}^{\infty} d\omega A(\omega) ln \frac{A(\omega)}{D(\omega)} \tag{2.63}$$

relative to a default model $D(\omega)$. Into this model information about the spectrum is encoded, e.g. the positivity and the normalization of the spectrum. In the MEM approach the quantity

$$Q[A] = \frac{1}{2}\chi^2[A] - \alpha S[A] \tag{2.64}$$

is minimized where χ is the goodness of fit functional

$$\chi^2[A] = \sum_n \frac{1}{\sigma_n^2} \int_\omega |K_n(\omega)A(\omega) - G_n(\omega)|^2 \tag{2.65}$$

which measures the difference between the spectrum generated from the Monte Carlo data and the actual Monte Carlo data. The parameter α controls how much weight is put onto the model $D(\omega)$ in the fitting process. If α is zero a least square fit is performed. For $\alpha \to \infty$ the model is recovered. Often α is chosen such that $\chi^2 \approx N$, where N is the number of data points. This guarantees that the difference between the model and the data are of the order of the error bars and thereby prevents overfitting.

An approach which generalizes the MEM is the stochastic analytic continuation [150]. In the Stochastic Analytic Continuation an average of many likely candidates is generated

as opposed to the most likely candidate of the analytical continuation in the MEM. The main advantage of the Stochastic Analytic Continuation is that it is possible to model spectra with sharp features and fine structures [150]. In the original work no reason for this proposal to average over many spectra was given, besides the empirical evidence that the resulting spectra were closer to the data of exact calculations. In [52] it was shown that the MEM is the mean-field solution of a system of interacting classical fields which can be related to the original problem of the analytical continuation. The stochastic analytic continuation can than be understood as a dynamical generalization which allows for thermal fluctuations around this mean-field solution. The mathematical formulation of the stochastic maxent derived in [52] includes an additional degree of freedom which can be identified as the default model which is present in the classic maxent but absent in the original stochastic analytic continuation. For obtaining our spectra we used an implementation from Fakher Assaad [151].
The typical quantity which is analytically continued to the real axis is the Greens function in τ since it is readily available as an output of the QMC. In the Greens function, however, a lot of information is encoded to which we have analytical access, e.g. the Hamiltonian H_k and the chemical potential μ. In the end the only thing which we do not know analytically and which is the quantity beyond non-correlated systems, which we want as an output of the AIM, is the self-energy $\Sigma(i\omega_n)$ and it is thus more reasonable to perform an analytical continuation directly of the self-energy to the real axis.
To make use of the same analytical continuation routines we already used for the Greens function the quantity that we want to analytically continue has to have a high frequency behaviour which falls off as $1/\omega_n$. If we perform the high frequency expansion of the self-energy of the single-band Hubbard model, however, we obtain

$$\Sigma_\sigma(i\omega_n) = U\langle n_{-\sigma}\rangle + U^2\langle n_{-\sigma}\rangle(1-\langle n_{-\sigma}\rangle)(i\omega_n)^{-1} + \mathcal{O}\left((i\omega_n)^{-2}\right). \tag{2.66}$$

This can be fixed by subtracting the zeroth moment and dividing by the first moment as outlined in [50]. This quantity can then has the right behavior and can be analytically continued. This formula is correct only for density-density interactions for one-band. For the density-density interaction it can be easily formulated also for more bands. If more complicated interactions are used additional four point quantities have to be measured in the Monte Carlo.
To test this approach with our solver we performed a comparison between data obtained by ED-calculations and our QMC. The test system consists of 1-band with an interaction of $U = 1$ and hybridization to bath sites listed in Table 2.1. The chemical potential is set to $\mu = 0.2904$, the inverse temperature is set to $\beta = 26$ and truncation to 3. 480000 measurements were performed for each of the 500bins. The first thing we checked is that the back transformed quantities look the same as the output of the QMC which can be seen in Figure 2.21.
The final check if everything works out is the comparison between the analytically continued self-energy of the QMC and the data from ED. As we can see in Figure 2.22 the

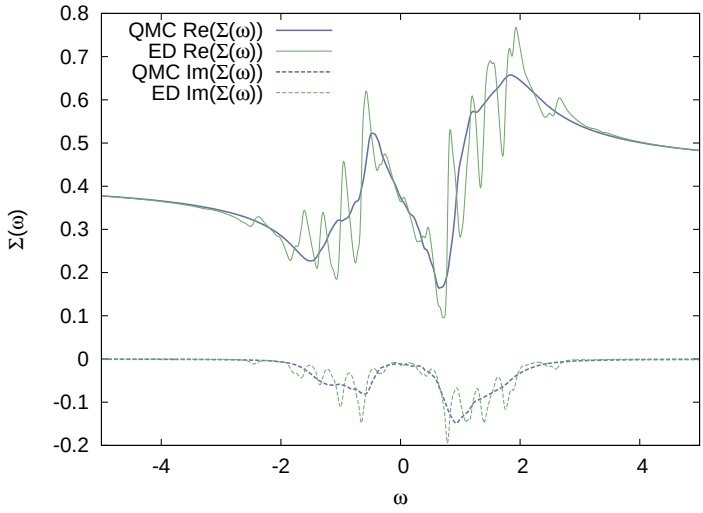

Figure 2.22.: Comparison of the analytical continuation to the real axis of data from QMC calculations and ED-data with the same hybridization function and local interaction.

	$\varepsilon(p_i)$	$V(p_i)$
p_1	0.9940	0.2605
p_2	0.1713	0.2320
p_3	-0.9926	0.2223
p_4	-0.1549	0.2350

Table 2.1.: The values of the hybridization function for the test system.

agreement is very good. The maxima and minima are at the same position and only the fast oscillations are not completely in agreement but rather smoothened out by the Stochastic Analytic Continuation. This should be less of a problem in calculations of realistic systems since the spikes of the ED hybridization functions are by construction not present in realistic systems. The ED-test data was kindly provided by Georg Rohringer.

2.7. Adding Non-Local Interactions

In the previous sections I showed how one can generate a model from first principle calculations and what happens if p-bands are added to a LDA+DMFT calculation. In the DMFT calculation the p-bands were treated as non-interacting and influenced the

calculation only by their hybridization with the d-bands. We could also go one step further than in the previous treatment and include correlations on the p-bands and between the p- and d-bands explicitly in the LDA+DMFT self-consistency. Since the orbitals are more extended and the treatment via the exact solution of an Anderson Impurity Model is numerically very expansive one can think of treating the p-bands in a Hartree way, which is also consistent within the DMFT for ligand p-bands.
The only diagram which contributes in the Hartree approximation is the bubble

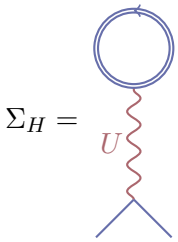

and the self-energy is therefore only depending on the densities

$$\Sigma_H^{mm} = \sum_{l,l\neq m} U_{lm}\langle n_l \rangle \tag{2.67}$$

where the indices m and l run over the orbitals and spins and $\langle n_l \rangle$ is the mean occupation of the orbital l. The interaction parameters U_{lm}, which span the correlated and uncorrelated subspace, in the equation above are hard to estimate since they depend crucially on the overlap of the p- and d-orbitals. Since there are currently no calculated values from first-principle available we kept them as a free parameters in the study, which I will present in 2.7.1. The main effect of including the interaction U_{pd} is an energy shift between the d- and p-bands which is self-consistently determined since it changes due to the reordering of charge. In our current scheme we do not take pd-spin coupling into account. Only on-site J_{dd} is treated exactly as before in the DMFT-scheme without pd-interaction.
Since the correlations on p-orbitals and between d- and p-orbitals are taken explicitly into account one also has to adjust the double counting correction which in the fully localized limit is given by

$$DC^{FLL} = \bar{U}_{dd(pp)}\left(n_{d(p)} - \frac{1}{2}\right) + \bar{U}_{dp} n_{p(d)}, \tag{2.68}$$

where we used the densities from LDA for $n_{d(p)}$ and $\bar{U}$ is the averaged interaction of (between) the subspace(s) denoted in the subscript. If the densities of the orbitals would not change during the self-consistent calculation this would exactly cancel the term coming from the dp-interaction. Thus one can think of the interaction as a self-consistently determined energy shift between the d- and p-orbitals.

The main difference in the self-consistency loop due to the inclusion of the Hartree self-energy is an additional step after solving the AIM. After obtaining a new self-energy we need to compute the densities of all orbitals via the Matsubara sum of the lattice Greens function. With these densities the additional quantity Σ_H is computed for the p- and d-orbitals via Equation (2.67).
We therefore obtain the following self-consistency loop:
(i) We calculate the local Greens function with the full self-energy containing the full correlation on the correlated orbitals and only the Hartree part on the other orbitals:

$$\mathbf{G}^{loc}_{full}(i\omega_n) = \frac{1}{N_{\vec{k}}} \sum_{\vec{k}} \left[(i\omega_n + \mu)\boldsymbol{\delta} - \mathbf{H}_{\vec{k}} - \boldsymbol{\Sigma}_{full}(i\omega_n) \right]^{-1}. \tag{2.69}$$

(ii) We project the Greens function onto the correlated orbitals using the projector $\boldsymbol{\mathcal{P}}_d$ and define the auxiliary AIM

$$\mathbf{G}^{loc}_{d} = \boldsymbol{\mathcal{P}}_d \mathbf{G}^{loc}_{full} \left[\boldsymbol{\mathcal{P}}_d\right]^{-1} \tag{2.70}$$

(iii) Using the local Greens function in the correlated subspace we define the bath Greens function of the auxiliary AIM

$$\left[\boldsymbol{\mathcal{G}}^{0}_{d}\right]^{-1} = \left[\mathbf{G}^{loc}_{d}\right]^{-1} + \boldsymbol{\Sigma}_d \tag{2.71}$$

and solve it.
(iv) After solving the auxiliary AIM we obtain a new self-energy for the correlated subspace $\boldsymbol{\Sigma}_d$ and calculate the densities $\langle n_l \rangle$ for each orbital using the Matsubara sum. Using the densities we can calculate the Hartree self-energy by employing Equation (2.67). Then we can calculate the full self-energy by

$$\boldsymbol{\Sigma}_{full} = \boldsymbol{\Sigma}_d + \boldsymbol{\Sigma}_H \tag{2.72}$$

which enters into the next self-consistency cycle.

w2d

The additional interaction parameters U_{pp} and U_{pd} can be specified via the parameters *Upp* and *Udp*.

2.7.1. Emery Model

This subsection is based on the following manuscript:
Importance of non-local copper-oxygen interaction for high T_C cuprates
P. Hansmann, **N. Parragh**, A. Toschi, G. Sangiovanni and K. Held
In preparation

In the beginning of this section I introduced the possibility to add interactions between d- and p-orbitals into the self-consistency cycle. In this section I want to present a study which applies this addition to a class of materials which has been in the focus of intensive investigations of the solid state community for the last decades, the cuprates. Since the discovery of the high-temperature super conductivity [152] by doping the charge-transfer insulating cuprates a great effort was undertaken by the theoretical community to come up with a model which describes the physics of it. The method which I have introduced so far, the DMFT, is, due to the anisotropic nature of the cuprates, not the best candidate for the description of this material. Ideally a method should be used which can also capture non-local spatial correlations which can be achieved by methods which I am going to briefly introduce in Section 2.8. Although a lot of studies were already conducted using such methods, e.g. [153, 154] no conclusion could be made yet if the Hubbard model is sufficient to describe the unconventional high-temperature superconductivity due to a number of numerical limitations.
In this study, however, we do not want to focus on the mechanism of the high-temperature superconductivity, but rather on the high-temperature regime in the undoped cuprates which are not correctly described to be non-magnetic insulating by LDA calculations [155]. The LDA+DMFT method was already successfully applied to the cuprates to analyze experimentally observed anomalies [156]. The restricted optical sum rule reported in [156] was studied in [157, 158, 159, 160] and a coherent structure which can be identified with the Zhang-Rice singlet, is found in [162, 161]. The reason that the description of the cuprates by means of the DMFT is reasonable for the high-temperature regime is that non-local correlations are less relevant [163, 164].
In this study we concentrate on the high-temperature insulating state of the cuprates using the LDA+DMFT scheme. A special focus is set on the reason why the system turns insulating when correlations are added to calculations performed in the single-particle picture. To obtain a clear picture for the nature of the insulating state an accurate low energy model of the system has to be created. In this work we used parameters which were obtained with the NMTO method [69] from first principle bandstructure calculations. For the cuprates the most important degrees of freedom which we need to keep in the downfolding procedure are correlated d-orbital and the p-orbitals which hybridize most strongly with the d-orbital, which are the p_x- and the p_y-orbital. This is the three

band Emery model which we are going to discuss in more detail soon.
As I already discussed in Section 2.5 the naive assumption that an inclusion of more degrees of freedom by keeping additional bands in the low energy Hamiltonian always improves the results is not correct. In the two studies which I presented in Section 2.5 we could show that the physics is changing by the inclusion of additional bands and it is not always clear which low energy Hamiltonian is the correct one.
In previous studies the p-bands, which were kept in the downfolded Hamiltonian, were treated as "spectators" which only influenced the calculation by their presence in the generation of the lattice Greens function. This treatment of the p-bands is motivated by the assumption that the p-orbitals are less localized than the d-orbitals and also almost completely filled. Since the radial part of oxygen p-orbitals is node-less and thus rather well localized this might, however, not lead to satisfying results. In the following study we will show that the effect of the U_{pp}-interaction is rather small, whereas the inclusion of the U_{pd}-interaction is responsible for the shape of the spectral function. It therefore controls the metal-insulator transition and the size of the charge transfer gap.

Model

Since the electrons predominantly move in the two-dimensional oxygen copper plane Emery suggested a low energy three-band Hamiltonian in 1987 [165]. He chose the orbitals with the strongest hybridization as the relevant degrees of freedom which are the Cu($3d_{x^2-y^2}$), O($2p_x$) and O($2p_y$) states.
There are also two other reasons why a three band model is the right choice. The first one is that stoichiometric compounds of the cuprates are antiferromagentically ordered charge-transfer insulators in the Zaanen-Sawatsky-Allen [167] classification scheme, for which the minimal model is a three band model [162]. Second, as noted in [154], the localized Cu $d_{x^2-y^2}$ orbital is so extended in the one band model that using only the on-site Coulomb repulsion is not justified.
For the hole-doped side an effective one-band model was constructed by Zhang-Rice [166] which is based on the idea that the hybridization forms a local singlet between the hole on the d-orbital and the additional doped hole on the oxygens, which moves through the lattice. The parameter range for which this one band description is accurate is, however, not clear [162]. Remnants of this quasi-particle can be found in LDA+DMFT results of the three band model which were also found in this study.
The model Hamiltonian proposed by Emery was put onto solid ground and extended by a downfolding from first-principle calculations performed by Andersen [168].

The starting point of the model by Andersen is the division of an eight band Hamiltonian, which was downfolded from the complete ab-initio Hamiltonian for $YBa_2Cu_3O_7$. Of these eight bands four have σ and four π character. The four π character orbitals (Cu_{xz}, Cu_{yz}, $O2_z$ and $O3_z$) can be neglected for non-dimpled planes, which is the case

$$h^{\mathrm{LDA}}(\vec{k}) \begin{pmatrix} h_d(\vec{k}) & h_{d,p1}(\vec{k}) & h_{d,p2}(\vec{k}) \\ h_{p1,d}(\vec{k}) & h_{p1}(\vec{k}) & h_{p1,p2}(\vec{k}) \\ h_{p2,d}(\vec{k}) & h_{p2,p1}(\vec{k}) & h_{p2}(\vec{k}) \end{pmatrix}$$

$$\begin{aligned}
h_d(\vec{k}) &= \varepsilon_d + 2\mathrm{t}_{dd}(\cos(k_x) + \cos(k_y)) + 4\mathrm{t}'_{dd}\cos(k_x)\cos(k_y) \\
h_{p1}(\vec{k}) &= \varepsilon_p + 2.0(\mathrm{t}'_{pp}\cos(k_x) + \mathrm{t}''_{pp}\cos(k_y) + 2\mathrm{t}'''_{pp}\cos(k_x)\cos(k_y)) \\
h_{p2}(\vec{k}) &= \varepsilon_p + 2.0(\mathrm{t}'_{pp}\cos(k_y) + \mathrm{t}''_{pp}\cos(k_x) + 2\mathrm{t}'''_{pp}\cos(k_y)\cos(k_x)) \\
h_{d,p1}(\vec{k}) &= 2((\mathrm{t}_{pd} + 2\mathrm{t}'_{pd}\cos(k_y))\sin(k_x/2) + (\mathrm{t}''_{pd} + 2\mathrm{t}'''_{pd}\cos(k_y))\sin(3k_x/2)) \\
h_{d,p2}(\vec{k}) &= -2.0((\mathrm{t}_{pd} + 2\mathrm{t}'_{pd}\cos(k_x))\sin(k_y/2) + (\mathrm{t}''_{pd} + 2\mathrm{t}'''_{pd}\cos(k_x))\sin(3k_y/2)) \\
h_{p1,p2}(\vec{k}) &= -4.0(\mathrm{t}_{pp}\sin(k_x/2)\sin(k_y/2) + \mathrm{t}''''_{pp}(\sin(3k_x/2)\sin(k_y/2) \\
&\qquad + \sin(3k_y/2)\sin(k_x/2)))
\end{aligned}$$

NMTO	$\varepsilon_d - \varepsilon_p$	t_{dd}	t_{pd}	t'_{pd}	t_{pp}	t'_{pp}	t''_{pp}	t'''_{pp}
N=0	0.43	−0.10	0.96	−0.1	0.15	−0.24	0.02	0.11
N=1	0.95	0.15	1.48	0.08	0.91	0.03	0.15	0.03

Table 2.2.: The extended Emery model [168] including p-p hopping and the numerical hopping integrals up to XY for 0MTO and 1MTO downfolding.

in our study. The reason for this is that these orbitals do not hybridize with the σ-block which contains the conduction band and the four σ character orbitals ($\mathrm{Cu}_{x^2-y^2}$, $\mathrm{O1}_x$, $\mathrm{O2}_y$ and Cu-s). If we want to obtain a three band model the Cu-s state needs to be integrated out. This leads to the addition of a 2nd-nearest-neighbour hopping ($\mathrm{O2}_x$-$\mathrm{O3}_y$), a 3rd-nearest-neighbour hopping ($\mathrm{O2}_x$-$\mathrm{O2}_x$ and $\mathrm{O3}_y$-$\mathrm{O3}_y$) and also a renormalization of ϵ_p. These changes are due to the inclusion of the Cu-s orbitals, the axial degree of freedom, into the tails of the neighbouring $\mathrm{O2}_x$ and $\mathrm{O3}_y$ orbitals. As discussed by Pavarini *et al.* in 2001 [169] this is the only material-dependent quantity of the downfolded Hamiltonian.

To obtain a quantitative description of the materials we used the results from NMTO techniques which I introduced in Section 2.4. For this study we use two different low en-

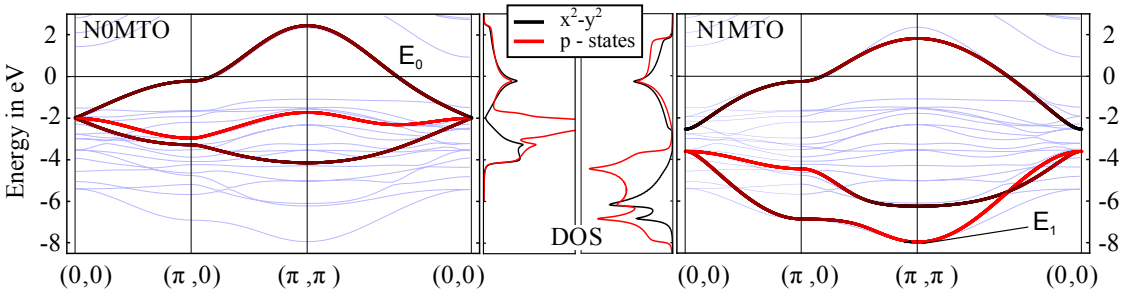

Figure 2.23.: Bandstructure and single particle density of states for the 0MTO and 1MTO model. The weight of the orbital character is color coded: black is the $3d_{x^2-y^2}$ character and red are the p-states.

ergy Hamiltonians. The first Hamiltonian is obtained via the 0MTO or LMTO technique with the energy dependence set to Fermi energy ε_F thus resulting in a bandstructure which gives the correct LDA Fermi surface and Fermi velocities. The second Hamiltonian we are going to use was obtained via the 1MTO technique with the second energy fixed to the bottom of the *pd*-bonding band. The analytical Hamiltonian is given in Table 2.2.

The bands calculated with these parameters for La_2CuO_4 [154] are shown in Figure 2.23. The LDA bandstructure is shown in both plots in light blue color while the LDA bandstructure of the NMTO bands are plotted in black for the $d_{x^2-y^2}$ and red for the p-orbitals. On the left side of Figure 2.23 the bands for 0MTO are plotted with the values for the hopping parameters and on-site energies as given in Table 2.2. On the right the bands are plotted for the 1MTO with the second energy fixed to the bottom of the *pd*-band. The resulting hopping amplitudes are bigger than the ones for 0MTO which is due to the spanning of a wider energy range which leads to less localized orbitals. An in-depth discussion of the parameters is given in [154].

In theoretical studies on for the high-temperature superconductors so far a major problem always occurred: the undoped LSCO material turns out to be metallic when *ab-initio* parameters for the *d*-*p*-splitting $\varepsilon_d - \varepsilon_p = \Delta_{dp}$ are used. The values are given by $\Delta_{dp} = 0.45$eV for the 0MTO and $\Delta_{dp} = 0.96$eV for 1MTO if we deduce them from the downfolded model. This problem was fixed in earlier studies by simply increasing the splitting by hand. This turns out to yield an insulating solution. The value typically used is $\Delta_{dp} \approx 3$eV [154, 162], without a real physical justification for this increase as pointed out in [154].

To obtain the results presented in this study we used the DMFT scheme as outlined in Section 2.5 and Section 2.7, thereby including the *dp*-interaction explicitly. For the analytical continuation we used the method as pointed out in Section 2.6 using an implementation of the stochastic maxent [151].

Results

The main conclusion we can draw from our study is twofold:
(i) A self consistently determined level splitting, which is due to the Hartree interaction U_{dp}, can drive the system insulating. This is a systematic improvement over earlier studies which needed to increase the level splitting by hand. The Hartree interaction was included in this study within the DMFT+Hartree approach, which I introduced in Section 2.7.
(ii) The U_{dd} values needed in this study to obtain insulating results are larger than the ones used in [154]. This can be attributed to the need to include more correlation effects, namely beyond the single site DMFT, to correctly describe the properties of the material.

0MTO Let us first look at the calculations of the 0MTO model. For these calculations we chose the interaction parameter $U_{dd} = 10$eV, for the correlated d-subspace, and $U_{pp} = 5$eV, for the p-subspace. The interaction between these two subspaces was varied from $U_{dp} = 0$ to $U_{dp} = 7$eV. The interaction parameters were chosen after consideration of cRPA calculations. The value of U_{dd} from cRPA calculations is given by $U_{dd}^{cRPA} = 8.9$eV [203]. Since the cRPA values are normally smaller than cLDA values we chose our interaction parameter a bit larger. The reason for this discrepancy lies in the frequency dependence of the cRPA interaction parameters, which is typically not taken into account. It was recently shown that one can take this frequency dependence into account by a Bose factor renormalization of the bandwidth, [170]. For U_{pd} and U_{pp} no estimates were yet published, to the best of our knowledge. Choosing the U_{pp} value smaller than the U_{dd} value is physically reasonable since the p-orbitals are more extended. We would also expect that the U_{dp} value is smaller than or at most equal to U_{pp}.
We analytically continued the self-energy to the real axis and generated the spectral functions for all the different values of the U_{dp} interaction parameters which are shown in Figure 2.24 using the technique outlined in Section 2.6. Looking at the spectral function for $U_{pd} = 0$eV one can see that, although the interaction values are large compared to the bandwidth of the system, the spectrum looks very similar to the non-interacting spectrum (see Figure 2.23). This can be understood by the fillings of the bands which are far from integer filling due to the hybridization between the d- and p-bands. By increasing the value of U_{pd}, following the plots in Figure 2.24 from left to right and top to bottom, the hybridization decreases, since the charge transfer from the d-states to p-states is now suppressed by the potential shift of the order of U_{pd}. A rather sudden metal to insulator transition can be observed, for values $U_{pd} \approx U_{pp}$, between $U_{pd} = 4$eV and $U_{pd} = 5$eV.
Looking at the spectrum for $U_{pd} = 4$eV we can see a gap between the d-states. The "upper Hubbard band" above the Fermi-energy with some p-character and a mixed d-p

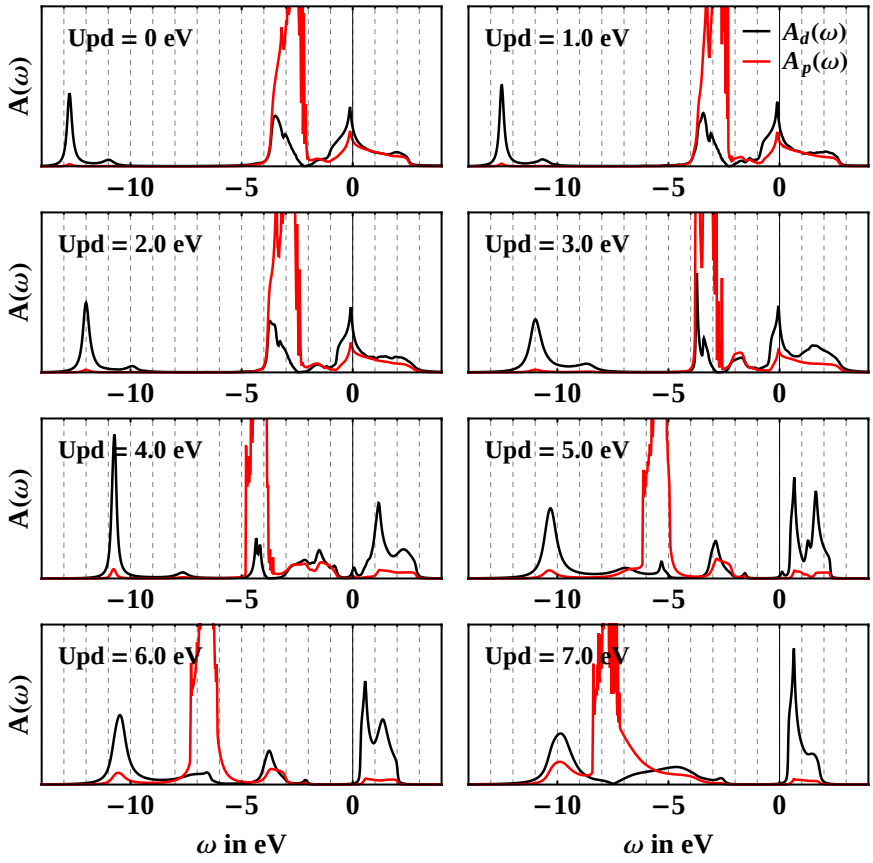

Figure 2.24.: The DMFT spectra for: 0MTO model, U_{dd} = 10eV, U_{pp} = 5eV and $0 < U_{pd} < 7$.

peak around −2eV. The "lower Hubbard band" is broad and centered around −12eV whereas most of the p-weight is centered around −5eV.

The inclusion of the Hartree self-energy into the DMFT scheme led to the desired effect. In previous studies without the artificial enhancement of the splitting between the d- and p-bands an insulating solution of the undoped cuprate could be found. The DMFT+Hartree scheme leads to suppression of the d-p hybridization which drives the metal-insulator transition. The value of U_{pd}, however, which is necessary to obtain insulating solution is rather large compared to the value of U_{dd} and might be unphysical. In the future cRPA studies will resolve the issue of the size of interaction parameters. A reason why the U_{pd} interaction necessary for the metal-insulator transition has to be that big could be that non-local correlations beyond DMFT are necessary for a realistic model. The second issue with this model is that the 0MTO is a downfolded Hamiltonian

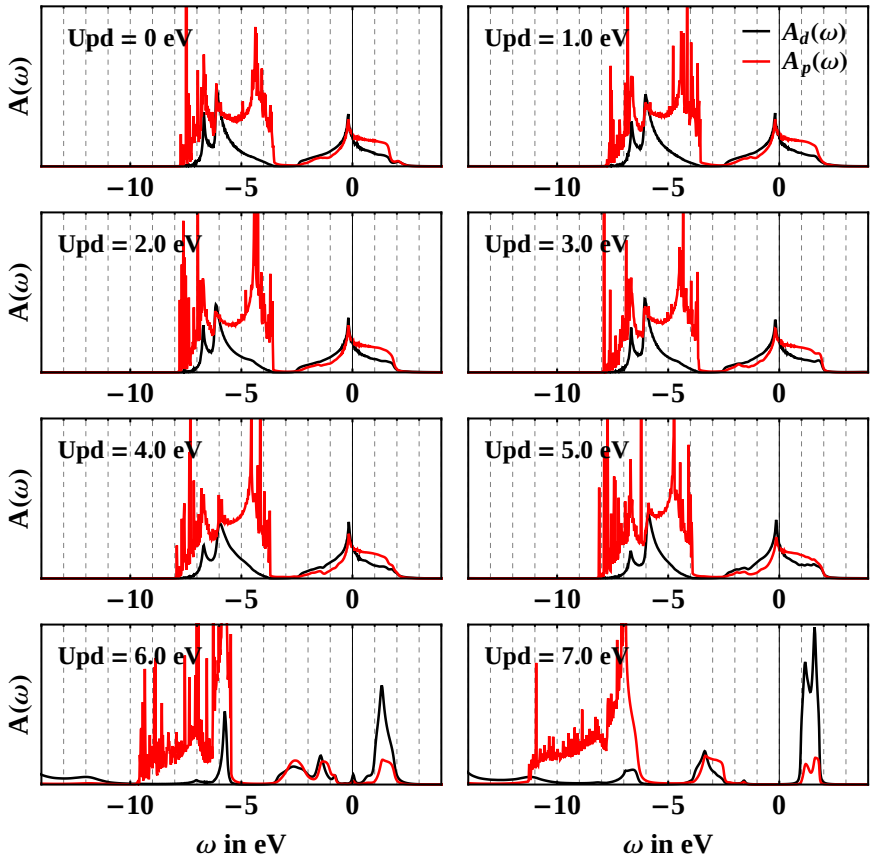

Figure 2.25.: The DMFT spectra for: 0MTO model, U_{dd} = 10eV, U_{pp} = 5eV and $0 < U_{pd} < 7$. Note that there is spectral weight for $U_{pd} > 5$ for $\omega < -15$eV.

which was designed to model the physics close to the Fermi edge. The question could thus arises if it is reasonable to study the excitations on an energy scale of some eV above and below the Fermi energy such as the *d-p* interplay using the 0MTO model. To address this issue we are going to perform the same discussion, as for the 0MTO model, on the 1MTO model, which is a more suitable model for a larger energy window.

1MTO We already mentioned previously that the only energy where the 0MTO is correctly reproducing the bandstructure is around the Fermi energy. When we want to obtain results which are reasonable also in the energy region of the *d-p* interplay the 1MTO model is a better choice. The reason for this is that the 1MTO model has been fixed not only to the Fermi energy but also to a second energy at the bottom of the oxygen *p*-bands ≈ -8eV. This fitting to two different energies yields a model

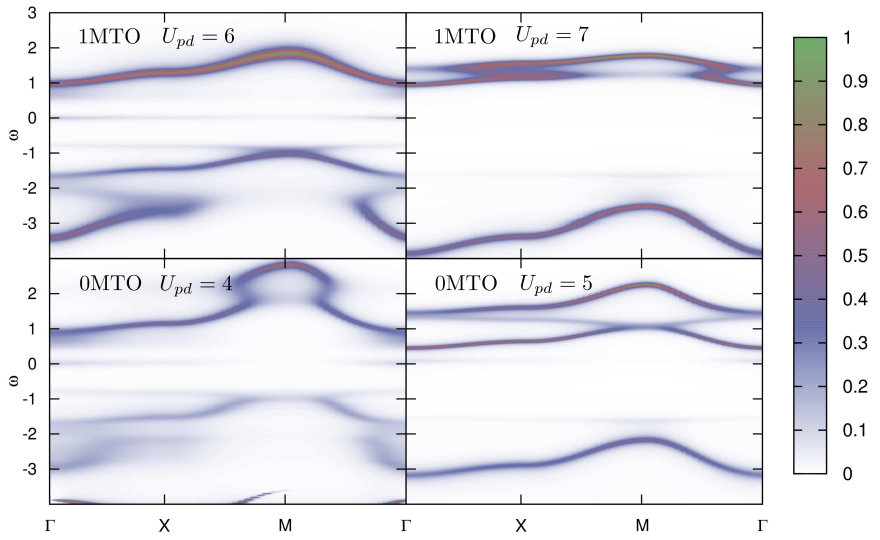

Figure 2.26.: The $\vec{k}$-resolved spectral function for the 0MTO model in the lower and the 1MTO model in the upper row. The two left panels are for $U_{dd} = 10$, $U_{pp} = 5$, $U_{pd} = 4$ eV and $U_{dd} = 13$, $U_{pp} = 7$, $U_{pd} = 6$ eV in the lower and upper row, respectively, i.e. before the charge-transfer metal-insulator transition. In the two right columns U_{pd} is increased by 1 keeping the other parameters fixed and therefore after the charge-transfer metal-insulator transition. For both models the mixed *pd*-state at ≈ -3eV becomes suddenly coherent as soon as we enter the insulating state. In the plot above $\Gamma = (0, 0)$, $X = (\pi, 0)$ and $M = (\pi, \pi)$.

which is less localized than the 0MTO model resulting in longer-ranged hoppings. As a consequence one would expect to need lower interaction parameters. Contrary to this this expectation the model stays metallic for the interaction parameters which we used for the 0MTO model. If we set the interaction parameters to larger values we can regain the insulating solution. The parameters are given by $U_{dd} = 13$eV and $U_{pp} = 7$eV. The parameter U_{dp} was again varied from $U_{dp} = 0$eV and $U_{dp} = 7$eV. The resulting spectra from this parameter scan are shown in Figure 2.25. The insulating state is reached for $U_{pd} = 6$eV. This parameter set is much larger than what one would expect from the arguments above and we thus conclude that the 1MTO model within DMFT+Hartree does not yield the physically correct result of a charge transfer gap in undoped cuprates within a reasonable parameter range.

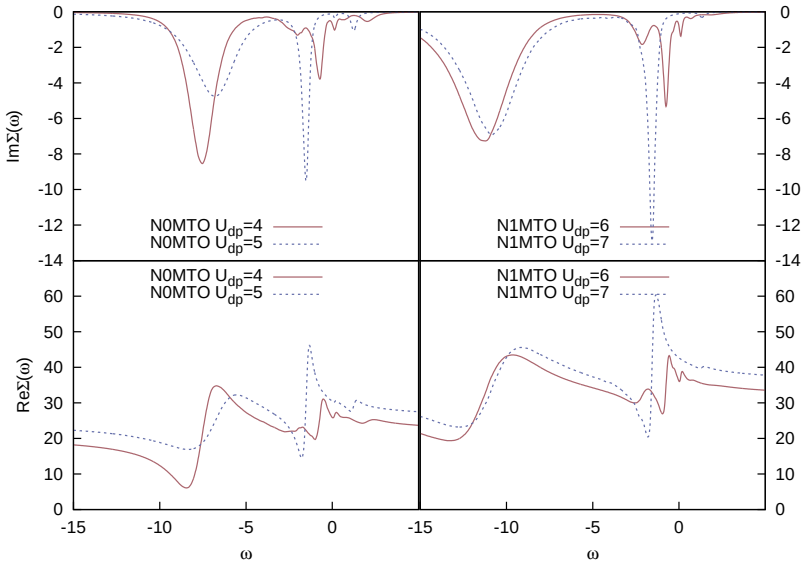

Figure 2.27.: The imaginary part (upper panels) and real part (lower panels) of the local DMFT d-self-energy on the real axis for the four cases plotted in Figure 2.26.

The mixed d-p peak The mixed d-p peak which can be seen in the $\vec{k}$-integrated spectral functions in Figure 2.24 at $U_{pd} = 5\text{eV}$ and in Figure 2.25 at $U_{pd} = 7\text{eV}$ around -3eV can be interpreted as the Zhang-Rice state. This is in agreement with previous studies [171, 172, 173]. The Zhang-Rice state is associated with a coherent state which we want to check by calculating the $\vec{k}$-resolved spectral function $A(\vec{k}, \omega)$ before and after the metal-insulator transition, which we can easily calculate using the retarded Greens function

$$A(\vec{k}, \omega) = -\frac{1}{\pi} ImG_R(\vec{k}, \omega) \tag{2.73}$$

$$= \left[(\omega^+ + \mu)\boldsymbol{\delta} - \mathbf{DC} - \mathbf{H}_{\vec{k}} - \boldsymbol{\Sigma}_{full}(\omega)\right]^{-1}. \tag{2.74}$$

The results for these values, i.e. $U_{pd} = 4, 5\text{eV}$ for 0MTO and $U_{pd} = 6, 7\text{eV}$ for 1MTO are shown in Figure 2.26. The corresponding self-energies are shown in Figure 2.27. We can see that $Im\Sigma$ and hence the coherence of the feature at $\approx -3\text{eV}$ changes dramatically when the system undergoes the metal-insulator transition. On the two left panels of Figure 2.26, where the system is on the metallic side of the phase diagram, the structure is incoherent whereas on the right two panels, where the system is in the insulating region, a very well defined quasi-particle peak emerges. If we look at the double-occupancies

(not shown) and the spectral weight at the Fermi level one can see that at the values for which the double-occupancies are suppressed most of the spectral weight gets shifted away from the Fermi level. The mixed peak is formed at this point and the material is a strongly correlated metal with only a small residual fraction of itinerant electrons. This feature, which we associate with the Zhang-Rice excitation, becomes more coherent when the spectral weight at the Fermi level is completely depleted, see Figure 2.27.

Conclusion

We want to stress again that the main goal of this study was to perform a calculation for the undoped LSCO compound without the artificial enlargement of the level splitting Δ_{dp}. The parameters we used in this study can in principle be calculated by cRPA or cLDA calculations and therefore no free parameter, which was needed in earlier studies, would enter the calculation. Our results prove that a self-consistently determined energy splitting due to the interaction between *d*- and *p*-orbitals can drive the metal-insulator transition. The physics of our 0MTO and 1MTO models is basically the same. The need for rather large interaction parameters for both models, but especially for the case of 1MTO, points to the conclusion that non-local correlations beyond DMFT+Hartree play an important role in the cuprates. A similar idea was recently proposed by Comanac *et al.* who analyzed experimental data for the optical conductivity of La_2CuO_4. They claim that the undoped cuprates cannot be described completely in terms of the Mott insulating DMFT picture [159].

2.8. Beyond Single Atoms and Local Interactions

The symmetry in real space of materials which show interesting properties in experiment is often broken and also long range interaction often play a role in the interesting effects that materials exhibit. So soon after the LDA+DMFT method was introduced extensions to treat more complex structures and non-local interactions were devised. For performing lattice calculations cluster extensions of the DMFT were introduced with the probably most famous ones being the cellular-DMFT [101] and the dynamical cluster approximation (DCA) [102, 103]. The main difference of the two methods is that the former is formulated in real space while the latter is formulated in momentum space. If the cluster is reduced to a single site both methods recover DMFT. Both methods allow to treat short range interaction of the length of the cluster size exactly while longer ranged interactions are treated on a mean-field level. These methods allow for the treatment of e.g. spin density waves or *d*-wave superconductivity. The drawback of these methods come from the finite size of the cluster which makes extrapolations to infinite clusters mandatory to access physical quantities in the thermodynamical limit. This cluster size itself is limited by the exponential growth of the Hilbert space which makes calculations of large clusters prohibitively expensive.

The second family of extensions to obtain correlations beyond a single atom are the diagrammatic extensions to the DMFT. Two well known diagrammatic extensions are the dual fermion approach (DF) [104] and the dynamical vertex approximation (DΓA) [105, 106, 107]. Both methods have in common that they are using two-particle quantities to introduce non-local correlations. The main difference is that the DF works in the dual fermion space which is reached via a Hubbard-Stratonovich transformation on the hopping term of the Hamiltonian, whereas the DΓA works directly in real space. The DΓA assumes the locality of the two-particle fully irreducible vertex, which leads to the inclusion of non-local contributions in the self-energy.

2.8.1. "Layer"-DMFT

Due to new techniques experimentalists have recently started to grow different substrates on top of each other which results in stacked materials consisting of different compounds. These layered materials show interesting new effects compared to bulk materials due to the interface between the two compounds. Similar to the formation of quantum wells, and thereby 2 dimensional electron gases (2DEG), in semiconductor interfaces a 2DEG can also form at the interface of oxides. The mechanism which generates the 2DEG is e.g. in the bilayer material $SrTiO_3/LaAlO_3$, which are both band insulators in the bulk, the formation of a potential and thus, when enough $LaAlO_3$-layers are present, a charge formation of half an electron at the interface [148]. The phase diagram of such oxide interfaces is much more varied and interesting compared to the one of semi-conductors since the constituents are d-electron systems, which, as we already know, are responsible for strong correlations. A possibility to calculate such layered materials, which was first presented in [108], is to simply model them by an enlarged unit cell. The treatment of such a system consists of: treating the on-site interaction for each layer in DMFT by mapping it onto an AIM but keeping the hopping between the layers by a $H_{\vec{k}}$ which explicitly contains all the layers of the enlarged unit cell.

The self-consistency cycle therefore becomes:
(i) We first calculate the local Greens function with a self-energy, which in general can also contain a Hartree part for the p-bands:

$$\mathbf{G}^{\mathrm{loc}}_{full}(i\omega_n) = \frac{1}{N_{\vec{k}}} \sum_{\vec{k}} \left[(i\omega_n + \mu)\boldsymbol{\delta} - \mathbf{DC} - \mathbf{H}_{\vec{k}} - \boldsymbol{\Sigma}_{full}(i\omega_n) \right]^{-1} \tag{2.75}$$

where the matrices have the size $\sum_l N_{l,d+p}$ where l is the layer index and $N_{l,d+p}$ is the number of p- and d-orbitals in the layer l.

(ii) Then we have to define the local correlated problem which is the correlated subspace of each layer l. This is done by projecting the full local Greens function $\mathbf{G}^{\mathrm{loc}}_{full}$ onto

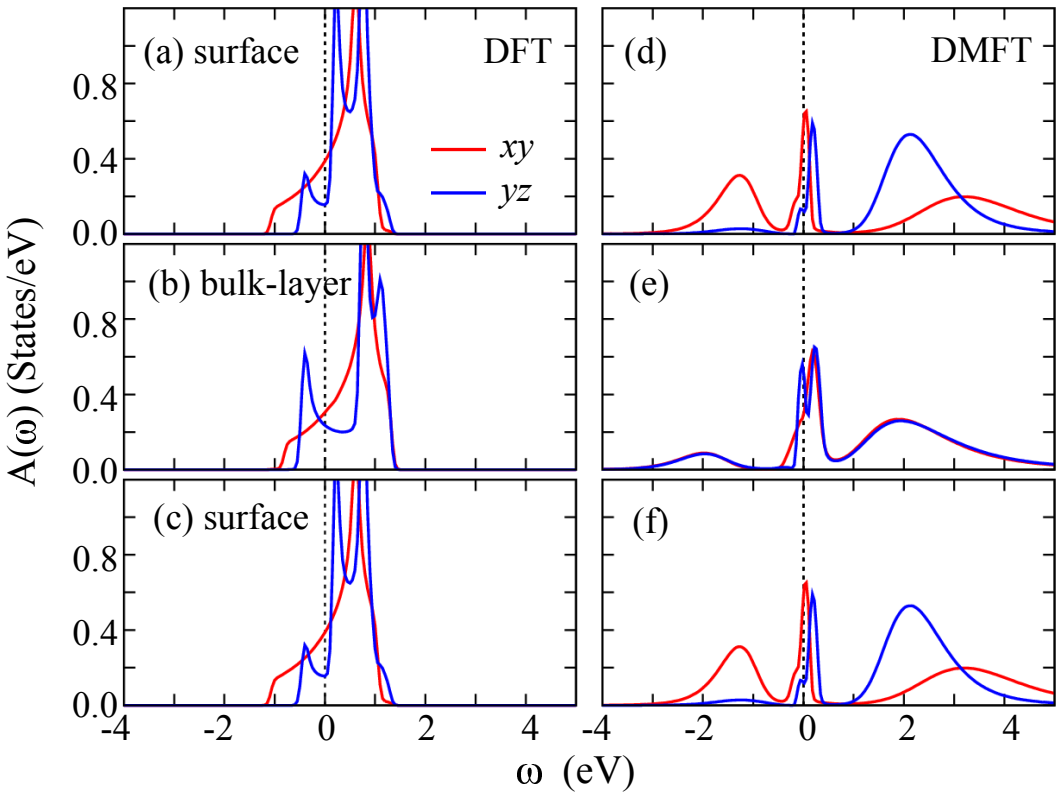

Figure 2.28.: Comparison of a "layer"-DMFT calculation of three free-standing layers of $SrVO_3$. One can see a difference of the weight of the spectral function at the Fermi-edge for the LDA and the layer-DMFT calculations of the V-d_{xy} and V-d_{yz} orbitals. Both calculations yield a metallic solution at $T = 300$K.

the correlated subspace of l via the projector $\boldsymbol{\mathcal{P}}_{l,d}$:

$$\mathbf{G}^{loc}_{l,d} = \boldsymbol{\mathcal{P}}_{l,d} \mathbf{G}^{loc}_{full} \left[\boldsymbol{\mathcal{P}}_{l,d}\right]^{-1} \tag{2.76}$$

(iii) In the next step we calculate the hybridization function to define the impurity problem:

$$\left[\boldsymbol{\mathcal{G}}^{0}_{l,d}\right]^{-1} = \left[\mathbf{G}^{loc}_{l,d}\right]^{-1} + \boldsymbol{\Sigma}_{l,d} \tag{2.77}$$

Such a self-consistency cycle neglects non-local correlations between the different atoms but takes the hopping between the atoms into account. Since the interaction on each

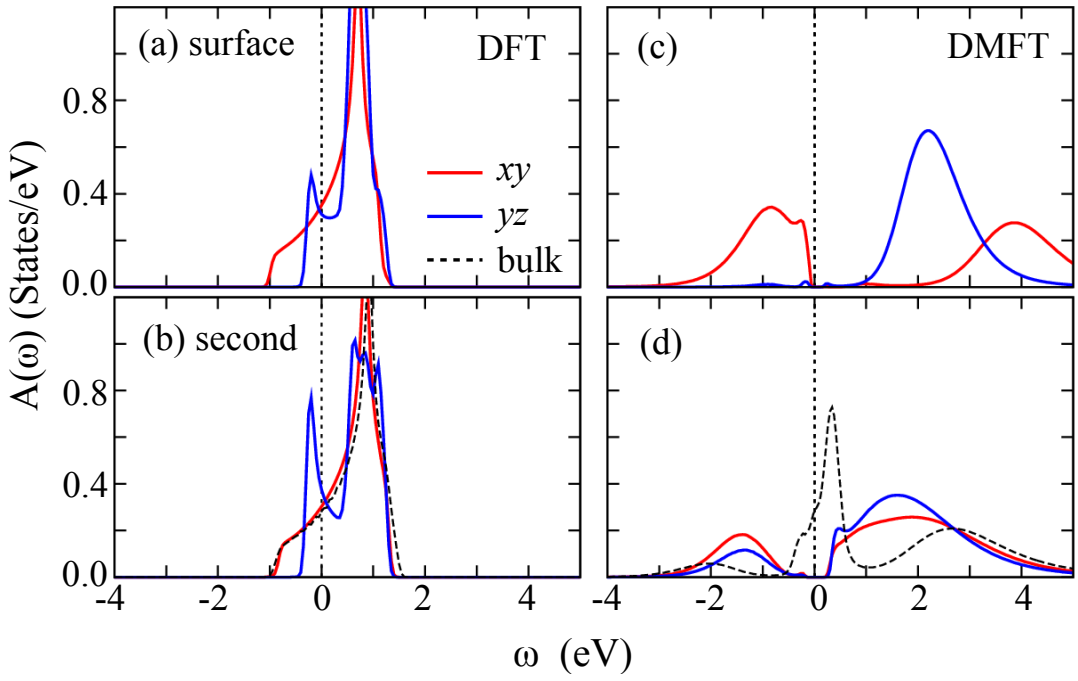

Figure 2.29.: Comparison of a "layer"-DMFT calculation of two layers of $SrVO_3$ on $SrTiO_3$. One can see that the spectral weight at the Fermi edge is disappearing in the DMFT calculation at $T = 300$K. Shown are the V-d_{xy} and V-d_{yz} orbitals.

layer can be different the impurity problem also has to be set up with the right interaction matrix U_{lijkm}.

Zhong *et. al.* are currently performing a study using *w2dynamics* for $SrVO_3$. The starting point of the study are *ab-initio Wien2k* [149] calculations within the generalized gradient approximation (GGA). The lattice constants are fixed to the experimental values of $a = 3.86$ for free standing layers of $SrVO_3$ and to $a = 3.92$ for $SrVO_3$ layers grown on a $SrTiO_3$ substrate. The thickness of the thin film layer is varied from $N = 2$ to $N = 5$. In this work only results for the most interesting $N = 2$ and $N = 3$ calculations will be shown.

Using these calculations a downfolding to a low energy effective Hamiltonian was performed and used as the input for a "layer"-DMFT calculation. The local Hamiltonian used is the Kanamori Hamiltonian which I am going to discuss in 3.1. The interaction parameters are set to $J = 0.75$ and $V = U - 2J$ while the inter-orbital Coulomb repulsion U is kept as a free parameter. The study is conducted at three different temperatures

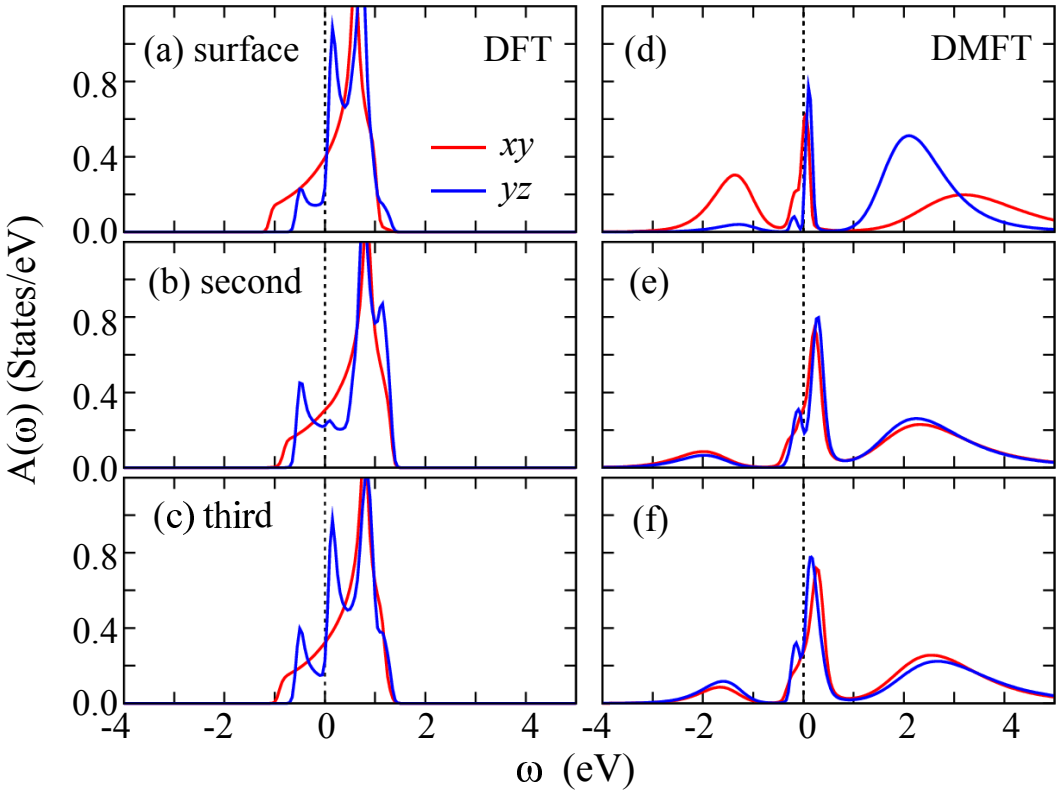

Figure 2.30.: Comparison of a "layer"-DMFT calculation of three layers of $SrVO_3$ on $SrTiO_3$. The spectral weight of the V-d_{xy} and V-d_{yz} orbitals are shown. At the Fermi energy the spectral weight is decreasing when the interaction is switched on, but the system stays metallic at $T = 300$K.

$T = 200$K, 300K and 400K. The correlated subspace, which is treated in the DMFT calculation, is the t_{2g} subspace on the Vanadium atom. The d_{xz} and d_{yz} orbitals are perpendicular to the plane while the d_{xy} orbital is in-plane.

For the free standing $SrVO_3$ with three layers the system is in the metallic regime for all parameters used in this study. The resulting spectra can be seen in Figure 2.30 at $T = 300$K. One can see that already in the non-interacting DFT result the DOS of the orbitals pointing perpendicular to the surface, d_{yz} and d_{xz} (not shown), are quite different from the DOS of the "bulk"-layer between the two surface layers. The orbital which points parallel to the surface, d_{xy}, is not altered at all.
Let us turn to $SrVO_3$ grown on a $SrTiO_3$ substrate. This changes the lattice parameter

of the system from $a = 3.86$ to $a = 3.92$. For the free standing $SrVO_3$ both layers are surface layers but now one is an interface layer to the $SrTiO_3$. In terms of numerical effort this means that the calculation is twice as expensive since the two impurity models are different now. In Figure 2.29 we see that the spectra of the surface layer in this calculation becomes insulating and the system acquires a strong orbital polarization. The d_{xy}-orbital is half-filled while the d_{yz}-orbital is completely empty for $U = 5.05$ and $T = 300$K.
Turning to a system of three $SrVO_3$ layers grown on a $SrTiO_3$ substrate, shown in Figure 2.30, we notice a striking change to the spectra of the two-layer system: The system is not insulating anymore for the parameters stated above. However the surface layer is very close to the metal-insulator transition as can be seen by the large renormalization of the quasi-particle peak.

Another interesting result is that the two-layer system undergoes a metal-insulator transition when temperature is tuned from 300K to 400K as can be seen from the spectra in Figure 2.31.

In summary one can say that the system studied here shows different behavior in a thin film configuration either free standing or grown on a substrate in the calculations compared to the bulk system of which the spectrum is shown in Figure 2.29. The two and three layer systems are both very close to the metal-insulator transition and the two layer system can be driven from one regime into the other by temperature and strain. The surface layer is extremely different from the other layers when $SrVO_3$ is grown on $SrTiO_3$. The transition is driven by a layer-dependent shrinking of the V-t_{2g} bandwidth caused by the reduced hopping along the z-direction. As discussed the layers undergo a metal-insulator transition for parameters considered in this study in the two-layer system. The insulating behavior is accompanied by a strong orbital polarization of the d_{xy}-orbital.

w2d

In *w2dynamics* the loop over layers is equivalent to a calculation in an enlarged unit cell. This is done by generating a Hamiltonian which has the size of the full problem (all layers) and provide the additional information how many correlated bands and uncorrelated bands are to be treated for each atom. The different interaction parameters can be provided by means of a u_matrix file whose first index denotes in this case the layers and not the inequivalent atoms.

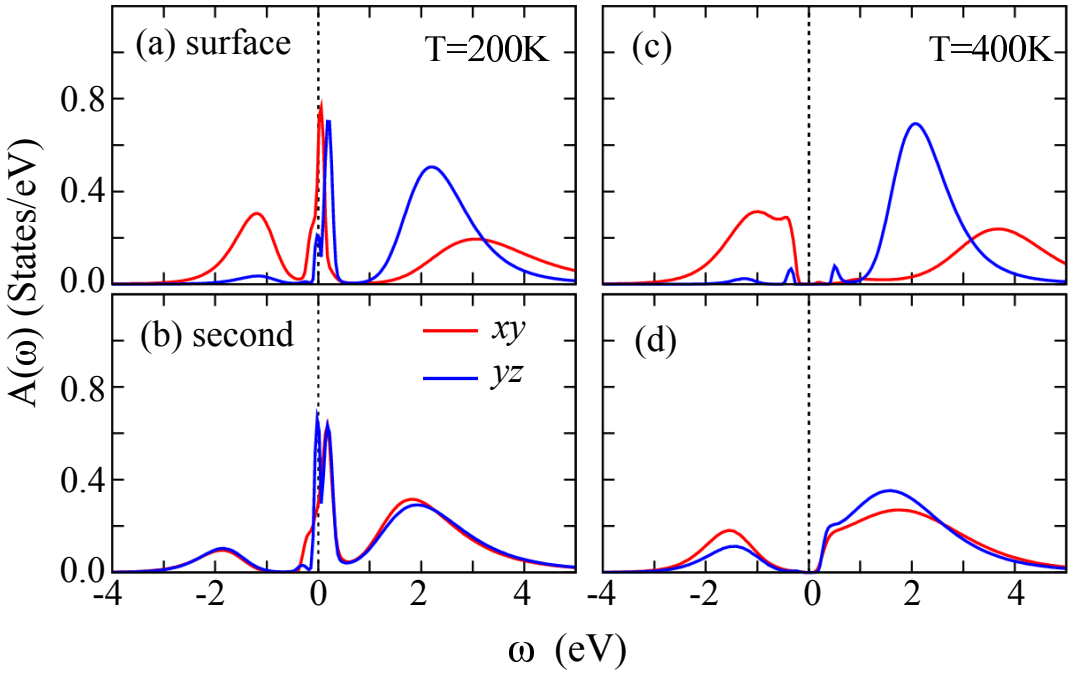

Figure 2.31.: Two layers of $SrVO_3$ on $SrTiO_3$. The spectral weight of the V-d_{xy} and V-d_{yz} orbitals are shown.The system undergoes a metal insulator transition when the temperature is decreased from $T = 200$K to $T = 400$K.

2.8.2. Nano-DΓA

The major problem when dealing with systems consisting of many correlated bands is, as we already mentioned, the exponential growth of the Hilbert space. It is thus not possible to treat large correlated systems on a nanoscopic scale exactly. In this section I will introduce the so called nano-DΓA which was presented in [109]. It is a novel tool to study electronic correlations on the nano scale theoretically. Opposed to lattices in which one can take advantage of the periodic structure, in nanoscopic systems one has to take into account inhomogeneous systems devoid of translational symmetry. For the interested reader I refer to the thesis of Angelo Valli [110].
Let us start by setting up a nanoscopic system, in which we suppress the spin indices for readability. It consists of N sites at fixed positions in space which are coupled to

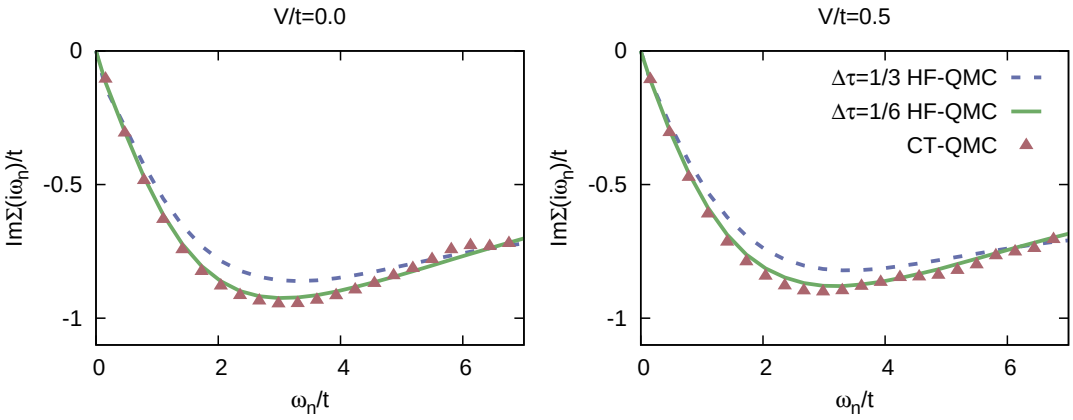

Figure 2.32.: Comparison of results for benzene obtained with the *w2dynamics* program compared to the ones obtained with the original implementation. The original implementation used the Hirsch-Fye QMC as an impurity solver and one can see the convergence of the results to the CT-QMC results with decreasing $\Delta\tau$. Compared are the self-energies of the self-consistent solutions.

the other sites via an inter-site hopping t_{ij}, which have a local Coulomb repulsion U_i and which might hybridize with the non-interacting environment i.e. a lead $V_{i\eta k}$. In the above quantities I suppressed the spin and orbital index for brevity. The full Hamiltonian is then given by

$$\mathbf{H}^{nano} = -\sum_{ij} t_{ij} c_i^\dagger c_j - \mu \sum_i c_i^\dagger c_i + \sum_{ijlmn} U_{ijlmn} c_i^\dagger c_i c_i c_i \tag{2.78}$$

$$+ \sum_{i\eta k} (V_{i\eta k} c_i^\dagger l_{\eta k} + V_{i\eta k}^* l_{\eta k}^\dagger c_i) + \sum_{\eta k} \varepsilon_{\eta k} l_{\eta k}^\dagger l_{\eta k}, \tag{2.79}$$

where $c_i^\dagger$ (c_i) and $l_{\eta k}^\dagger$ ($l_\eta k$) are the creation (annihilation) operators for electrons on site i and in lead η state k with energy $\varepsilon_{\eta k}$.
Since the Hamiltonian above is impossible to solve exactly in the case of many coupled impurities the main idea of the nano-DΓA comes into play. The full problem is reduced to a set of N auxiliary single-site Anderson impurity models, thus the Hilbert space only grows exponentially for the on-site problem. Furthermore the AIMs can be solved independently. For this reason each AIM which is locally equivalent to an already solved AIM need not be solved again. Exploiting the symmetries further reduces the numerical cost of calculations and we only have to solve $N_{ineq} < N$ AIMs. The numerically most

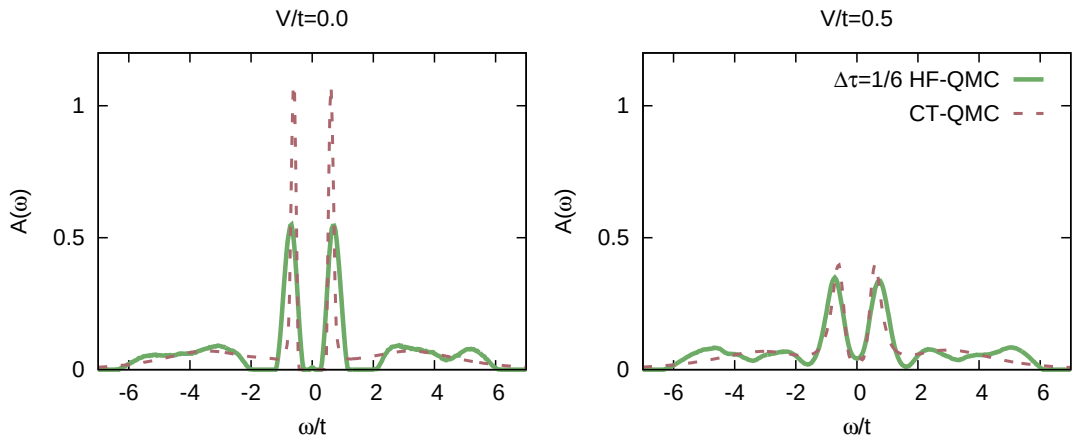

Figure 2.33.: Similar to Fig. 2.32 only here the spectra obtained from MEM calculations are compared.

demanding part, the solution of the AIM, therefore only increases linearly in the nano-DΓA making large nano structures accessible; if we restrict the treatment to the first order of only local diagrams which results in a nano-DMFT approximation. Neglecting non-local correlations can be a reasonable choice, as pointed out in [110], if: (i) The interaction U is zero, which is the trivial case. (ii) The sites are decoupled $t_{ij} = 0$; similar to the atomic limit in the lattice problem. (iii) The hybridization is strong $V_{i\eta k} \to \infty$ and each site is coupled to its own lead. Then the hybridization is the dominating energy scale effectively decoupling the sites. (iv) If each site has a large number of neighbouring sites, then non-local correlations are less important.

The self-consistency loop is then given by the following steps:
(i) Define the full Greens function of the nanoscopic problem in real space

$$\mathbf{G}_{full}(i\omega_n) = \left[(\mu + i\omega_n)\boldsymbol{\delta} - \mathbf{DC} - \mathbf{H}^{nano} - \boldsymbol{\Sigma}_{full}(i\omega_n)\right]^{-1}. \tag{2.80}$$

(ii) Then we have to project onto the correlated subspace of each inequivalent atom using the projector $\boldsymbol{\mathcal{P}}_i$

$$\mathbf{G}_{ineq} = \boldsymbol{\mathcal{P}}_i \mathbf{G}_{full} \left[\boldsymbol{\mathcal{P}}_i\right]^{-1} \tag{2.81}$$

As in the layer-DMFT the interaction can also be different for each inequivalent atom thus the impurity problem has to be set up with the right interaction matrix U_{jlmn}.
(iii) To define the impurity problem we then use

$$\left[\boldsymbol{\mathcal{G}}_i^0\right]^{-1} = \left[\mathbf{G}_i\right]^{-1} + \boldsymbol{\Sigma}_i \tag{2.82}$$

As in the previous DMFT-schemes this loop is iterated until convergence is reached.
I show results for nano-DMFT calculations performed within *w2dynamics* compared to results from the original implementation by Angelo Valli in Fig. 2.32 and 2.33.

w2d

To perform nano-DMFT calculations in *w2dynamics* the *DOS* has to be set to *nano*. Additionally the parameter *nanonstructure* has to be set. This is a string which defines the nanostructure used as a postfix for the additional files which need to be provided.
*lead.*nanostructure In the first line the number of leads is given and in the subsequent lines the DOS of the hybridization. Possible values are *flat* for a flat DOS and *semi* for a semi-circular density of states as the first column. In the second column and third column the bandwidth of the DOS has to be specified for spin-up and spin-down respectively and finally in the last two columns the chemical potential again for spin-up and spin-down .
*site.*nanostructure In the first line of this file the number of atoms of the nano-structure, the number of inequivalent atoms, the number of d-bands and the number of p-bands per atom is given. In the subsequent lines the atoms belonging to a class of inequivalent atoms are listed in a line.
*t.*nanostructure The hopping is specified in this file in the following way: Every line contains the indices #atom1 #orbital1 #atom2 #orbital2 #spin Re(t) Im(t). Only the upper half of the t-matrix needs to be specified the lower half automatically generated.
*V.*nanostructure The hybridization strength to the leads is provided in this file. The format is: #lead #atom #orbital #spin Re(V) Im(V).
The input files for the calculation in this section are given in Appendix A.4.

2.9. Conclusion

In this chapter I first briefly introduced the density functional theory (DFT) and its local density approximation (LDA). This has been and still is the numerical work horse of the computational solid state community. To overcome the limitations of this method a merger with the dynamical mean-field theory (DMFT) was proposed which is called LDA+DMFT. With this method and a method for approximating the strength of the local interaction one is, in principle, able to perform ab-initio calculations for strongly correlated materials. There are however still some issues and open questions with the combination of these two methods.
The first methodological issue I described in Section 2.3 is the subtraction of terms which are already included in the LDA. I gave an overview of these so called double counting corrections and commented briefly on their applicability.
Then, in Section 2.4, I discuss another problem when one wants to perform DMFT

calculations on top of LDA calculations, which is the downfolding which can lead to different effective bandstructures and thus physics depending on the procedure used. There is another open question which is coupled to this, which regards the bands which one actually treats in the self-consistency cycle. The self-consistency cycle which allows us to treat an enlarged basis set is introduced in Section 2.5. The question if we also take uncorrelated p-bands into account and what the effect on the system, if p-bands are taken into account, is still not fully answered. To answer at least a part of this question we made two studies. The first study concerned itself with the change of the shape of the Fermi surface when interactions are taken into account via DMFT in systems in which the d-bands are split apart by a crystal-field. In earlier studies it was found that the initial splitting is always enhanced when only d-bands are taken into account. This result was, however, contradicted by a study that included p-bands which found exactly the opposite effect. We could show that the main effect on the crystal-field splitting is due to the different filling of the d-orbitals which in turn leads to the different effective crystal-fields. This could be proven since results of the calculations on a dp-basis could qualitatively be reproduced by a calculation on a d-basis with the occupancy taken from the dp-calculation. The effect on the Fermi-surface is thus mostly driven by the filling of the d-orbitals.
In the second study, of the DMFT result dependence on the basis set, we chose an even simpler model consisting of one correlated and one uncorrelated band. Using this model we studied the spin-susceptibility w.r.t. the hybridization between the d- and p-bands which shows a clear dependence on the hybridization. There are also new structures developing, which are not present in systems without hybridization, which could maybe even be measured experimentally thus hinting us at the importance of p-bands in low energy models for certain systems. Another measured quantity which develops a structure in the presence of p-bands is the expansion-order histogram of the hybridization expansion continuous-time quantum Monte Carlo (CT-HYB). By introducing a new quantity, the expansion-resolved density matrix, we could show that the new structure in the expansion-order histogram is due to the new channel which opens as soon as the hybridization between the d- and p-bands is switched on.
Another question concerning the LDA+DMFT method is if the interaction between d- and p-electrons and the interaction in the p-manifold has to be treated explicitly. In the DMFT every non-local interaction except the Hartree part is cancelled. This Hartree part of the interaction can still be treated in the self-consistency loop and its value can change due to charge redistributions. We used this DMFT+Hartree, see Section 2.7, approach to study one mother compound of the cuprates which is insulating in experiments but which in LDA+DMFT studies without artificially increasing the double counting correction always turned out metallic. We could show in the study presented in Section 2.7 that with the DMFT+Hartree approach an insulating solution can be found.
In Section 2.8 I presented two exemplary studies showcasing the extendibility of the code framework to more complex structures. One using the “layer”-DMFT which is ap-

plicable to studies of heterostructures. For this extension I presented some preliminary results for $SrVO_3$ layers on $SrTiO_3$. The second extension I showed is the application of the code to nano systems using the nano-DMFT. For this class of problems I present some benchmark results comparing calculations with the CT-HYB to already published results.

3. Local Interactions

In this chapter I will first introduce the full Coulomb interaction of free atoms and its relation to the density-density interaction. In Section 3.1 I will discuss the Kanamori interaction, present a new set of quantum numbers for it and investigate the orbital selective Mott transition using this interaction in a model system. Following that, in Section 3.2 I will give a short introduction to cobalt oxygen compounds and present a study on $SrCoO_3$. Then in Section 3.3 I will introduce an algorithm which finds the optimal structure, for CT-HYB calculations, for arbitrary local Hamiltonians. Finally, in Section 3.4, I will discuss different local interactions often used in LDA+DMFT studies.

Introduction

In the previous chapter, I focused on the self-consistently determined hybridization of the impurity problem in DMFT, but the question which interaction is suitable for which problems was never discussed in detail in this thesis. This point will be addressed now by discussing different interactions in the atomic limit.
If we want to describe any two particle interaction, which is conserving the total particle number and the total spin in z-direction, we can write it in the following way:

$$H^{\mathrm{U}} = \frac{1}{2} \sum_{m,m',m'',m'''} \sum_{\sigma\sigma'} U_{mm'm''m'''} d^{\dagger}_{m\sigma} d^{\dagger}_{m'\sigma'} d_{m'''\sigma} d_{m''\sigma'}. \tag{3.1}$$

The question which interaction, or equivalently which U-matrix, to use is connected to the multiplet structure of the problem at hand. If we treat d- or f-electrons we often use the Coulomb interaction rotated into the crystal-field basis of the problem. By doing this, we assume that the local interaction is almost spherical, even when embedded in a lattice. This interaction then commutes with the total spin $\vec{S}^2$ and, if there is no crystal-field present, with the total angular momentum $\vec{L}^2$. The reason why this approximation is often quite good is that the multipole part of the interaction cannot be screened effectively by the conduction electrons. It is thus instructive to understand the Coulomb interaction and I will therefore now give a brief introduction to it.
The tensor elements of the general Coulomb interaction can be written as

$$\begin{aligned} U^{\mathrm{C}}_{mm'm''m'''} &= \langle mm'|V_{ee}|m''m'''\rangle \\ &= \int \mathrm{d}\vec{r}\, \mathrm{d}\vec{r}'\; \Phi^{*}_{m\sigma}(\vec{r}) \Phi^{*}_{m'\sigma'}(\vec{r}')\; \frac{1}{|\vec{r}-\vec{r}'|}\; \Phi_{m''\sigma'}(\vec{r}) \Phi_{m'''\sigma}(\vec{r}'). \end{aligned} \tag{3.2}$$

where Φ are the spinors which are given for the atomic orbitals of the Hydrogen-type atom by

$$\Phi(\vec{r})_\sigma = R_{nl}(r)Y_{lm}(\theta,\phi)\chi_\sigma \tag{3.3}$$

Since the spin operator commutes with $|\vec{r}-\vec{r}'|^{-1}$ the Coulomb Hamiltonian matrix is diagonal in spin indices and I will thus suppress the spin index in the further discussion. As a direct consequence the Coulomb interaction does not change the spin of electrons and S_z, the total spin in z-direction is a conserved quantity. This was already implicitly assumed as I introduced the Hamiltonian above with a non-spin dependent U-matrix. Now we expand $|\vec{r}-\vec{r}'|^{-1}$ in terms of spherical harmonics

$$\frac{1}{|\vec{r}-\vec{r}'|} = \sum_{k=0}^{\infty} \frac{r_<^k}{r_>^{k+1}} \frac{4\pi}{2k+1} \sum_{q=-k}^{k} Y_{qk}(\theta',\phi')Y_{qk}^*(\theta,\phi), \tag{3.4}$$

where $r_<$ and $r_>$ is the smaller and greater value of $\vec{r}_1$ and $\vec{r}_2$ respectively. In a further step we express the spherical harmonics by associated Legendre functions $P_{lm}(\cos(\theta))$. This leads us to the following integrals over the azimuthal angles ϕ_i

$$\sum_{m=-l}^{l} \int_0^{2\pi} d\phi e^{i(M-m+m'')\phi} \int_0^{2\pi} d\phi'\, e^{i(M-m'''+m')\phi'} \tag{3.5}$$

which is different from zero only if $M-m+m''=0$ and $M-m'''+m'=0$. This reflects the condition that the Coulomb interaction preserves the total angular momentum. We can now introduce shorthand expressions for the total angular part which reads

$$a_k(mm',m''m''') = \frac{4\pi}{2k+1} \sum_{q=-k}^{k} \langle lm|Y_{qk}(\theta',\phi')|lm'\rangle \langle lm''|Y_{qk}^*(\theta,\phi)|lm'''\rangle \tag{3.6}$$

and the radial part, which can not be analytically computed, (the so-called Slater integrals)

$$F^k = \int \mathrm{d}r\ r^2 \int \mathrm{d}r'(r')^2 R_{nl}^2(r) \frac{r_<^k}{r_>^{k+1}} R_{nl}^2(r'). \tag{3.7}$$

Putting everything together we obtain the expression for the interaction tensor in spherical symmetry

$$U^{\mathrm{C}}_{mm'm''m'''} = \sum_{k=0}^{2l} a_k(mm',m'''m'')F^k. \tag{3.8}$$

and the Hamiltonian with the full Coulomb interaction

$$H^{\mathrm{C}} = \frac{1}{2} \sum_{m,m',m'',m'''} \sum_{\sigma\sigma'} U^{\mathrm{C}}_{mm'm''m'''} d^\dagger_{m\sigma} d^\dagger_{m'\sigma'} d_{m''\sigma'} d_{m'''\sigma}. \tag{3.9}$$

If the interaction is really spherically symmetric and not calculated with ab-initio methods one can chose an alternative parametrization without any further approximations which consists of only two parameters U and J

$$\begin{aligned} U &= F^0 = \frac{1}{(2l+1)^2} \sum_{mm'} U_{mm'mm'} \\ U - J &= \frac{1}{2l(2l+1)} \sum_{mm'} (U_{mm'mm'} - U_{mm'm'm}) \end{aligned} \tag{3.10}$$

For d-electrons the only Slater integrals which are non-zero are F^0, F^2 and F^4. For these electrons the exact identity $J = \frac{1}{14}(F^2 + F^4)$ can be obtained from the expression above. It is noteworthy that the ratio between the two Slater integrals F^2 and F^4 turns out to be almost constant and for transition metal ions given by $\frac{F^4}{F^2} = 5/8$ [126, 127].

Density-Density Interaction

The Coulomb integrals which have the highest contribution to the interaction are the direct integral $U_{mm'mm'}$ and the exchange integral $U_{mm'm'm}$ (with $m \neq m'$ for the exchange integral)

$$U_{mm'mm'} = U_{mm'} = \sum_{k=0}^{2l} a_k(mm, m'm') F^k \tag{3.11}$$

$$U_{mm'm'm} = J_{mm'} = \sum_{k=0}^{2l} a_k(mm', m'm) F^k. \tag{3.12}$$

The largest contributions we neglect if we only use these parts of the interaction matrix are spin-flip and pair-hopping terms which are $\propto J_{mm'}$ [40]. The spin-flip term of the interaction flips the spins which are anti-parallel in two different singly occupied orbitals and the pair-hopping transfers two spins of a doubly occupied orbital into an empty one. Other contributions which we neglect have more than two different orbital indices. The question if such an approximation is appropriate cannot be answered in general and I will get back to this issue in Section 3.4. It will, however, always lead to a wrong multiplet structure and thus properties of the system. Therefore ground state observables as well as certain spectral functions, which are sensitive to such level structure, have to be handled with care. The great popularity of the density-density type interaction scheme and the reason why it is still frequently used is that it does not lead to sign problems for a lot of older QMC algorithms and there are special algorithms for the CT-HYB which makes the treatment of density-density terms a lot faster as I discussed in 1.3.1.

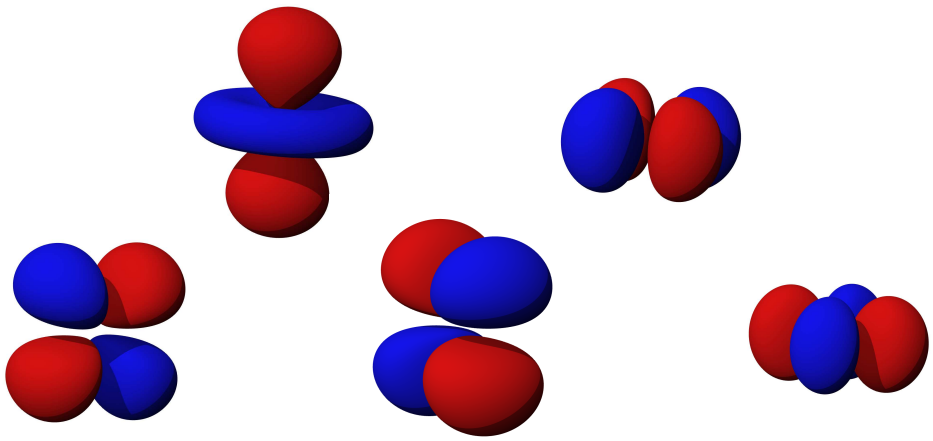

Figure 3.1.: The real valued electronic d-orbitals of principle quantum number $n = 3$. In cubic symmetry the upper two orbitals are belonging to the e_g subset consisting of the $d_{3z^2-r^2}$ and $d_{x^2-y^2}$ orbital and the lower orbitals to the t_{2g} subset consisting of d_{xy}, d_{yz} and d_{xz}. Plots of the orbitals taken from [125].

The Hamiltonian can be written in the following way in this approximation

$$H_{\mathrm{f}}^{\mathrm{d-d}} = \sum_{m} U_{mm} \hat{n}_{m\uparrow} \hat{n}_{m\downarrow} + \sum_{m \neq m'} U_{mm'} \hat{n}_{m\uparrow} \hat{n}_{m'\downarrow} + \sum_{m<m',\sigma} (U_{mm'} - J_{mm'}) \hat{n}_{m\sigma} \hat{n}_{m'\sigma} \quad (3.13)$$

or if only mean interaction values are used the more model like density-density Hamiltonian with averaged interaction strengths

$$H_{\mathrm{m}}^{\mathrm{d-d}} = U \sum_{m} \hat{n}_{m\uparrow} \hat{n}_{m\downarrow} + U' \sum_{m \neq m'} \hat{n}_{m\uparrow} \hat{n}_{m'\downarrow} + (U' - J) \sum_{m<m'\sigma} \hat{n}_{m\sigma} \hat{n}_{m'\sigma}. \quad (3.14)$$

For lattice calculations the representation of the orbitals in spherical harmonics is not suitable since, for atoms in a lattice structure, this symmetry is broken. We thus want to write the interaction into a more suitable basis, i.e. the basis of the crystal-field. For cubic lattices the basis of choice are the cubic harmonics d which can be expressed as

$$\begin{aligned}
d_{xy} &= -\frac{i}{\sqrt{2}}\left[Y_2^2 - Y_2^{-2}\right] \\
d_{yz} &= \frac{i}{\sqrt{2}}\left[Y_2^1 + Y_2^{-1}\right] \\
d_{3z^2-r^2} &= Y_2^0 \\
d_{xz} &= -\frac{1}{i\sqrt{2}}\left[Y_2^1 - Y_2^{-1}\right] \\
d_{x^2-y^2} &= \frac{1}{\sqrt{2}}\left[Y_2^2 + Y_2^{-2}\right]
\end{aligned}$$

using the complex spherical harmonics Y_{lm}. The orbitals are depicted in Fig. 3.1 where the angular part is shown. The phase of the wavefunction is depicted with the color red and blue. In an octahedral crystal-field the d_{xy}, d_{yz} and d_{xz} are split from the $d_{3z^2-r^2}$ and $d_{x^2-y^2}$. The former manifold is called t_{2g} and the latter e_g. In the H_m^{d-d} above U' is often assumed to be $U-2J$ which is exact for octahedral crystal-fields in the t_{2g} and e_g subspace.
Focusing on d-systems we introduce, similar to [40], the following quantities:

$$\begin{aligned} U_0 &= F^0 + \frac{8}{7}\frac{F^2}{14} + \frac{72}{63}\frac{F^4}{14} \\ J_1 &= \frac{6}{7}\frac{F^2}{14} + \frac{40}{63}\frac{F^4}{14} \\ J_2 &= \frac{8}{7}\frac{F^2}{14} + \frac{30}{63}\frac{F^4}{14} \\ J_3 &= 4J_1 - 3J_2 \\ J_4 &= 3J_1 - 2J_2. \end{aligned}$$

With these quantities the interaction matrices $U_{mm'}$ can be written as

$$U_{mm'} = \begin{pmatrix} U_0 & U_0-2J_1 & U_0-2J_2 & U_0-2J_1 & U_0-2J_3 \\ U_0-2J_1 & U_0 & U_0-2J_4 & U_0-2J_1 & U_0-2J_1 \\ U_0-2J_2 & U_0-2J_4 & U_0 & U_0-2J_4 & U_0-2J_2 \\ U_0-2J_1 & U_0-2J_1 & U_0-2J_4 & U_0 & U_0-2J_1 \\ U_0-2J_3 & U_0-2J_1 & U_0-2J_2 & U_0-2J_1 & U_0 \end{pmatrix} \tag{3.15}$$

The basis the matrix is written in is given by: $\left(d_{xy}, d_{yz}, d_{3z^2-r^2}, d_{xz}, d_{x^2-y^2}\right)$. One can understand which values of the $U_{mm'}$ matrix above are the same if one takes a look at the orbitals of the d-electrons in a cubic system, as shown in Fig. 3.1. The interaction between d_{xy}, d_{yz} and d_{xz} has to be the same since all of them can be transformed into each other by a rotation of $\pi/2$ around an in-plane axis, thus making the interaction in the t_{2g} manifold equivalent. The interaction between $d_{x^2-y^2}$ and d_{yz}, d_{xz} is equivalent since d_{yz} and d_{xz} can be transformed into each other by the same rotation, but d_{xy} and $d_{x^2-y^2}$ are rotated into each other by an in-plane rotation of $\pi/2$ and therefore their interaction is different. Following this argument the interaction of $d_{x^2-y^2}$ and d_{xy} with $d_{3z^2-r^2}$ is the same as is the interaction between d_{yz}, d_{xz} and $d_{3z^2-r^2}$.
The exchange interaction $J_{mm'}$ reads

$$J_{mm'} = \begin{pmatrix} U_0 & J_1 & J_2 & J_1 & J_3 \\ J_1 & U_0 & J_4 & J_1 & J_1 \\ J_2 & J_4 & U_0 & J_4 & J_2 \\ J_1 & J_1 & J_4 & U_0 & J_1 \\ J_3 & J_1 & J_2 & J_1 & U_0 \end{pmatrix} \tag{3.16}$$

and its structure can be understood in the same way as the structure of $U_{mm'}$.
The above matrices are the density-density part of the full U-matrix given by Eq. (3.1) transformed to a cubic symmetry.
The above matrices are often combined into one matrix for compactness which is given by

$$U^{\sigma\sigma'}_{mm'} = \left(\begin{array}{c|c} U_{mm'} - J_{mm'} & U_{mm'} \\ \hline U_{mm'} & U_{mm'} - J_{mm'} \end{array}\right). \tag{3.17}$$

The diagonal blocks are the spin diagonal parts and the off-diagonal blocks are the spin off-diagonal parts of the interaction matrix. As I mentioned already the interaction matrix is not spin dependent. The spin structure is only generated by the fermionic creation/annihilation operators, but the interaction can be more easily understood this way.

w2d

If one wants to use the mean density-density Hamiltonian one needs to set the parameter *Hamiltonian* to *Density* and also specify the mean values for U with the key *Udd*, U' with the key *Vdd* and J with the key *Jdd*.
If one wants to use the full interaction matrix instead of averaged values one can set the parameter *Hamiltonian* to *ReadUmatrix*. The file containing the U-matrix has to be named *u_matrix.dat*. The format of the file is: If a line starts with # the line is treated as a comment and is ignored. The first non-comment line of the file should contain the number of bands of the subspace the interaction is defined on: *nbands* BANDS. The following lines contain the non-zero elements of the interaction with the indices of the scattering event as the first four numbers/symbols, e.g. from orbital 1 $\uparrow$ and orbital 2 $\downarrow$ to orbital 1 $\downarrow$ orbital 2 $\uparrow$: 1d 2u 2d 1u *value*, where *value* is the interaction strength for this scattering event.

In the crystal-field basis one often finds quite a large splitting between certain subsets of one multiplet, e.g. $SrVO_3$, thus leading to a sufficient description of the correlated problem by only including the subset closest to the Fermi energy. We used this already in Section 2.5.1 and Section 2.7.1. There the energy splitting between the band(s) at the Fermi energy and the rest of the same multiplet is considered so large that the other orbitals can be completely neglected.
If we want to use a density-density type of description for the interaction of a subset we can simply take the related part of the interaction matrices above. Sometimes, however, we want to include additional terms to be closer to a realistic description. I will discuss one such approximation in Section 3.1.
The interaction matrices we use for the calculation are in general not going to be the

ones from a spherical symmetric problem and, most significantly, the interactions are going to be screened making their values smaller then the ones of free atoms. Especially the static monopole part is going to be heavily reduced compared to its bare value. The value of F^0, e.g., is reduced in $SrVO_3$ from 19.5 to 3.2 while J is only reduced from 1.06 to 0.85 [195]. If we want to calculate a physical system from first principle we will want to calculate the parameters from first principle. Currently there are two approaches to obtain them.
The older approach is to calculate the interaction parameters directly in LDA and was named constrained-LDA (cLDA) [128]. The interaction parameters are calculated by taking the second derivative of the total energy as a function of the density on a site without hopping. A newer approach, constrained random phase approximation (cRPA) [129], is calculating the screened interaction parameters by computing the polarization processes in the random phase approximation *outside* the downfolded subspace. Both methods are calculating the interaction matrices in a certain basis which ideally should then also be used in the DMFT calculation.

3.1. SU(2) Symmetry

Since the density-density interaction is neglecting important terms of the Coulomb interaction one is tempted to come up with another interaction including those terms again. One part of the interaction, is e.g. the spin-flip part, giving contributions to the Coulomb interaction, as already mentioned, of the order J. This is one of the candidates one would want to take into account. The general Kanamori interaction is doing exactly this. It is given by

$$\begin{aligned} H_{\mathrm{m}}^{\mathrm{GK}} = \quad & \sum_{m} U \hat{n}_{m\uparrow}\hat{n}_{m\downarrow} + \sum_{m>m'\sigma} \left[U' \hat{n}_{m\sigma}\hat{n}_{m'-\sigma} + (U'-J)\hat{n}_{m\sigma}\hat{n}_{m'\sigma}\right] \\ & - \sum_{m\neq m'} (J_x d^\dagger_{m\downarrow} d^\dagger_{m'\uparrow} d_{m'\downarrow} d_{m\uparrow} + J_p d^\dagger_{m'\uparrow} d^\dagger_{m'\downarrow} d_{m\uparrow} d_{m\downarrow} + h.c.). \end{aligned}$$

In the Hamiltonian above one can see again the terms which we already know from the density-density interaction discussed in the previous section. The additional terms, called spin-flip and pair-hopping, are flipping the directions of the spins of two electrons in different orbitals with opposite spin and transfer a pair of electrons from one orbital to another. We introduced independent parameters for the Hund's coupling J, the pair-hopping J_p and the spin-flip J_x. To see what the additional terms actually lead to we

now follow [130] and introduce the total charge, spin and orbital isospin generators

$$\begin{aligned}\hat{N} &= \sum_{m\sigma} \hat{n}_{m\sigma} \\ \hat{S} &= \frac{1}{2} \sum_{m} \sum_{\sigma\sigma'} d^{\dagger}_{m\sigma} \vec{\tau}_{\sigma\sigma'} d_{m\sigma'} \\ L_m &= i \sum_{m'm''} \sum_{\sigma} \epsilon_{mm'm''} d^{\dagger}_{m'\sigma} d_{m''\sigma}\end{aligned} \tag{3.18}$$

where $\vec{\tau}_{\sigma\sigma'}$ are the Pauli matrices. Using these we can rewrite the Kanamori Hamiltonian into

$$\begin{aligned}H^{GK}_{m} = &\frac{1}{4}(3U' - U)\hat{N}(\hat{N} - 1) + (U' - U)\vec{S}^2 + \frac{1}{2}(U' - U + J)\vec{L}^2 + (\frac{7}{4}U - \frac{7}{4}U' - J)\hat{N} \\ &+ (U' - U + J + J_P) \sum_{m \neq m'} d^{\dagger}_{m\uparrow} d^{\dagger}_{m\downarrow} d_{m'\downarrow} d_{m'\uparrow} + (J - J_x) \sum_{m \neq m'} d^{\dagger}_{m\uparrow} d_{m\downarrow} d^{\dagger}_{m'\downarrow} d_{m'\uparrow}.\end{aligned} \tag{3.19}$$

If we set $J_x = J$ and $J_p = U - U' - J$ the Hamiltonian above reduces to the first line and it obtains the full $U(1)_C \otimes SU(2)_S \otimes SO(3)_O$ symmetry for the charge C, the spin S and the orbitals O. If we now take the physical situation of the t_{2g} orbitals into account we see that the interaction integrals for a screened Coulomb interaction are given by

$$U = \int d\vec{r}\, d\vec{r}' \Phi^*_{m\sigma}(\vec{r}) \Phi^*_{m\sigma'}(\vec{r}') V_c(\vec{r}, \vec{r}') \Phi_{m\sigma'}(\vec{r}) \Phi_{m\sigma}(\vec{r}') \tag{3.20}$$

$$U' = \int d\vec{r}\, d\vec{r}' \Phi^*_{m\sigma}(\vec{r}) \Phi^*_{m'\sigma'}(\vec{r}') V_c(\vec{r}, \vec{r}') \Phi_{m\sigma'}(\vec{r}) \Phi_{m'\sigma}(\vec{r}') \tag{3.21}$$

$$J = \int d\vec{r}\, d\vec{r}' \Phi^*_{m\sigma}(\vec{r}) \Phi^*_{m'\sigma'}(\vec{r}') V_c(\vec{r}, \vec{r}') \Phi_{m'\sigma'}(\vec{r}) \Phi_{m\sigma}(\vec{r}'). \tag{3.22}$$

All the other integrals yield zero due to symmetry. In this case $J = J_x = J_p$ and we can see from Equation (3.19) that the interaction is rotationally invariant if

$$U' = U - 2J. \tag{3.23}$$

Using this we arrive at the Kanamori Hamiltonian for the t_{2g} band expressed via Equation (3.18)

$$H^{\mathrm{K_{t2g}}} = (U - 3J)\frac{\hat{N}(\hat{N} - 1)}{2} - 2J\vec{S}^2 - \frac{J}{2}\vec{L}^2 + \frac{5}{2}J\hat{N}. \tag{3.24}$$

From the definition of the $\vec{L}$ operator Equation (3.18) we can immediately see that L_z is not diagonal in this basis. Equivalently the Hamiltonian can be written in its original

form [131]

$$H_m^{\mathrm{K}} = U \sum_m \hat{n}_{m\uparrow}\hat{n}_{m\downarrow} + V \sum_{m\neq m'} \hat{n}_{m\uparrow}\hat{n}_{m'\downarrow} + (V-J) \sum_{m<m',\sigma} \hat{n}_{m,\sigma}\hat{n}_{m',\sigma} \tag{3.25}$$

$$- J \sum_{m\neq m'} d^\dagger_{m\uparrow} d_{m\downarrow} d^\dagger_{m'\downarrow} d_{m'\uparrow} + J \sum_{m\neq m'} d^\dagger_{m\uparrow} d^\dagger_{m\downarrow} d_{m'\downarrow} d_{m'\uparrow}. \tag{3.26}$$

For the t_{2g} case, if the approximation of a spherical symmetry is justified, the Kanamori parameters can be expressed via the Slater integrals by

$$U = F^0 + \frac{4}{49}F^2 + \frac{4}{49}F^4 \tag{3.27}$$

$$V = F^0 - \frac{2}{49} - \frac{4}{441}F^4 \tag{3.28}$$

$$J = \frac{3}{49}F^2 + \frac{20}{441}F^4. \tag{3.29}$$

In solids the interaction which we have to consider is the screened Coulomb interaction which in general is not spherical symmetric anymore and thus the relations above are not exact, but often the deviation is small and therefore the relations are reasonable approximations.
The situation is different [130] for the e_g orbital for which we can not define an integer numbered orbital momentum quantum number anymore since there are only two orbitals. The Kanamori Hamiltonian can be written, using the orbital isospin generator

$$\vec{T} = \frac{1}{2}\sum_\sigma d^\dagger_{m\sigma}\vec{\tau}_{mm'}d_{m'\sigma}, \tag{3.30}$$

as

$$H^{\mathrm{K_{eg}}} = (U-J)\frac{\hat{N}(\hat{N}-1)}{2} + 2J(T_x^2 + T_z^2) - J\hat{N}. \tag{3.31}$$

or again equivalently as Equation (3.26). Care has to be taken that J for the e_g orbital is given by

$$J = \frac{8}{7}\frac{F^2}{14} + \frac{30}{63}\frac{F^4}{14} \tag{3.32}$$

if we again assume that the assumption of a spherical symmetry in the lattice is justified. The Kanamori Hamiltonian is the full Coulomb interaction for the two and three band case. It however becomes an approximation if we want to do five band calculations. For such calculations the Kanamori interaction can be thought of as an intermediate approximation between the density-density and the full interaction.
In the Kanamori scheme typically a mean value for the interaction parameters is assumed and thus a Hamiltonian in the form of Equation (3.26). One can argue, similarly as for

the density-density interaction, that using the full U-matrix for the Kanamori processes is more accurate and thus an interaction in the form

$$H_{\mathrm{f}}^{\mathrm{K}} = \sum_{m} U_{mm} \hat{n}_{m\uparrow} \hat{n}_{m\downarrow} + \sum_{m \neq m'} U_{mm'} \hat{n}_{m\uparrow} \hat{n}_{m'\downarrow} + \sum_{m<m',\sigma} (U_{mm'} - J_{mm'}) \hat{n}_{m\sigma} \hat{n}_{m'\sigma} - \sum_{m \neq m'} J_{mm'} d^{\dagger}_{m\uparrow} d_{m\downarrow} d^{\dagger}_{m'\downarrow} d_{m'\uparrow} + \sum_{m \neq m'} J_{mm'} d^{\dagger}_{m\uparrow} d^{\dagger}_{m\downarrow} d_{m'\downarrow} d_{m'\uparrow} \tag{3.33}$$

should be used. We will come back to the differences of these two approximations in Section 3.4 where we will study different interactions w.r.t. the crystal-field.

w2d

If one wants to use the Kanamori interaction in its mean form one can simply specify the *Hamiltonian* to be *Kanamori* in the input file and set the mean interaction parameters *Udd*, *Vdd* and *Jdd* to the right values. Similar to defining the density-density interaction in the introduction to this chapter.

3.1.1. PS-Quantum Number

This subsection is based on the following paper:
Conserved quantities of SU(2)-invariant interactions for correlated fermions and the advantages for quantum Monte Carlo simulations.
N. Parragh, A. Toschi, K. Held and G. Sangiovanni
Phys. Rev. B **86**, 155158 (2012).

As I already mentioned in Section 1.3 a possibility to speed up calculations, when one uses an algorithm for general interactions, is to use quantum numbers which commute with the local Hamiltonian. This allows for a block diagonal representation of the Hamiltonian and thus leads to smaller matrices which can be treated with less numerical effort. Such quantum numbers, which are typically not only used in the context of calculations with CT-HYB implementations but also in ED or Lanczos calculations, are the total number of particles N_t and the total spin projection on the z-axis S_z. This already leads to a significant reduction of the block size, but for calculations with more than three orbitals the block size is already quite big with the biggest block reaching a size of 100×100 for systems with five orbitals. To further improve the performance one can try to find additional good quantum numbers for a given local interaction. In this section I am going to introduce a new additional set of good quantum numbers which we called **PS** since the idea is based on the projection of the spin in each orbital.
Already in the last section I discussed that the Kanamori Hamiltonian provides a simple extension to the density-density Hamiltonian which, by addition of spin-flip and pair-hopping terms, restores the SU(2) symmetry and leads to physics which could not be described without the additional terms. The main problem when dealing with this interaction is the need to find efficient ways to treat these additional terms. Since the segment algorithm is not suitable anymore one has to either use the matrix algorithm or the Krylov algorithm which are both sped up significantly if the block size of the local Hamiltonian is further reduced. In the Krylov algorithm, which we are using, we work in the occupation number basis. This basis is going to be denoted in the following form

$|$  $\rangle$. (3.34)

In the above formula we have color coded the singly occupied orbitals in blue and the empty/doubly-occupied orbitals in red. In this basis it can be easily seen that density-density terms of the Kanamori interaction, the first line in Equation (3.33), are diagonal and do not change the state of the system. On the other hand the spin-flip and pair-hopping terms generate off-diagonal elements in the Hamiltonian.
As I discussed in Section 3.1 the Kanamori Hamiltonian preserves the SU(2)-symmetry and thus $\vec{S}^2$ is a good quantum number. This quantum number is however not useful

for the CT-HYB since it can not be implemented in a reasonable manner as I am going to explain soon. Another well known quantity which is preserved and which one might assume could be used for this interaction is the so called seniority number which was introduced by G. Racah [88]. This quantum number counts the number of doubly occupied orbitals. It is easy to see that this is also conserved by the Kanamori interaction since the spin-flip only flips spins and the pair-hopping term transfers pairs of electrons. The problem when using the seniority as a conserved quantity to divide the Hamiltonian into blocks is the introduction of ambiguity when one applies the creation or annihilation operator to a block. Let us consider the following states in a three orbital system: $|\uparrow,\downarrow,0\rangle$ and $|\uparrow,0,\downarrow\rangle$. They both belong to the same block with the seniority number of 0. If we would now apply the creation operator $d^\dagger_{2,\uparrow}$ on the states we reach the following two states: $|\uparrow,\uparrow\downarrow,0\rangle$ and $|\uparrow,\uparrow,\downarrow\rangle$. These two states have the seniority number 1 and 0 respectively and thus the creation operator would connect the starting states which belong to one block to the end states in two different blocks. This would lead to a forking of the states which we would need to consider in the local trace and this would make the implementation difficult. A very similar argument can be made for $\vec{S}^2$ if we think of the spin singlet and spin triplet which are mixtures of $|\uparrow,\downarrow\rangle$ and $|\downarrow,\uparrow\rangle$ but which would belong to different blocks.
For the case of the Kanamori Hamiltonian we have made a crucial observation. The off-diagonal elements of the interaction never change the pattern of singly occupied orbitals. This can be quite easily understood by the following sketch

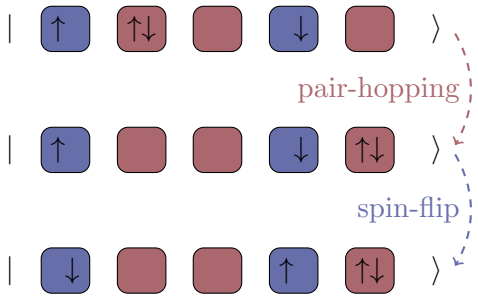

(3.35)

From this sketch it is clear that the spin-flip and pair-hopping term change only the spin orientation in singly occupied orbitals or changes doubly occupied orbitals into empty ones and vice-versa. This results in the conversation of the position of singly occupied orbitals. Thus, although the Kanamori Hamiltonian contains processes between different orbitals, for each orbital a projector onto singly occupations of this orbital (PS) commutes with the Hamiltonian. This defines a vector of operators and corresponding quantum numbers

$$\mathbf{PS} = \left\{(n_{a,\uparrow} - n_{a,\downarrow})^2\right\} \quad \text{for} \quad a = 1, ...N_{orb}. \tag{3.36}$$

If an orbital is singly occupied the term $(n_{a,\uparrow} - n_{a,\downarrow})^2$ in the equation above yields 1 whereas, if an orbital is doubly occupied or empty, the term yields 0, thus proving

	$N\ S_z$	$N\ S_z$ **PS**
N_{orb}	max/mean	max/mean
1	1/1.00	1/1.00
2	4/1.78	2/1.14
3	9/4.00	3/1.45
4	36/10.24	6/2.00
5	100/28.44	10/2.90
6	400/83.59	20/4.41
7	1225/256.00	35/6.92

Table 3.1.: A comparison of the maximal and mean block size of the Kanamori Hamiltonian using the total number of electrons, the total spin in z-direction and (on the right) the **PS** quantum number.

the projective property. The vector of quantum numbers, one for each orbital, will be denoted by **PS** henceforth. It can be thought of as a binary sequence encoding the information about the pattern of singly occupied orbitals. Something along the line of the seniority quantum number has already been previously used for calculations of the Anderson impurity model in [89].

As we show in Table 3.1 the labeling of blocks with **PS** additionally to N_t and S_z leads to a tremendous reduction of the block size of the local Hamiltonian. This of course also affects the size of the creation and annihilation operators. This is, however, not that crucial in the Krylov implementation since they are very sparse in the occupation number basis in which the calculations are performed. The important fact which makes this conserved quantity useful for implementations is that each of the blocks is only connected to one other block via a creation or annihilation operator labeled by an orbital and spin quantum number.

The most straightforward implementation of **PS**, which we also used in our code, is to introduce a label which maps the set of quantum numbers to a single number and which, in the computational context, comes naturally as $\sum_a 2^a (n_{a,\uparrow} - n_{a,\downarrow})^2$. This information is then used in our code to generate the local Hamiltonian in a block-diagonal structure. The maximum and mean block sizes of the Hamiltonian generated with **PS** are summarized in Table 3.1. This already let's us assume a huge speedup especially when dealing with a large number of orbitals if we use **PS** additionally to N_t and S_z as a conserved quantity. The block sizes, for example, of a Hamiltonian with seven orbitals are of two orders of magnitude smaller than the block size of the same Hamiltonian when the **PS** quantum number is not used. Speaking in a general manner the large reduction results form the fact that as the number of states in the Hamiltonian increase exponentially so does the size of the set of quantum numbers thus suppressing the exponential growth of the block size.

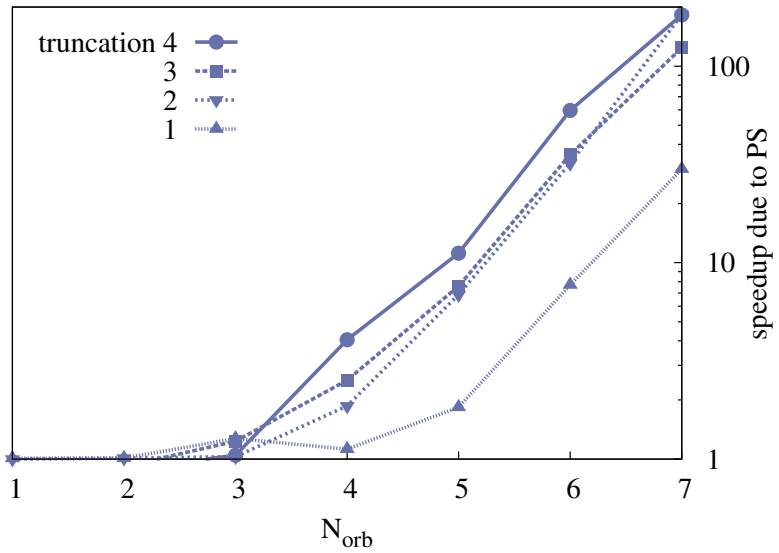

Figure 3.2.: We show the ratio of CT-HYB runtime (speedup) with and without the **PS** for otherwise identical calculations. For each calculation three independent measurements of the runtime were done and the mean value of the three calculations was taken for the plot. The error of the timing results is of the order of the symbols. The calculations were done for 4 different values of the truncation with the first one only taking into account the lowest multiplet and then progressively adding one additional multiplet. When the number of orbitals is seven the energy range covered is of the order of U.

For testing the approach with smaller block sizes and to show how big the speedup in actual calculations with the Krylov algorithm is we performed single shot simulations on an Anderson Impurity model. For the bands we used a semi-circular density of states with a half-bandwidth of $D = 2\text{eV}$. The number of bands N_{orb} was varied between 1 and 7 for this benchmark. The interaction parameters were chosen to be of intermediate strength with respect to the bandwidth of the system, namely $U = D$ and $J = 0.25$. We used a rather low temperature of $\beta = 100\text{eV}^{-1}$ to obtain traces with a sizeable amount of hybridization events. For the chemical potential we chose the half-filling condition $\mu_{HF} = (N_{orb} - 1/2)U - (N_{orb} - 1)5/2J$. This leads to time-evolutions which are often using the blocks with the biggest size of the Hamiltonian since the block of the Hamiltonian for the half-filled states is the biggest one. The calculations were performed with the same code with and without **PS** as single core jobs on an AMD machine. Since one also needs to check the convergence regarding the outer states when performing calculations we also varied the number of truncated outer states.

In Figure 3.2 we show the result of the calculations described above. To benchmark the runtime we performed three independent calculations for each set of parameters and took the mean of the three calculations. The ratio of two calculations with identical parameters except for the use of the **PS** number was then taken and plotted. In the figure one can see that for calculations with an outer truncation not restricted to the lowest multiplet, which is typically the case at room temperature, the speedup is already one order of magnitude for five band calculations and a really remarkable increase in speed is obtained for seven bands where the speedup is two orders of magnitude. This speedup makes the calculation of seven orbital systems feasible on todays computers and also allows us to go to parameter regions which were previously prohibitively expensive.

Application to an orbital-selective Mott transition

As an application to a model problem the orbital selective Mott transition was chosen. This is a physical situation which only recently was studied extensively with the rise of Anderson impurity model solvers able to treat Kanamori interactions on more than two bands. The main point of such models is to study what happens when the degeneracy of the orbitals is lifted due to a crystal field or the bandwidth of two orbitals is different due to different hopping parameters. This has the consequence that the interaction affects each orbital differently leading to new behavior.
The most pronounced effect is the orbital selective Mott phase (OSMP)[111] in which a subset of the correlated orbitals becomes localized while the others stay itinerant. One class of materials to which this concept applies are double-exchange systems like the manganites $La_{1-x}Sr_xMnO_3$ where the t_{2g} electrons form a localized spin while the e_g electrons are itinerant. The parameter which is promoting the OSMP and the associated orbital-selective Mott transition (OSMT) is the Hund's rule coupling J see e.g. [185]. As Koga at al. noted in [113, 114] there is no delocalization energy gained from an electron added in an orbital from hopping processes involving an electron in another orbital. This effectively decouples the Hubbard bands of different orbitals and the OSMT is simply the Mott transition for each individual orbital. The spins, in contrast, are best described by a double exchange model due to the scattering of the itinerant electrons on the localized ones [115, 116].
In this example to test the speedup we considered a system whose degeneracy is lifted by a crystal-field. We sketch the model system in Figure 3.3. The model consists of a central band and (an) upper band(s) whose center of mass is shifted up by Δ and (a) lower band(s) whose center of mass is shifted down by Δ. The number of lower bands and upper bands was varied from one to three thus resulting in a model with up to seven correlated bands. The bandwidth of each band was set to $2D$ with D being half the bandwidth and the crystal field parameter $\Delta = 0.7D$. The local interaction of the Hubbard model was constructed using the Kanamori Hamiltonian which is SU(2)

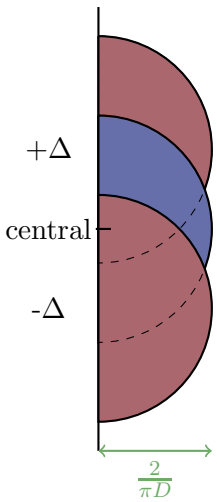

Figure 3.3.: The model used to study the orbital selective Mott transition. The model consists of three to seven bands. There is always a central band present and one up to three bands shifted up/down by Δ. The maximum of the density of states is given by $\frac{2}{\pi D}$.

symmetric as I discussed in Section 3.1. In this model we assumed a cubic symmetry thus resulting in only two independent interaction parameters. The parameter U/D which was varied to obtain the OSMT and the Hund's coupling parameter J which was set to $J = 0.25U$. The inverse temperature was set to $\beta D = 100$ for all calculations. All calculations were performed at truncation= 1. The stability of the results was confirmed by redoing calculations with more multiplets included.
Previous studies of the OSMT mostly used models with two or three correlated orbitals. In this study we want to study the robustness of the OSMT when more orbitals are involved. To this end we set the number of orbitals to $N_{orb} = 3, 5$ and 7. The only studies we know of which already took into account more than three orbitals were the ones of [117] and [46]. Both considered different models than the one we use here. The first one was treating the interaction with a slave-spin mean-field solver and the latter only considered the filling-driven OSMT.

The results we obtained are shown in Figure 3.4. We compared the values for the $N_{orb} = 3$ calculation with the ones reported in the literature [118] which are in very good agreement. The OSMT is stable to the addition of more orbitals, but the coexistence region where the central band is already insulating and the shifted bands are still metallic is shrinking when more bands are included. The quantity we examined and also plotted in Figure 3.4 is the spectral weight at the Fermi energy which can be easily obtained

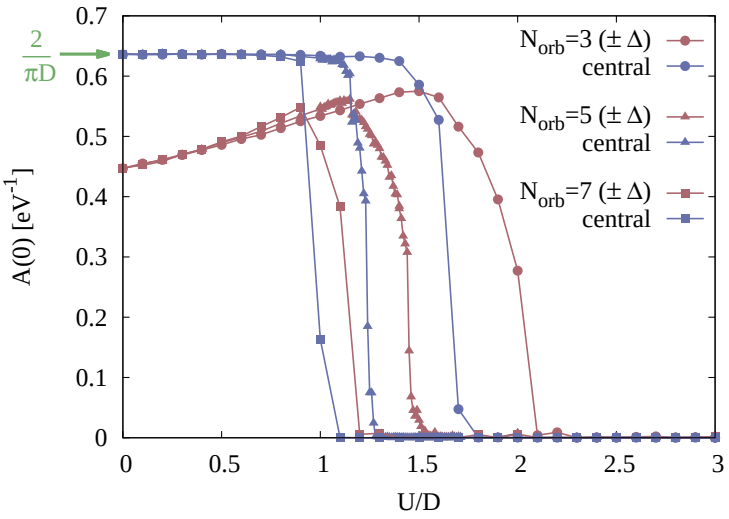

Figure 3.4.: The spectral weight of the bands at the Fermi energy calculated via the value of $G(\tau = \beta/2)$. In the case of the central band one can see that the value is fixed to the one of the non-interacting case $\frac{2}{\pi D}$

from the Greens function in imaginary time τ. The correspondence is given by $A(0) = \frac{\beta}{\pi} G(\tau = \beta/2)$.
The shrinking of the coexistence region of an insulting central band and metallic shifted bands when more bands are added to the model is a consequence of the Hund's coupling J. In calculations where $J = 0$ the opposite effect would have been observed since the mobility of the electrons is increased due to the added orbitals and thus the critical value for U to reach an insulating state would have increased. This effect, however, is counteracted by the Hund's coupling which suppresses orbital fluctuations and thus increases the insulating region. This observation is consistent with the findings in [118, 119, 120].

Conclusion

In conclusion we found a new invariant for SU(2)-symmetric Kanamori Hamiltonians, i.e. the pattern of the single occupation of each orbital. Using this invariant we defined a label which leads to very small blocks of matrices. As a consequence there is a large speed up when dealing with correlated systems in CT-HYB of up to two orders of magnitude for the parameter region in this study. This opens new possibilities for studying systems comfortably which were previously computationally very demanding. As an application we studied the OSMT at half-filling of a model with one central band and could show

that it exists up to seven orbitals. We could ascribe the shrinking of the coexistence region to the presence of a large J. Although the Kanamori Hamiltonian already includes the largest contributions of the full Slater parametrized Coulomb interaction a study of systems with the full interaction is critical in order to know how big the additional contributions really are. Such a study, which takes the full Hamiltonian into account, would benefit immensely if similar conserved quantities could be found. In Section 3.3 I will discuss this issue. A material for which a full five band description is crucial is Co for which I am going to present a study in the next section.

3.2. Cobalt Oxygen Compounds

After many decades of studying the diverse cobalt oxygen compounds some answers to basic questions regarding these materials are still elusive. The materials exhibit some of the most fascinating phenomena in solid state physics like: metal-insulator transition [206], large magneto resistance [207], super conductivity [208] and various kinds of magnetic ordering [209, 210].
The reason why the cobalt oxygen compounds have such a wide variety of possible phases is due to the multitude of valence states the cobalt atom in a compound can realize [132]. Possible valence electrons states are Co^{2+} up to Co^{4+} ions. Furthermore the energy of the low-spin state, which is the state with a minimum $\vec{S}^2$, the high-spin state, the state with a maximum $\vec{S}^2$, which is also the ground state in a free ion due to Hund's rule, and the intermediate state, which is somewhere between the high and low spin state, are almost degenerate in some systems. This generates the peculiar magnetic transitions mentioned above. These different spin states for the various valences are depicted in Figure 3.5. In $LaCoO_3$, e.g., the thermal mixing of the non-magnetic ground state and the magnetic first excited state leads to an entropy-driven transition from a non-magnetic to a magnetic state of Co^{3+}. These materials therefore are one of the prime examples of a competition between the crystal-field splitting versus Hund's exchange, which makes a study with a realistic interaction necessary as was pointed out in [132].
Since the important quantity which needs to be calculated, the local state of the correlated atoms, can be measured in CT-HYB, studies were done for the cobalt oxygen compounds in e.g. [133, 95]. One can measure the site-reduced density matrix which I already mentioned in 1.4 or the more involved object, its time resolved relative, the imaginary time state-state correlation matrix $C_{AB}(\tau)$ [133]

$$C_{AB}(\tau) = \langle \hat{P}_A(\tau)\hat{P}_B(0)\rangle \tag{3.37}$$

where $\hat{P}_A = |A\rangle \langle A|$ is the state resolved density matrix with $|A\rangle$ a many-body state in the Fock space. The weight of the density matrix is simply how probable it is that the system is in a certain state during the simulation, which gives the important information of the probability to find the system in a certain local state. However it makes it impossible to

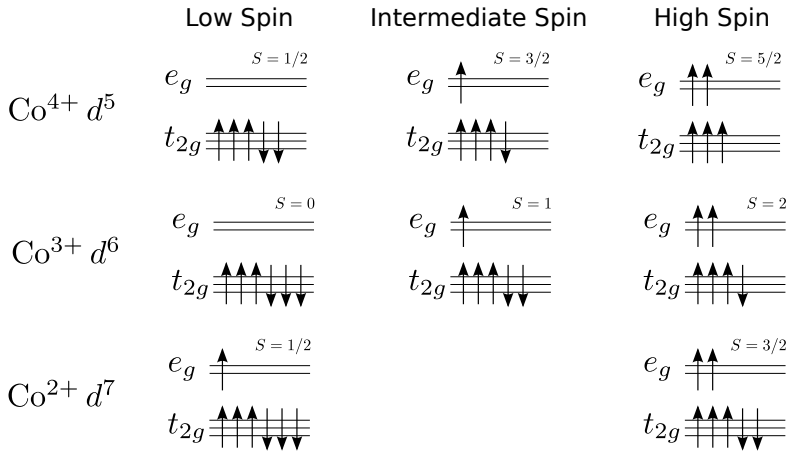

Figure 3.5.: The possible valences and spin states of the Co ion in the octahedral crystal-field. The d-shell is split into the t_{2g} and e_g subshells.

distinguish between thermal fluctuations and imaginary time evolution between states. If one looks at the time resolved quantity, however, the off-diagonal elements are an indication how probable the transition between any of the states due to imaginary time evolution is. In the following study the magnetic ground state of $SrCoO_3$ is investigated.

3.2.1. $SrCoO_3$

This subsection is based on the following paper:
Spin State of Negative Charge-Transfer Material $SrCoO_3$

J. Kuneš, V. Křápek, **N.Parragh**, G. Sangiovanni, A. Toschi and A. V. Kozhevnikov

Phys. Rev. Let. **109**, 117206 (2012).

The cobalt oxygen compounds are, as I mentioned before, very well studied, but the spin ground state of the Co atom in the compound is not yet clarified. An example for a cobalt oxygen compound with a very interesting magnetic behavior is $La_{1-x}Sr_xO_3$. The undoped compound is a non-magnetic insulator and it turns into a spin-glass for low doping [176]. For higher doping the system is a ferromagnetic metal and stays this way up to stochiometric $SrCoO_3$. When the system is doped the valence states of the Co atoms change from Co^{3+} to Co^{4+}. For the $SrCoO_3$ compound an intermediate spin state (IS) was suggested as the ground state [174, 175] based on work by Goodenough [177]. Although this state can never be stabilized in an isolated ion it could be stabilized by the covalent Co-O binding. In the current work we want to investigate the local state of the Co atom in the paramagnetic phase (PM) by means of LDA+DMFT. While in the original work [95] also the ferromagnetic phase was studied I am going to focus on the paramagnetic phase since in this phase a comparison of two local interactions, $H_f^{\mathrm{d-d}}$, Equation (3.13), and H_m^{K}, Equation (3.26), was performed.
The study was conducted starting from first principle calculations performed with the Wien2K [149] density functional code. The converged bandstructure was then projected onto a Wannier function basis spanning the Co-d and O-p bands. I outlined the general principles of this method in Section 2.4. The interaction parameters were calculated using the constrained random-phase approximation [129]. In this calculation the proposal in [178] to screen the bare Coulomb interaction by a reduced polarization, which does not contain transitions between O-p and Co-d bands, was used. The mean unscreened values for the interaction are $U = 10.83$eV and $J = 0.76$eV. These values are used throughout this study to generate the density-density and mean Kanamori interaction introduced in Chapter 3. The self-consistency scheme as outlined in Section 2.5 was then used to include interactions. We performed the calculations with the double-counting correction defined by Equation (2.30). The density-density interaction calculations were performed using a segment-algorithm code [179] while the SU(2) symmetric calculations were carried out using *w2dynamics*.

The self-consistently determined self-energy is shown in Figure 3.6(c),(d). For the density-density interaction the self-energy was analytically continued to the real-axis as outlined in Section 2.6. The impact of the Kanamori approximation on the self-

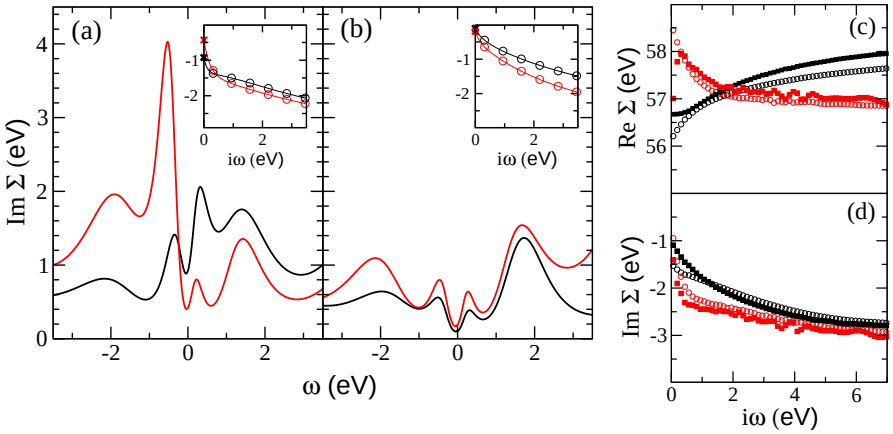

Figure 3.6.: On the left a comparison of the imaginary part of the self-energy on the real axis between the paramagnetic and the ferromagnetic phase at $T = 1160$K. The t_{2g} self-energy is plotted in red and the e_g self-energy is plotted in black (for the FM phase only the minority t_{2g} and majority e_g are shown). The inset shows the same on the Matsubara axis. On the right a comparison of the self-energies of the H_f^{d-d} (open circles) and the H_m^K (filled squares) at $T = 232$K. Taken from [95].

consistently determined self-energy is illustrated in the right plot of Figure 3.6. The self-energies were calculated at $T = 232$K a temperature regime in which differences coming from the different local interactions should be well pronounced. The general agreement of the self-energies is rather good, although at Matsubara frequencies close to zero a deviation of the density-density self-energies from the Kanamori self-energies can be seen. The extrapolation of the e_g self-energy to zero (black color in the plot) indicates that the e_g electrons are more strongly scattered at the Co atom for the case of the density-density interaction. This is reasonable if we consider that the density-density interaction describes electrons with an Ising like spin while the SU(2)-symmetric interaction describes electrons with a Heisenberg like spin. The Ising spin is more rigid and thus leads to a stronger scattering as was already found in studies of the two-band Hubbard model [180].

To study the local state of the Co atoms the CT-HYB is the ideal method. Usually one either considers the $\vec{k}$-space to study the itinerant properties of the electrons or one switches to real space to describe the physics of the localized electrons. We are using the already introduced reduced density matrix operator Equation (1.60) for the interacting atom to quantify how much time an atom spends in a specific many-body state. If we sum over the diagonal contributions of a certain occupancy we obtain the statistics for

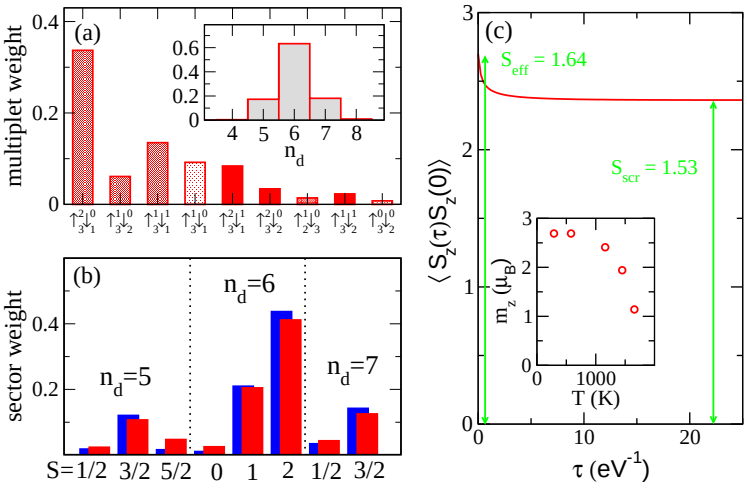

Figure 3.7.: In the upper left panel the dominant multiplets for the density-density interaction. In the inset weights of the configurations d^4, d^5, d^6, d^7, d^8 at $T = 232$K. In (b) the weights of the interactions H_f^{d-d} (red) and H_m^K (blue) are compared for different charge and spin sectors. In (c) the local spin-spin correlation function for H_f^{d-d} and in the inset the temperature dependence of the local moment on Co in the FM phase. Taken from [95].

the valence states (d^5, d^6,...) which we show in Figure 3.7(a) for the density-density interaction. Additionally the atomic multiplets with the largest weights are shown, also only for the density-density interaction. Since the multiplets are different for the SU(2)-symmetric interaction a direct comparison cannot be done. Contrary as to what is expected from chemical intuition the state with the highest probability is the d^6 configuration and not the Co^{4+} state. The configurations d^5 and d^7 are almost equally often visited which is consistent with a metallic behavior [181, 182]. For a comparison between the density-density interaction and the SU(2)-symmetric interaction, for reasons given above, a direct comparison of the multiplet weights is not possible. A quantity which we can, however, compare are the weights of sectors labeled by total number of electrons and total spin. A measure of the spin for the density-density interaction is given by $|S_z|$ while the total spin for the Kanamori interaction is $S = \sqrt{S_x^2 + S_y^2 + S_z^2}$. We calculated the weight by first rotating the site-reduced density matrix into the eigenbasis of $\vec{S}^2$ and then summing the weights of the different eigenstates corresponding to a set of quantum numbers. The result is shown in Figure 3.7(b) and the two are in good agreement. This justifies to use quantities from the density-density interaction calculation, which are prohibitively expensive to measure with the Kanamori interaction. This good agreement is probably due to the fact that the main contribution of the high-spin state is captured

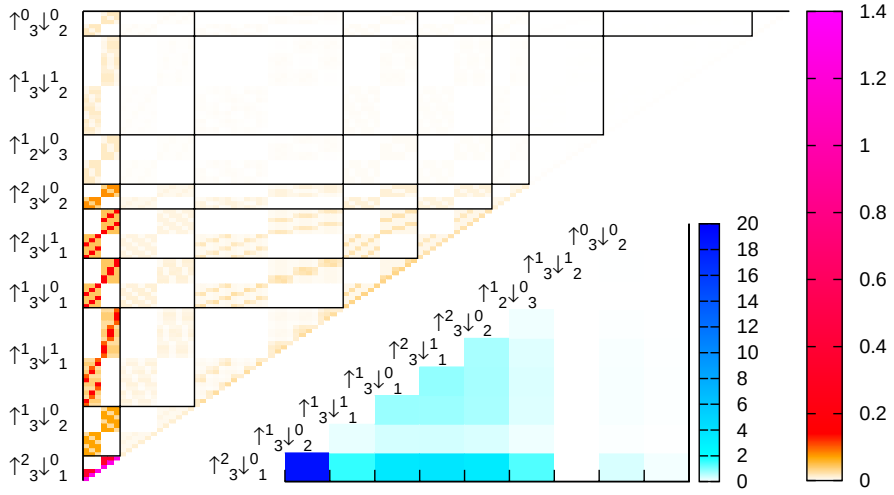

Figure 3.8.: Depicted are the matrix Π_{AB} for configurations shown in Figure 3.7 at $T = 232$K state-by-state (upper left) and its contribution to the spin susceptibility resolved by multiplet pairs (lower right). Taken from [95].

by both local interactions. The good agreement for the state weights, should, however, not be seen as a guarantee that all observables show similar behavior in both approximations. We would expect differences especially for quantities to which the multiplets contribute differently, which, e.g., is the FM T_c. Studies show that the density-density interaction overestimates T_c systematically [183].
Next we want to take a look at the origin of the local moments. To this end we calculate the local spin susceptibility. The susceptibility is shown in Figure 3.7(c) for the density-density interaction. The flattening out after the initial decay is indicative for the local moment behavior. The instantaneous magnetic moment of the two calculations were calculated by $\langle S_z^2 \rangle_{DD} = S_{eff}^2$ and $\langle S^2 \rangle_{SU(2)} = S_{eff}(S_{eff}+1)$. The effective moment S_{eff} of the density-density interaction is given by ≈ 1.64 and the effective moment of the SU(2)-symmetric interaction by ≈ 1.61. For the density-density interaction we can also calculate the PM moment of the Co atom by $S_{scr} = \langle S_z(\beta/2)S_z(0)\rangle$, which yields $3.06\mu_B$. This is very close to the saturated moment on the Co atom in the FM phase, $2.7\mu_B$ as well as to the LSDA value of $2.58\mu_B$, which were calculated in the original study, and also the experimental saturation magnetization of $2.5\mu_B$ [184].

We can then ask the question if the PM moment is associated with a particular multiplet or to multiplets, if it has a fractional value, thereby interpreting it as a mixture of the contributions of different multiplets. Let us note that it is not always possible to express the susceptibility as a sum of contributions of different multiplets. To show this[133]

we take the imaginary time state-state correlation matrix $C_{AB}(\tau)$ from Equation (3.37) and define the time integrated quantity

$$\Pi_{AB} = \int_0^\beta d\tau \, C_{AB}(\tau). \tag{3.38}$$

Using this we can express the spin susceptibility in the paramagnetic state as

$$\chi = \int_0^\beta d\tau \, \langle m_z(\tau) m_z(0) \rangle \tag{3.39}$$

$$= \sum_{A,B} m_z(A) m_z(B) \Pi_{AB}, \tag{3.40}$$

where A and B run over all atomic many-body states. The sum above can only be divided into a sum over individual multiplets if the matrix Π_{AB} is diagonal. A trivial example is an isolated atom for which Π_{AB} is diagonal in the basis of atomic eigenstates. The state correlation matrix Π_{AB} for the density-density interaction is shown in Figure 3.8 for the multiplets with the largest weights. The part of the state correlation matrix we show contains 70% of the total weight. In each black rectangle we can see a block structure. This structure is due to the fact that only for states with the same spin orientation sizable off-diagonal elements exist. There does not seem to be another apparent block structure and we thus conclude that essentially all other states are connected by evolution in imaginary time. Therefore we come to the conclusion that the system is not in a mixed state of HS and IS. In the lower right panel of Figure 3.8 we show the contributions of the multiplet pairs to the spin susceptibility. The most dominant contribution comes from the HS-HS pair with a contribution of 23%, with sizeable contributions coming from other blocks.

In contrast to earlier studies, e.g. [174, 175] we want to state that we used first principle calculations and focused on qualitative aspects. These previous studies claimed that the IS state dominates the ground state of $SrCoO_3$. In the study by Zhuang *et al.* [175] the unrestricted Hartree-Fock method was used and therefore quantum and thermal fluctuations could not be accounted for, which makes our study a systematic improvement. Potze *et al.* [174] on the other hand used ED calculations on a small cluster. They found an IS cluster ground state which can be visualized by a d^6 atomic HS state on Co, similar to our result, with an antiferromagnetically oriented ligand hole. In their calculation the formation of a bound $d^6\underline{L}$ is inevitable, since in the cluster the ligand hole has only one Co partner and it is thus strongly correlated with it. This model certainly exaggerates the correlation and the Co-O correlation in a metal might be different. In our calculations the correlations between the Co and the ligand are only taken into account in a mean-field way, i.e. the Co atom senses the same average environment with $\approx 1/3$ O holes per ligand irrespective of its own instantaneous state.

As a concluding remark we want to state that our findings of a dominant d^6 HS state

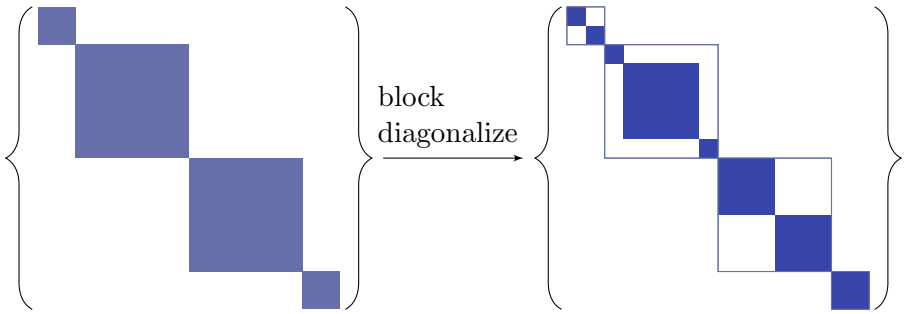

Figure 3.9.: The first step of the algorithm consists of reducing the matrix of the local Hamiltonian, which is already written in a block diagonal form with the help of N and S_z, to its minimal block diagonal form.

are in agreement with x-ray absorption experiments [174]. The long-time properties are affected by the evolution in imaginary time connecting different multiplets, therefore no conclusions can be made from the multiplet weights. Similar to the findings in $LaCoO_3$ [133] we would expect to obtain definable LS, IS and HS states if the system would be insulating. The comparison of the density-density calculations with the SU(2)-symmetric calculations showed a quite good agreement with only small quantitative differences and we can thus conclude that the Kanamori interaction does not have a strong influence on the local spin state in $SrCoO_3$.

3.3. Generating the Minimal Block Size

As I already mentioned it is important to find the minimal block diagonal structure of the local Hamiltonian especially when we want to treat systems with many correlated orbitals. Simply finding the block diagonal structure, however, is not enough. The structure of the Hamiltonian also has to obey the following second rule. Any creation or annihilation operator acting on one block of the Hamiltonian can only connect this block to one other block. Otherwise we would need to keep track of forking processes which would make the implementation of the CT-HYB algorithm cumbersome. As I already mentioned in Section 3.1.1 this is the case for the seniority quantum number which thus cannot be used in CT-HYB calculations.

It is very hard to find good quantum numbers based on symmetries for general interactions. Already for the full Coulomb interaction in the cubic basis it is very difficult except for the obvious choices of N and S_z. So in a general system a brute force approach to tackle this problem might be a good idea. In this section I will present one possible

implementation of such a brute force attempt and I will also show which impact the minimal block diagonal structure of the Hamiltonian has on the block size for a cubic system with Coulomb interaction.
As a starting point I will use a Hamiltonian which is already block diagonalized using N and S_z, the total number of electrons and the total spin in z-direction, as good quantum numbers. This is not really a prerequisite but it increases the speed of the brute force block diagonalization considerably. As a first step the Hamiltonian is fully block diagonalized. The general idea behind the following code is to find the connected entries of a matrix:

```
blocks.append(block(diags.pop))

for block in blocks
  for diag in block.diags
    for offdiag in diag.offdiags
      if offdiag.diag not in block
        block.append(offdiag.diag)
        diags.remove(offdiag.diag)
      end if
    end for offdiag
  end for diag
  if diags is empty
    done
  else
    blocks.append(block(diags.pop))
  end if
end for block
```

where diag is a diagonal element of the Hamiltonian and offdiag is an off-diagonal element. In the first line I create a new block object consisting of one diagonal element which I pop from the list of all diags, i.e. all diagonal elements of the Hamiltonian, and append it to the list of all blocks. Then I cycle over all blocks, in the first step consisting of the one element. Then I cycle over all the diagonal elements in this block and over all offdiagonals belonging to this diagonal. Then all the diagonals connected via the offdiagonals are added to the current block if they are not already contained in the block and the diagonals are removed from the list of all diagonal elements. I then check if the list of diagonals is empty, if it is then I am done otherwise I create a new block with the first element in the list of diagonals.

The above algorithm is applied to each block diagonal part of the Hamiltonian which was generated with the quantum numbers N and S_z. After this the Hamiltonian is completely block diagonal but it does not satisfy the condition that each operator only

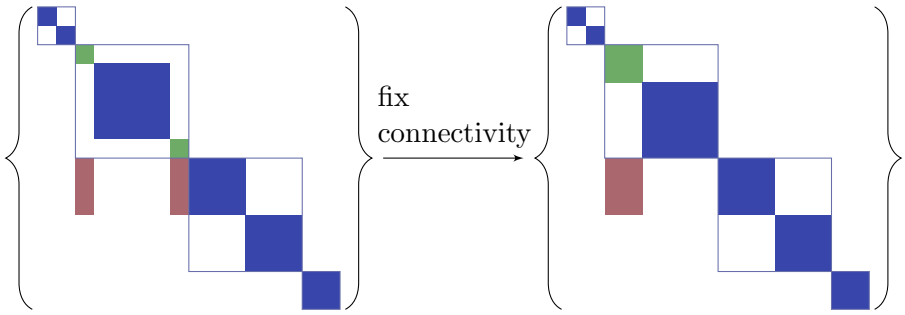

Figure 3.10.: In the second step of the algorithm the connectivity of all blocks due to all creation/annihilation operators is fixed.

connects one block with one other block yet. To achieve this we use the following algorithm:

```
while change
  change = false
  for index in operator.indices
    generate(index.blocks.connects)
    for block in blocks
      for connect1 in index.block.connects
        for connect2 in index.block.connects
          if connect1.block != connect2.block and connect1 != connect2 then
    blocks.append(block(connect1.block, connect2.block))
    blocks.remove(connect1.block)
    blocks.remove(connect2.block)
    change = true
    cycle index loop
  end if
end for connect1
      end for connect2
    end for block
  end for index
end while
```

In the first loop I cycle over the indices of the creation/annihilation operators, i.e. the band, spin and creation/annihilation numbers. Then I generate the information which block is connected to which other block via this operator. The next loop cycles over all blocks, then a loop twice over all connections this block has to other blocks is performed. Then we need to check if one block is connected to more than one other block via the

		$N\ S_z$	minimal
N_{orb}	interaction	max/mean	max/mean
5	Density	100/28.44	1/1.
5	Kanamori	100/28.44	10/2.90
5	Coulomb	100/28.44	28/7.816

Table 3.2.: A comparison of the maximal and mean block size of different interactions using the total number of electrons N, the total spin in z-direction S_z and the minimal block size generated with the algorithm presented in this section.

operator specified by index. If this is the case the two blocks are joined to one block and the loop over indices needs to be redone and the information which operator connects which blocks needs to be rebuilt. The whole loop is reiterated until there is no change anymore.
With these two steps we obtain a Hamiltonian which is in the minimal form usable for a CT-HYB calculation. The impact this has is still sizable if we compare it to only using N and S_z for the full Coulomb Hamiltonian on five correlated bands as can be seen in Table 3.2. For the density-density interaction the algorithm finds the expected block size of one since this interaction does not contain off-diagonal elements since the occupation number basis is the eigenbasis of this interaction. For the Kanamori interaction the block size is the same as with the PS quantum number I introduced in Section 3.1.1. Thus the PS quantum number already yields the optimal structure. For the Coulomb interaction in the cubic crystal-field the biggest block is reduced by a factor of ≈ 4 and also the mean block size is reduced by a similar factor. We thus expect that the calculation time for the Coulomb interaction is reduced by a similar factor, based on the benchmarks we performed for the Kanamori interaction in Section 3.1.1.

w2d

To use the algorithm for calculating the minimal block structure one has to set the parameter *QuantumNumbers* to *All*.

3.4. Comparison of interactions in octahedral crystal-fields

(In Section 3.2.1 we already briefly mentioned that the approximation of the local interaction can have an influence on the physical properties of the system. One of the most well known influences is the one on the local spin which is more rigid when a density-density interaction is used than when the local interaction is described by the SU(2)-symmetric Kanamori Hamiltonian [180]. In this part of my thesis I am going to

discuss the different types of the local interaction with the help of the Tanabe-Sugano diagrams [126]. The Tanabe-Sugano diagrams where introduced in 1954 by Tanabe and Sugano to study the absorption spectra of complex ions in an octahedral crystal-field. In these diagrams the energy of the multiplets is plotted over the crystal-field and the energy of the ground state is always taken to be zero. These diagrams enable us to study the high-spin low-spin transition in the interactions which I introduced in the introduction of Chapter 3 and Section 3.1. In the Tanabe-Sugano diagrams both the energies and the crystal-field are plotted in units of the Racah parameter B [211] which is a measure for the energy scale of the multiplet splitting and therefore the diagrams are applicable to all interactions with a similar relation between F_2 and F_4. This ratio is set to $F^4 = {}^5/_8 F^2$ for reasons explained in the introduction of this chapter.
In this study we are going to assume that the multiplet structure of the Coulomb interaction is not violated, i.e. we assume that the spherical symmetry is retained in the crystal-field of the solid. Thus the Coulomb interaction is treated as giving us the right degeneracies and energies and we will check the approximations of the interactions for deviations to the result of the Coulomb interaction. In realistic calculations of the U-matrix via cRPA calculations it can be seen that this is not completely the case [191]. Thus the degeneracy of interactions in realistic compounds would be different than the one we observe in the diagrams below, but the general argument that the disregard of certain processes in the interaction leads to different degeneracies of the multiplets, which are presented below, is still valid. The generation of the minimal block diagonal structure presented in Section 3.3 can be used for arbitrary interaction matrices. If interaction matrices are used a check for very small elements, in relation to other elements, is useful. If these elements are set to zero more symmetries of the interaction can be exploited by the algorithm presented in section 3.3 and thus the calculation time can be improved.
The interaction parameters which we are going to use in this section are given by $F_0 = 4$, $F_2 = 8.615$ and $F_4 = 5.3846$. These are reasonable parameters for a transition metal compound. The interaction values lead to the Racah parameter $B = 0.114766$, which is calculated by the relation $B = 1/49 F_2 - 5/441 F_4$. We are going to use it for the construction of the Tanabe-Sugano diagrams . The other two Racah parameters are related to the Slater integrals by $A = F_0 - 49/441 F_4$ and $C = 35/441 F_4$.
The major difference of the interactions in a five band system with and without crystal-field can be seen in Table 3.3 and Table 3.4 and also in the Tanabe-Sugano diagrams which I show after the tables. We are comparing the interactions of the full Coulomb H^{C}, Equation (3.9), rotated into the crystal-field basis, the Kanamori, with averaged interaction parameters H_f^{K}, Equation (3.26), and with the full interaction matrix H_f^{K}, Equation (3.33), and the density-density type, with averaged interaction parameters $H_m^{\mathrm{d-d}}$, Equation (3.14), and with the full interaction matrix $H_f^{\mathrm{d-d}}$, Equation (3.13). One can see in Table 3.3 that already without a crystal-field the ground-state degeneracy between the t_{2g} and e_g states is lifted for the interactions with the full U-matrix. If

we focus on the H_f^k interaction there are only 6 different states with the lowest energy which can be associated with the fully occupied e_g orbital and an e_g-t_{2g} mixed state. This can be quite easily seen from Figure 3.11. The ground state energy at zero crystal-field splits into two degenerate states when the crystal-field is turned on. The one with the largest derivative w.r.t. to the crystal-field which is given by 2Δ can be identified with the state with two electrons in the e_g while the other derivative w.r.t. to the crystal-field is given by Δ and it can be identified as a state with an electron in the e_g and an electron in the t_{2g}. On can also see from Table 3.3 and Table 3.4 that the degeneracy of the states is never the same as for the Coulomb interaction which we assumed to be closest to a realistic interaction in a compound. Thus quantities which depend on the degeneracy of the multiplets as e.g. the entropy or the thermal conductance might not be accurately predicted by any of the approximations of the full interaction.
As I already mentioned in Section 3.2.1 another quantity which can be quite sensible to the multiplicity is the magnetic transition temperature. In Section 3.2.1 we also compared the local spin of two different interactions, namely the H_f^{d-d} and the H_m^K, and we saw that the magnetic moment is almost the same, 1.64 and 1.61 respectively. We attributed this to the fact that with both interactions and the value of the crystal-field present in the compound $SrCoO_3$ the interactions are on the same side of the high spin low spin transition. The local atomic multiplets are of course only half of the picture since the hybridization of the bath allows for hoppings to different energetically excited states with a probability which cannot be a priori predicted from the atomic multiplets alone. The finding of this study indicates that the local magnetic moment can be quite accurately calculated even within the density-density approximation of the local interaction as long as the local interaction is far aways from the the HS-LS transition.
The crystal-field at which the HS-LS transition occurs is in very good agreement between the H^C and H_f^K for d^4, d^5, d^6 and d^7 which can be seen from the point were the ground state changes in the Figure 3.14, Figure 3.15, Figure 3.16 and Figure 3.17. This leads us to the conclusion that the H_f^K would be the approximation of choice when the simulation is mostly visiting these local states and the crystal-field value of the studied system is close to the transition.
For a crystal-field close to zero the interactions using the full U-matrix show a very peculiar behavior. For such crystal-fields the degeneracy of the e_g and t_{2g} multiplets is lifted which is obviously unphysical. The reason for this lifting of the degeneracy can be easily understood if we take as an example the d^2 configuration. Using this configuration and the interaction matrices Equation (3.15) and Equation (3.16) we can easily calculate the interaction which is different in the t_{2g} and e_g manifold but also between the e_g and t_{2g} manifolds. This means that whenever the crystal-field of a system is small compared to the interaction parameters the application of the full U-matrix in the Kanamori and density-density approximation might lead to wrong results. We assume that even the occupancies of the t_{2g} and e_g manifolds is then wrongly predicted by the calculations.
In conclusion one is always best advised to use the full interaction matrix with all pos-

sible local processes, but if the computational effort does not allow this the right choice of the interaction is of importance and the Tanabe-Sugano diagrams presented in this section can help in this decision. In the future a systematic study of the different interactions in the context of DMFT can lead to a better judgment of the applicability of the different interaction approximations in different parameter regimes. This can be of enormous help since, even though the current implementation of the CT-HYB is the most suitable for many orbital systems and general interactions, five orbital calculations with full interaction are still computationally very demanding.

H^C	ε	$\vec{S}^2$	$\vec{L}$	H_f^K	ε	$\vec{S}^2$	H_m^K	ε	$\vec{S}^2$	H_f^{d-d}	ε	$\lvert S_z\rvert$	H_m^{d-d}	ε	$\lvert S_z\rvert$
2.484		2	F	2.484		2	3.000		2	2.484		1	3.000		1
2.484		2	F	2.484		2	3.000		2	2.484		1	3.000		1
2.484		2	F	2.484		2	3.000		2	2.484		1	3.000		1
2.484		2	F	2.484		2	3.000		2	2.484		1	3.000		1
2.484		2	F	2.484		2	3.000		2	2.828		1	3.000		1
2.484		2	F	2.484		2	3.000		2	2.828		1	3.000		1
2.484		2	F	2.828		2	3.000		2	2.828		1	3.000		1
2.484		2	F	2.828		2	3.000		2	2.828		1	3.000		1
2.484		2	F	2.828		2	3.000		2	2.828		1	3.000		1
2.484		2	F	2.828		2	3.000		2	2.828		1	3.000		1
2.484		2	F	2.828		2	3.000		2	2.828		1	3.000		1
2.484		2	F	2.828		2	3.000		2	2.828		1	3.000		1
2.484		2	F	2.828		2	3.000		2	2.828		1	3.000		1
2.484		2	F	2.828		2	3.000		2	3.370		0	3.000		1
2.484		2	F	2.828		2	3.000		2	3.370		0	3.000		1
2.484		2	F	2.828		2	3.000		2	3.370		0	3.000		1
2.484		2	F	2.828		2	3.000		2	3.370		0	3.000		1
2.484		2	F	2.828		2	3.000		2	3.516		1	3.000		1
2.484		2	F	2.828		2	3.000		2	3.516		1	3.000		1
2.484		2	F	2.828		2	3.000		2	3.516		1	3.714		0
3.912		0	D	3.516		2	3.000		2	3.516		1	3.714		0
3.912		0	D	3.516		2	3.000		2	3.600		0	3.714		0
3.912		0	D	3.516		2	3.000		2	3.600		0	3.714		0
3.912		0	D	3.516		2	3.000		2	3.600		0	3.714		0
3.912		0	D	3.516		2	3.000		2	3.600		0	3.714		0
4.205		2	P	3.516		2	3.000		2	3.600		0	3.714		0
4.205		2	P	3.861		2	3.000		2	3.600		0	3.714		0
4.205		2	P	3.861		2	3.000		2	3.600		0	3.714		0
4.205		2	P	3.861		2	3.000		2	3.600		0	3.714		0
4.205		2	P	3.912		0	4.429		0	3.600		0	3.714		0
4.205		2	P	4.256		0	4.429		0	3.600		0	3.714		0
4.205		2	P	4.256		0	4.429		0	3.861		1	3.714		0
4.205		2	P	4.371		0	4.429		0	3.861		1	3.714		0
4.205		2	P	4.371		0	4.429		0	4.059		0	3.714		0
4.715		0	G	4.371		0	4.429		0	4.059		0	3.714		0
4.715		0	G	4.371		0	4.429		0	4.059		0	3.714		0
4.715		0	G	4.371		0	4.429		0	4.059		0	3.714		0
4.715		0	G	4.371		0	4.429		0	4.288		0	3.714		0
4.715		0	G	4.601		0	4.429		0	4.288		0	3.714		0
4.715		0	G	4.601		0	4.429		0	5.143		0	5.143		0
4.715		0	G	4.715		0	4.429		0	5.143		0	5.143		0
4.715		0	G	4.715		0	4.429		0	5.143		0	5.143		0
4.715		0	G	4.715		0	4.429		0	5.143		0	5.143		0
8.000		0	S	8.000		0	8.000		0	5.143		0	5.143		0

Table 3.3.: The eigenergies, spin quantum number, $\vec{S}^2$ for Coulomb and Kanamori and $|S_z|$ for density-density, and orbital angular momentum quantum number $\vec{L}^2$, for the Coulomb interaction, for 2 electrons.

H^C	ε	$\vec{S}^2$	H_f^K	ε	$\vec{S}^2$	H_m^K	ε	$\vec{S}^2$	H_f^{d-d}	ε	$\lvert S_z\rvert$	H_m^{d-d}	ε	$\lvert S_z\rvert$
-5.215		2	-5.172		2	-5.000		2	-5.172		1	-5.000		1
-5.215		2	-5.172		2	-5.000		2	-5.172		1	-5.000		1
-5.215		2	-5.172		2	-5.000		2	-5.172		1	-5.000		1
-5.215		2	-5.172		2	-5.000		2	-5.172		1	-5.000		1
-5.215		2	-5.172		2	-5.000		2	-5.172		1	-5.000		1
-5.215		2	-5.172		2	-5.000		2	-5.172		1	-5.000		1
-5.215		2	-5.172		2	-5.000		2	-4.400		0	-4.286		0
-5.215		2	-5.172		2	-5.000		2	-4.400		0	-4.286		0
-5.215		2	-5.172		2	-5.000		2	-4.400		0	-4.286		0
-3.645		0	-3.637		0	-3.571		0	-4.400		0	-4.286		0
-3.645		0	-3.629		0	-3.571		0	-4.400		0	-4.286		0
-3.645		0	-3.629		0	-3.571		0	-4.400		0	-4.286		0
-3.637		0	-3.629		0	-3.571		0	-3.294		0	-3.597		0
-3.637		0	-3.629		0	-3.571		0	-2.857		0	-2.857		0
-1.447		0	-1.447		0	-1.586		0	-2.857		0	-2.857		0
4.484		2	4.484		2	5.000		2	4.484		1	5.000		1
4.484		2	4.484		2	5.000		2	4.484		1	5.000		1
4.484		2	4.484		2	5.000		2	4.828		1	5.000		1
4.484		2	4.828		2	5.000		2	4.828		1	5.000		1
4.484		2	4.828		2	5.000		2	4.828		1	5.000		1
4.484		2	4.828		2	5.000		2	4.828		1	5.000		1
4.484		2	4.828		2	5.000		2	5.370		0	5.000		1
4.484		2	4.828		2	5.000		2	5.370		0	5.000		1
4.484		2	4.828		2	5.000		2	5.516		1	5.000		1
5.904		2	5.516		2	5.000		2	5.516		1	5.000		1
5.904		2	5.516		2	5.000		2	5.516		1	5.000		1
5.904		2	5.516		2	5.000		2	5.516		1	5.000		1
5.904		2	5.516		2	5.000		2	5.600		0	5.714		0
5.904		2	5.516		2	5.000		2	5.600		0	5.714		0
5.904		2	5.516		2	5.000		2	5.600		0	5.714		0
5.904		2	5.861		2	5.000		2	5.600		0	5.714		0
5.904		2	5.861		2	5.000		2	5.861		1	5.714		0
5.904		2	5.861		2	5.000		2	5.861		1	5.714		0
6.272		0	6.256		0	6.429		0	6.059		0	5.714		0
6.272		0	6.371		0	6.429		0	6.059		0	5.714		0
6.272		0	6.371		0	6.429		0	6.059		0	5.714		0
6.715		0	6.601		0	6.429		0	6.059		0	5.714		0
6.715		0	6.601		0	6.429		0	6.288		0	5.714		0
6.715		0	6.715		0	6.429		0	7.143		0	7.143		0
14.480		2	14.480		2	15.000		2	14.480		1	15.000		1
14.480		2	14.480		2	15.000		2	14.480		1	15.000		1
14.480		2	14.480		2	15.000		2	15.370		0	15.710		0
16.260		0	16.260		0	16.430		0	15.370		0	15.710		0
16.260		0	16.260		0	16.430		0	16.720		0	16.450		0
18.160		0	18.160		0	18.010		0	17.140		0	17.140		0

Table 3.4.: The eigenergies, spin quantum number, $\vec{S}^2$ for Coulomb and Kanamori and $|S_z|$ for density-density interaction, in an octahedral crystal-field $\Delta = 1$eV for 2 electrons..

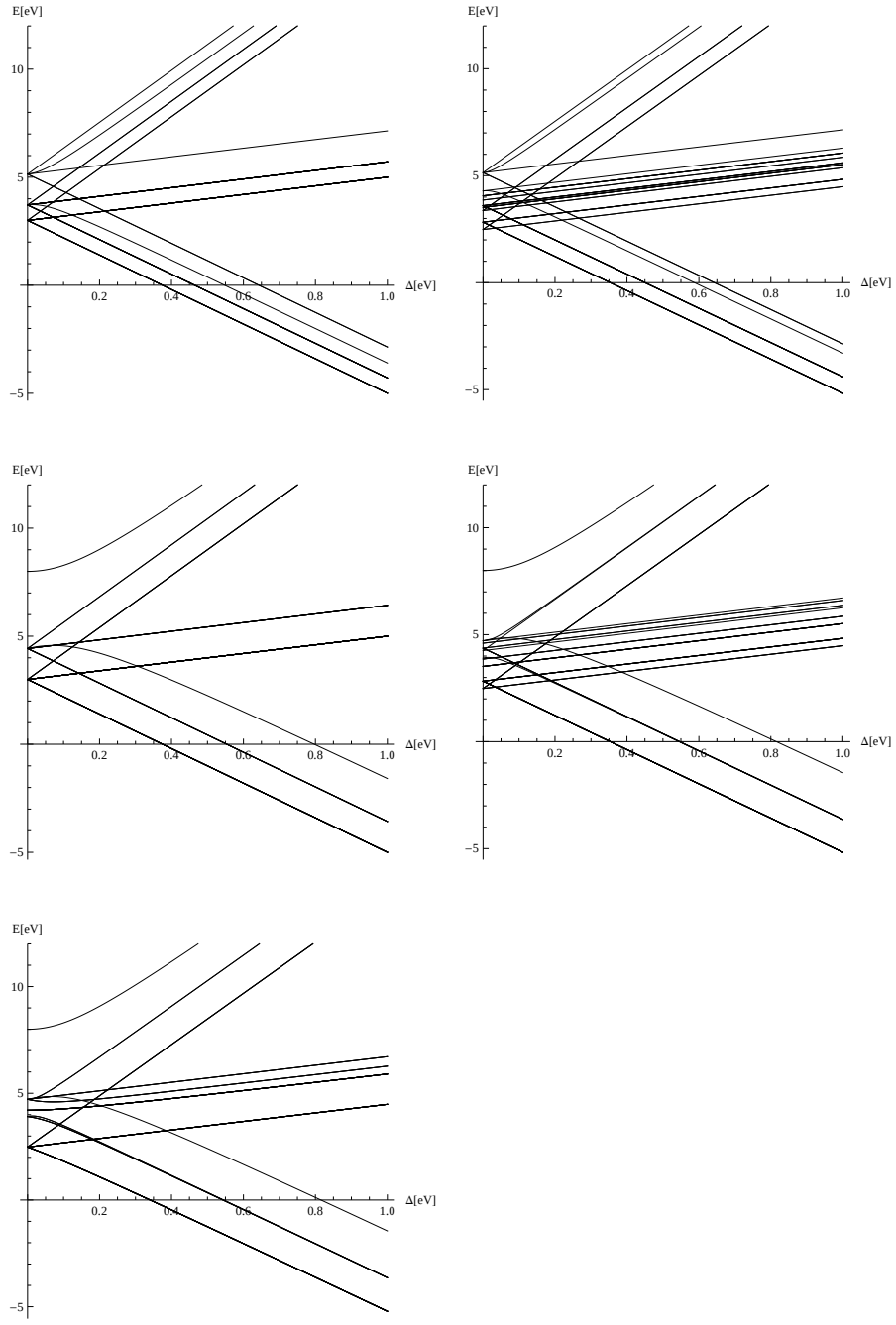

Figure 3.11.: From left to right and from top to bottom the energy levels E of the H_m^{d-d}, H_f^{d-d}, H_m^K, H_f^K and H^C interaction over the crystal-field parameter Δ for 2 electrons.

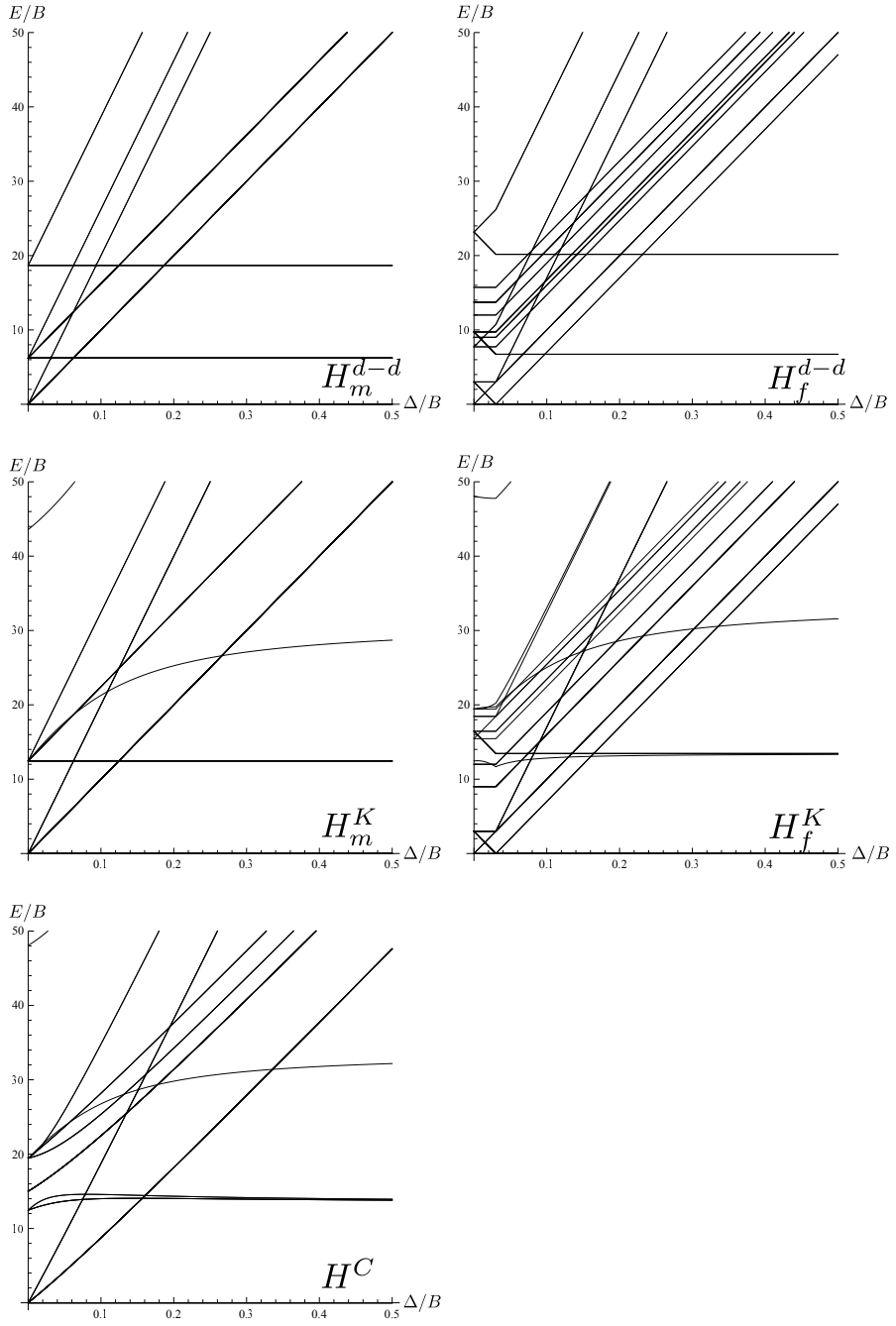

Figure 3.12.: From left to right and from top to bottom the Tanabe-Sugano diagram of the H_m^{d-d}, H_f^{d-d}, H_m^K, H_f^K and H^C interaction for 2 electrons.

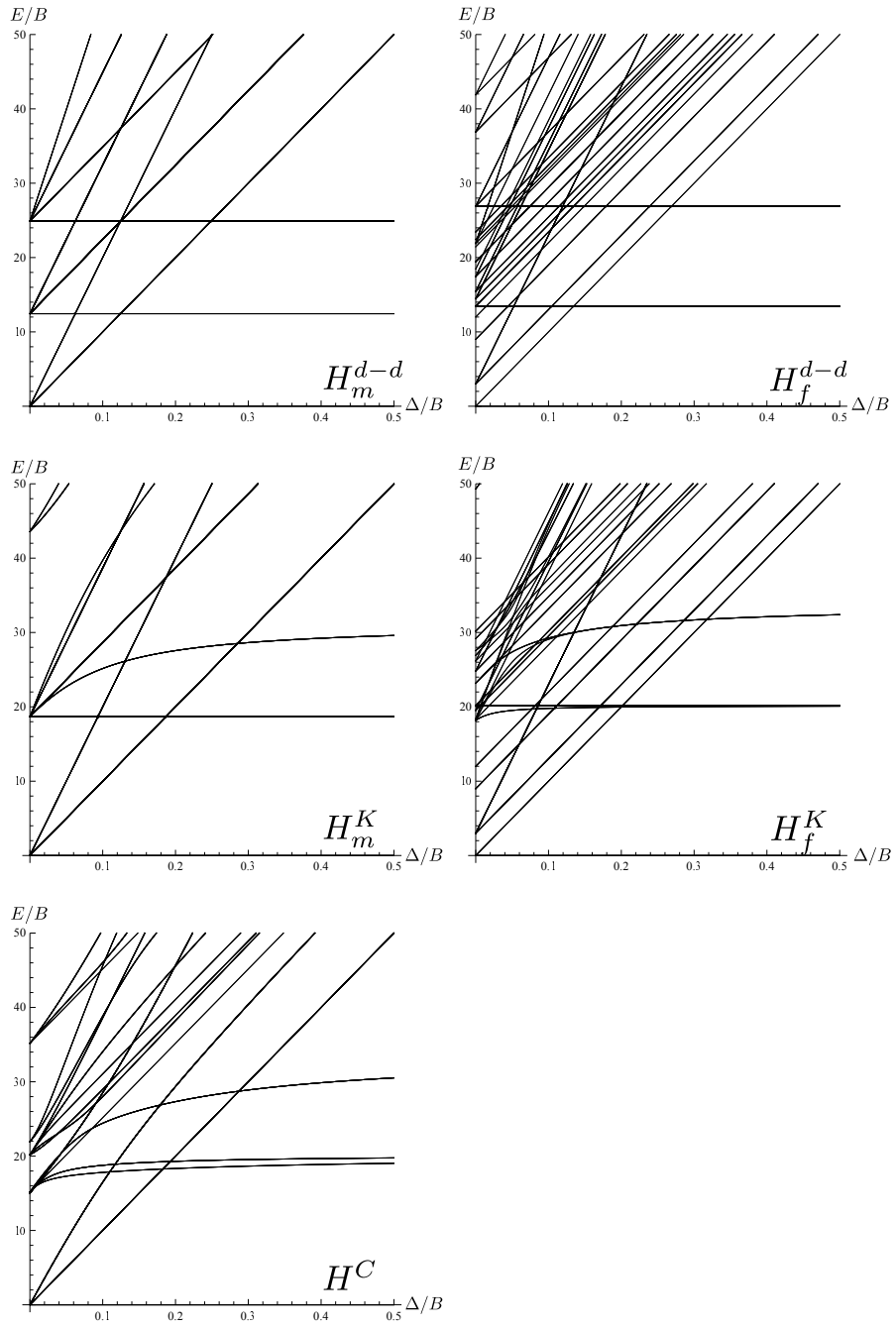

Figure 3.13.: From left to right and from top to bottom the Tanabe-Sugano diagram of the H_m^{d-d}, H_f^{d-d}, H_m^K, H_f^K and H^C interaction for 3 electrons.

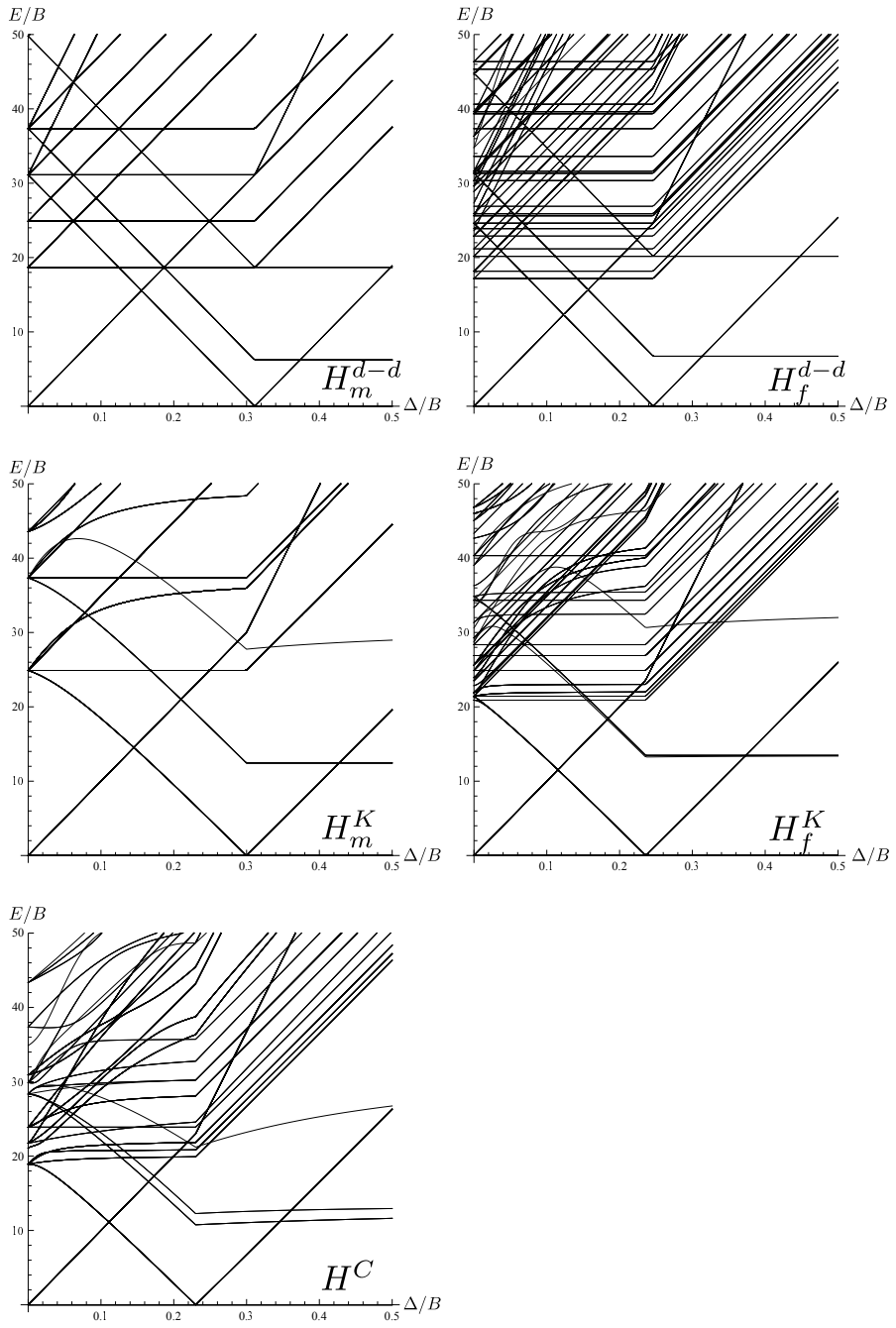

Figure 3.14.: From left to right and from top to bottom the Tanabe-Sugano diagram of the H_m^{d-d}, H_f^{d-d}, H_m^K, H_f^K and H^C interaction for 4 electrons.

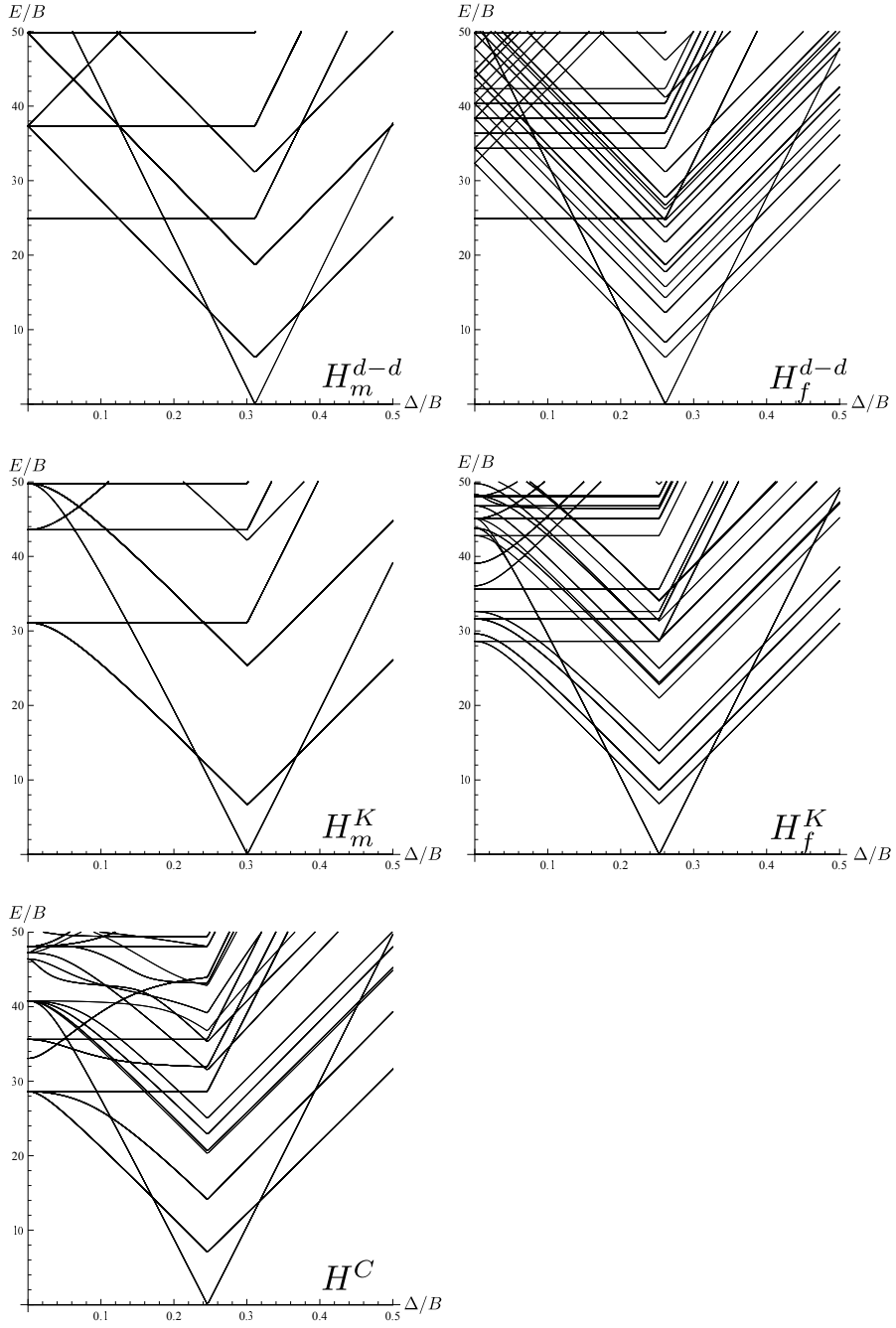

Figure 3.15.: From left to right and from top to bottom the Tanabe-Sugano diagram of the H_m^{d-d}, H_f^{d-d}, H_m^K, H_f^K and H^C interaction for 5 electrons.

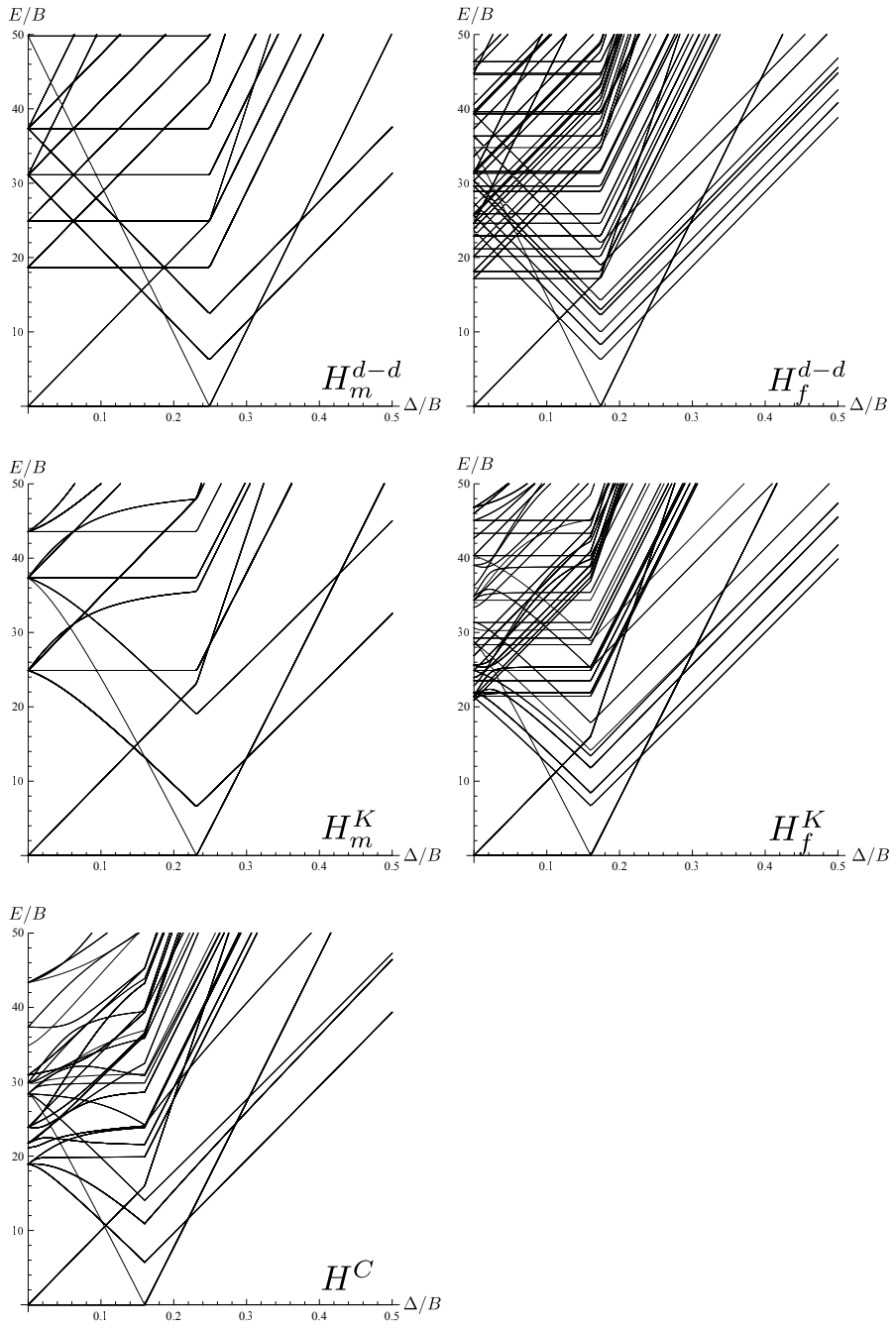

Figure 3.16.: From left to right and from top to bottom the Tanabe-Sugano diagram of the H_m^{d-d}, H_f^{d-d}, H_m^K, H_f^K and H^C interaction for 6 electrons.

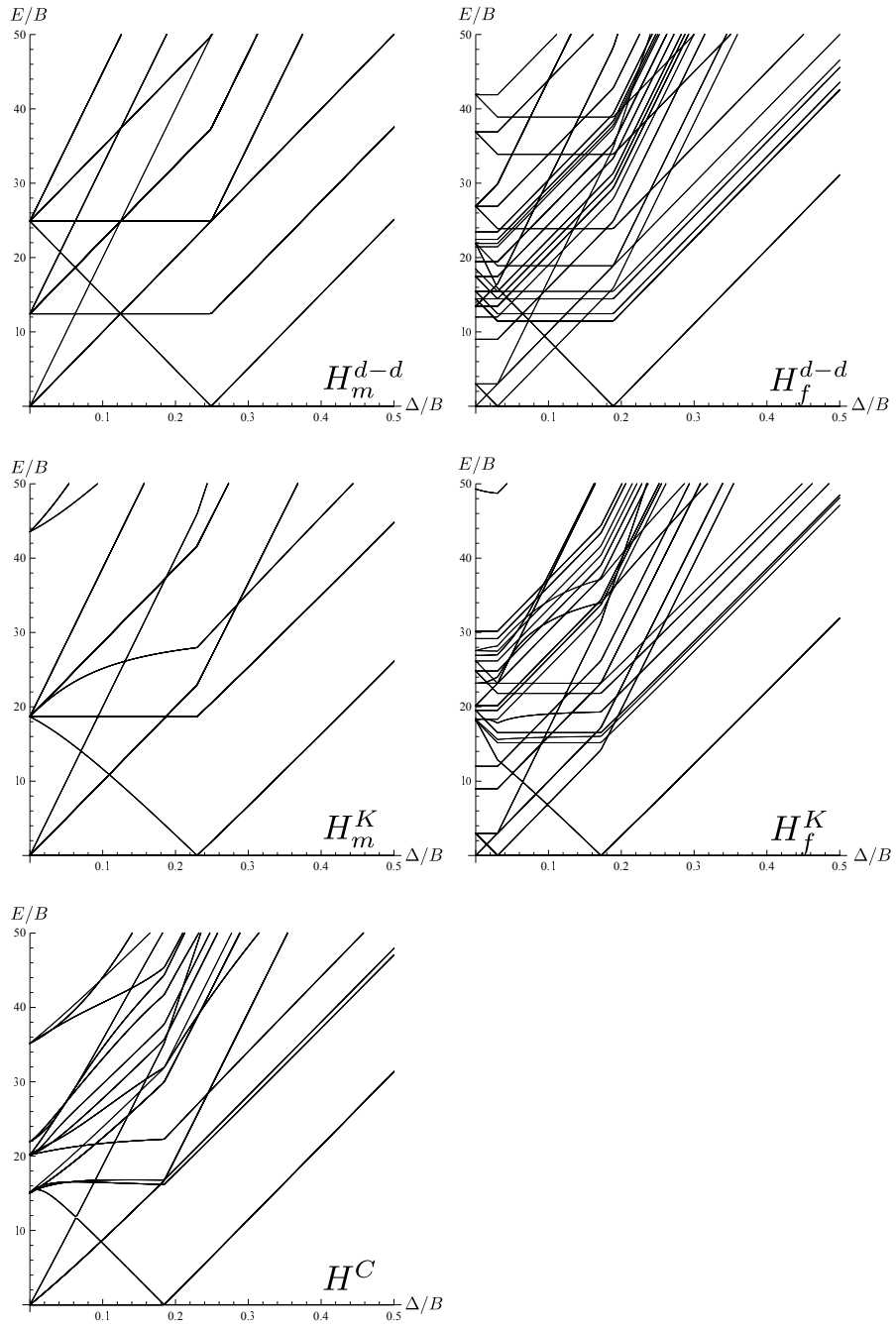

Figure 3.17.: From left to right and from top to bottom the Tanabe-Sugano diagram of the H_m^{d-d}, H_f^{d-d}, H_m^K, H_f^K and H^C interaction for 7 electrons.

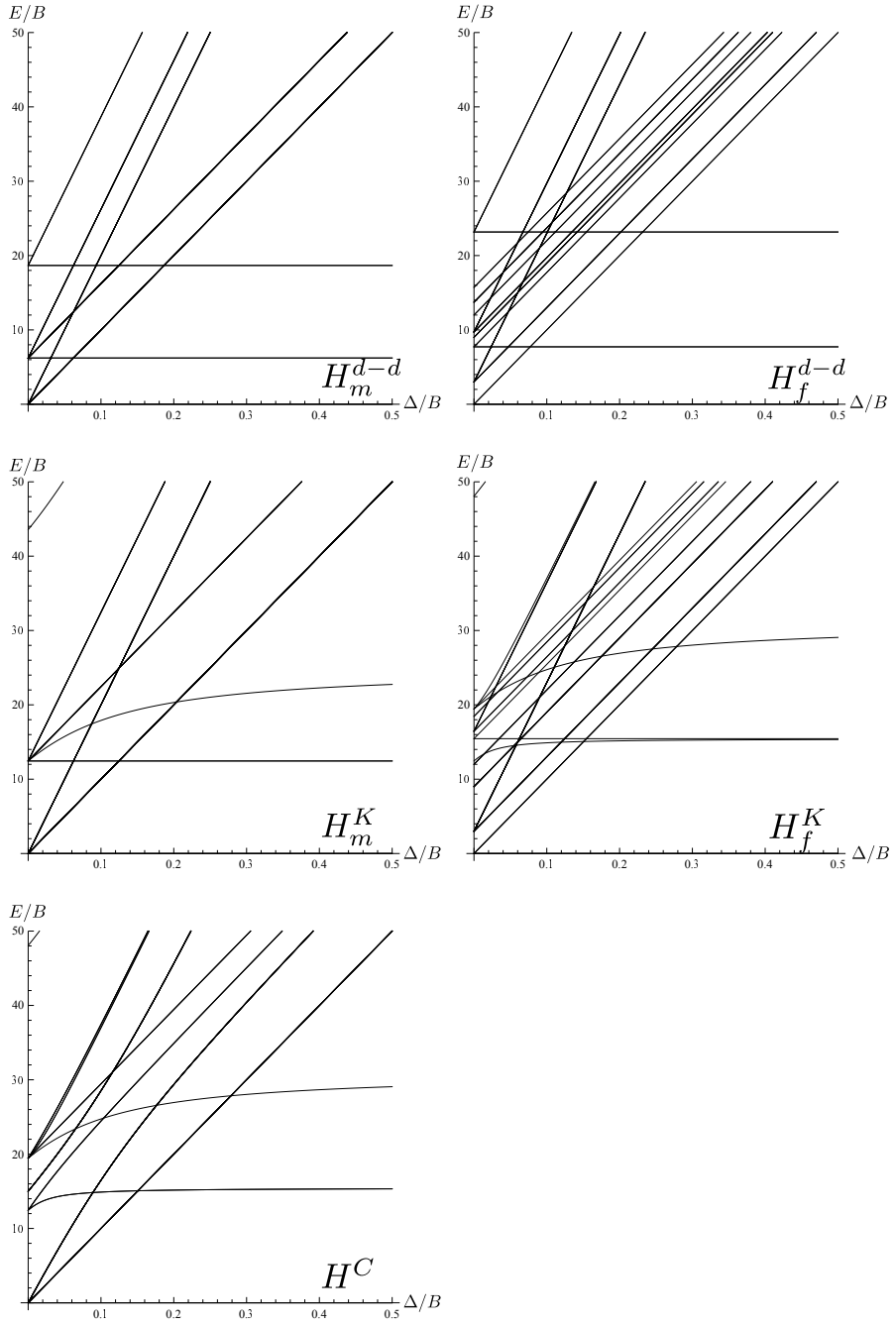

Figure 3.18.: From left to right and from top to bottom the Tanabe-Sugano diagram of the H_m^{d-d}, H_f^{d-d}, H_m^K, H_f^K and H^C interaction for 8 electrons.

3.5. Conclusion

After studying the effects of the self-consistently determined hybridization on the outcome of DMFT calculations in the last chapter I discussed the second part of the Anderson impurity model, the local interaction, in this chapter. To this end I described and discussed some of the most commonly used local interactions and their relation to each other.
Even though the hybridization expansion continuous-time quantum Monte Carlo (CT-HYB) is able to treat arbitrary interactions the use of such general interactions leads to computationally very demanding calculations. Thus studies which make use of a general interaction using U-matrices generated form first principle calculations are still not widely performed. One way, which does not involve a further approximation, to reduce the time it takes the CT-HYB to solve the Anderson impurity model, is to use good quantum numbers, i.e. conserved quantities of the local interaction which fulfill certain other properties. We have been able to show that for one of the most often used more general interactions, in comparison with the simple density-density interaction, the Kanamori interaction, introduced in Section 3.1, a whole set of quantum numbers, that we called PS, commutes with the local Hamiltonian. The reason why we named the set PS is that it projects spins onto the orbitals. Using this special "quantum number" we have been able to go up to seven orbital systems and study the orbital selective Mott transition.
In another study, which I present in Section 3.2, calculations were performed using the Kanamori interaction with the help of PS and also with the density-density interaction using a segment algorithm for $SrCoO_3$. We showed that $SrCoO_3$ cannot be locally described by a certain local spin state but transitions between different spin states with different weights have to be taken into account.
Since we also want to treat arbitrary interactions in the CT-HYB an effort was made to numerically find the minimal block structure for the calculations. This could be achieved by an algorithm, which I introduce in Section 3.3. It performs operations on the local interaction matrix in Fock space enforcing all the requirements for a block diagonal structure to be usable in CT-HYB. This helped in drastically reducing the size of the matrix for the test case of a Coulomb interaction matrix rotated into an octahedral crystal-field. A reduction of 70% for the largest block was found which makes such calculations in the future more tractable.
A first step towards an application of general interactions was taken in Section 3.4. An interesting transition in systems, which at least in the atomic limit is only depending on the value of the crystal-field, is the local spin state of the system. A good way to study this transition considering the local interaction only are the Tanabe-Sugano diagrams. In Section 3.4 I present the Tanabe-Sugano diagrams for all interactions introduced in this chapter and discuss the change in the local interaction w.r.t. to the crystal-field. We come to the conclusion that the different interactions are applicable only to certain

regimes of the crystal-field and for certain fillings of the system. The full picture will become more clear once we perform more thorough studies using DMFT on model systems.

Summary

The main objective of this work was to implement a continuous-time solver for the Anderson impurity model and a flexible self-consistency loop based on the dynamical mean-field theory in its different flavors. This goal was achieved in the course of this work and a program package called *w2dynamics* was made publicly available on `http://git.physik.uni-wuerzburg.de/`. The program was then applied to different systems to obtain a deeper understanding of the relation between the self-consistently determined hybridization and the self-consistent solution. Also the interaction used in the Anderson impurity model plays an important aspect in solids. Since the use of the full interaction matrix is numerically expensive techniques to reduce the computational effort were developed and the effect of approximations, which can further decrease the cost of simulations, was studied.

In Chapter 1 the Anderson impurity model and its physics were introduced. Then a number of solvers were presented and the choice of the hybridization expansion continuous-time quantum Monte Carlo (CT-HYB) solver was motivated. The theoretical ground works for the Monte Carlo in general and the CT-HYB were then outlined. After the theoretical discussion of CT-HYB different algorithms for this method were presented. This was followed by an introduction of how measurements are performed in the quantum Monte Carlo (QMC) before I finally showed a benchmark acquired with *w2dynamics*.

In Chapter 2 I first introduced LDA+DMFT and its two main ingredients to perform realistic calculations for strongly correlated electron systems. The density functional theory (DFT) in its local density approximation (LDA) and the dynamical mean-field theory (DMFT). In the following sections I described methods which are needed for the merger of LDA and DMFT. These are methods for subtracting interactions which are already treated in the LDA and for obtaining low energy Hamiltonians in real space. Two studies which were conducted during the course of this thesis are presented after this introduction. One is about the effect the local interaction has on a crystal-field between d-orbitals, a situation which is e.g. present in the Nickelates. The second study is about a simpler model, the generalized periodic Anderson model. In this model there is only one d- and one p-orbital present and the hybridization between the two can be easily tuned. After a short excursion, on the analytical continuation to the real axis and the inclusion of non-local Hartree type interactions in the DFMT self-consistency loop, a study was presented which shows that such non-local interactions can widen the gap between the d- and p-bands thus leading to insulating results for a mother compound of the high-T_c cuprates. Finally I presented results obtained with extensions to the DMFT

loop which enable us to calculate layered materials and nanoscopic structures. The results shown are still of preliminary nature. In the future diagrammatic extensions will be important to include non-local correlations in the self-consistency. To this end the two-particle Greens function is needed. The efficient measurement of this quantity is still subject of on going research and different methods to implement its measurement are currently tested with our code. Another important extension to the code is the measurement of the spin susceptibility which can be accumulated in the simulation without the need of the full two-particle object. This is another currently ongoing development project in *w2dynamics*.
In Chapter 3 I introduced the full Coulomb U-matrix, which is a good starting point to analyze the interaction in solids. After that I introduced the density-density interaction and showed how one can arrive at the interaction parameters for it starting from the full U-matrix. In the next section I introduced yet another interaction, which is SU(2) symmetric. We found a new set of quantum numbers for this interaction which is usable to quicken CT-HYB calculations. This new set of quantum numbers was used to study the orbital-selective Mott transition in up to seven orbitals and for investigating the spin ground state of the $SrCoO_3$ compound. Then an algorithm was presented which allows us to find symmetries in general interactions to speedup calculations. Finally I presented a study of the local interactions using Tanabe-Sugano diagrams. In the future a study which systematically examines the effect of different local interactions on observables is going to be of great importance to help us to decide which interaction can be used for certain systems. Using the algorithmic improvements developed and implemented during this work such a study is feasible now.

A. w2dynamics

In the main part of this thesis I have shown some current and future applications of the software package *w2dynamics*. In this part I want to add a bit of information about this package. *w2dynamics* is mainly consisting of two independent building blocks

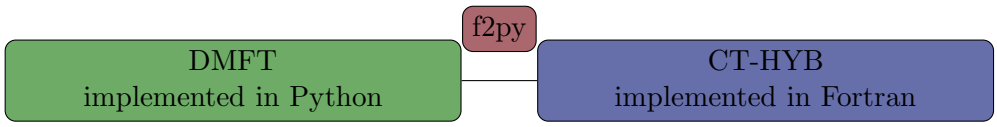

Figure A.1.: The two building blocks of *w2dynamics* and their glue *f2py*.

depicted in Figure A.1. The self-consistency cycle based on the DMFT, see Section 2.2, is completely implemented in Python while the CT-HYB, which I introduced in Section 1.3, is implemented in Fortran 90. The general idea behind this coding structure is that the self-consistency cycle can be rather complex and there is often the need to adapt it for individual cases, but it is not computationally demanding. Additionally a multitude of readily available modules can be used in Python which makes the implementation of extensions fast and less error prone. The CT-HYB, on the other hand, is numerically very demanding but is not often subject to change, thus a fast compiled language is more suitable for this task. The clear separation of the two building blocks has the additional advantage that each of them can also be, in principle, used without the other. One could, e.g., use another impurity solver in the Python scripts or use the impurity solver alone or for another problem altogether.
To connect the two computer languages one needs to build an interface which is then used to generate a Python module out of the Fortran code. Building this interface can be automatically performed by f2py [193]. A problem, however, is arising when one uses this tool. The Fortran standard does not enforce a certain binary structure for allocatable arrays or pointers and thus types of such structures can not be in general handed over from Fortran to Python or vice-versa. A solution to this problem was put forward in [201] and is used in the code which is interfaced in *w2dynamics*. This, however, still has the limitation that not all data structures are available in Python but only the subset of them for which this workaround is implemented. These structures are all declared in the file *CTQMC.F90* while the data structures in other files are not available from Python. The output of the calculations are stored in the HFD5 file format [194] which is a binary file format resembling a data base. This is advantageous since the arrays which we

obtain from calculations can simply be "dumped" into this file and later retrieved easily. Also, in contrast to the commonly used way of storing information in an ASCII file, no accuracy is lost due to the truncation of numbers and the files are in general smaller since the representation of numbers in strings is typically not efficient. Another advantage is the speed of such a file format which is especially made for the purpose of storing large arrays. A disadvantage of the HDF5 file format is that the typical command line tools, which were used for ASCII files, will no longer work. With *w2dynamics* a specialized tool is distributed which is very useful in substituting the use of these command line tools. The tool is executed by *hf.py* and it prints the possible parameters to the standard output of the command line when no parameters are given, or via the *help* parameter. This tool was developed by Markus Wallerberger.
In the following two subsections I will present a flow-chart for the initialization of the Fortran module and give some implementation details of the two building of *w2dynacmis* blocks which I introduced here. Following this I will present a listing of parameters which are used in the parameter file of *w2dynamics*.

A.1. DMFT

The Python part of the program takes care of the self-consistency loop and all the lattice specific parts of the calculation. The main loop is implemented in *DMFT.py* in which the loop itself and the parallelization of the AIM-solver is implemented. Also the output of the program is managed therein.
In *lattices.py* the different lattice structures are implemented which specialize the abstract class *Lattice*. The self-consistency loop based on DMFT which is implemented in *DMFT.py* is applicable to a very diverse set of problems as e.g. the nano-DMFT or the layer-DMFT which I briefly discussed in Section 2.8.
In Figure A.2 I show the general structure of the *Lattice* class. The *Lattice* class has all the subroutines necessary to implement the self-consistency scheme of which some are abstract. In the scheme the only abstractly defined subroutines are denoted in italic. Since the class Lattice contains abstract subroutines it cannot be instantiated itself. The derived classes cover all the various lattices used in this thesis. There is also a class for the impurity, depicted in Figure A.3, which is very small in Python since the main task is performed in the Fortran module. Since the Fortran part of the program does not know anything about the lattice and the different inequivalent atoms this information needs to be stored in the Python structure. Also the number of bands and other lattice specifics as e.g. the impurity chemical potential needs to be handled by it. Another reason why it is necessary for this information to be stored in the Python class is that the Fortran module gets generated for each impurity and then destructed again to be used for the next impurity. Thus the information contained in the Fortran module is lost after the impurity problem is solved.

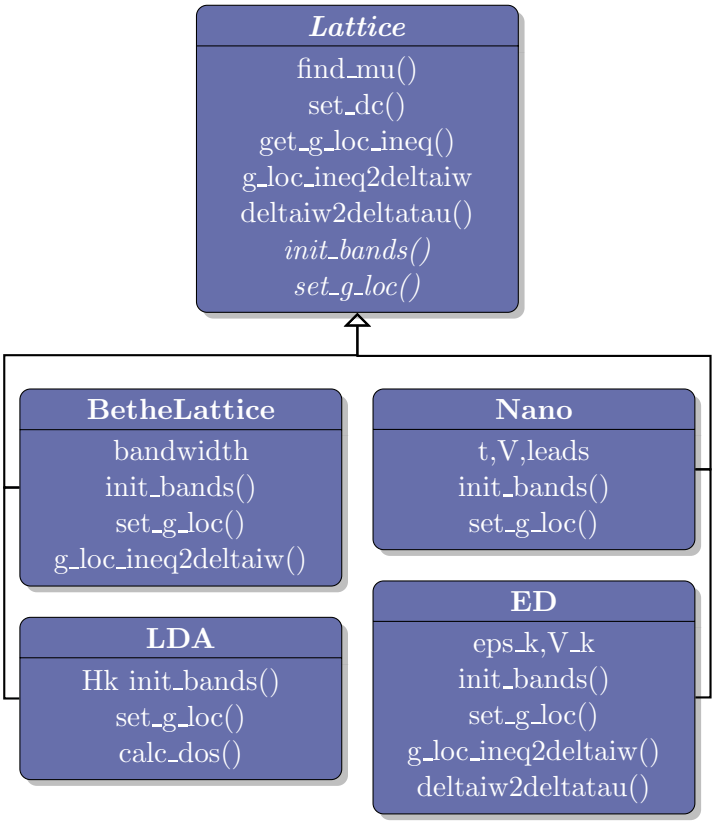

Figure A.2.: The Lattice class and the specialized classes for different lattices.

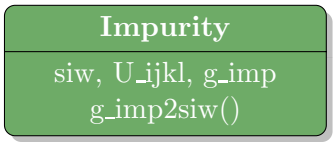

Figure A.3.: The Python class handling the impurity.

A.2. CT-HYB

In this section I am going to introduce the structure and inner workings of the Fortran code. Each source file of the Fortran code has a main subroutine written into it for testing purposes. Compilation of these test programs can be achieved by executing the Makefile in the *ctqmc_fortran* subdirectory of the code with the target *Test_*filename_without_extension.
In Figure A.4 I show a flowchart of the different steps that are performed before the Monte Carlo simulation starts. First one needs to define the basis which consists of binary representations of the impurity states. To this end the bits of an integer are interpreted as 1 for an orbital/spin being occupied and 0 for an orbital/spin being empty. Then the block diagonal structure of the Hamiltonian is generated by putting states with the same set of quantum numbers into the same block. After that the creation/annihilation operators are generated in matrix form for the block structure of the Hamiltonian. Then the matrices for the block diagonal form of the Hamiltonian is generated and the one-particle elements are stored in it. In the next step the U-matrix is created with which we then generate the two-particle part of the Hamiltonian by using the creation and annihilation operators and the U-matrix with $\sum_{ijkl\sigma\sigma'} U_{ijkl} c^\dagger_{i\sigma} c^\dagger_{j\sigma'} c_{k\sigma'} c_{l\sigma}$. The eigenvalues which we need for finding the states that need to be taken into account in the local trace and also the eigenvectors which we need as starting points for the calculation of the local trace. This is performed by the next two steps. Then all the matrices which were generated are stored in the states structure in sparse format. In the next three steps the matrices for the measurements in the ctqmc module, the local trace in the trace module and the Fourier transform is initialized. With these steps all the data structure needed for the Monte Carlo is generated and the Monte Carlo steps as depicted in Figure 1.3 is carried out.
Below I show a table which is listing all the Fortran source files and the functionality implemented therein.

Filename	Comment
AngularMomentum.F90	In this file the generation of Gaunt coefficients is implemented using the 3jm-symbols.
Parameters.F90	The data structure and routines to read parameters either from a file or from a string. The parameters are stored in a singly linked list and parameters can be obtained from this structure by special functions returning value(s) for a given key (string).
Lanczos.F90	This file contains subroutines to perform the transformation into the Krylov space and the time evolution in it. See introduction to Chapter 1 and Section 1.3.1.

Filename	Comment
MatrixUpdate.F90	The subroutines for performing full matrix updates, i.e. wrapper for the LAPACK routines to invert matrices and calculate determinants, and subrotines for partial matrix updates, i.e. inversion by partitioning as outlined in Section 1.3, are implemented in this file.
Operator.F90	The creation/annihilation operators and local Hamiltonians in the block diagonal structure are implemented in this file.
SparseMatrix.F90	This file contains subroutines to transform a dense matrix into a sparse matrix in compressed sparse row (csr) format, see e.g. [49]. Also subroutines to multiply sparse matrices with vectors are implemented therein.
States.F90	In this file the structure to store states and operators are implemented. The subroutines to associate certain states with a certain block are also implemented in States.F90. The states are identified by their binary representation of integers with the different spins grouped in blocks, e.g. the state $\|\uparrow \ , \ \downarrow\rangle$ is associated with the binary pattern 1001 where the least significant bit is to the right and the spin up block is the less significant block. This binary pattern corresponds to the integer 9. In the file subroutines to calculate quantum numbers, which are diagonal in the occupation numbers basis, are also implemented.
LegendrePoly.F90	A module which generates Legendre polynomials, see Section 1.4, is implemented in here.
MersenneTwister.F90	The implementation of the random number generator Mersenne twister [192].
Progress.F90	Implementation of a progress bar.
Trace.F90	In this file a doubly linked list to store the local trace and its nodes is implemented. Also routines to generate new operators in the local trace and routines to check if the local trace yields a finite value due to quantum numbers and to calculate the value of the local trace are implemented therein.
CTQMC.F90	The implementation of the Monte Carlo procedure, the proposal of moves and measurements are implemented in this file.
Signals.F90	In this file the handling of system signals is implemented.
interaction.F90	Implementation to generate the U-matrix for different interactions. *Deprecated will be replaced by a Python script.*

Filename	Comment
nfft.F90	The wrapper for the fast Fourier transform on non-equidistant meshes.

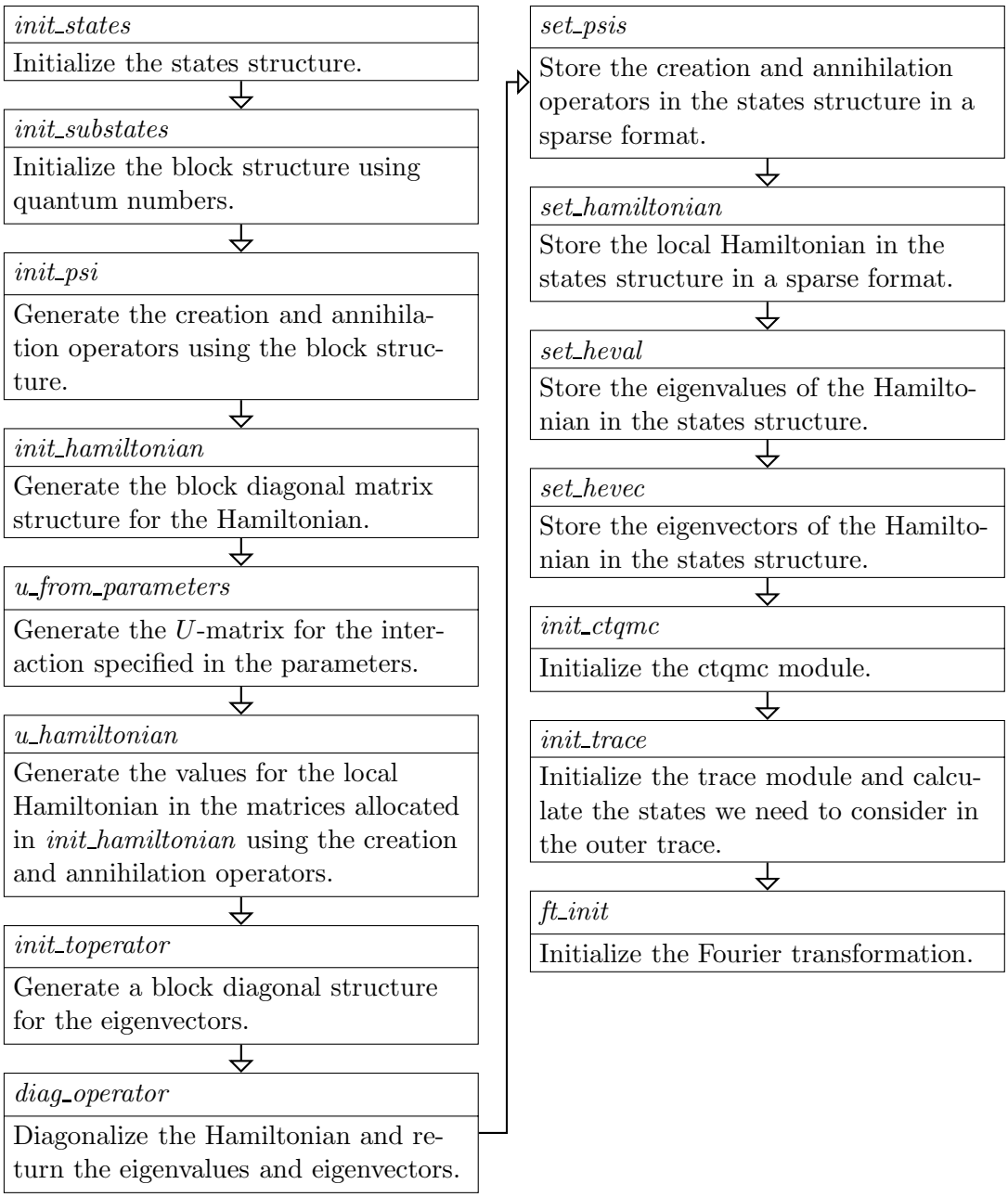

Figure A.4.: The program initialization flow before the Monte Carlo simulation starts.

A.3. Parameters

In this section I am presenting a list of parameters for *w2dynamics* which should cover the most important parameters for simple calculations. For more advanced calculations like nano-DMFT calculations I refer to the index which will point you to the right page in my thesis.

A.3.1. Values defining the system

Parameter	Comment
DOS	Defines the type of lattice that is used. Currently supported are *Bethe*, *Bethe_in_tau*, *ReadIn*, *EDcheck*, *nano* and *readDelta*. For *Bethe* and *Bethe_in_tau* a semi-circular density of state is used for each bath. If *ReadIn* is chosen a k-dependent Hamiltonian is read in and used to generate the lattice Greens function. When *EDcheck* is set then a file *epsk* and *Vk* is read in to generate a hybridization function with ED parameters. If *nano* is set then a system in real-space is read in using the files which are described in Section 2.8.2. Finally when *readDelta* is used then the hybridization function is directly read from a file. mandatory if: always value: {`ReadIn, Bethe, Bethe_in_tau, EDcheck, nano, readDelta`} format: string default: `Bethe` example: `DOS=Bethe`

Parameter	Comment

HkFile	Specifies the file containing the H(k) read in if the DOS is set to ReadIn.
	mandatory if: `DOS=ReadIn`; ignored otherwise
	value: *filename*
	format: string
	default: none
	example: `HkFile=Hkdmft.dat`
	format of the k-point file:
	`#k-points #atoms #d-bands #p-bands #ligands per atom`
	`#k_x #k_y #k_z`
	`#re #im #re #im`
	`#re #im #re #im`
	`#k_x....`
	`.`

nanostructure	Specifies the prefix of the files read in for defining the real space nano structure. See Section 2.8.2 for details. mandatory if: `DOS=nano`; ignored otherwise value: *filename-prefix* format: string default: None. example: `nanonstructure=benzene`
beta	Defines the inverse temperature in [eV^-1] used in the simulation. mandatory if: always value: #beta format: float default: 100. example: `beta=100.`
mu	The chemical potential (mu) of the system. mandatory if: always value: #chemical potential format: float default: *none* example: `mu=2.0`

Parameter	Comment
half-bandwidth	List of the half-bandwidth (D) of each band of a Bethe model system. The Bethe lattice has a semicircular density of states and analytic self-consistency equations are used in the DMFT loop. mandatory if: `DOS = {Bethe, Bethe_in_tau}` value: `#D,...,` format: list of float default: *none* example: `half-bandwidth=2.,2.,` (2 band system with equal half-bandwidths)
EPSEQ	If there is more than one atom in the unit cell this parameter defines the ε-criterion for them to be considered equivalent. mandatory if: always, but only used if there is more than one atom in the unit cell value: `#EPSEQ` format: float default: *2e-2* example: `EPSN=0.02`
dc	Specifies the double-counting correction. For the different double-counting corrections see Section 2.3. mandatory if: *DOS=Readin* and *p*-bands and/or more than one atom in the unit cell. Ignored otherwise. value: *fll*, *amf*, *number* format: string default: *fll* example: *dc=amf*
dc_value	Specifies a number which is then used as the double-counting correction. mandatory if: *dc=number* ignored otherwise. value: `#DC` format: float default: 0.0 example: *dc_value*=2.68

A.3.2. Interaction

Parameter	Comment

Parameter	Comment
Hamiltonian	Defines the local interaction on the impurity. Possible options are `Density` and `Kanamori`. The Density interaction has the form: $$H_{loc} = \sum_a U n_{a,\uparrow} n_{a,\downarrow} + \sum_{a>b,\sigma} \Big[U' n_{a,\sigma} n_{b,-\sigma} + (U' - J) n_{a,\sigma} n_{b,\sigma} \Big]$$ while the Kanamori interaction has the additional spin-flip and pair-hopping terms for SU(2)-symmetry: $$H_{loc} = \sum_a U n_{a,\uparrow} n_{a,\downarrow} + \sum_{a>b,\sigma} \Big[U' n_{a,\sigma} n_{b,-\sigma} + (U' - J) n_{a,\sigma} n_{b,\sigma} \Big]$$ $$- \sum_{a \neq b} J (d^\dagger_{a,\downarrow} d^\dagger_{b,\uparrow} d_{b,\downarrow} d_{a,\uparrow} + d^\dagger_{b,\uparrow} d^\dagger_{b,\downarrow} d_{a,\uparrow} d_{a,\downarrow} + h.c.).$$ mandatory if: always value: {`Density,Kanamori`} format: string default: `Density` example: `Hamiltonian=Density`
crystalfield	If the system is a Bethe lattice or if the Hamiltonian in k-space is read in a crystal field can be switched on to separate the bands. mandatory if: never value: `#crystalfield,...,` format: list of float default: *none* example: `crystalfield=0.,1.,` (2 band system with one band shifted upward in energy)
Udd	Intra-orbital interaction parameter U used in the local interaction defined above. mandatory if: always value: `#Udd` format: float default: 0.0 example: `Udd=2.`

Parameter	Comment
Jdd	Hund parameter J used in the local interaction defined above. mandatory if: more than one orbital present value: `#Jdd` format: float default: 0.0 example: `Jdd=0.5`
Vdd	Inter-orbital local interaction parameter U' used in the local interaction defined above. mandatory if: more than one orbital present value: `#Vdd` format: float default: 0.0 example: `Vdd=1.`
Upp	Intra-orbital interaction parameter U used for the Hartree interaction in the p-manifold. mandatory if: always value: `#Upp` format: float default: 0.0 example: `Upp=2.`
Jpp	Hund parameter J used for the Hartree interaction in the p-manifold. mandatory if: always value: `#Jpp` format: float default: 0.0 example: `Jpp=0.5`
Vpp	Inter-orbital interaction parameter U' used for the Hartree interaction in the p-manifold. mandatory if: Vpp value: `#Vpp` format: float default: 0.0 example: `Vpp=1.`

Parameter	Comment
Udp	Inter-orbital interaction parameter U used for the Hartree interaction between the p- and d-manifold. mandatory if: always value: `#Udp` format: float default: 0.0 example: `Udp=2.`
Jdp	Hund parameter J used for the Hartree interaction between the p- and d-manifold mandatory if: always value: `#Jdp` format: float default: 0.0 example: `Jdp=0.5`
QuantumNumbers	Specifies which quantum numbers to use. The list of quantum numbers is separated by spaces. Possible values are Nt, which is the conservation of the particle number, Szt, the conservation of the total spin in z-direction, Qzt, the PS-quantum number defined in Section 3.1.1, Azt, the conservation for each one particle quantum number and All, for which the algorithm in Section 3.3 is used to search for the minimal block size automatically. mandatory if: always value: Nt, Szt, Qzt, Azt, All format: space separated list of strings default: $Nt\ Szt\ Qzt$ if *Hamiltonian=Kanamori*; $Nt\ Szt\ Azt$ if *Hamiltonian=Density* example: *QuantumNumbers=Nt Szt*

A.3.3. QMC

Parameter	Comment

Parameter	Comment
Nwarmups	The number of steps before starting the measurement in the QMC. mandatory if: always value: `#Nwarmups` format: integer default: *none* example: `Nwarmups=10000`
Nmeas	Number of measurements in the QMC of each quantity mandatory if: always value: `#Nmeas` format: integer default: *none* example: `NMeas=10000`
NCorr	Number of steps bewteen measurements (∼autocorrelation time). A reasonable approxiamtion is: #(mean expansion order)/#(probaility of acceptance) mandatory if: always value: `#NCorr` format: integer default: 100 example: `NCorr=100`
NSeed	The random number seed. mandatory if: always value: `#NSeed` format: integer default: 43890 example: `NSeed=12345`
MaxHisto	The size of the Histogram arrays. If the expansion order in a channel is larger then the counter of the last value in the array will be increased. mandatory if: always value: `#MaxHisto` format: integer default: 500 example: `MaxHisto=1000`

Parameter	Comment
MeasDensityMatrix	Switch for measuring the density matrix. Beware can get quite large (1024×1024 for 5 band systems. mandatory if: always value: switch format: integer default: 0 example: `MeasDensityMatrix=1`
MeasExpResDensityMatrix	Switch for measuring the expansion resolved density matrix. Beware can get very large ($1024 \times 1024 \times$MaxHisto$\times$Nd$\times 2$ for 5 band systems. mandatory if: always value: switch format: integer default: 0 example: `MeasExpResDensityMatrix=1`
MeasGiw	Switch for measuring the Greens function directly in $i\omega_n$. mandatory if: always value: switch format: integer default: 0 example: `MeasGiw=1`
truncation	Number of multiplets used in the outer truncation of the local trace. mandatory if: always value: `#truncation` format: integer default: 1 example: `truncation=1`

Parameter	Comment
EPSLANC	Convergence criterion for the Lanczos time evolution see Section 1.3.1. This is set to a reasonable value. Do not touch if you do not know what your are doing! mandatory if: always value: `#EPSLANC` format: float default: 1e-15 example: `EPSLANC=1e-14`
EPSTRACEVEC	ε-criterion for a vector in the local trace to be considered zero. This is set to a reasonable value. Do not touch if you do not know what your are doing! mandatory if: always value: `#EPSTRACEVEC` format: float default: 1e-15 example: `EPSTRACEVEC=1e-14`
EPSSANDWICH	ε-criterion for a braket in the local trace to be considered zero. This is set to a reasonable value. Do not touch if you do not know what your are doing! mandatory if: always value: `#EPSSANDWICH` format: float default: 1e-15 example: `EPSSANDWICH=1e-14`
EPSEVEC	ε-criterion for elements of the eigenvectors to be considered zero. Removes numerical noise in the calculation. This is set to a reasonable value. Do not touch if you do not know what your are doing! mandatory if: always value: `#EPSEVEC` format: float default: 1e-15 example: `EPSEVEC=1e-14`

Parameter	Comment
PercentageGlobalMove	Defines how high the percentage of global moves is in the simulation. mandatory if: always value: `#PercentageGlobalMove` format: float default: 0.001 example: `PercentageGlobalMove=0.01`

A.3.4. Discretization

Parameter	Comment
Ntau	The discretization on the imaginary time axis used to store the measurement of $G(\tau)$. Applicable to gtau in the output file. mandatory if: always value: `#Ntau` format: integer default: 1000 example: `Ntau=1000`
Nftau	The discretization on the imaginary time axis used to for the hybridization function $\Delta(\tau)$. Since we are using a high-frequency model this can be set to very large values without suffering from problems in the Fourier transform. mandatory if: always value: `#Nftau` format: integer default: 5000 example: `Nftau=10000`
Niw	The number of positive Matsubara frequencies used for $\Sigma(i\omega)$ and $G(i\omega)$. mandatory if: always value: `#Niw` format: integer default: 2000 example: `Niw=2000`

Parameter	Comment
NLegMax	The number of Legendre coefficients of the local Greens function measured in the QMC. See Section 1.4 mandatory if: always value: `#NLegMax` format: integer default: 100 example: `NLegMax=100`
NLegOrder	The number of Legendre coefficients of the local Greens function used in calculating the local Greens function in Matsubara frequencies. See Section 1.4 mandatory if: always value: `#NLegOrder` format: integer default: 100 example: `NLegOrder=30`
FourPnt	Switch for measuring the 2-particle Greens function. 0 no measurement, 1 measurement in imaginary time, 2 measurement in Legendre coefficients, 3 both measurements. mandatory if: always value: `#FourPnt` format: integer default: 0 example: `FourPnt=1`
N4tau	Number of tau bins for the 2-particle Greens function. mandatory if: *FourPnt*=1, *FourPnt*=3 value: `#N4tau` format: integer default: 1 example: `N4tau=100`
N4leg	Number of Legendre coefficients to measure for the 2-particle Greens function. mandatory if: *FourPnt*=2, *FourPnt*=3 value: `#N4leg` format: integer default: 2 example: `N4leg=100`

Parameter	Comment
N4iwf	Number of fermionic Matsubara frequencies to measure for the 2-particle Greens function. mandatory if: always value: `#N4iwf` format: integer default: 0 example: `Niwf=30`
N4iwb	Number of bosonic Matsubara frequencies to measure for the 2-particle Greens function. mandatory if: always value: `#N4iwb` format: integer default: 0 example: `Niwb=10`
Neps	The number of points for the numerical integration of the density of states. mandatory if: always value: `#Neps` format: integer default: 1000 example: `Neps=2000`
Neps	The number of k-points in the Hamiltonian. Automatically set by the Python script. mandatory if: never value: `#Neps` format: integer default: None example: `Nk=None`

Parameter	Comment
totdens	The number of electrons per atom in the system. Used when the chemical potential is adjusted and for calculating the double counting correction. mandatory if: `DOS=Bethe`:chemical potential is variable; `DOS=ReadIn`: always value: `#electrons/atom` format: float default: *none* example: `totdens=2.`
EPSN	Defines the upper error between the number of electrons the system should contain and the number of electrons the system contain as calculated by w2dynamic. mandatory if: chemical potential is variable value: `#EPSN` format: float default: *none* example: `EPSN=0.001`
EPSLDAN	The ε-criterion for the μ search with the non-interacting system. mandatory if: *DOS=Readin* value: `#EPSLDAN` format: float default: *0.00001* example: `EPSLDAN=0.001`

A.3.5. DMFT

Parameter	Comment
DMFTsteps	The number of DMFT steps the code performs. mandatory if: DMFT steps are required value: `#DMFTsteps` format: integer default: 1 example: `DMFTsteps=0`

Parameter	Comment
StatisticSteps	The number of steps the code performs only measuring quantities without updating the hybridization function. mandatory if: Statistic steps are required. value: `#StatisticSteps` format: integer default: 0 example: `StatisticSteps=10`
SelfEnergy	Defines if the self-energy is calculated using Dyson equation or improved estimators [204]. The improved estimators currently only work for density-density interaction. mandatory if: always value: *dyson*, *improved* format: string default: dyson example: `SelfEnergy=improved`
FTType	Defines how the local Greens function in $i\omega_n$ is calculated. Either via a simple Fourier transform from $G(\tau)$ *plain* or from the Greens function projected on Legendre polynomials *legendre*. mandatory if: always value: *plain*, *legendre* format: string default: legendre example: `FTType=legendre`
mixing	Defines how much of the old self-energy is mixed to the new one. If this parameter is set to 0 only the new self-energy is used. mandatory if: always value: `#mixing` format: float 0 <mixing< 1 default: 0 example: `mixing=0.5`

A.3.6. IO

Parameter	Comment

Parameter	Comment
FileNamePrefix	A prefix is attached before the default filename of the output file containing the time and date the calculation started. This parameter defines the prefix. mandatory if: never value: *prefix* format: string default: ” example: `FileNamePrefix=SrVO`
readold	Specifies which iteration of an old file should be used to restart a calculaton. No file is read if this parameter is set to 0. If this parameter is set to -1 the last iteration of a file is used. mandatory if: an old calculation should be continued value: `#readold` format: integer default: 0 example: `readold=3`
fileold	This parameter specifies the name of the file which should be read for a continuation of an old calculation. mandatory if: an old calculation should be continued value: *filename* format: string default: *none* example: `fileold=old.hdf5`

A.3.7. Symmetries

Parameter	Comment
ParaMag	This parameter specifies if a system should be treated as paramagnetic (1) or not paramagnetic (0). If so the symmetry is enforced. mandatory if: always value: {`0,1`} format: integer default: `1` example: `ParaMag=1`

Parameter	Comment
AF	This parameter specifies if an antiferromagnetic self-consistency should be used. This means that the spin up hybridization function is coupled to the down impurity electron and vice-versa. mandatory if: always value: {0,1} format: integer default: 0 example: AF=1
se-shift	This parameter is used to give the system a "kick" into a symmetry broken phase. In the first iteration the real part of the self-energy is set to this value for the spin up electron. mandatory if: always value: #se-shift format: float default: 0. example: se-shift=0.5

A.4. Input files nano-DΓA benzene

The input files for the nano benzene calculation, $V/t = 0.5$. For details see [110].

lead.benzene

```
6
flat 2.0 2.0 0.0 0.0
flat 2.0 2.0 0.0 0.0
flat 2.0 2.0 0.0 0.0
flat 2.0 2.0 0.0 0.0
flat 2.0 2.0 0.0 0.0
flat 2.0 2.0 0.0 0.0
```

site.benzene

```
6 1 1 0
0 1 2 3 4 5
```

t.benzene

```
0 0 0 0 0 0.0 0.0
1 0 1 0 0 0.0 0.0
```

```
2 0 2 0 0 0.0 0.0
3 0 3 0 0 0.0 0.0
4 0 4 0 0 0.0 0.0
5 0 5 0 0 0.0 0.0
0 0 1 0 0 -1.0 0.0
1 0 2 0 0 -1.0 0.0
2 0 3 0 0 -1.0 0.0
3 0 4 0 0 -1.0 0.0
4 0 5 0 0 -1.0 0.0
5 0 0 0 0 -1.0 0.0
0 0 2 0 0 0.0 0.0
1 0 3 0 0 0.0 0.0
2 0 4 0 0 0.0 0.0
3 0 5 0 0 0.0 0.0
4 0 0 0 0 0.0 0.0
5 0 1 0 0 0.0 0.0
0 0 3 0 0 0.0 0.0
1 0 4 0 0 0.0 0.0
2 0 5 0 0 0.0 0.0
0 0 0 0 1 0.0 0.0
1 0 1 0 1 0.0 0.0
2 0 2 0 1 0.0 0.0
3 0 3 0 1 0.0 0.0
4 0 4 0 1 0.0 0.0
5 0 5 0 1 0.0 0.0
0 0 1 0 1 -1.0 0.0
1 0 2 0 1 -1.0 0.0
2 0 3 0 1 -1.0 0.0
3 0 4 0 1 -1.0 0.0
4 0 5 0 1 -1.0 0.0
5 0 0 0 1 -1.0 0.0
0 0 2 0 1 0.0 0.0
1 0 3 0 1 0.0 0.0
2 0 4 0 1 0.0 0.0
3 0 5 0 1 0.0 0.0
4 0 0 0 1 0.0 0.0
5 0 1 0 1 0.0 0.0
0 0 3 0 1 0.0 0.0
1 0 4 0 1 0.0 0.0
2 0 5 0 1 0.0 0.0
```

V.benzene

```
0 0 0 0 0.50 0.0
1 1 0 0 0.50 0.0
2 2 0 0 0.50 0.0
3 3 0 0 0.50 0.0
4 4 0 0 0.50 0.0
5 5 0 0 0.50 0.0
0 0 0 1 0.50 0.0
1 1 0 1 0.50 0.0
2 2 0 1 0.50 0.0
3 3 0 1 0.50 0.0
4 4 0 1 0.50 0.0
5 5 0 1 0.50 0.0
```

Index

Bibliography

[1] M. WD. Tyrrell, *Hunting and gathering in the early silicon age.*, Handbook of organizational culture and climate, 85 (2000).

[2] I. M. Ross, *The foundation of the silicon age.*, Bell Labs technical journal **2**, 3 (1997).

[3] R. C. Thompson, S. H. Swan, C. J. Moore and F. S. vom Saal, *Our plastic age.* Philosophical Transactions of the Royal Society B: Biological Sciences **364**, 1973 (2009).

[4] N. W. Ashcroft and N. D. Mermin, *Solid State Physics*, Cengage Learning 978-0030839931, (1976).

[5] W. Kohn, *Nobel Lecture: Electronic structure of matterwave functions and density functionals*, Rev. Mod. Phys. **71**, 1253 (1999).

[6] J. W. Negele and H. Orland, *Quantum many-particle systems*, Addison-Wesley New York, ISBN 9780738200521 (1988).

[7] P. W. Anderson, *Localized Magnetic States in Metals*, Phys. Rev. **124**, 41 (1961)

[8] J. Kondo, *Resistance Minimum in Dilute Magnetic Alloys*, Progress of Theoretical Physics **32**, 37 (1964).

[9] P. W. Anderson, *Local Moments and Localized States*, Nobelprize.org. Nobel Media AB 2013. Web. 13 Aug 2013, http://www.nobelprize.org/nobel_prizes/physics/laureates/1977/anderson-lecture.html.

[10] P. Coleman, *Lectures on the Physics of Highly Correlated Systems VI*, 79 (2002), arXiv:cond-mat/0206003, (2002).

[11] A. C. Hewson, *The Kondo Problem to Heavy Fermions* Cambridge University Press, ISBN-13: 978-0521599474 (1997).

[12] B. Surer, M. Troyer, P. Werner, T. O. Wehling, A. M. Läuchli, A. Wilhelm and A. I. Lichtenstein, *Multiorbital Kondo physics of Co in Cu hosts*, Phys. Rev. B **85**, 085114 (2012).

[13] S. Gardonio, M. Karolak, T. O. Wehling, L. Petaccia, S. Lizzit, A. Goldoni, A. I. Lichtenstein, and C. Carbone, *Excitation Spectra of Transition-Metal Atoms on the Ag (100) Surface Controlled by Hunds Exchange*, Phys. Rev. Lett. **110**, 186404 (2013).

[14] J. Hubbard,*Electron Correlations in Narrow Energy Bands*, Proc. Roy. Soc. A **276**, 238 (1963).

[15] M. Caffarel and W. Krauth, *Exact diagonalization approach to correlated fermions in infinite dimensions: Mott transition and superconductivity*, Phys. Rev. Lett. **72**, 1545 (1994).

[16] J. K. Freericks and V. Zlatić, *Exact dynamical mean-field theory of the Falicov-Kimball model*, Rev. Mod. Phys. **75**, 1333 (2003).

[17] C. Lanczos, *Cornelius Lanczos, An Iteration Method for the Solution of the Eigenvalue Problem of Linear Differential and Integral Operators*, J. Res. Nat. Bur. Stand. **49**, 255 (1950).

[18] A.Georges and G. Kotliar, *Hubbard model in infinite dimensions*, Phys. Rev. B **45**, 6479 (1992).

[19] Y. Kuramoto, *Self-consistent perturbation theory for dynamics of valence fluctuations*, Z. Phys. B **53**, 37 (1983).

[20] J. Kroha, P. Wölfle and T. A. Costi, *Unified Description of Fermi and Non-Fermi Liquid Behavior in a Conserving Slave Boson Approximation for Strongly Correlated Impurity Models*, Phys. Rev. Lett. **79**, 261264 (1997).

[21] A. Costi, J. Kroha and P. Wölfle, Phys. Rev. B **53**, *Spectral properties of the Anderson impurity model: Comparison of numerical-renormalization-group and noncrossing-approximation results*, 1850 (1996).

[22] K. Haule, S. Kirchner, J. Kroha and P. Wölfle, *Anderson impurity model at finite Coulomb interaction U: Generalized noncrossing approximation*, Phys. Rev. B **64**, 155111 (2001).

[23] K. Wilson, *The renormalization group: Critical phenomena and the Kondo problem*, Rev. Mod. Phys. **47**, 773 (1975).

[24] M. Karski, C. Raas and G. S.Uhrig, *Single-particle dynamics in the vicinity of the Mott-Hubbard metal-to-insulator transition*, Phys. Rev. B **77**, 075116 (2008).

[25] T. D. Kühner and S. R. White, *Dynamical correlation functions using the density matrix renormalization group*, Phys. Rev. B **60**, 335 (1999).

[26] J. E. Hirsch and R. M. Fye, *Monte Carlo Method for Magnetic Impurities in Metals*, Phys. Rev. Lett. **56**, 2521 (1986).

[27] H. F. Trotter, *On the product of semi-groups of operators*, Proc. Am. Math. Soc. **10**, 545 (1959)

[28] M. Suzuki, *Relationship between d-Dimensional Quantal Spin Systems and (d+1)-Dimensional Ising Systems*, Prog. Theor. Phys. **56**, 1454 (1976)

[29] J. E. Hirsch, *Discrete Hubbard-Stratonovich transformation for fermion lattice models*, Phys. Rev. B **28**, 4059 (1983)

[30] S. Sakai, R. Arita and H. Aoki, *Numerical algorithm for the double-orbital Hubbard model:Hund-coupled pairing symmetry in the doped case*, Phys. Rev. B **70**, 172504 (2004).

[31] N. V. Prokofev, B. V. Svistunov and I. S. Tupitsyn , *Exact Quantum Monte Carlo Process for the Statistics of Discrete Systems*, JETP Letters **64**, 911 (1996).

[32] B. B. Beard and U.–J. Wiese, *Simulations of Discrete Quantum Systems in Continuous Euclidean Time*, Phys. Rev. Lett. **77**, 5130 (1996).

[33] S. M. A. Rombouts, K. Heyde and N. Jachowicz, *Quantum Monte Carlo Method for Fermions, Free of Discretization Errors*, Phys. Rev. Lett. **82**, 4155 (1999).

[34] A. N. Rubtsov and A. I. Lichtenstein, *Continuous time quantum Monte Carlo method for fermions: beyond auxiliary field framework*, JETP Letters **80**, 67 (2004).

[35] P. Werner and A. J. Millis, *Hybridization expansion impurity solver: General formulation and application to Kondo lattice and two-orbital models*, Phys. Rev. B **74**, 155107 (2006).

[36] P. Werner, A. Comanac, L. Medici, M. Troyer and A. J. Millis, *Continuous-Time Solver for Quantum Impurity Models*, Phys. Rev. Lett. **97**, 076405 (2006).

[37] E. Gull, P. Werner, O. Parcollet, and M. Troyer, *Continuous-time auxiliary-field Monte Carlo for quantum impurity models*, Europhys. Lett. **82**, 57003 (2008).

[38] N. V. Prokofev and B. V. Svistunov, *Polaron Problem by Diagrammatic Quantum Monte Carlo* Phys. Rev. Lett. **81**, 2514 (1998).

[39] J. Otsuki, H. Kusunose, P. Werner and Y. Kuramoto, *Continuous-Time Quantum Monte Carlo Method for the CoqblinSchrieffer Model*, J. Phys. Soc. Jpn. **76**, 114707 (2007).

[40] E. Pavarini, E. Koch, D. Vollhardt and A. I. Liechtenstein, *The LDA+DMFT approach to strongly correlated materials*, ISBN 978-3-89336-734-4 (2011).

[41] N. Metropolis, A. W. Rosenbluth, M. N. Rosenbluth, A. H. Teller and E. Teller, *Equation of State Calculations by Fast Computing Machines*, J. Chem. Phys. **21**, 1087 (1953).

[42] W. K. Hastings, *Monte Carlo sampling methods using Markov chains and their applications*, Biometrika **57**, 97 (1970).

[43] M. Troyer and U.–J. Wiese, *Computational Complexity and Fundamental Limitations to Fermionic Quantum Monte Carlo Simulations*, Phys. Rev. Lett. **94**, 170201 (2005).

[44] J. Yoo, S. Chandrasekharan, R. K. Kaul, D. Ullmo and H. U. Baranger, *On the sign problem in the HirschFye algorithm for impurity problems*, J. Phys. A: Math. Gen. **38**, 10307 (2005).

[45] K. Haule, *Quantum Monte Carlo impurity solver for cluster dynamical mean-field theory and electronic structure calculations with adjustable cluster base*, Phys. Rev. B **75**, 155113 (2007).

[46] A. M. Läuchli and P. Werner, *Krylov implementation of the hybridization expansion impurity solver and application to 5-orbital models*, Phys. Rev. B **80**, 235117 (2009).

[47] E. Gull, *Continuous-time quantum Monte Carlo algorithms for fermions*, PhD-Thesis Eidgenössische Technische Hochschule ETH Zürich, 18124 (2008).

[48] T. J. Park and J. C. Light, *Unitary quantum time evolution by iterative Lanczos reduction*, J. Chem. Phys. **85**, 5870 (1986).

[49] W. H. Press, S. A. Teukolsky, W. T. Vetterling and B. P.Flannery, *Numerical Recipes in C*, ISBN 0-521-43108-5 (1992).

[50] X. Wang, E. Gull, L. Medici, M. Capone and A. J. Millis, *Antiferromagnetism and the gap of a Mott insulator: Results from analytic continuation of the self-energy*, Phys. Rev. B **80**, 045101 (2009).

[51] S. Fuchs, T. Pruschke and M. Jarrell, *Analytic continuation of quantum Monte Carlo data by stochastic analytical inference*, Phys. Rev. E **81**, 056701 (2010).

[52] K. S. D. Beach, *Identifying the maximum entropy method as a special limit of stochastic analytic continuation*, arXiv:cond-mat/0403055v1, (2004).

[53] M. Hochbruck and C. Lubich, *On Krylov Subspace Approximations to the Matrix Exponential Operator*, SIAM J. Numer. Anal. **34**, 1911 (1997).

[54] L. Boehnke, H. Hafermann, M. Ferrero, F. Lechermann and O. Parcollet, *Orthogonal polynomial representation of imaginary-time Greens functions*, Phys. Rev. B **84**, 075145 (2011).

[55] P. Hohenberg and W. Kohn, *Inhomogeneous Electron Gas*, Phys. Rev. **136**, B864 (1964).

[56] M. Levy, *Universal variational functionals of electron densities, first-order density matrices, and natural spin-orbitals and solution of the v-representability problem*, Proc. Natl. Acad. Sci. USA **76**, 6062 (1979).

[57] R. O. Jones and O. Gunnarsson, *The density functional formalism, its applications and prospects*, Rev. Mod. Phys. **61**, 689 (1989).

[58] W. Kohn and L. J. Sham, *Self-Consistent Equations Including Exchange and Correlation Effects*, Phys. Rev. **140**, A1133 (1965).

[59] E. Schrödinger, *An Undulatory Theory of the Mechanics of Atoms and Molecules*, Phys. Rev. **28**, 1049 (1926).

[60] W. Metzner and D. Vollhardt, *Correlated Lattice Fermions in $d = \infty$ Dimensions*, Phys. Rev. Let. **62**, 324 (1989).

[61] E. Müller-Hartmann, *Correlated fermions on a lattice in high dimensions*, Z. Phys. B **74**, 507 (1989).

[62] E. Müller-Hartmann, *Fermions on a lattice in high dimensions.*, Int. J. Mod. Phys. B **3**, 2169 (1989).

[63] E. Müller-Hartmann, *The Hubbard model at high dimensions: some exact results and weak coupling theory*, Z. Phys. B **76**, 211 (1989).

[64] M. Karolak, G. Ulm, T. Wehling, V. Mazurenko, A. Poteryaev, A. Lichtenstein, *Double counting in LDA+DMFT The example of NiO*, J. Electron. Spectrosc. Relat. Phenom. **181**,11 (2010).

[65] F. Lechermann, A. Georges, A. Poteryaev, S. Biermann, M. Posternak, A. Yamasaki and O. K. Andersen, *Dynamical mean-field theory using Wannier functions: A flexible route to electronic structure calculations of strongly correlated materials*, Phys. Rev. B **74**, 125120 (2006).

[66] B. Amadon, F. Lechermann, A. Georges, F. Jollet, T. O. Wehling and A. I. Lichtenstein, *Plane-wave based electronic structure calculations for correlated materials using dynamical mean-field theory and projected local orbitals*, Phys. Rev. B **77**, 205112 (2008).

[67] M. Karolak, T. O. Wehling, F. Lechermann and A. I. Lichtenstein, *General DFT + + method implemented with projector augmented waves: electronic structure of $SrVO_3$ and the Mott transition in Ca_{2x} Sr_x RuO_4*, Journal of Physics: Condensed Matter **23**, 085601 (2011).

[68] N. Marzari, I. Souza and D. Vanderbilt, *An Introduction to Maximally-Localized Wannier Functions*, Psi-K Scientific Highlight of the Month **57**, (2003).

[69] O. K. Andersen, T. Saha-Dasgupta, S. Ezhov, L. Tsetseris, O. Jepsen, R. W. Tank, C. Arcangeli and G. Krier, *Third-generation MTOs*, Psi-k Newsletter **45**, (2001).

[70] E. Zurek, O. Japsen and O. K. Andersen, *NMTO Wannier-like functions for insulators and metals*, Chem. Phys. Chem. **6**, 1934 (2005).

[71] W. Kohn and N. Rostocker, *Solution of the Schrdinger Equation in Periodic Lattices with an Application to Metallic Lithium*, Phys. Rev. **94**, 1111 (1954).

[72] M. Zwierzycki and O. K. Andersen, *The Overlapping Muffin-Tin Approximation*, Proceedings of the European Conference Physics of Magnetism 2008, (2009).

[73] J. Kuneš, V. Anisimov, S. L. Skornyakov, A. V. Lukoyanov and D. Vollhardt, *NiO: Correlated Band Structure of a Charge-Transfer Insulator*, Phys. Rev. Let. **99**, 156404 (2007).

[74] N. Parragh, G. Sangiovanni, P. Hansmann, S. Hummel, K. Held and A. Toschi, *Effective crystal field and Fermi surface topology: a comparison of d- and dp-orbital models.*, arXiv:1303.2099v3, (2013).

[75] J. Kuneš, L. Baldassarre, B. Schächner, K. Rabia, C. A. Kuntscher, Dm. M. Korotin, V. I. Anisimov, J. A. McLeod, E. Z. Kurmaev and A. Moewes, *Metal-insulator transition in $NiS_{2-x}Se_x$*, Phys. Rev. B **81**, 35122 (2010).

[76] A. Perucchi, C. Marini, M. Valentini, P. Postorino, R. Sopracase, P. Dore, P. Hansmann, O. Jepsen, G. Sangiovanni, A. Toschi, K. Held, D. Topwal, D. D. Sarma and S. Lupi, *Pressure and alloying effects on the metal to insulator transition in $NiS_{2-x}Se_x$ studied by infrared spectroscopy.*, Phys. Rev. B **80**, 073101 (2009).

[77] M. Aichhorn, L. Pourovskii, V. Vildosola, M. Ferrero, O. Parcollet, T. Miyake, A. Georges and S. Biermann, *Dynamical mean-field theory within an augmented plane-wave framework: Assessing electronic correlations in the iron pnictide $LaFeAsO$*, Phys. Rev. B **80**, 85101 (2009).

[78] S. L. Skornyakov, A. V. Efremov, N. A. Skorikov, M. A. Korotin, Yu. A. Izyumov, V. I. Anisimov, A. V. Kozhevnikov and D. Vollhardt, *Classification of the electronic correlation strength in the iron pnictides: The case of the parent compound $BaFe_2As_2$*, Phys. Rev. B **80**, 92501 (2009).

[79] S. L. Skornyakov, A. A. Katanin and V. I. Anisimov, *Linear-Temperature Dependence of Static Magnetic Susceptibility in LaFeAsO from Dynamical Mean-Field Theory*, Phys. Rev. Lett. **106**, 47007 (2011).

[80] M. Aichhorn, L. Pourovskii and A. Georges, *Importance of electronic correlations for structural and magnetic properties of the iron pnictide superconductor LaFeAsO*, Phys. Rev. B **84**, 54529 (2011).

[81] K. Held, http://online.kitp.ucsb.edu/online/cem02/held/ (unpublished), (2002).

[82] X. Wang, M. J. Han, L. de' Medici, H. Park, C. A. Marianetti and A. J. Millis, *Covalency, double-counting, and the metal-insulator phase diagram in transition metal oxides*, Phys. Rev. B **86**, 195136 (2012).

[83] M. J. Han, X. Wang, C. A. Marianetti and A. J. Millis, *Dynamical Mean-Field Theory of Nickelate Superlattices*, Phys. Rev. Lett. **107**, 206804 (2011).

[84] P. Hansmann, X. Yang, A. Toschi, G. Khaliullin, O. K. Andersen and K. Held. *Turning a Nickelate Fermi Surface into a Cupratelike One through Heterostructuring*, Phys. Rev. Lett. **103**, 16401 (2009).

[85] P. Hansmann, A. Toschi, X. Yang, O. K. Andersen and K. Held, *Electronic structure of nickelates: From two-dimensional heterostructures to three-dimensional bulk materials*, Phys. Rev. B **82**, 235123 (2010).

[86] J. C. Slater and G. F. Koster, *Simplified LCAO Method for the Periodic Potential Problem*, Phys Rev **94**, 1498 (1954).

[87] F. Lechermann, S. Biermann and A. Georges, *Interorbital Charge Transfers and Fermi-Surface Deformations in Strongly Correlated Metals: Models, $BaVS_3$ and Na_xCoO_2*, Progress of Theoretical Physics Supplement **160**, 233 (2005).

[88] G. Racah, *Theory of Complex Spectra. III*, Phys. Rev. **63**, 367 (1943).

[89] S. Capponi and F. F. Assaad, *Spin and charge dynamics of the ferromagnetic and antiferromagnetic two-dimensional half-filled Kondo lattice model*, Phys. Rev. B **63**, 155114 (2001).

[90] S. Sugano, Y. Tanabe and H. Kamimura, *Multiplets of transition-metal ions in crystals*, Academic Press, (1970).

[91] N. F. Mott, *Metal-Insulator Transition*, Rev. Mod. Phys. **40**, 677 (1968).

[92] A. Georges, G. Kotliar, W. Krauth and M. J. Rozenberg, *Dynamical mean-field theory of strongly correlated fermion systems and the limit of infinite dimensions*, Rev. Mod. Phys. **68**, 13 (1996).

[93] A. I. Lichtenstein, M. I. Katsnelson and G. Kotliar, *Finite-Temperature Magnetism of Transition Metals: An* ab initio *Dynamical Mean-Field Theory*, Phys. Rev. Lett. **87**, 067205 (2001).

[94] S. Y. Savrasov, G. Kotliar and E. Abrahams, *Correlated electrons in δ-plutonium within a dynmacil mean-field picture*, Nature **410**, 793 (2001).

[95] J. Kuneš, V. Křapek, N. Parragh, G. Sangiovanni, A. Toschi and A. V. Kozhevnikov, *Spin State of Negative Charge-Transfer Material* $SrCoO_3$, Phys. Rev. Lett. **109**, 117206 (2012).

[96] V. I. Anisimov, J. Zaanen, O. K. Andersen, *Band theory and Mott insulators: Hubbard* U *instead of Stoner* I, Phys. Rev. B **44**, 943 (1991).

[97] M. T. Czyżyk and G. A. Sawatzky, *Local-density functional and on-site correlations: The electronic structure of* La_2CuO_4 *and* $LaCuO_3$, Phys. Rev. B **49**, 14211 (1994).

[98] I. V. Solovyev, P. H. Dederichs and V. I. Anisimov, *Corrected atomic limit in the local-density approximation and the electronic structure of* d *impurities in Rb*, Phys. Rev. B **50**, 16861 (1994).

[99] J. Braun, J. Minár, H. Ebert, M. I. Katsnelson and A. I. Lichtenstein, *Spectral Function of Ferromagnetic* 3*d Metals: A Self-Consistent* LSDA + DMFT *Approach Combined with the One-Step Model of Photoemission*, Phys. Rev. Lett. **97**, 227601 (2006).

[100] B. Amadon, F. Lechermann, A. Georges, F. Jollet, T. O. Wehling and A. I. Lichtenstein, *Plane-wave based electronic structure calculations for correlated materials using dynamical mean-field theory and projected local orbitals*, Phys. Rev. B **77**, 205112 (2008).

[101] G. Kotliar, S. Y. Savrasov, G. Pálsson and G. Biroli, *Cellular Dynamical Mean Field Approach to Strongly Correlated Systems*, Phys. Rev. Lett. **87**, 186401 (2001).

[102] M. H. Hettler, A. N. Tahvildar-Zadeh, M. Jarrell, T. Pruschke and H. R. Krishnamurthy, *Nonlocal dynamical correlations of strongly interacting electron systems*, Phys. Rev. B **58**, 7475 (1998).

[103] M. H. Hettler, M. Mukherjee, M. Jarrell and H. R. Krishnamurthy, *Dynamical cluster approximation: Nonlocal dynamics of correlated electron systems*, Phys. Rev. B **61**, 12739 (2000).

[104] A. N. Rubtsov, M. I. Katsnelson and A. I. Lichtenstein, *Dual fermion approach to nonlocal correlations in the Hubbard model*, Phys. Rev. B **77**, 033101 (2008).

[105] A. Toschi, A. A. Katanin and K. Held, *Dynamical vertex approximation: A step beyond dynamical mean-field theory*, Phys. Rev. B **75**, 045118 (2007).

[106] K. Held, A. A. Katanin and A. Toschi, *Dynamical vertex approximation - an introduction*, Progr. Theor. Phys. Suppl. **176**, 117 (2008).

[107] A. A. Katanin, A. Toschi and K. Held, *Comparing pertinent effects of antiferromagnetic fluctuations in the two- and three-dimensional Hubbard model*, Phys. Rev. B **80**, 075104 (2009).

[108] P. Hansmann, *LDA+DMFT: From bulk to heterostructures*, PhD-Thesis (2010).

[109] A. Valli, G. Sangiovanni, O. Gunnarsson, A. Toschi and K. Held, *Dynamical Vertex Approximation for Nanoscopic Systems*, Phys. Rev. Lett. **24**, 246402 (2010).

[110] A. Valli, *Electronic correlations at the nanoscale*, PhD-Thesis TU Wien, (2013).

[111] V. Anisimov, I. Nekrasov, D. Konakov, T. Rice and M. Sigrist, *Orbital-selective Mott-insulator transition in* $Ca_2 - xSr_xRuO_4$, Eur. Phys. J. B **25**, 191 (2002).

[112] L. de'Medici, A. Georges and S. Biermann, *Orbital-selective Mott transition in multiband systems: Slave-spin representation and dynamical mean-field theory*, Phys. Rev. B **72**, 205124 (2005).

[113] A. Koga, N. Kawakami, T. M. Rice and M. Sigrist, *Orbital-Selective Mott Transitions in the Degenerate Hubbard Model* Phys. Rev. Lett. **92**, 216402 (2004).

[114] A. Koga, N. Kawakami, T. M. Rice and M. Sigrist, *Spin, charge, and orbital fluctuations in a multiorbital Mott insulator*, Phys. Rev. B **72**, 045128 (2005).

[115] S. Biermann, L. de'Medici and A. Georges, *Non-Fermi-Liquid Behavior and Double-Exchange Physics in Orbital-Selective Mott Systems*, Phys. Rev. Lett. **95**, 206401 (2005).

[116] T. Costi and A. Liebsch, *Non-Fermi-liquid phases in the two-band Hubbard model: finite-temperature exact diagonalization study of Hund's rule coupling*, Eur. Phys. J. B **51**, 523 (2006).

[117] L. de'Medici, S. R. Hassan and M. Capone, *Genesis of Coexisting Itinerant and Localized Electrons inIronPnictides*, J. Supercond, Nov. Magn. **22**, 535 (2009).

[118] L. de'Medici, *Hund's coupling and its key role in tuning multiorbital correlations*, Phys. Rev. B **83**, 205112 (2011).

[119] K. Haule and G. Kotliar, *Coherenceincoherence crossover in the normal state of iron oxypnictides and importance of Hund's rule coupling*, New. J. Phys. **11**, 025021 (2009).

[120] A. O. Shorikov, M. A. Korotin, S. V. Streltsov, S. L. Skornyakov, D. M. Korotin and V. I. Anisimov, *Coulomb correlation effects in LaOFeAs: LDA+DMFT(QMC) study*, arXiv:0804.3283, (2008).

[121] S. Biermann, F. Aryasetiawan and A. Georges, *First-Principles Approach to the Electronic Structure of Strongly Correlated Systems: Combining the GW Approximation and Dynamical Mean-Field Theory*, Phys. Rev. Lett. **90**, 086402 (2003).

[122] C. Taranto, M. Kaltak, N. Parragh, G. Sangiovanni, G. Kresse, A. Toschi and K. Held, *Comparing GW +DMFT and LDA+DMFT for the testbed material $SrVO_3$*, arXiv:1211.1324, (2012).

[123] J. Kuneš, R. Arita, P. Wissgott, A. Toschi, H. Ikeda and K. Held, *Wien2wannier: From linearized augmented plane waves to maximally localized Wannier functions*, Comp.Phys.Commun. **181**, 1888 (2010).

[124] A. A. Mostofi, J. R. Yates, Y.–S. Lee, I. Souza, D. Vanderbilt and N. Marzari, *Wannier90: A Tool for Obtaining Maximally-Localised Wannier Functions*, Comput. Phys. Commun. **178**, 685 (2008).

[125] https://en.wikipedia.org/wiki/Cubic_harmonic, 23.7.2013.

[126] Y. Tanabe and S. Sugano, *On the absorption spectra of complex ions ii*, J. Phys. Soc. Jpn. **5**, 766 (1954).

[127] F. M. F. de Groot, J. C. Fuggle, B. T. Thole and G. A. Sawatzky, *2 p x-ray absorption of 3 d transition-metal compounds: An atomic multiplet description including the crystal field*, Phys. Rev. B **42**, 54595468 (1990).

[128] O. Gunnarsson, O. K. Andersen, O. Jepsen and J. Zaanen, *Density-functional calculation of the parameters in the Anderson model: Application to Mn in CdTe*, Phys. Rev. B **39**, 1708 (1989).

[129] F. Aryasetiawan, M. Imada, A. Georges, G. Kotliar, S. Biermann and A. I. Lichtenstein, *Frequency-dependent local interactions and low-energy effective models from electronic structure calculations*, Phys. Rev. B **70**, 195104 (2004).

[130] A. Georges, L. de' Medici and J. Mravlje, *Strong Correlations from Hunds Coupling*, Annu. Rev. Cond. Mat. Phys. **4**, 137 (2013).

[131] J. Kanamori, *Electron Correlation and Ferromagnetism of Transition Metals*, Prog. Theor. Phys. **30**, 275 (1963).

[132] M. Haverkort, *Spin and orbital degrees of freedom in transition metal oxides and oxide thin films studied by soft x-ray absorption spectroscopy*, PhD-thesis Universität zu Köln, (2005).

[133] J. Kuneš, P. Novăk , V. Křápek, D. Novosekov, Dm. M. Korotin and V. I. Anisimov, *Spin state transition and covalent bonding in $LaCoO_3$*, Phys. Rev. B **86**, 195104 (2012).

[134] F. Gebhard, *The Mott Metal-Insulator Transitioni: Models and Methods (Springer Tracts in Modern Physics*, Springer Verlag Berlin Heidelberg, ISBN-13: 978-3642082634 (2000).

[135] S. R. White and R. M. Noack, *Real-space quantum renormalization groups*, Phys. Rev. Let. **68**, 3487 (1992).

[136] N. Blümer, *Mott-Hubbard Metal-Insulator Transition and Optical Conductivity in High Dimensions*, PhD-Thesis Universität Augsburg, (2002).

[137] K. Held, *Electronic structure calculations using dynamical mean field theory*, Adv. Phys. **56**, 829 (2007).

[138] A. Georges, G. Kotliar, W. Krauth and M. J. Rozenberg, *Dynamical mean-field theory of strongly correlated fermion systems and the limit of infinite dimensions*, Rev. Mod. Phys. **68**, 13 (1996).

[139] C. Knecht, *Numerische Analyse des Hubbard-Modells im Rahmen der Dynamischen Molekularfeld-Theorie*, Diploma-Thesis Joannes Gutenberg-Universität, (2003).

[140] O. Gunnarsson, G. Sangiovanni, A. Valli, and M. W. Haverkort, emphFourier transformation and response functions, Phys. Rev. B **82**, 233104 (2010).

[141] E. Koch, G. Sangiovanni and O. Gunnarsson, *Sum rules and bath parametrization for quantum cluster theories*, Phys. Rev. B **78**, 115102 (2008).

[142] N. Marzari, A. Mostofi,Y. A. Arash, R. Jonathan, I. Souza and D. Vanderbilt, *Maximally localized Wannier functions: Theory and applications*, Rev. Mod. Phys. **84**, 1419 (2012).

[143] G. H. Wannier, *The Structure of Electronic Excitation Levels in Insulating Crystals*, Phys. Rev. **52**, 191 (1937).

[144] J. Des Cloizeaux, *Energy Bands and Projection Operators in a Crystal: Analytic and Asymptotic Properties*, Phys. Rev. **135**, A685 (1964).

[145] N. Marzari and D. Vanderbilt, *Maximally localized generalized Wannier functions for composite energy bands*, Phys. Rev. B **56**, 12847 (1997).

[146] P.–O. Löwdin, *A Note on the QuantumMechanical Perturbation Theory*, J. Chem. Phys. **19**, 1396 (1951).

[147] I. V. Solovyev, *Lattice distortion and magnetic ground state of* $YTiO_3$ *and* $LaTiO_3$, Phys. Rev. B **69**, 134403 (2004).

[148] J. Mannhart, D. H. A. Blank, H. Y. Hwang, A. J. Millis and J.–M. Triscone, *Two-Dimensional Electron Gases at Oxide Interfaces*, MRS Bull. **33**, 1027 (2008).

[149] P. Blaha, K. Schwarz, G. K. H. Madsen, D. Kvasnicka and J. Luitz, *WIEN2k, An Augmented Plane Wave + Local Orbitals Program for Calculating Crystal Properties*, (Karlheinz Schwarz, Techn. Universität Wien, Austria), ISBN 3-9501031-1-2 (2001).

[150] A. W. Sandvik, *Stochastic method for analytic continuation of quantum Monte Carlo data*, Phys. Rev. B **57**, 10287 (1998).

[151] A. Abendschein and F. F. Assaad, *Temperature dependence of spectral functions for the one-dimensional hubbard model: Comparison with experiments*, Phys. Rev. B **73**, 165119 (2006).

[152] J. G. Bednorz and K. A. Müller, *Possible High* T_c *Superconductivity in the Ba-La-Cu-O System*, Z. Phys B – Condensed Matter **64**, 189 (1986).

[153] M. Aichhorn, E. Arrigoni, M. Potthoff and W. Hanke, *Antiferromagnetic to superconducting phase transition in the hole- and electron-doped Hubbard model at zero temperature*, Phys. Rev. B **74**, 024508 (2006).

[154] P. R. C. Kent, T. Saha–Dasgupta, O. Jepsen, O. K. Andersen, A. Macridin, T. A. Maier, M. Jarrell and T. C. Schulthess, Phys. Rev. B **78**, 035132 (2008).

[155] J. Zaanen, O. Jepsen, O. Gunnarsson, A. T. Paxton, O. K. Andersen and A. Svane, *What can be learned about high* T_c *cuprates from local density theory?*, Phys. C **153**, 1636 (1988).

[156] H. J. A. Molegraaf, C. Presura, D. van der Marel, P. H. Kes and M. Li, *Superconductivity-Induced Transfer of In-Plane Spectral Weight in* $Bi_2Sr_2CaCu_2O_{8+\delta}$, Science **295**, 2239 (2002).

[157] A. Toschi, M. Capone, M. Ortolani, P. Calvani, S. Lupi and C. Castellani, *Temperature Dependence of the Optical Spectral Weight in the Cuprates: Role of Electron Correlations*, Phys. Rev. Let. **95**, 097002 (2005).

[158] A. Toschi and M. Capone, *Optical sum rule anomalies in the cuprates: Interplay between strong correlation and electronic band structure*, Phys. Rev. B **77**, 014518 (2008).

[159] A. Comanac, L. de' Medici, M. Capone and A. J. Millis, *Optical conductivity and the correlation strength of high-temperature copper-oxide superconductors*, Nat. Phys. **4**, 287 (2008).

[160] D. Nicoletti, O. Limaj, P. Calvani, G. Rohringer, A. Toschi, G. Sangiovanni, M. Capone, K. Held, S. Ono, Y. Ando and S. Lupi, *High-Temperature Optical Spectral Weight and Fermi-liquid Renormalization in Bi-Based Cuprate Superconductors*, Phys. Rev. Let. **105**, 077002 (2010).

[161] L. deMedici, X. Wang, M. Capone and A. J. Millis, *Correlation strength, gaps, and particle-hole asymmetry in high-T_c cuprates: A dynamical mean field study of the three-band copper-oxide model*, Phys. Rev. B **80**, 054501 (2009).

[162] C. Weber, K. Haule and G. Kotliar, *Optical weights and waterfalls in doped charge-transfer insulators: A local density approximation and dynamical mean-field theory study of $La_{2-x}Sr_xCuO_4$*, Phys. Rev. B **78**, 134519 (2008).

[163] G. Rohringer, A. Toschi, A. Katanin and K. Held, *Critical Properties of the Half-Filled Hubbard Model in Three Dimensions*, Phys. Rev. Let. **107**, 256402 (2011).

[164] S. Fuchs, E. Gull, L. Pollet, E. Burovski, E. Kozik, T. Pruschke and M. Troyer, *Thermodynamics of the 3D Hubbard Model on Approaching the Néel Transition*, Phys. Rev. Let. **106**, 030401 (2011).

[165] V. J. Emery, *Theory of High-T_c Superconductivity in Oxides*, Phys. Rev. Let. **58**, 2794 (1987).

[166] F. C. Zhang and T. M. Rice, *Effective Hamiltonian for the superconducting Cu oxides*, Phys. Rev. B **37**, 3759 (1988).

[167] J. Zaanen, G. A. Sawatzky and J. W. Allen, *Band gaps and electronic structure of transition-metal compounds*, Phys. Rev. Let. **55**, 418 (1985).

[168] O. K. Andersen, A. I. Liechtenstein, O. Jepsen and F. Paulsen, *LDA Energy Bands, Low-Energy Hamiltonians, $t', t'', t_\perp(\mathbf{k}), and J_\perp$.*, J. Phys. Chem. Solids **56**, 1573 (1995).

[169] E. Pavarini, I. Dasgupta, T. Saha–Dasgupta, O. Jepsen and O. K. Andersen, *Band-Structure Trend in Hole-Doped Cuprates and Correlation with T_{cmax}*, Phys. Rev. Let. **87**, 47003 (2001).

[170] M. Casula, Ph. Werner, L. Vaugier, F. Aryasetiawan, T. Miyake, A. J. Millis and S. Biermann, *Low-Energy Models for Correlated Materials: Bandwidth Renormalization from Coulombic Screening*, Phys. Rev. Lett. **109**, 126408 (2012).

[171] Q. Yin, A. Gordienko, X. Wan and S. Y. Savrasov, *Calculated Momentum Dependence of Zhang-Rice States in Transition Metal Oxides*, Phys. Rev. Lett. **100**, 066406 (2008).

[172] C. Weber, K. Haule and G. Kotliar, *Strength of correlations in electron- and hole-doped cuprates*, Nat. Phys. **6**, 574 (2010).

[173] X. Wang, L. de' Medici, A. J. Millis, *Role of oxygen-oxygen hopping in the three-band copper-oxide model: Quasiparticle weight, metal insulator and magnetic phase boundaries, gap values, and optical conductivity*, Phys. Rev. B **83**, 094501 (2011).

[174] R. H. Potze, G. A. Sawatzky and M. Abbate, *Possibility for an intermediate-spin ground state in the charge-transfer material* $SrCoO_3$, Phys. Rev. B **51**, 11501 (1995).

[175] M. Zhuang, W. Zhang, A. Hu and N. Ming, *Possible magnetic ground state in the perovskite* $SrCoO_3$, Phys. Rev. B **57**, 13655 (1998).

[176] K. Asai, O. Yokokura, N. Nishimori, H. Chou, J. M. Tranquada, G. Shirane, S. Higuchi, Y. Okajima and K. Kohn, *Neutron-scattering study of the spin-state transition and magnetic correlations in* $La_{1-x}Sr_xCoO_3$ *(*$x = 0$*) and* 0.08, Phys. Rev. B **50**, 3025 (1994).

[177] J. B. Goodenough, *Coexistence of localized and itinerant d electrons*, Mat. Res. Bull. **6**, 967 (1971).

[178] T. Miyake, K. Nakamura, R. Arita and M. Imada, *Comparison of Ab initio Low-Energy Models for LaFePO, LaFeAsO,* $BaFe_2As_2$*, LiFeAs, FeSe, and FeTe: Electron Correlation and Covalency*, J. Phys. Soc. Jpn. **79**, 044705 (2010).

[179] A. F. Albuquerque, F. Alet, P. Corboz, P. Dayal, A. Feiguin, S. Fuchs, L. Gamper, E. Gull, S. G urtler, A. Honecker, R. Igarashi, M. K orner, A. Kozhevnikov, A. L auchli, S. R. Manmana, M. Matsumoto, I. P. McCulloch, F. Michel,R. M. Noack, G. Pawłowski, L. Pollet, T. Pruschke, U. Schollw ock, S. Todo, S. Trebst, M. Troyer, P. Werner and S. Wessel, *The* $\{ALPS\}$ *project release 1.3: Open-source software for strongly correlated systems*, J. Magn. Magn. Mater. **310**, 1187 (2007).

[180] A. Liebsch and T. A. Costi, *Non-Fermi-liquid phases in the two-band Hubbard model: finite-temperature exact diagonalization study of Hund's rule coupling*, Eur. Phys. J. B **51**, 523 (2006).

[181] A. K. McMahan, R. T. Scalettar and M. Jarrell, *Screening of* $4f$ *moments and delocalization in the compressed light rare earths*, Phys. Rev. B **80**, 235105 (2009).

[182] E. R. Ylvisaker, J. Kuneš, A. K. McMahan, and W. E. Pickett, *Charge Fluctuations and the Valence Transition in Yb under Pressure*, Phys. Rev. Lett. **102**, 246401 (2009).

[183] J. Kuneš, Dm. M. Korotin, M. A. Korotin, V. I. Anisimov, P. Werner, *Pressure-Driven Metal-Insulator Transition in Hematite from Dynamical Mean-Field Theory*, Phys. Rev. Lett. **102**, 146402 (2009).

[184] Y. Long, Y. Kaneko, S. Ishiwata, Y. Taguchi and Y. Tokura, *Synthesis of cubic $SrCoO_3$ single crystal and its anisotropic magnetic and transport properties*, J. Phys.: Condens. Matter **23**, 245601 (2011).

[185] L. de' Medici, A. Georges, G. Kotliar and S. Biermann, *Mott Transition and Kondo Screening in f-Electron Metals*, Phys. Rev. Lett. **95**, 066402 (2005).

[186] M. Jarrell, H. Akhlaghpour and Th. Pruschke, *Periodic Anderson model in infinite dimensions*, Phys. Rev. Lett. **70**, 1670 (1993).

[187] M. Jarrell, *Symmetric periodic Anderson model in infinite dimensions*, Phys. Rev. B **51**, 7429 (1995).

[188] M. Jarrell and J. E. Gubernatis, *Bayesian inference and the analytic continuation of imaginary-time quantum Monte Carlo data*, Phys. Rep. **269**, 133 (1996).

[189] Th. Pruschke, R. Bulla and M. Jarrell, *Low-energy scale of the periodic Anderson model*, Phys. Rev. B **61**, 12799 (2000).

[190] P. Werner, A. J. Millis, *High-Spin to Low-Spin and Orbital Polarization Transitions in Multiorbital Mott Systems*, Phys. Rev. Lett. **99**, 126405 (2007).

[191] E. Şaşıoğlu, A. Schindlmayr, C. Friedrich, F. Freimuth, S. Blügel, *Wannier-function approach to spin excitations in solids*, Phys. Rev. B **81**, 54434 (2010).

[192] M. Matsumoto and T. Nishimura, *Mersenne Twister: A 623-dimensionally equidistributed uniform pseudorandom number generator*, ACM Trans. on Modeling and Computer Simulation **8**, 3 (1998).

[193] P. Peterson, *F2PY: a tool for connecting Fortran and Python programs*, Int. J. Computational Science and Engineering **4**, 296 (2009).

[194] The HDF Group. Hierarchical data format version 5, 2000-2010. http://www.hdfgroup.org/HDF5.

[195] L. Vaugier, H. Jiang and S. Biermann, *Hubbard U and Hund exchange J in transition metal oxides: Screening versus localization trends from constrained random phase approximation*, Phys. Rev. B **86**, 165105 (2012).

[196] E. Benckiser, M. W. Haverkort, S. Br uc, E. Goering, S. Macke, A. Frañó, X. Yang, O. K. Andersen, G. Cristiani, H.-U. Habermeier, A. V. Boris, I. Zegkinoglou,

P. Wochner, H.-J. Kim, V. Hinkov and B. Keimer, *Orbital reflectometry of oxide heterostructures*, Nat. Mat. **10**, 189 (2011).

[197] M. Uchida, K. Ishizaka, P. Hansmann, Y. Kaneko, Y. Ishida, X. Yang, R. Kumai, A. Toschi, Y. Onose, R. Arita, K. Held, O. K. Andersen, S. Shin and Y. Tokura, *Pseudogap of Metallic Layered Nickelate* $R_{2-x}\mathrm{Sr}_x\mathrm{NiO}_4$ *(*R = Nd, Eu*) Crystals Measured Using Angle-Resolved Photoemission Spectroscopy*, Phys. Rev. Let. **106**, 027001 (2011).

[198] M. Uchida, K. Ishizaka, P. Hansmann, X. Yang, M. Sakano, J. Miyawaki, R. Arita, Y. Kaneko, Y. Takata, M. Oura, A. Toschi, K. Held, A. Chainani, O. K. Andersen, S. Shin and Y. Tokura, *Orbital characters of three-dimensional Fermi surfaces in* $Eu_{2-x}Sr_xNiO_4$ *as probed by soft-x-ray angle-resolved photoemission spectroscopy*, Phys. Rev. B **84**, 241109 (2011).

[199] Ph. Werner, E. Gull, M. Troyer and A. J. Millis, *Spin Freezing Transition and Non-Fermi-Liquid Self-Energy in a Three-Orbital Model*, Phys. Rev. Lett. **101**, 166405 (2008).

[200] X. Wang, M. J. Han, L. de' Medici, H. Park, C. A. Marianetti and A. J. Millis, *Covalency, double-counting, and the metal-insulator phase diagram in transition metal oxides*, Phys. Rev. B **86**, 195136 (2012).

[201] A. Pletzer, D. McCune, S. Muszala, S. Vadlamani and S. Kruger, *Exposing Fortran Derived Types to C and Other Languages*, Computing in Science Engineering **10**, 86 (2008).

[202] N. Sergueev, Q.-F. Sun, H. Guo, B. G. Wang J. Wang, *Spin-polarized transport through a quantum dot: Anderson model with on-site Coulomb repulsion*, Phys. Rev. B **65**, 165303 (2002).

[203] P. Hansmann, L. Vaugier and S. Biermann, *private communication.*

[204] H. Hafermann, K. R. Patton and Ph. Werner, *Improved estimators for the self-energy and vertex function in hybridization-expansion continuous-time quantum Monte Carlo simulations*, Phys. Rev. B **80**, 205106 (2012).

[205] H. J. Vidberg and J. W. Serene, *Solving the Eliashberg Equations by Means of N-Point Padé Approximants*, J. Low Temp. Phys. **29**, 179 (1977).

[206] G. Thornton, B. C. Tofield and D. E. Williams, *Spin state equilibria and the semiconductor to metal transition of* $LaCoO_3$, Solid State Commun. **44**, 1213 (1982).

[207] G. Briceño, H. Chang, X. Sun, P. G. Schultz and X.-D. Xiang, *A Class of Cobalt Oxide Magnetoresistance Materials Discovered with Combinatorial Synthesis*, Science **270**, 273 (1995).

[208] K. Takada, H. Sakurai, E. Takayama-Muromachi, F. Izumi, R. A. Dilanian and T. Sasaki, *Superconductivity in two-dimensional CoO_2 layers*, Nature **422**, 53 (2003).

[209] K. Asai, P. Gehring, H. Chou and G. Shirane, *Temperature-induced magnetism in* $LaCoO_3$, Phys. Rev. B **40**, 10982 (1989).

[210] R. Caciuffo, D. Rinaldi, G. Barucca, J. Mira, J. Rivas, M. A. Señarís-Rodríguez, P. G. Radaelli, D. Fiorani and J. B. Goodenough, *Structural details and magnetic order of* $La_{1-x}Sr_xCoO_3$ ($x <\approx 0.3$), Phys. Rev. B **59**, 1068 (1999).

[211] G. Racah, *Theory of Complex Spectra. II*, Phys. Rev. **62**, 438 (1942).

[212] J. P. Perdew and W. Yue, *Accurate and simple density functional for the electronic exchange energy: Generalized gradient approximation*, Phys. Rev. B **33**, 8800 (1986).

[213] A. D. Becke, *Density-functional exchange-energy approximation with correct asymptotic behavior*, Phys. Rev. A **38**, 3098 (1988).

[214] A. D. Becke *A new mixing of HartreeFock and local densityfunctional theories*, J. Chem. Phys. **98**, 1372 (1993).

[215] A. D. Becke *Densityfunctional thermochemistry. III. The role of exact exchange*, J. Chem. Phys. **98**, 5648 (1993).

Acknowledgements

First and foremost I want to thank my supervisor Giorgio Sangiovanni. He was always supportive and came up with new ideas when I was stuck. He is not only a great physicist but also a nice person who I always enjoyed working with. I also want to thank my group in Würzburg for making my thesis writing an enjoyable time in the office.
When I moved to Würzburg our group was quite small, but I was warmly welcomed by Fakher Assad and his group for which I want to thank them. The beach volleyball matches always were a welcome leisure time activity in the summer.
I am grateful that Karsten Held offered me the opportunity to start my PhD in Vienna. He and his group stayed very influential even after the move and I want to thank him for his advices and my colleagues and office mates in Vienna for the good time.
My PhD would not have been the same without my stay in Tokyo. I want to thank Ryotaro Arita for his invitation and him and his group members for introducing me to a bit of the culture, food and life of Japan.
Many people helped me during the code development, either by providing benchmarks or by explaining algorithmic details to me, I appreciated your help very much. I am also grateful to all people who in the second half of my PhD started to collaborate with me on the code development.
I also want to thank the many friends and colleagues who accompanied me on the way and my sisters, Sophie and Stephanie and their family for always being there for me.
The people without whom all this would not have been possible, my parents Rita and Laci, I want to thank with all of my heart for always trusting and believing in me.
And last but not least the person who came here with me and who supported me during the hard times of my thesis, enjoyed the good times with me and cheered me on. Thank you for taking the chance, Anna.